Stony Brook University

Image reconstruction theory and implementation for low-dose X-ray computed tomography

A Dissertation Presented

by

Yan Liu

to

The Graduate School

in Partial Fulfillment of the Requirements

for the Degree of

Doctor of Philosophy

in

Electrical Engineering

Stony Brook University

December 2014

Stony Brook University
The Graduate School

Yan Liu

We, the dissertation committee for the above candidate for the
Doctor of Philosophy degree, hereby recommend
acceptance of this dissertation.

_____
Dr. Jerome Z. Liang – Dissertation Advisor
Professor of Radiology and Computer Science

_____
Dr. Thomas G. Robertazzi – Co-Advisor
Professor of Electrical and Computer Engineering

_____
Dr. Muralidhara Subbarao - Chairperson of Defense
Professor of Electrical and Computer Engineering

_____
Dr. Gene Gindi – Committee Members
Associate Professor of Electrical and Computer Engineering and Radiology

_____
Dr. William H. Moore – Committee Members
Associate Professor of Radiology, MD

This dissertation is accepted by the Graduate School

_____
Charles Taber
Dean of the Graduate School

Abstract of the Dissertation

Image reconstruction theory and implementation for low-dose X-ray computed tomography

by

Yan Liu

Doctor of Philosophy

in

Electrical Engineering

Stony Brook University

2014

The excessive X-ray radiation exposure during clinical examinations has been reported to be linked to increase lifetime risk of cancers in patients. Directly lower computed tomography (CT) dose without improving reconstruction technique will degrade the image quality and is not acceptable. The objective of this dissertation is investigating novel reconstruction methods to improve image quality in low-dose cases. In practice, it is usually more convenient to improve the conventional analytical methods by refining projection model and designing new filters due to the fast computing time and low computational complexity. However, the reconstructions from analytical methods are still sensitive to artifacts and photon noise; therefore, the improved analytical methods may not be applicable to low-dose CT reconstructions. Recently, iterative image reconstruction methods have been found to be very effective in low-dose CT reconstruction and can be mainly classified into two categories: statistical iterative reconstruction methods and algebraic iterative reconstruction methods. The statistical iterative reconstruction methods, which incorporate statistical noise model, prior model and projection geometry, have shown the ability to reduce noise and improve resolution for image reconstruction from low-mAs projection data. The algebraic iterative reconstruction methods, which were originally invented in 1970s, have been improved in the past decade to reconstruct image from sparse-view projection data, particularly when adequate prior models are used as objective functions. In this dissertation, four improved reconstruction methods are proposed and discussed for different types of low-dose data (for example: low-mAs and sparse-view data). Both computer simulation and real data (i.e., physical phantom and patients' data) are used for evaluations. The clinical potentials of the proposed methods are also exploited in this dissertation.

To my parents and grandparents

Contents

List of Figures

List of Tables

List of Acronyms

AL	augmented Lagrangian
ADMM	alternating direction method of multiplier
ADSIR	adaptive dictionary based statistical iterative reconstruction
AUC	area under the curve
ART	algebraic reconstruction technique
ASD	adaptive steepest descent
AwTV	adaptive-weighted total variation
CHO	channelized Hotelling observer
CB	cone beam
CBCT	cone-beam computed tomography
CS	compressed sensing
CT	computed tomography
CNR	contrast noise ratio
DNA	Deoxyribonucleic acid
DD	distance driven
EL	Euler-Lagrange
EPTV	TV-based edge preserving
ESF	edge spread function
FB	fan beam
FBP	filtered backprojection
FDK	Feldkamp–Davis –Kress
FOV	field of view
FWHM	full-width at half-maximum
GGMRF	generalized Gaussian Markov random field
GS	Gauss-Seidel
HU	Hounsfield Unit
ICD	iterative coordinate descent
IR	iterative reconstruction
IRB	Institutional Review Board
kVp	kilovoltage-peak
LI	linear interpolation
MAP	maximum *a posteriori*
mAs	milliampere-seconds
MSE	mean square error
ML	maximum likelihood
MRF	Markov random field
OS	ordered subsets
PICCS	prior image constraint compressed sensing
POCS	projection onto convex sets

PRWLS	penalized re-weighted least-squares
PUWLS	penalized uniform weighted least square strategy
PWLS	penalized weighted least-squares
RIP	restricted isometry property
ROC	receiver of characteristic
ROI	region of interest
RWLS	re-weighted least-squares
SART	simultaneous algebraic reconstruction technique
SF	separable footprint
SF-TR	SF using the trapezoid functions in the transaxial direction only
SF-TT	SF using the trapezoid functions in both transaxial and axial directions
SIR	statistics-based iterative algorithms
SNR	signal-to-noise ratio
TFE	tangent field estimation
TV	total variation
TVS	total variation stokes
UQI	universal quality index
VSW	volume-shadow weighting
WLS	weighted least-squares
1D	one-dimensional
2D	two-dimensional
3D	three-dimensional

Acknowledgements

First of all, I would like to express my deepest gratitude to my dissertation adviser, Prof. Jerome Z. Liang, for his excellent guidance, caring, patience, encouragement and financial support during my thesis research. Indeed, this dissertation would never have been completed without his enthusiasm, dedication and great support. Also I would like to appreciate Prof. Thomas Robertazzi for coordinating the collaboration between the Department of Electrical and Computer Engineering and the Department of Radiology and for his valuable comments on my dissertation. I would also like to thank my dissertation committee –Prof. Murali Subbarao, Prof. Gene Gindi and Prof. William Moore for their precious time and valuable suggestions.

I would like to thank all the members and alumni of the Laboratory for Imaging Research and Informatics (IRIS lab): especially Dr. Jianhua Ma, Dr. Yi Fan, Dr. Jing Wang and Dr. Hongbing Lu for their software packages and kindly advises for reconstruction and noise reduction of low-dose computed tomography; Dr. Hongbing Zhu, Dr. Qin Lin, Bowen Song, Yang Zhang, Hao Zhang, Lin Chen, Dr. Huafeng Wang and Ke Wang for their helpful discussions as well as their excellent works on medical imaging; Prof. William Moore for his clinical guidance; Priya Bhattacharji for her assistance on clinical data management. I'm also thankful to my mentor Dr. Zhou Yu and scientists: Dr. Yu Zou and Dr. Wenli Wang from Toshiba Medical Research Institute at USA (TMRU) for their advices and contributions in spectral computed tomography image reconstruction.

Finally, I would like to thank Ke. Her support, encouragement, quiet patience and unwavering love were undeniably the bedrock upon which the past ten years of my life have been built. I think my parents, Zhaojie Liu and Xiuhua Gao for their love, patience, encouragement and support in all my life. Also I thank Ke's parents, Mingwei Wang and Liping Xu for their support and trust in the past ten years. I would like to thank my grandparents, Yongcai Liu, Jingzhen Wei and Lianqing Zhou for their love and understanding.

This work was supported in part by the NIH/NCI under grant #CA143111 and #CA082402. Some of the text, figures and tables are appeared in publications: "Adaptive-weighted total variation minimization for sparse data toward low-dose x-ray computed tomography image reconstruction" Physics in Medicine and Biology, 57, 7923-7956, 2012, "Total Variation-Stokes Strategy for Sparse-View X-ray CT Image Reconstruction", IEEE Transaction on Medical Imaging, 33 (3), 749 – 763, 2014; and "Low-mAs X-ray CT image reconstruction by adaptive-weighted TV constrained penalized re-weighted least-squares", Journal of X-ray Science and Technology， 22 (4), 437-57,2014. Based on the copyright agreement with IOP Publishing Limited, IEEE and IOS Press, Yan Liu has the rights to include partial/full articles in thesis.

Chapter 1 . History and fundamental of x-ray CT physics

Computed Tomography (CT) was the first non-invasive imaging technique and has evolved into an indispensable imaging method in clinical routine [7]. In 2007, it was estimated that more than 62 million CT scans were obtained in the United States [6]. When X-ray radiation penetrates the patients' body, it transfers part of its energy to the tissues and cause radiation damage, which may break molecular bonds, such as those in Deoxyribonucleic acid (DNA). [35]. In view of the lifetime negative effects of X-ray exposure to the human body, minimizing the exposure risk has been one of the major endeavors in current CT examinations [6, 24].

In this chapter, I will give an introduction of X-ray CT, including a brief review of CT history, the fundamentals of X-ray physics, the necessity of lower CT dosage and current low-dose CT reconstruction techniques.

1.1.History of X-ray CT

In 1895, W. Röntgen discovered a new kind of radiation, which was named as X-ray. He took the very first picture of his wife's hand by using X-rays. He received the Nobel Prize for physics in 1901 for the remarkable contribution of discovery of the X-ray [7]. In 1917, J. Radon published his epochal work on providing formulas for the inverse transform of the reconstruction problem. In 1956, R. N. Bracewell derived the technique of solving inverse problem by using inverse Fourier transform [5]. In 1963, A. M. Cormack reported the mathematical implementation for tomographic reconstruction [16]. In 1971, Sir G. Housfield and J. Ambrose published the first clinical scans with an EMI head scanner [16]. A. M. Cormack and Sir. G. Hounsfield are pioneers of medical CT and received the Nobel Prize for Medicine in 1979 for their epochal work during the 1960s and 1970s [16]. Since then, the CT imaging technique was widely used for different clinical applications and dramatically improved on both hardware and software.

The type of CT scanner built by EMI in 1971 is called the first-generation CT. In this first-generation scanner, only one pencil beam is measured at a time, the X-ray source and detector were move parallel to acquire a group of projection data in each individual projection view [35]. Figure 1.1 shows the geometry of the first commercial first-generation CT scanners from Siemens in 1974 [7]. Although the results from first-generation CT scanners were promising, the scan took about 4.5min for a CT scanner. In addition to the drawback of long X-ray exposure that mentioned before, the patient motion during one scan can decrease the image quality. To eliminate such drawback, the second-generation scanners were introduced in 1975. The geometry of second generation scanners is shown in Figure 1.2.

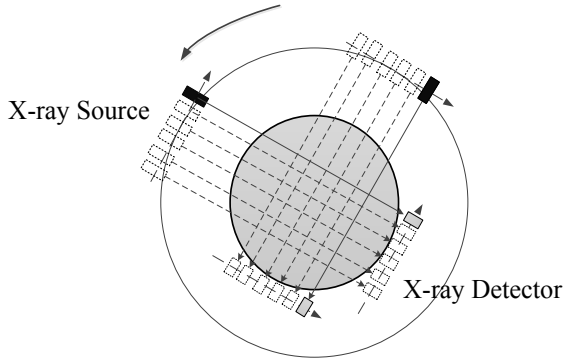

Figure 1.1 First-generation CT scanner geometry

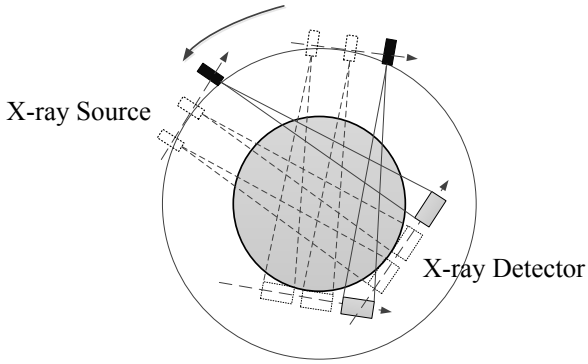

Figure 1.2 Second-generation CT scanner geometry

In second-generation CT scanner, the rotation steps were reduced by using multiple detectors, which can detect several pencil beams simultaneously. The duration for one scan is under 20 sec, which is far less than the required time of first-generation CT scanner. Although the scanning time is dramatically decrease by second-generation scanner compared to the first-generation. The field of view (FOV) of the object for each projection still very small and require a movement for both source and detector in each view. In the third-generation scanner, as shown in Figure 1.3, the fan shape detector contains a large number of detectors, and the FOV can cover the whole object in each view. This eliminated the time consuming translation stage allowing scan time to be significantly reduced. This design dramatically improved the practicality of CT. By using slip rings for power and data transmission, the gantry could rotate at constant speed during successive scans, the scan time reduced to 0.5 sec or less [35].

Fourth generation scanners were introduced almost simultaneously with the third generation to solve the detector stability and aliasing. In order to increase sampling density during the entire scan, instead of a row of detectors which moved with the X-ray source, fourth generation scanners used a stationary 360 degree ring of detectors (see Figure 1.4). In this design, only the fan shaped X-ray beam rotates around the patient. As compared to the third-generation geometry, the new generation has a high sampling rate, which determined by the number of projection measurements. While the fourth generation scanner has high sampling rate, it is not practical for a number of reasons. The major problem is the scattering issue in fourth generation scanner; it is hard to reduce

the scatter-to-primary ratio by hardware. In addition, the large number of detectors required to form the complete ring increase the cost of CT scanner [89]. Therefore, only a few fourth generation scanners were constructed and nearly all state-of-art clinical CT machines employ the third generation scanner geometry.

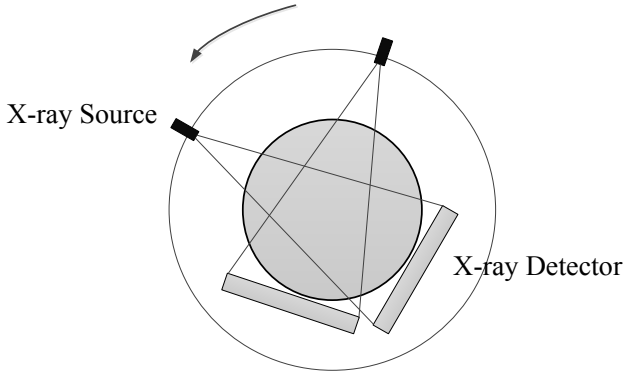

Figure 1.3 Third-generation CT scanner geometry

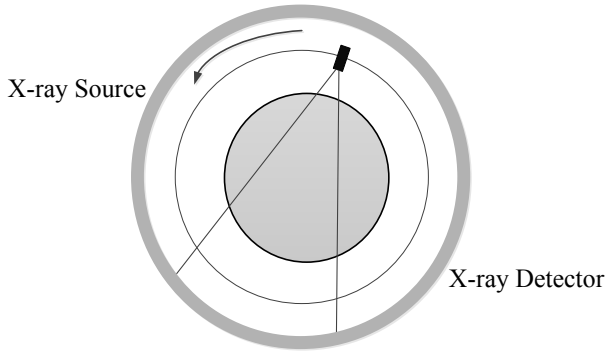

Figure 1.4 Fourth-generation CT scanner geometry

Despite numerous technological developments in the 1980s, it still took a long time for a large volume scan when a slice-by-slice scanner was used [89]. This long scan time was unacceptable for many clinical situations because it indeed impact image coverage and contrast utilization. For example, once a contrast agent is injected to a patient, the entire scan should be completed during the same phase of contrast uptake (e.g., the arterial phase or venous phase), and a prolonged scan time results suboptimal contrast-enhanced-images [35]. Another example is the breath motion during the scan. The slice-by-slice scanner results the misregistration between slices because it is almost impossible to scan the entire organ with one breath-hold.

To overcome these difficulties, the helical/spiral scanners were introduced in the late 1980s and early 1990s [32, 44]. In helical/spiral CT scanner, the projection data are continuously acquired while the patient is translated at a constant speed. Therefore a large volumetric projection data can be rapidly acquired along the patient's longitudinal axis. In order to further improve the volume coverage and scan time, the multi-slice detector technology was introduced to acquire several slices data simultaneously during one rotation. As the development of hardware technology, the CT manufacturers were able to provide detector with more and more detector rows. Nowadays, most CT

manufacturers are able to provide 64-slice helical/spiral CT scanners compared to four-slice CT scanner in 1998.

Although helical/spiral CT scanners has significant improve the volume coverage, many applications require large three-dimensional (3D) volume coverage and very thin slice thickness in a short scanning time such as CT angiography [35]. Projection data acquired in multi-slice cone-beam geometry offers large volume coverage and thin slice image reconstruction and, therefore, multi-slice cone-beam CT (CBCT) has been widely used in clinics such as radiation therapy [6]. In 2013, Toshiba launched their newest 320-slice multi-slice CT scanner (i.e., Aquilion ONE ViSION Edition) which can provides 640 reconstructions at one rotation. The scan time is only 0.275 second and the slice thickness is 0.5 mm.

1.2.Fundamentals of X-ray CT imaging

1.2.1 Production of X-rays

The X-ray tube is one of the most important components in CT scanners, which can generate photons for CT scan. The X-ray tube basically consists of two components: cathode and anode within a vacuum tube. The cathode provides high-speed electrons and anode is the target used to generate X-ray photons. The X-ray photons are produced when a substance is bombarded by high-speed electrons. As far as we know, about 99% of the input energy is converted to heat in the X-ray tube due to the ionization of the target atoms[35]. In this type of interaction, no X-ray was produced.

In addition to the ionization of the target atoms, there are three types of interactions could generate X-ray when the electrons approach the nucleus of the target atom: (1) the electron suffers a radiation loss and produce white radiation which covers the entire range of the energy spectrum; (2) the high speed electron collides with the inner shell electrons of the target tom and liberates the inner shell electron [35]; (3) the electron collides a nucleus directly and its entire energy appears as bremsstrahlung. Since multiple interactions could happen in the anode, the incident photons may have different energies. Figure 1.5 [98] illustrates the X-ray tube energy spectrum of a tungsten anode produced by different acceleration tube voltages

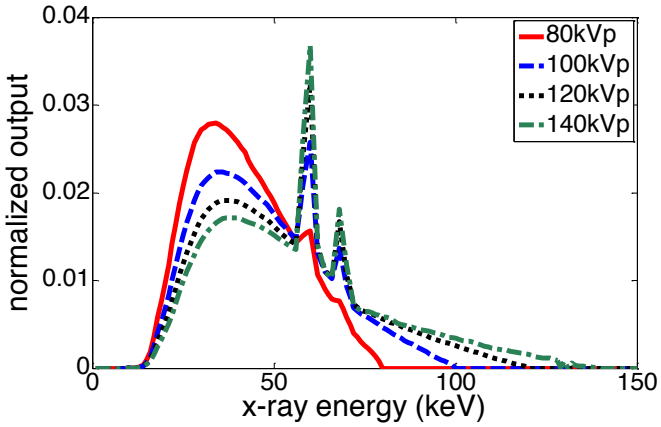

Figure 1.5 X-ray energy spectrum for tube voltage at 80, 100, 120 and 140kVp

1.2.2 Photon-matter interaction

The X-ray is known to have very high, material-dependent capability of matter of penetration [7]. As the X-ray passes through an object, the number of photons decreases exponentially along the projection path due to the absorption and scattering i.e., photoelectric absorption, coherent/Rayleigh scattering and Compton scattering). At each location, the loss of the photons can be characterized by the local attenuation coefficient, which is denoted by μ hereafter [89]. The attenuate coefficients for different material are energy dependent. Due to the energy spectrum produced by the X-ray tube, the received photons always have different energies. This procedure was mathematically described by the well-known Lambert-Beer's Law:

$$I(l) = \int I_0(E,\gamma) D(E) \exp\left[-\int_l \mu(E,x,y)dl\right] dE, \tag{1.1}$$

where $I(l)$ is the measured photons at path l, $I_0(E,\gamma)$ is the incident photon spectra after the bowtie filter at channel index γ, $D(E)$ denotes the detector responsivity , $\mu(E,x,y)$ is the energy dependent attenuation coefficient located at location (x,y).

In practice, in order to decrease numerical complexity, most of image reconstruction algorithms assume the X-ray photons have the same energy level; therefore, the relationship between the incident photon number $I_0(\gamma)$ and the measured photons number $I(l)$ can be simplified as:

$$I(l) = I_0(\gamma) \exp\left(-\int_l \mu(x,y)dl\right), \tag{1.2}$$

The difference between Eq. (1.1) and Eq. (1.2) is normally called as beam-hardening artifacts.

In clinics, to enhance the contrast differences between different tissue types, the attenuation coefficients are conventionally rescaled to CT number:

$$\text{CT number} = \frac{\mu - \mu_{water}}{\mu_{water}} \times 1000, \tag{1.3}$$

where μ_{water} indicates the attenuation coefficient of water. The CT number unit is called Hounsfield Unit (HU), named after Sir G. N Hounsfield. By definition, the CT number is zero for water and -1000 HU for air. The CT numbers of soft tissue range from -100 HU to 60 HU and Bone range from 250 HU to over 1000 HU [89].

1.2.3 X-ray detection

Since the interaction principles between X-ray photons and matters, the X-ray quanta are not measured directly. They are often detected through the interaction products (e.g. emitted photoelectrons) [7]. As far as we know, there are two types of detectors for CT: direct detectors (e.g. xenon detectors) and indirect detectors (e.g. solid-state detectors) [89]. The xenon detectors are used nowadays for low-end single-slice CT scanners due to the low cost. It depends on the ionization of xenon and the detection efficiency for this type of detector is low. When the X-ray photon enters the xenon detectors, the radiation is able to ionize the high-pressure xenon gas. Then the positive ions migrate to the cathodes and electrons migrate to the anodes and the current signal is used as a measurement of the X-ray flux entering the detector.

Another current state-of-the-art detector type is the solid-state scintillator detector, which has been equipped by almost all CT systems nowadays. Such a detector essentially consists of two main component: scintillation medium and photon detector [7]. When the X-ray enters the detectors, the short-wave X-ray quanta are converted into long-wave radiation (i.e. light) inside the scintillation, then, the light is subsequently detected by a photodiode mounted on the crystal. Due to the fact that the mass density of the xenon is about three magnitudes smaller than the mass density of the solid-state detector material, the effective absorption of quanta is significantly improved.

Another important component for X-ray detector is the anti-scatter collimator, which filters out the photons not traveling along the source-to-detector path. The scatter artifacts therefore are suppressed. The design of collimator is very complicated and beyond the scope of our study, we will not include it in this dissertation.

1.2.4 Projection data readout

In practice, the projection data are often saved in particular formats by different venders. Normally, the raw data from the CT scanner often contains two types of headers. The first type of hearders is often arranged at the beginning of the raw data file. It may contains the software version, patient's information (such as scanning date/time, patient identification number, etc) and scanning protocols (such as tube current and tube voltage, slices numbers, scanning time for one rotation, coach position, etc). In practice, it is almost impossible for the researchers to readout above information without particular software provided by venders.

The second type of headers is arranged at the beginning of each frame, it may contain some particular information for each projection view. Although the contents of this part are not touchable by researchers, most venders would like to provide the size of header at each frame. By neglecting the frame headers with known size, it is possible to read out the projection data at each frame.

Besides the headers issue, the sinogram data from the raw files are often scaled in particular ways, which may have some specific physical meanings. A scale factor is often desired to rescale the projection data. In our clinical data studies, with the help from Siemens Engineers, we can readout the correct projection data from each frame.

1.3. Low-dose CT and low-dose CT image reconstruction techniques

The excessive X-ray radiation exposure during clinical exams has been reported to be linked to increase lifetime risk of cancers in patients [6, 24]. Therefore, the issue of radiation dose reduction during the X-ray CT inspection has been raised and received great attention. Directly lower CT dose without improving reconstruction technique will degrade the image quality and is not acceptable. The motivation of this dissertation is investigating novel low-dose CT numerical algorithms to improve low-dose CT image qualities.

To our knowledge, two classes of strategies have been widely discussed for radiation reduction: (1) lower the X-ray flux towards each detector bins (by lower X-ray tube current–measured by mAs or lower X-ray tube voltage–measured by kVp); and (2) lower the required number of projection views during the inspection. The strategy of adjustment in mAs or kVp usually leads to noisy projection data at each view and results in inconsistent images compared to the data from normal-mAs or kVp scan. The

inconsistency may cause image artifacts. The latter strategy usually suffers aliasing artifacts due to insufficient angular sampling and may also cause image artifacts. As a result, the diagnostic quality of the CT images could be degraded if inadequate methods are applied during the image reconstruction operations. To address these problems, various image processing and reconstruction methods with capability for noise suppression and recovery of missing data have been reported [3, 4, 13-15, 17, 20, 21, 25, 26, 33, 37, 45, 46, 48, 52-54, 57, 58, 62, 63, 65, 69, 77, 79, 80, 85, 87, 92, 93, 96, 100, 101, 104, 105, 107].

The first method focuses on restoring the ideal line integrals sinogram data (i.e., projection data after log-transformation) from acquired low-mAs (or low-kVp) projection data [21, 25, 26, 45, 46, 48, 54, 57, 58, 63, 77, 92, 93]. The objective of these methods is improving the image quality via either statistics-based sinogram restoration [21, 45, 46, 48, 58, 92] or statistics-based iterative image reconstruction [25, 26, 63, 93]. For example, the noise properties of low-mAs CT sinogram data were studied by analyzing repeatedly-scanned data from a commercial CT scanner and a nonlinear relationship between the sample mean and variance of the acquired low-mAs sinogram data was determined [48, 57, 63]. The relationship provides reasonable theoretical predictions of the variance of the projection data for statistical CT image reconstruction. Based on the relationship, the CT image can be reconstructed from the acquired low-mAs or low-kVp scans by minimizing the penalized re-weighted least-squares (PRWLS) cost function, where the re-weighting is due to the dependence of the variance on the mean because of the non-stationary noise property [4, 33, 52, 93]. In contrast, the penalized weighted least-squares (PWLS) method doesn't consider the dependence of the variance on the mean. The variances remain unchanged even the mean values have been updated. Such restoration principle can be also applied for sinogram restoration based on the penalized likelihood function [45, 46]. A series of general sophisticated CT image reconstruction algorithms were also reported [25, 26].

The second method focuses on reconstructing the CT image from acquired sparse-view data with adequate prior information about the desired image [13, 33, 51, 52, 79, 80, 101]. In 2006, Donoho proposed the concept of Compressed Sensing (CS) and proved that sparse signals or piecewise images could be satisfactorily reconstructed from far less sampling data than the requirement of the Nyquist sampling theorem [23]. However, for CT image reconstruction, the associated transfer matrix of sparse signals in the transfer domain is less likely to meet the restricted isometry property (RIP) condition [8, 9, 79, 80]. Therefore, an exact implementation of the CS theorem for low-dose CT may not be feasible. An alternative solution, which is called as adaptive steepest-descent-POCS (ASD-POCS) method, was invented by Sidky *et al* by minimizing the total variation (TV) of the desired image for CT image reconstruction from sparse projection views [79, 80]. In their method, both fan-beam and cone-beam artifacts from sparse or limited projection views can be efficiently suppressed compared to other classical methods, e.g., the well-known expectation maximization algorithm. Recently, a more general term of TV, called adaptive-weighted total variation (AwTV) model, was proposed to improve the preservation of edge details by bringing the local information into the above conventional TV model [52]. Besides the ASD-POCS method and its general case: AwTV-POCS method, a prior image-constrained compressed sensing (PICCS) method and Dictionary learning methods were introduced to further reduce the number of required projection

views by incorporating prior images or patch information to the CS theorem [13, 101]. We also proposed a total-variation stokes-POCS (TVS-POCS) to improve the weakness of the conventional TV and AwTV model.

In this dissertation, I will focus on the low-dose CT image reconstruction algorithms on both (1) lower the mAs level and (2) lower the number of projection views cases.

Chapter 2 . CT image reconstruction methods

The CT image reconstruction problem is essentially an inverse problem. The photons were attenuated when the corresponding X-ray penetrate the object. The aim of the CT image reconstruction is recovering the amount of attenuated photons at each location with known incident photons and detected photons. Based on the nature of the algorithms utilized in those methods, the image reconstruct methods can be classified to categories: analytical approach and iterative reconstruction approach. The iterative reconstruction approach can be further divided to statistical model based iterative image reconstruction approach and algebraic based iterative image reconstruction approach. In this chapter, I will briefly review the three types of CT image reconstruction strategies that commonly used nowadays.

2.1 Analytical methods for image reconstruction

The analytical methods for CT image reconstructions have been widely used for commercial CT scanner. Compared to other reconstruction method, this method is advanced in fast computational time and linear noise property. In this section, I will briefly review the Fourier slice theorem and two-dimensional (2D) filtered back-projection (FBP) method based on the derivations in [41]. Then, a conventional linear interpolation based 3D Feldkam-Davis-Kress (FDK) method will be discussed. An advanced volume-shadow-weighting based FDK algorithm which aimed to suppress the non-uniform noise across the FOV will be elaborated in chapter 3.

2.1.1. Fourier slice theorem and 2D filtered back-projection method

The analytical approach is based on the Fourier slice theorem, which theoretically illustrate the equivalency of the one-dimensional Fourier transform of projection data and the two-dimensional Fourier transform of the desired image $f(x,y)$. Let $F(u,v)$ be the 2D Fourier transform of the image function as [41]:

$$F(u,v)=\int_{-\infty}^{\infty}\int_{-\infty}^{\infty}f(x,y)e^{-j2\pi(ux+vy)}dxdy, \tag{2.1}$$

Define a projection at an angle θ, in the (t,s) coordinate system a projection $P_\theta(t)$ along lines of constant *t* is defined as:

$$P_\theta(t)=\int_{-\infty}^{\infty}f(t,s)ds=\int_{-\infty}^{\infty}\int_{-\infty}^{\infty}f(x,y)\delta(x\cos\theta+y\sin\theta-t)dxdy, \tag{2.2}$$

where

$$t=x\cos\theta+y\sin\theta \text{ and } s=-x\sin\theta+y\sin\theta, \tag{2.3}$$

The one-dimensional Fourier transform of projection $P_\theta(t)$ is:

$$S_\theta(w)=\int_{-\infty}^{\infty}P_\theta(t)e^{-j2\pi wt}dt, \tag{2.4}$$

where (w,θ) is the polar coordinate representation of (u,v):

$$u=w\cos\theta, \tag{2.5}$$

$$v = w\sin\theta, \tag{2.6}$$

Substituting Eq. (2.4) into the Eq. (2.2), we get the following equation [89]:

$$\begin{aligned} S_\theta(w) &= \int_{-\infty}^{\infty}\left[\int_{-\infty}^{\infty}\int_{-\infty}^{\infty} f(x,y)\delta(x\cos\theta + y\sin\theta - t)dxdy\right]\exp(-j2\pi wt)dt \\ &= \int_{-\infty}^{\infty}\int_{-\infty}^{\infty} f(x,y)\exp(-j2\pi w(x\cos\theta + y\sin\theta))dxdy \\ &= \int_{-\infty}^{\infty}\int_{-\infty}^{\infty} f(x,y)\exp(-j2\pi(ux+vy)dxdy \\ &= F(u,v), \end{aligned} \tag{2.7}$$

This equation indicates that by taking the one-dimensional Fourier transform for each projection at angles $\theta_1,\theta_2,...,\theta_k$, the values of two-dimensional Fourier transform $F(u,v)$ on radial lines can be determined. This is the essential idea of the Fourier slice theorem. Therefore, if an infinite number of projections are taken, then $F(u,v)$ would be known at all points in the *uv*-plane [41]. Then the desired image function $f(x,y)$ can be reconstructed by using the two-dimensional inverse Fourier transform:

$$f(x,y) = \int_{-\infty}^{\infty}\int_{-\infty}^{\infty} F(u,v)e^{j2\pi(uv+vy)}dudv, \tag{2.8}$$

If we substitute Eq. (2.5) and Eq. (2.6) into Eq. (2.8), we can get:

$$\begin{aligned} f(x,y) &= \int_0^{\pi}\left[\int_{-\infty}^{\infty} F(w,\theta)|w|e^{j2\pi wt}\,dw\right]d\theta \\ &= \int_0^{\pi}\left[\int_{-\infty}^{\infty} S_\theta(w)|w|e^{j2\pi wt}\,dw\right]d\theta, \end{aligned} \tag{2.9}$$

This equation can be expressed as:

$$f(x,y) = \int_0^{\pi} Q_\theta(x\cos\theta + y\sin\theta)d\theta, \tag{2.10}$$

where

$$Q_\theta(t) = \int_{-\infty}^{\infty} S_\theta(w)|w|e^{j2\pi wt}dw, \tag{2.11}$$

Eq. (2.11) represents a filtering operation where $Q_\theta(t)$ is called a "filtered projection" and $|w|$ is the frequency response of the ramp filter. Eq. (2.11) indicates the desired image can be obtained by adding the filtered projections at different angles. Therefore, this algorithm is called as filtered back-projection algorithm. Due to the accuracy and computational efficiency, the FBP algorithm is the most prevalent algorithm for CT image reconstruction.

2.1.2. Three dimensional Feldkam-Davis-Kress method

Due to the geometry advance of cone-beam (CB) CT, most commercial clinical CT scanner applied multi-channel detector plane to acquire multi-slice sinogram simultaneously. In order to solve the 3D image reconstruction problem, the FBP algorithm was improved and adapted to 3D for CBCT image reconstruction, which is called as Feldkam-Davis-Kress algorithm. In this section, I will briefly review the mathematics of FDK algorithm. An advanced FDK algorithm, which aimed to solve the non-uniform noise across the FOV, will be presented in Chapter 3.

There are two types of CB detector configurations depending on the sampling methods: equiangular intervals on a curve detector and equispace intervals on a flat panel detector [70]. In

this study, we take the equispace CB configuration to show our adaptive approach. For simplicity, a circular source trajectory is used and the source of X-rays is assumed as an ideal point. The introduced methods and experiments can be readily extended to the equiangular CB configuration and helical source trajectory.

A typical CB FDK algorithm for reconstruction of 3D image $f(x,y,z)$ from flat panel projection data with equispatial rays is given by [41]:

$$f_{FDK}(x,y,z)=\frac{1}{2}\int_0^{2\pi}\frac{R\cdot D}{(R-s)^2}\cdot\bar{p}\left(\beta,i\left(x,y,z,\beta\right),j\left(x,y,z,\beta\right)\right)d\beta, \tag{2.12}$$

where

$$\bar{p}\left(\beta,i,j\right)=\left(\frac{D}{\sqrt{D^2+(i\cdot\Delta_i)^2+(j\cdot\Delta_j)^2}}\,p\left(\beta,i,j\right)\right)*h(j), \tag{2.13}$$

β denotes the projection angle, R is the distance from the X-ray source to the rotation axis in voxel unit, as shown in Fig. (2.12), D is the distance from the X-ray source to the detector plane in voxel unit, i and j are the row and column indices of the corresponding detector cells on the 2D detector domain, respectively, Δ_i and Δ_j are the detector size along the i and j directions in voxel unit, p denotes the projection data, h represents the 1D ramp filter, * is the convolution operator, and t and s are the location indices of a point rotated by the angular displacement of the source-detector array, which are defined as [41]:

$$t=x\cos\beta+y\sin\beta \quad \text{and} \quad s=-x\sin\beta+y\cos\beta, \tag{2.14}$$

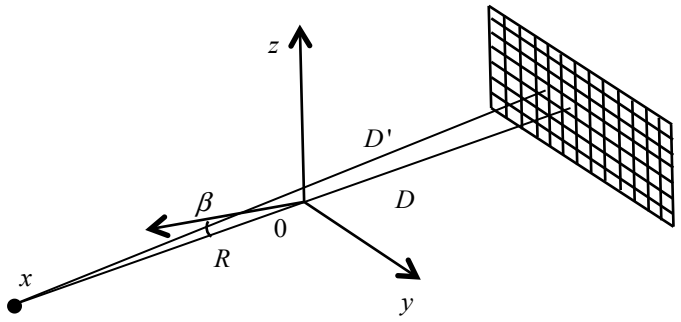

Figure 2.1 Coordinates and CB geometry in CT

In practice, due to the digitalization of the desired image and sampled data, the FDK algorithm is implemented in the discrete form. Let $\Delta\beta=2\pi/N$ and $\beta_n=n\Delta\beta$, where N is the total number of projection views over 2π rotation and $n=0,1,...,N-1$, $\Delta\beta$ is the source increment. Let $i=-I/2,-I/2+1,...,I/2-1,I/2$ and $j=-J/2,-J/2+1,\ ...,J/2-1,J/2$, where ($I$+1) denotes the total number of detector rows and (J+1) is the total number of detector columns. Then the samples of the projection data can be denoted as $p(\beta_n,i,j)$. Assume that a ray, which goes through both the source and the concerned voxel, intersects the detector at detector cell (k, l), the contribution of detector cells to the concerned voxel at angle β_n can be linear interpolated (LI) from the nearby detector cells of (k, l). Therefore in the linear interpolation based FDK (LI-FDK) algorithm, the reconstructed image can be expressed as:

$$f_{LI-FDK}(x,y,z)=\frac{\Delta\beta}{2}\sum_{n=0}^{N-1}\frac{R\cdot D}{\left(R+x\sin\beta_n-y\cos\beta_n\right)^2}\times\left\{(1-\kappa)\left[(1-\xi)\bar{p}(\beta_n,i,j)+\xi\bar{p}(\beta_n,i+1,j)\right]\right.$$

$$\left.+\kappa\left[(1-\xi)\bar{p}(\beta_n,i,j+1)+\xi\bar{p}(\beta_n,i+1,j+1)\right]\right\},\tag{2.15}$$

where $\kappa=l-\lfloor l\rfloor$ and $\xi=k-\lfloor k\rfloor$, $\lfloor k\rfloor$ denotes the largest integer smaller than *k*, $\lfloor l\rfloor$ denotes the largest integer smaller than *l*. $\bar{p}(\beta_n,i,j)$ denotes the filtered projection data:

$$\bar{p}(\beta_n,i,j)=\sum_{m=-J/2}^{J/2}\frac{D}{\sqrt{D^2+(i\cdot\Delta_i)^2+(m\cdot\Delta_j)^2}}p(\beta_n,i,m)h(j-m)\tag{2.16}$$

m denotes a column index at the *i-th* row of the detector.

2.2 Statistical model based iterative reconstruction

While the FBP method could be used for CT image reconstruction, one disadvantage of FBP is that it essentially weights all X-rays equally [7]. Since the polychromatic property of the X-ray spectrum, the CT image suffers artifacts, such as the beam-hardening and metal artifacts, etc. Therefore, iterative reconstruction methods are often served as alternative ways by giving adaptive weights to reduce the influence of the rays which have large variances. The statistic model based iterative reconstruction (SIR) method is one of the prevalent methods for CT image reconstruction. It has the potential to improve image quality for low-dose CT in noise reduction and artifacts removal. Compared to the conventional FBP and FDK algorithm, the SIR follows the maximum a *posterior* (MAP) estimation, its cost function often consists of two parts: (1) data fidelity term from statistical noise modeling and (2) regularization term from the prior knowledge of the desired image. This section reviews the noise modeling of conventional CT and variance estimation in projection data. The conventional PWLS based image reconstructions are also reviewed in this section.

2.2.1 Statistical modeling of CT

The statistical modeling of CT plays a critical role in SIR, an accurate modeling can benefit the image quality. Previous studies have extensively investigated the statistical modeling of CT in either transmission domain or sinogram domain. In CT measurements noise usually contains two principal sources, i.e., quantum statistical noise and electronic noise, wherein the quantum statistical noise is due to the limited number of photons collected by the detector and the electronic noise results from electronic fluctuation in the detector photodiode and other electronic components [63].

In clinical CT systems, due to the bottleneck of photon-counting detectors, such as the pile-up effects, the energy-integrating detectors are more popular and used by most CT vendors. Compared to the photon-counting detectors, which counts the number of received photons, the signal of energy-integrating detectors are proportional to the total photon energy deposited on the detectors. Due to the wide photon energies range distributed in the clinically relevant diagnostic CT, – 30 to 140 keV [111], it is necessary to integrate the X-ray spectrum in the statistical noise modeling. As far as we know, Compound Poisson model [98] can accurately describe the noise property of the detected photon numbers in CT scanners based on the energy spectrum of the X-

ray quanta. However, it is numerically difficult to derive an exact form of the likelihood function for iterative image reconstruction algorithm development [99]. To facilitate the compound Poisson statistics [63, 98], various approximations have been proposed either in the transmission domain (before the log-transform) using a scaled Poisson [47] or in the sinogram domain (after the log-transform) using a nonlinear mean-variance dependent Gaussian density [48, 95]. In the following part of this dissertation, we assume the X-ray source produces mono-energy photons, and use the widely accepted simple Poisson model to approximate the statistics modeling of X-ray photons [26, 54, 62, 69, 92, 96, 101]. In addition to the quantum statistical noise, the present of the electronic background noise in the low-dose CT scan should not be neglected due to the low signal to noise ratio (SNR) of the acquired projection data. In low-dose case (i.e., low-mAs), the measured transmission data I can be assumed to statistically follow the Poisson distribution upon a Gaussian distributed electronic background noise [63]:

$$I = Poisson(\lambda) + Normal(m_e, \sigma_e^2), \tag{2.17}$$

where λ is the mean of Poisson distribution, m_e and σ_e^2 are the mean and variance of the Gaussian distribution from the electronic background noise. In reality, the mean m_e of the electronic noise is often calibrated to be zero (i.e., 'dark current correction') and the associative variance slightly changes due to different settings of tube current, voltage and durations in a same CT scanner [63]. Hence, in a single scan, the variance of electronic background noise can be considered as uniform distribution.

2.2.2 Variance estimation in projection domain

According to our statistical moment analysis of CT measurement in [63], the mean and variance of transmission data I can be described as:

$$E(I) = \lambda + m_e; \;\; Var(I) = \lambda + \sigma_e^2, \tag{2.18}$$

From the Lambert-Beer's law, the measurement p along the attenuation path i is approximately calculated by:

$$p_i = \ln \frac{I_{i0}}{I_i} = \ln(I_{i0}) - \ln(I_i), \tag{2.19}$$

where I_{i0} is the mean number of incident photons along the attenuation path i, p_i denotes the log-transformed projection datum along path i. Based on Eq. (2.19), it is possible to estimate the variance of projection data with known noise properties of detected photons. Due to the nonlinearity of Eq. (2.19), Taylor expansion is applied to linearize the formula. Based on our previous study, by doing the three-order Taylor expansion of Eq. (2.19) at the expectation point of EI, the mean-variance relationship in CT projection domain by considering the effect of the Gaussian distributed electronic background noise can be mathematically expressed as [63]:

$$\sigma_{p_i}^2 = \frac{1}{I_{i0}} \exp(\bar{p}_i) \left(1 + \frac{\sigma_{e,i}^2 - 1.25}{I_{i0}} \exp(\bar{p}_i) \right), \tag{2.20}$$

where $\sigma_{p_i}^2$ represents the estimated variance of measuring projection datum p_i, $\sigma_{p_i}^2$ is the variance of the electronic noise associated with the measurement on projection datum p_i. The variance of the electronic background noise at specific energy level can be investigated by analyzing the repeated realizations from a physical phantom. Figure 2.2 shows the relationship

between the variance of the electronic noise and the mAs level for Siemens 16 slices SOMATOM CT scanner at 120kVp.

From Eq. (2.20) we can see that the variance of the projection data can be estimated with known the expectation value of projection data. In reality, it is impossible to acquire repeated realizations due to the intensive X-ray dose exposure to the patients. Therefore, in our following SIR algorithm, we use the acquired sinogram data value as the initial value in Eq. (2.20) and update the variance values based on the updated forward projection data.

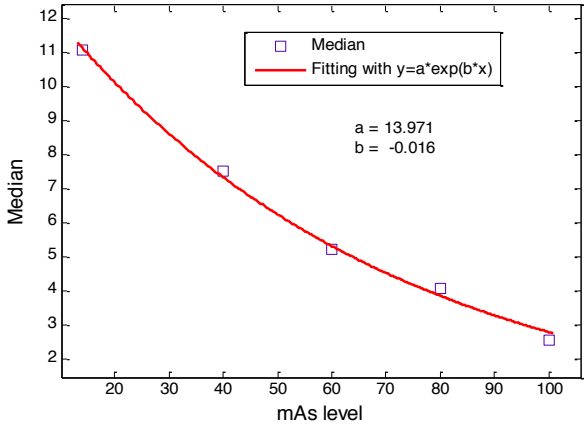

Figure 2.2 The relationship between the variance of the electronic noise and the mAs level

2.2.3 Penalized re-weighted least squares strategy for image reconstruction

The penalized re-weighted least squares (PRWLS) strategy follows the MAP estimation, its cost function often consists of two parts: (1) data fidelity term (i.e., weighted least squares) from the likelihood function of the statistical modeling and (2) regularization term from the prior knowledge of the desired image. Directly utilizing the likelihood function of the Poisson plus Gaussian model is numerically difficult. In order to solve this problem, many approximation models were investigated such as the shifted Poisson approximation in [47, 102], and simple Poisson [47]or simple Gaussian model [48, 55, 91] with variance estimated from Poisson [48] or Poisson plus Gaussian model [63]. In the following part, I briefly review the derivation of weighted least squares function from the simple Poisson model [26].

Assuming the projection data at each projection bins are statistically independent, the joint probability distribution function (*pdf*) of Poisson distribution can be mathematically expressed as:

$$P(I \mid \mu) = \prod_i \frac{(\lambda_i)^{I_i} \exp(-\lambda_i)}{I_i!} \tag{2.21}$$

The corresponding log-likelihood function can be written as:

$$L(I \mid \mu) = \ln P(I \mid \mu) = \sum_i (I_i \ln \lambda_i - \lambda_i - \ln(I_i!)) \tag{2.22}$$

For convenience, we substitute Eq. (2.22) and ignore the constant terms, we have

$$L(I \mid \mu) = -\sum_i (I_i [\mathbf{A}\mu]_i + I_{0i} \, \mathrm{e}^{-[\mathbf{A}\mu]_i}) \tag{2.23}$$

where $\mathbf{A}$ represents the system transfer matrix, which depends on the projection geometry, and its elements of $a_{i,j}$ can be calculated as the length of the intersection of projection ray i with

voxel j, μ is the vector of ideal attenuation coefficients. Applying a second-order Taylor's expansion to Eq. (2.23) around a measured projection data and ignoring the irrelevant terms, yields:

$$L(p\,|\,\mu) \approx -\sum_i \frac{w_i}{2}(\hat{p}_i - \bar{p}_i)^2 = -\frac{1}{2}\left\|\hat{p}_i - \mathbf{A}\mu\right\|_W^2 \tag{2.24}$$

where $\hat{p}$ is the acquired projection data and W is the statistical weighting. From Eq. (2.20), it can be observed that a larger $\bar{p}_i$ value, indicating less X-ray photons being detected in the detector, will have a larger variance. Thus, a smaller SNR is expected due to the Poisson noise nature of the detected photons. On the contrary, a smaller $\bar{p}_i$ value will result in a higher SNR. Due to this property, the inverse of the $\sigma_{p_i}^2$ in Eq. (2.20) shall be used as the weights W for the WLS term, i.e., a lower SNR shall contribute less for the estimate of the ideal projection and a higher SNR will contribute more for the estimation. In reality, the images are reconstructed from only one scan and the mean line integral $\bar{p}_i$ are not available. Therefore, a one-step-later reweighted strategy was implemented to estimate $\sigma_{p_i}^2$ from the measured projection data [93]. This Strategy makes sense that the re-projection operations from the reconstructed image are much closer to the mean of the ideal log-transformed projection.

For CT image reconstruction, using the terminologies described in the previous study [92], the associated cost function of PRWLS can mathematically be written as:

$$\Phi(\mu) = (\hat{p} - A\mu)^T \Sigma^{-1}(\hat{p} - A\mu) + \beta R(\mu), \tag{2.25}$$

The first term on the right hand side is named as the data fidelity term described as a re-weighted least-squares (RWLS) measurement wherein the matrix Σ is a diagonal matrix and its *i-th* element denotes the variance of the projection datum at detector i as defined by Eq. (2.20). Due to the dependence of the variance on the mean, Σ is adjusted accordantly based on the updated expectation value of projection data. Directly minimizing the RWLS measure, similar to the maximum-likelihood (ML) approach, usually leads to unacceptable results [46]. Thus, a penalty R (the second term in the right hand side of Eq. (2.25)) is often desired for a successful solution. The hyper-parameter $\beta > 0$ is designed to control the strength of the penalty term $R(\mu)$ in Eq. (2.25). Consequently, the desired image can be yielded by solving the following objective function:

$$\mu^* = \arg\min_{\mu \geq 0} \Phi(\mu), \tag{2.26}$$

As for the selection of penalty term $R(\mu)$, many forms have been explored as an *a priori* constraint to regularize the RWLS solution, such as the isotropic quadratic prior [92] and anisotropic quadratic prior [93], by attempting to adapt different weighting coefficients under the framework of MRF. Recently, based on the hypothesis of the piece-wise constant property of the to-be-estimated image, several TV-based prior models [20, 79, 80] were proposed for CT image reconstruction. However, these models often suffer over-smooth in the cases of the desired images containing low-contrast edges. To address the drawback of TV-based prior models, an adaptive weighted total variation prior model was introduced by our group recently [52] for sparse-views CT image reconstruction with significant gains than the conventional TV model in terms of edge details preservation. In Chapter 4, an AwTV prior model based PRWLS (AwTV-PRWLS) method for low-mAs CT image reconstruction will be discussed in detail.

2.3 Algebraic based iterative image reconstruction

The algebraic based iterative image reconstruction is a class of iterative algorithm that reconstructs CT images by successive and repeated applications of several projection operators from a series of angular projection data. The most famous algebraic based iterative image reconstruction method was named as algebraic reconstruction technique (ART) [31], which has been used for CT image reconstruction for decades. In this section, I first briefly review the mathematics of the simultaneous ART (SART) algorithm, an improved ART algorithm by realize several projection rays simultaneously. Then discuss an improved algebraic based iterative image reconstruction algorithm – total variation projection onto convex sets (TV-POCS) algorithm, which is one of the popular method for image reconstruction from sparse view data, will be reviewed.

2.3.1. Review of the simultaneous algebraic reconstruction technique

In the ideal CT imaging system, the acquired data and the desired image are often assumed to satisfy the following equations:

$$P = A\mu, \tag{2.27}$$

From Eq. (2.27) it can be observed that the image reconstruction problem is essentially an inverse problem. Therefore an image can be estimated by minimizing the distance between the measured and estimated projection data. The associative update scheme can be described as follows:

$$\mu_j^{(k+1)} = \mu_j^{(k)} + \frac{\omega}{A_{+,j}} \sum_{i=1}^{M} \frac{A_{i,j}}{A_{i,+}} \left(p_i - \bar{p}_i(\mu^{(k)}) \right), \tag{2.28}$$

$$A_{i,+} = \sum_{j=1}^{N} A_{i,j} \quad \text{for} \quad i=1,\ldots,M, \tag{2.29}$$

$$A_{+,j} = \sum_{i=1}^{M} A_{i,j} \quad \text{for} \quad j=1,\ldots,N, \tag{2.30}$$

$$\bar{p}(\mu) = A\mu, \tag{2.31}$$

where $A_{i,j}$ is an $M \times N$ system matrix according to the projection geometry [40] (M was defined before as the total number of image voxels and N is the total number of data samples). ω is a relax parameter for updating the current estimate of the image. k indicates the iterative number. Due to the solutions mainly depends on the repeat realizations of several linear equations simultaneously, the above method is often called as SART image reconstruction method. In clinical CT, based on our previous discussing about X-ray matter intersection issue in chapter 1, the desired attenuation coefficients are non-negative. Therefore, non-negative constraints are always used to ensure the non-negative property of the attenuation coefficients. The new ART/SART algorithm with non-negative constraints is often called as projection onto-convex sets algorithm.

Mathematically, it is easy to understand the SART algorithm converges to a unique solution due to the equality of Eq. (2.31). However, in reality, due to the inconsistency of real measurements (i.e., noise and artifacts) and under-determinate of specific linear systems such as sparse-view CT acquisitions, the SART (or POCS) fails to converge to a unique solution. Therefore an objective function is desired to pick up one solution from multiple choices. In the following section, a recently investigated TV-POCS method [79, 80], which can produce promising results for image reconstruction from sparse-view data, are discussed.

2.3.2. Review of total variation-projection onto convex sets method

For CT image reconstruction from real measurements, the classic filtered back-projection (FBP) method always suffers from noticeable artifacts and noise due to ill condition of the measured data [79, 80]. To mitigate the artifacts and noise, a prior information is often desired to yield a satisfactory CT images. The total variation (TV) model is one of the promising model to address the noise by based on the assumption of piecewise constant distribution for the desired image. Mathematically, the TV of the to-be-reconstructed image, i.e., $\|\mu\|_{TV}$, is defined as:

$$\|\mu\|_{TV} = \sum_{s,t} \sqrt{\left(\mu_{s,t} - \mu_{s-1,t}\right)^2 + \left(\mu_{s,t} - \mu_{s,t-1}\right)^2}, \tag{2.32}$$

where s and t are the indices of the location of the attenuation coefficients.

A satisfactory CT image may be yielded by solving the following constrained optimization problem [79, 80]:

$$\min_{\mu \geq 0} \|\mu\|_{TV} \quad \text{subject to} \quad |p - A\mu| \leq \varepsilon \tag{2.33}$$

where ε is an error tolerance factor depends on the projection data noise level.

In order to solve the problem described in Eq. (2.33), two independent operating steps are involved in the implementation of their algorithm. In the first step, an initially estimated image is updated iteratively to fulfill the data constraints and an intermediate image is yielded by the POCS strategy. The second step of the TV-POCS algorithm updates iteratively the intermediate image estimated from the above first step to minimize the TV of the to-be-estimated image. The two steps are executed alternatively until a stop criterion is met [79, 80]. The TVS-POCS method have shown that by minimizing the TV of the to-be-estimated image with some data and other constraints, a piecewise-smooth X-ray CT can be reconstructed from sparse-view projection data without introducing noticeable artifacts. However, due to the piecewise constant assumption for the image, a conventional TV minimization algorithm often suffers from over-smoothness on the edges of the resulting image and patchy artifacts in the uniform area. In order to solve this problem, two optimal models: AwTV and total variation stokes (TVS) are designed to mitigate the drawback of conventional TV model. The details of the proposed models will be discussed in chapter 4, 5, and 6.

2.4 Discussion and conclusion

In this chapter we briefly reviewed three types of CT image reconstruction methods: (1) Analytical methods; (2) Statistical model based iterative image reconstruction methods; (3) Algebraic based iterative image reconstruction methods. Compared to the iterative methods, the analytical methods are advanced in fast computational time and linear noise property in the reconstructed images. The drawback of this method is the reconstructed images are often reported to suffer the artifacts and noise due to the inconsistency of projection data. In contrast, compared to the analytical methods, the iterative methods are advanced in noise suppression and artifacts removal, however, it may require a long time for convergence and the results are often show nonlinear noise.

In the following chapters, I will introduce four different image reconstruction algorithms to improve the three types of image reconstruction methods discussed in this chapter. In chapter 3, a novel volume shadow weighting based FDK algorithm is introduced to solve the non-uniform noise appeared in the conventional FDK results. In chapter 4, 5, an AwTV model was proposed to illuminate the over smoothing issue of the conventional TV model. The corresponding AwTV-PRWLS algorithm for low-mAs CT image reconstruction and AwTV-POCS algorithm

for sparse view CT image reconstruction are studied and compared to the conventional TV based PRWLS (TV-PRWLS) algorithm and TV-POCS algorithm. In chapter 6, a novel TVS model based CT image reconstruction algorithm data is presented to suppress the patchy artifacts. The gains of the TVS method for clinical data was studied and presented in chapter 7. The details of the improved image reconstruction algorithms can be also found in my previous publications [49-53, 55].

Chapter 3 . A volume-shadow weighting based FDK algorithm for cone-beam CT image reconstruction

Based on our previous discussion in chapter 2, the FDK algorithm has been used prevalently for cone-beam computed tomography image reconstruction in the past decades. However, images reconstructed by the standard FDK algorithm were reported to suffer from non-uniform noise and artifacts caused by the unsuitable filtering or back-projection geometry models. This chapter describes a new geometry model-based weighting scheme in the back-projection step to enhance the performance of the conventional FDK algorithm. The intersecting volume between X-ray beam and an image voxel is estimated from the shadows of the volume on a fixed common plane and adaptive common plane and then used as the geometry model or weight in the back-projection step of the FDK algorithm to replace the commonly used LI geometry model. For comparison purpose, the distance-driven (DD) back-projector, which is the current state-of-the-art in the geometry models, was implemented in a similar fashion as the presented volume model. Digital phantom study demonstrated a uniformly-distributed noise by the proposed volume-shadow weighting based FDK (VSW-FDK) algorithm in the stationary noise case. A similar observation was also seen in an experimental study using repeated scans on a physical phantom. In the physical phantom study, the proposed VSW-FDK algorithm showed up to 34.13% contrast-to-ratio (CNR) improvement and 38.62% resolution improvement compared to the LI-FDK algorithm and up to 12.19% CNR improvement and 18.24% resolution improvement compared to the DD based-FDK (DD-FDK) algorithm at a fixed noise level. The variance stabilization with the proposed VSW-FDK algorithm was further observed in a clinical study on a head and neck cancer patient, where up to 35.30% standard deviation reduction for LI-based FDK algorithm (LI-FDK) and up to 32.50% reduction for DD-FDK were achieved. The proposed VSW-FDK algorithm shows the potential to achieve better noise property and resolution than the conventional LI-FDK and the state-of-the-art DD-FDK algorithms. While it consumes about four times slower than the LI-FDK algorithm and has similar computing time with the DD-FDK algorithm on a DELL PC with Intel Xeon E5-1603 2.8GHz CPU and 64GB RAM, the gain in suppressing noise while preserving fine structures by the proposed VSW-FDK algorithm is worth. As computers get more powerful, the gain is expected to be more significant.

3.1 Introduction

In CT clinical utility, many applications require large 3D volume coverage and very thin image slices in a short scanning time such as CT angiography [35]. Projection data acquired in CB geometry offers large volume coverage and thin slice image reconstruction and, therefore, CBCT has been widely used in clinics such as radiation therapy [38]. The most prevalent method for 3D image reconstruction from CBCT projection data is the FDK algorithm, which extends the 2D FBP algorithm to 3D by

considering the contributions of all the tiled fan-beams to the object [28, 41]. However, it has been reported that undesirable non-uniform noise will present in the FDK-reconstructed image when a conventional LI is used in the back-projection step [27, 50, 94, 103]. Thus, the conventional LI-FDK makes the noise level across the FOV unpredictable.

According to the previous studies, the non-uniform noise behavior may be caused by the distance-dependent /position-dependent factor in the CB FDK reconstruction formula [36, 71, 94, 103]. To overcome this weakness, various improved algorithms have been proposed in the past decades for 2D fan-beam (FB) or 3D CBCT image reconstruction. A typical strategy includes modifying the filtering step, while retaining the use of spatially invariant back-projection step, such as using shift variant filters in the filtering step [71] or replacing the conventional ramp filtering step with Hilbert transform [22, 68, 103]. Although this method can improve the non-uniform noise along transaxial direction for 2D FB CT image reconstruction, it fails to modulate the off-plane cone angle along the axial direction for 3D CBCT image reconstruction.

Another strategy is to retain homogeneous ramp filtering in the filtering step, while using a spatially variant weighting in the back-projection step [18, 56, 86, 94]. Compared to the first strategy, it is more applicable for suppressing the noise in both transaxial and axial directions by integrating the in-plane and off-plane cone angle factors in the spatially variant weighting operation. In this study, we focus on an adaptive approach, which belongs to the second strategy, where the X-ray beam is considered as a "fat" pencil beam and the intersection of the X-ray beam with 3D image voxels are utilized as spatially variant weights in the back-projection steps. The intersections depend on the distance from the X-ray source to a concerned image voxel and, therefore, have the potential to mitigate the distance-dependent factor in the FDK formula.

Although the adaptive approach mentioned above is straightforward, direct calculation of the intersecting volumes can be difficult in implementation and requires innovative ideas to overcome the high arithmetic complexity for computational efficiency. Various techniques have been investigated to calculate the intersection volumes by using approximations [18, 56]. Among those techniques, the DD technique is the current state-of-the-art projection and back-projection operators for 3D CT modeling. It maps the boundaries of image voxels and detector cells onto one common plane and assumes the intersecting area by rectangles [18, 56]. Then the overlapping areas between the image voxels and detector cells on the common plane are calculated and used as weights for projection and back-projection. Previous study has shown that the rectangle assumption fails and large errors occur when the azimuthal angles are close to the odd multiples of $\pi/4$ [56]. To overcome these drawbacks, an improved Separable Footprints (SF) technique was investigated by using the trapezoid functions in the transaxial direction only (i.e. SF-TR method) or in both transaxial and axial directions (i.e., SF-TT) [56]. In the SF technique, the 2D footprint function is approximately separated to two 1D trapezoid functions. Then the two trapezoid functions are multiplied and used as weights for the projection and back-projection. Although the SF technique was claimed to improve the accuracy of the DD technique, both the SF technique and DD technique fail to accurately describe the irregular intersecting volume between the X-ray beam and 3D object because the shape of intersecting volume cannot be accurately represented by a

single area function. Therefore, DD and SF may not be the best solution due to the failure of describing the actual intersections between X-ray beam and image voxels.

In this study we invent a novel VSW-FDK algorithm which has low arithmetic complexity and high accuracy for CBCT reconstruction. In our proposed algorithm, the calculation of the irregular 3D intersecting volume is converted to calculating the areas of two polygons. The shadows of the intersecting volumes between the pencil-beam X-ray and the image voxels on both the fixed common plane and the adaptive common plane were calculated and used as weighting factors in the back-projection step [50], while the homogeneous ramp filtering retains. Intuitively, the intersecting volume estimated from two polygon areas considers more variations and is expected to be more accurate than the estimation from a single rectangle or trapezoid area, which distinguishes our proposed technique to the previous DD and SF techniques.

3.2 The proposed VSW-FDK algorithm

From Eq. (2.15), we can find that each plane along the *z* direction (i.e., axial direction) in the cone is considered separately as FB geometry and the final 3D reconstruction is produced by considering the contribution from all the tiled fan beams [28, 41]. In our previous FB FBP algorithm study [94], we found that the samplings by the X-ray source and detector are highly dependent on the distance from the X-ray source to the concerned image pixel in the 2D domain and the imaging quality is degraded if this distance-dependent sampling is not adequately treated during the image reconstruction. Due to the geometric similarity between the FB and transaxial plane of the CB geometry, the term $1/\left(R+x\sin\beta_n-y\cos\beta_n\right)^2$ in the FDK algorithm is conjectured to introduce similar distance-dependent samplings artifacts as introduced in [94]. Therefore, the intersecting volume between the X-ray beam and the voxels which reflects the distance-dependent sampling is therefore desired in the 3D back-projection step in order to overcome the relative sampling differences. Thus, our proposed FDK algorithm incorporating the spatially variant volume weighting can be mathematically expressed as:

$$f_{VSW-FDK}(x,y,z)=\frac{\Delta\beta}{2}\sum_{n=0}^{N-1}\frac{R\cdot D}{\left(R+x\sin\beta_n-y\cos\beta_n\right)^2}\times\left\{\sum_u\sum_v W_{n,u,v}\,\bar{p}\left(\beta_n,u,v\right)\right\}, \quad (3.1)$$

where $W_{n,u,v}$ is the normalized spatially variant volume weighting to the filtered projection $\bar{p}\left(\beta_n,u,v\right)$, u and v are referred to the row and column indices of the neighbor detector bins around the detector bin $\left(i,j\right)$, respectively.

Figure 3.1 shows a representative geometry between the X-ray beam and the 3D voxels for illustration purpose. For the purpose of describing the proposed VSW technique in CBCT geometry, two common planes are defined as follows:

***A fixed common plane*:** This plane is perpendicular to the two edges of the detector plane and the z-axis (rotation axis) (i.e., X-Y plane in Figure 3.1(a));

An adaptive common plane: This plane is perpendicular to the fixed common plane and also parallel to the two surfaces of the concerned voxel cube ((i.e., cube surfaces A and B as shown in Figure 3.1(b)) and corresponding X-Z plane as shown in Figure 3.1(c)). However, during the gantry rotation in CBCT practice, the projection of the X-ray source on the adaptive common plane moves close to the object, as indicated by the arrow in Figure 3.1 (c). To avoid the overlap of the projections of the source and object on the

adaptive plane during the gantry rotation, we empirically shift the adaptive common plane when β reaches the odd multiple of 45-degree (i.e., from X-Z plane to Y-Z plane or from Y-Z plane to X-Z plane).

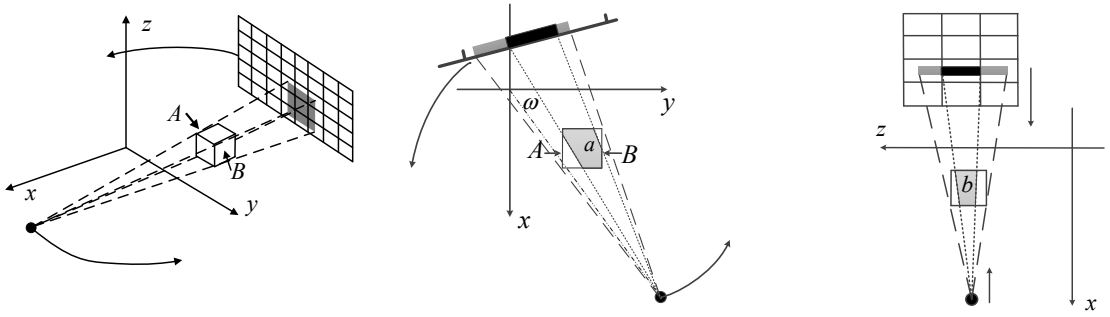

(a) (b) (c)

Figure 3.1. Illustration of the VSW technique for back-projection of a concerned voxel: (a) intersecting volume model, (b) projected onto the fixed common plane (i.e., X-Y plane), (c) projected onto the initial adaptive common plane (i.e., X-Z plane).

Inspired by the separable ideas as introduced in [18, 56, 94], we separated the 3D CBCT geometry to two 2D FB geometries (i.e., shadows on two common planes) and the intersecting areas (i.e., *a* and *b* in Figure 3.1) in the two 2D FB geometries were used to estimate the intersecting volume in 3D. The calculation of the intersecting areas with known FB projection geometries can be found in [94]. In this study, three cases were considered when we calculated the interaction FB area: (1) Pencil-beam covers the whole voxel, where the intersection is a rectangle; (2) Pencil-beam covers most of the voxel, where the intersection is a polygon (e.g., *a* and *b* in Figure 3.1); (3) Pencil-beam covers small part of the voxel, where the intersection is a triangle. The contribution of the concerned detector bin (i.e., indicated by black in Figure 3.1) to the concerned voxel is:

$$W_{n,u,v} = \frac{a}{\Delta^2} \cdot \frac{b}{\Delta^2} \cdot \Delta^3 = \frac{a \cdot b}{\Delta}, \tag{3.2}$$

where Δ indicates the voxel unit of the desired image, *a* and *b* are the actual size of the intersecting areas on two common planes in voxel^2 unit. From this equation we can observe that due to the distance dependent properties of *a* and *b*, $W_{n,u,v}$ is also distance dependent. In addition, the sum of all weights related to the concerned voxel cube equal to 1 [50], which indicates the corresponding weights for one voxel meet the normalization condition. The back-projection of the concerned voxel at specific projection angle can be calculated from the accumulation of all detector bins' contributions to the concerned voxel (i.e., $\sum_u \sum_v W_{n,u,v} \bar{p}(\beta_n, u, v)$).

It should be mentioned that the distance from the source to the rotation axis (i.e., R_{acp}) and the distance from the source to the detector (i.e., D_{acp}) in the 2D FB projection geometry on the adaptive common plane shadow (i.e., Figure 3.1(c)) may depend on the rotation angle and can change during the gantry rotation:

$$R_{acp} = R \times \cos\omega \text{ and } D_{acp} = D \times \cos\omega, \tag{3.3}$$

where ω is the angle between the adaptive common plane and the ray going through both the source and the origin as indicated in Figure 3.1 (b), D' denotes the distance from the source to the specific detector column (i.e., channel), as shown in Figure 2.1.

3.3 Noise properties in image domain

3.3.1 Noise properties of the conventional LI-FDK reconstruction algorithm

In the previous studies [71, 94], the data noises of the detector column had been assumed as uncorrelated and stationary in FB geometry. In this study, due to the decomposable characteristics of CB geometry along the axial direction, it is reasonable to assume that the data noises of detector cells are uncorrelated and stationary. Therefore, without reconstructing the image, the variance of the desired FDK image $f_{LI-FDK}(x,y,z)$ by using the LI technique in the back-projection step can be computed by:

$$\begin{aligned}\mathrm{var}\left(f_{LI-FDK}(x,y,z)\right) = q_0\left(\Delta\beta\right)^2 \sum_{n=0}^{N-1} \frac{R^2 \times D^2}{4\left(R + x\sin\beta_n - y\cos\beta_n\right)^4} \\ \times \sum_{m=-J/2}^{J/2} \left\{ \left[(1-\kappa)(1-\xi)G(i,j) + \kappa(1-\xi)G(i,j+1) \right]^2 + \left[\xi(1-\kappa)G(i+1,j) + \kappa\xi G(i+1,j+1) \right]^2 \right\},\end{aligned} \tag{3.4}$$

where

$$G(i,j) = \frac{D}{\sqrt{D^2 + (i\cdot\Delta_i)^2 + (m\cdot\Delta_j)^2}} h(j-m), \tag{3.5}$$

q_0 is a constant and indicates noise level [71, 94]. Eq. (3.4) reflects that the variance distribution across the FOV depends on the $1/\left(R + x\sin\beta_n \cdot\Delta - y\cos\beta_n\cdot\Delta\right)^2$ term in the LI-FDK algorithm of Eq. (2.15).

3.3.2 Noise properties of the proposed VSW-FDK algorithm

In our proposed VSW-FDK algorithm, the spatially-variant weighting $W_{n,u,v}$ is calculated from the intersecting volumes between the pencil-beam X-ray with the voxels in CB geometry as indicated in Eq. (3.2) and, therefore, eliminate the effect of the $1/\left(R + x\sin\beta_n - y\cos\beta_n\right)^2$ term. The variance of the reconstructed image can be computed on the same assumption in the previous section:

$$\mathrm{var}\left(f_{VSW-FDK}(x,y,z)\right) = q_0\left(\Delta\beta\right)^2 \sum_{n=0}^{N-1} \frac{R^2 \times D^2}{4\left(R + x\sin\beta_n - y\cos\beta_n\right)^4} \times \sum_{m=-J/2}^{J/2} \sum_{u} \left\{ \sum_{v} W_{n,u,v} G(u,v) \right\}^2 \tag{3.6}$$

3.4 Digital sphere phantom study

In our computer simulation study, a uniform (i.e., intensities equal to 1) 3D sphere was used for evaluating the noise properties. The sphere had a diameter of 256 voxel units. The source-to-detector distance was 450 voxel units and the source-to-object distance was 300 voxel units. There were 512 views over a 2π rotation and each projection data contained 256 detector rows and 513 equispace detector columns. In order to reduce the computation load, we assumed, in this study, the detector bin size was

1×1 voxel unit. The noise-free projection data were calculated based on the known densities and intersecting length of the ray with the 3D phantom. To save computational time during the repeated realization experiments, we only reconstructed the centered 16 slices as the volume image.

To illustrate the spatially variant property of the weights calculated in Eq. (3.2), we plot the weights along the central ray of the CB projection, which goes through the diameter of a discretized sphere at view angle 0 as an example in Figure 3.2. From this example we can observe that the designed spatially variant weights depend on the distance from the source to the concerned voxel.

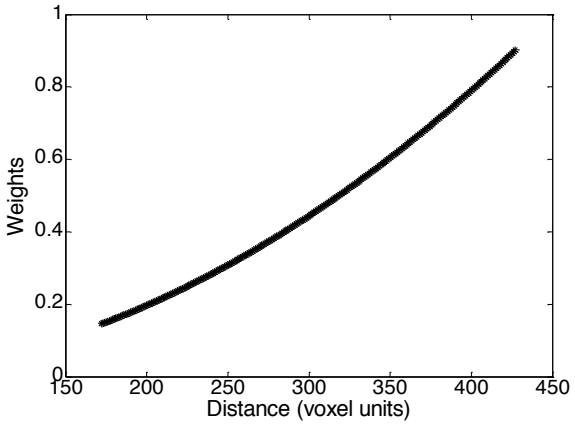

Figure 3.2. A typical relationship between the intersecting volume of voxels along the central ray of the central slice of the CB projection and distance of a concerned voxel from the X-ray source.

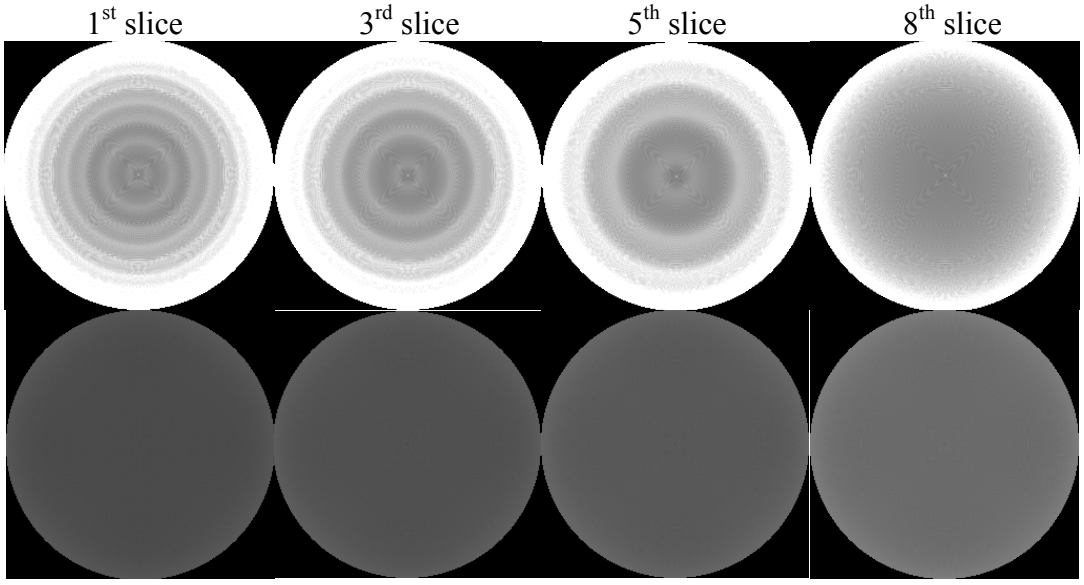

Figure 3.3. Theoretically predicted variance images. The first row shows the theoretically predicted variance images from Eq. (3.4) of LI-FDK. The second row shows the theoretically predicted variance images from Eq. (3.6) of VSW-FDK. The display window is [0, 0.002] voxel unit^{-1}.

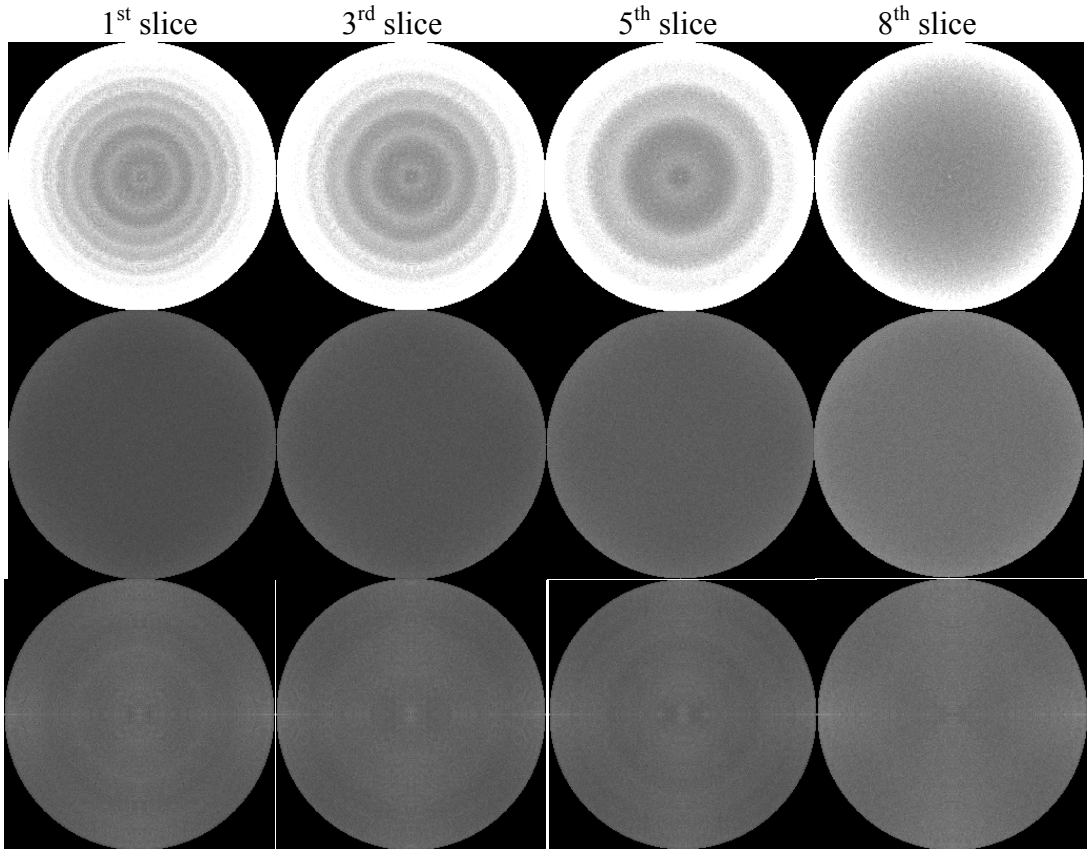

Figure 3.4. Empirically determined variance images. The first row shows the empirically determined variance images by LI-FDK from the 800 noisy realizations. The second row shows the empirically determined variance images by VSW-FDK from the 800 noisy realizations. The third row shows the empirically determined variance images by DD-FDK from the 800 noisy realizations. The display window is [0, 0.002] voxel unit^{-1}.

Figure 3.3 shows the theoretically predicted variance images at the 1st, 3rd, 5th and 8th slices (i.e., the closest slice to the central plane) by the LI-FDK (i.e., Eq.(3.4)) and the VSW-FDK (i.e., Eq. (3.6)) algorithms, respectively. Our assumption in this digital phantom study is that if the noise is uniformly distributed in the projection images, the noise in the reconstructed images should be also uniformly distributed [50, 71, 94, 103]. It can be seen that the theoretically predicted variances of the LI-FDK algorithm suffered from the non-uniformity and ring effects caused by the off-plane cone angle. However, the VSW-FDK algorithm produced relatively uniform variance images, where the ring effects in the 1st, 3rd and 5th slices were efficiently suppressed as shown in the second row of Figure 3.3.

To verify the above theoretically predicted results, we empirically calculated the corresponding variance images from multiple noisy realizations. Total of 800 noisy projection data were simulated by adding stationary Gaussian noises (in this study, we let mean equal to zero and standard deviation equal to 0.4% of the maximum value of the projection data) to the noise-free projection data. Using these 800 sets of noisy projection data, we first conducted 800 image reconstructions by the LI-FDK and VSW-FDK algorithms, respectively, and then computed their variance images in different slices

from their corresponding 800 reconstructions, as shown in the first and second row of Figure 3.4. The results are consistent with our theoretically predicted results as shown in Figure 3.4.

In order to evaluate the benefits of the proposed technique compared to the current state-of-the-art DD technique, we calculated the variance images of the DD-FDK algorithm [19] from the 800 image realization as references and shown in the third row of Figure 3.4. It is noticed that the results from the DD-FDK algorithm also show some ring effect across the FOV as that of the LI-FDK. This ring effect is believed due to the modeling inaccuracy of the DD technique.

To show more details, we plotted the horizontal profiles through the 128th row of the above images. The results show that both the spatially variant VSW-FDK and DD-FDK algorithms can retain relatively uniform noise levels, while the spatially invariant LI-FDK algorithm altered the uniformity properties. In addition, although the variance image from the VSW-FDK algorithm is close to the DD-FDK result in the most central slice (i.e., 8th slice), as the cone-angle increased along the axial direction (i.e., 5th, 3rd and 1st slice), the proposed VSW-FDK algorithm performed better than the DD-FDK algorithm.

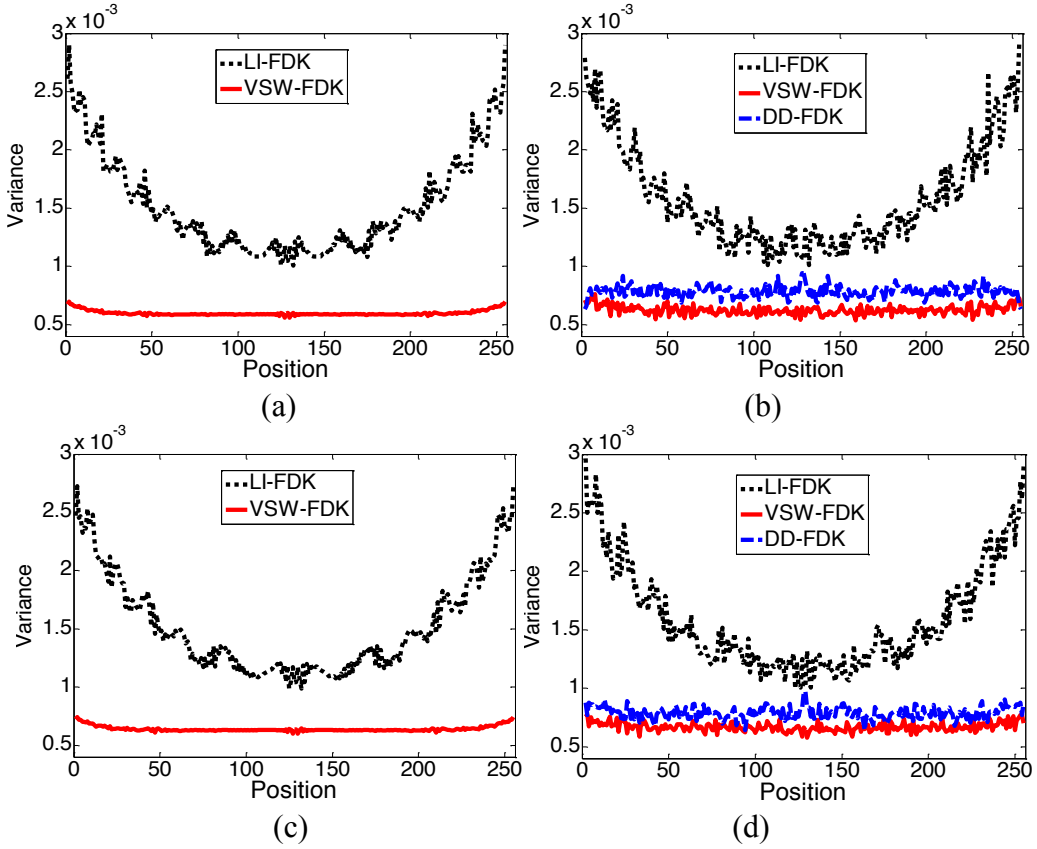

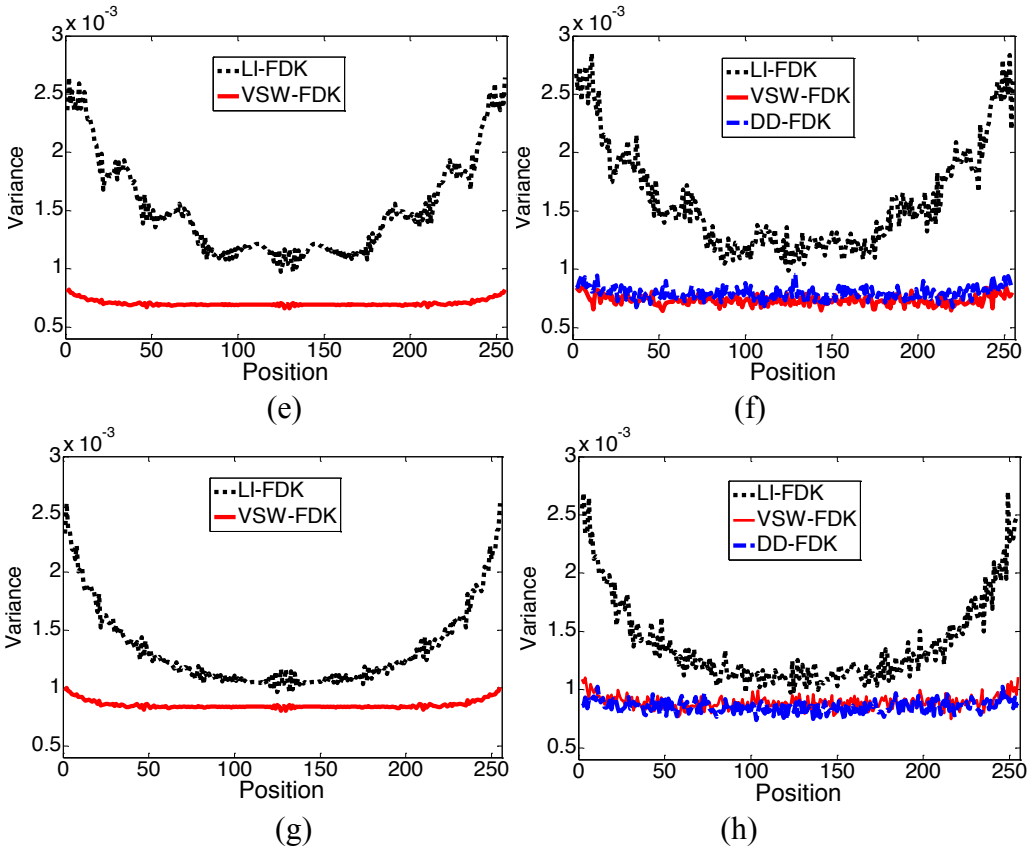

Figure 3.5. Horizontal profiles through the 255th row of the variance images. (a), (c), (e) and (g) are the theoretically predicted variance images at 1st, 3rd, 5th and 8th slices, respectively. (b), (d), (f) and (h) are the empirically determined variance images from the 800 noisy realizations at 1st, 3rd, 5th and 8th slices, respectively.

3.5 Physical phantom study

3.5.1 Anthropomorphic torso physical phantom study

To further validate the benefits of the proposed VSW-FDK algorithm in a more realistic situation, we conducted physical phantom studies by using repeated scan data from a commercial X-ray CT scanner. Compared to the computer simulated noisy projection data in the digital phantom study, the physical phantom projection data contain non-stationary signal-dependent noise, such as photon quantum Poisson noise in the transmission data, which are more complicated than the simulated stationary noise. The theoretical derivation of variance prediction in non-stationary noise case is tedious and numerically complicated [71, 94]. Therefore, repeated scans are the choice for the validation. Despite the theoretical difficulty, the following experimental results indicate that the variances and overall noise in the reconstructed images of the VSW-FDK algorithm are noticeably smaller than that of the LI-FDK and DD-FDK algorithms.

The first phantom experimental study was performed using data from the anthropomorphic torso phantom (Radiology Support Devices, Inc., Long Beach, CA) as shown in Figure 3.6 using a Siemens SOMATOM Sensation 16 CT scanner. The phantom was repeatedly scanned 177 times in the step-and-shoot mode at a fixed bed position. The tube voltage was set to 120kVp and the tube current was set to 100mAs.

The number of channels in each detector row was 672, the fan angle increment for each channel was 0.0775862° and the bin size along the *z* axis was 0.75mm. The radius of the focal spot circle was 570mm, and distance between the source and the detector plane was 1,040mm. The FOV was 51.2×51.2cm^2 with the corresponding pixel size of 1×1mm^2. The output projection data were divided by the scaling parameter 2294.5 to convert to the line integrals in projection domain [63].

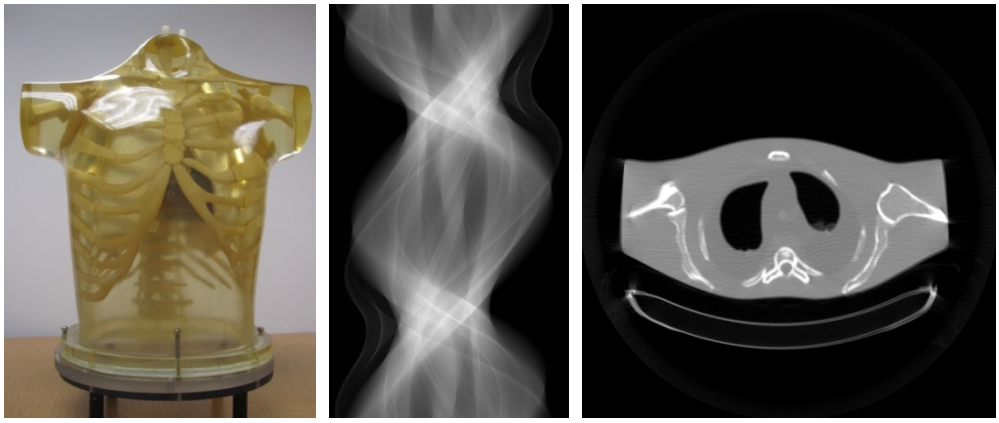

(a) (b) (c)

Figure 3.6. (a) Illustration of the anthropomorphic torso phantom. (b) an acquired sinogram data from one slice of the 16 detector rows. (c) a slice of the CT transverse image reccontructed by the VSW-FDK algorithm.

To calculate the variance images, we first reconstructed 512×512 images from the 177 repeated scanning data by the LI-FDK, DD-FDK, and VSW-FDK algorithms, respectively. Then, we calculated the variance images from the 177 reconstructions. The variance images of the 5th and 7th slices are shown in Figure 3.7, where the variance images of the LI-FDK algorithm show a large variance values along the longitudinal axis of the transverse plane, which is caused by the long attenuation path along that direction. The second row displays the results from the DD-FDK algorithm, where the variance level is much lower than that of the LI-FDK result but still higher than that of the VSW-FDK result. The third row of Figure 3.7 displays the variance images from the proposed VSW-FDK algorithm. From the VSW-FDK results we can observe that the overall noise levels were greatly decreased as compared to the LI-FDK and DD-FDK results. Their difference also can be appreciated by inspecting the horizontal profiles through the 256th row of the variance images, as shown in Figure 3.8. High non-uniformity variance is seen in the LI-FDK result while a relatively uniform variance is observed in the DD-FDK and VSW-FDK results, where the VSW result is better that DD result. These results demonstrate that the VSW-FDK outperforms the other two algorithms in this physical phantom study.

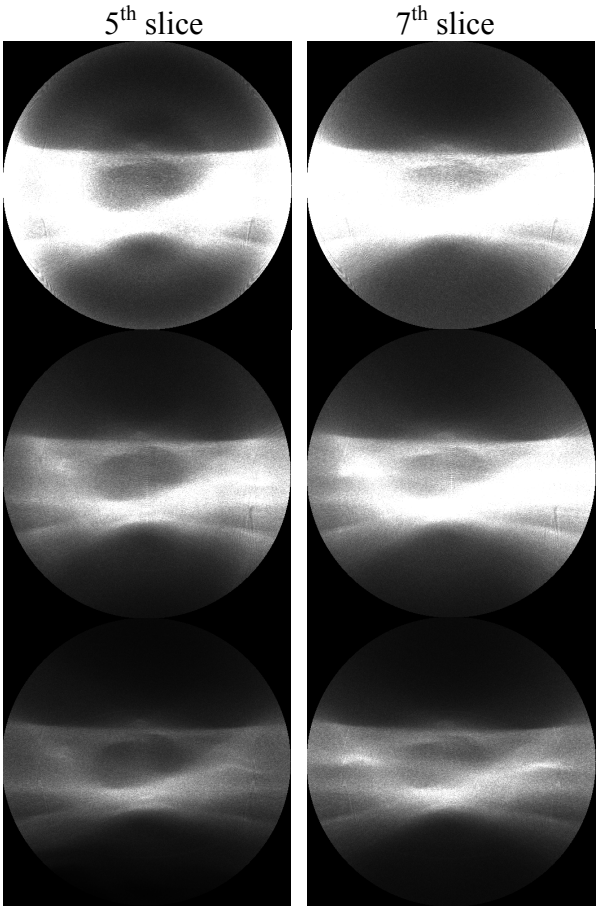

Figure 3.7. Variance images from physical phantom. The first row shows variance images by LI-FDK. The second row shows variance images by DD-FDK. The third row shows variance images by VSW-FDK. The display window is $[0,\ 2\times10^{-6}]$ mm^{-1}.

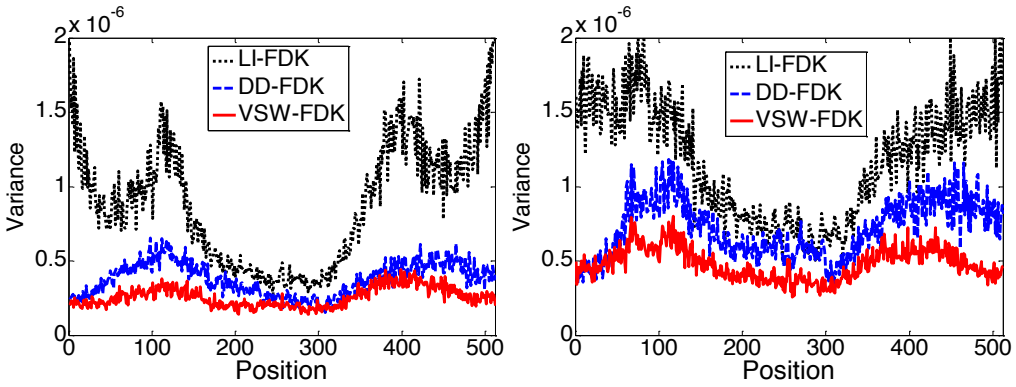

(a) (b)

Figure 3.8. Horizontal profiles through the 256th row of the physical phantom variance images at 5th and 7th slices, respectively.

3.5.2 CatPhan® 600 physical phantom study

To further evaluate the quality of the reconstructed images by using the VSW-FDK algorithm, we performed another phantom experimental study using CBCT projections acquired from the CatPhan® 600 physical phantom by an Acuity Simulator (Varian Medical System, Palo Alto, CA) [50, 91]. The X-ray tube voltage was set to 125 kVp and the tube current was set to be 80 mA, the duration of the X-ray pulse at each projection view was 12ms. A total of 634 projection views were acquired for a fully 360-degree rotation on a circular orbit. The source-to-axis distance was 100cm and source-to-detector distance was 150cm. The dimension of each acquired projection image was 397 mm×298 mm, containing 1024×768 pixels. In this study, considering the phantom size along longitudinal direction, total of 140 slice images with voxel size of 0.5×0.5×0.5 mm^3 were reconstructed by the LI-FDK, DD-FDK and VSW-FDK algorithms, respectively.

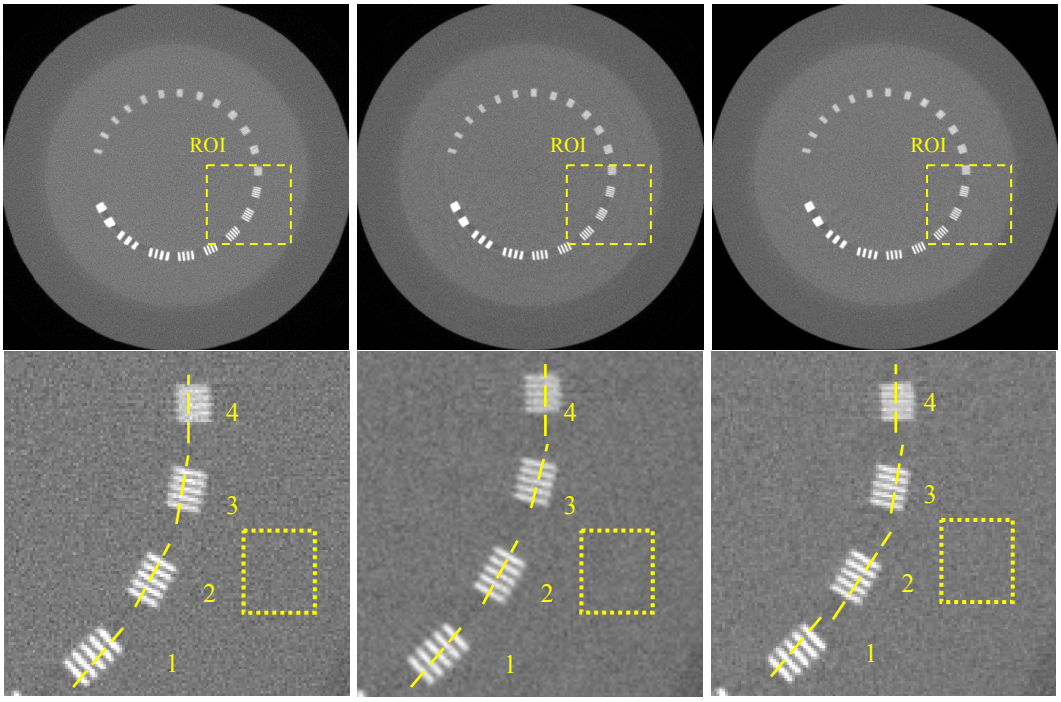

(a) (b) (c)

Figure 3.9. CatPhan® 600 phantom results comparison at 19th slice: (a) The transverse image of the 19th slice from LI-FDK result. (b) The transverse image of the 19th slice from DD-FDK result. (c) The transverse image of the 19th slice from VSW-FDK result. The display window is [0, 0.034] mm^{-1}.

The 19^{th} slice of image contains several strips of different sizes and contrasts as shown in Figure 3.9 and it was used for studies on the fine structures. The results show that the CT image reconstructed by the VSW-FDK algorithm has lower noise level and higher resolution, see the region of interest (ROI) in Figure 3.9. To inspect the details of the reconstructed images, we plotted four profiles perpendicular to the four types of strips in the ROI as shown in Figure 3.10. The profiles in Figure 3.10 are consistent with our observations in Figure 3.9, i.e., for the strips of larger size and higher contrast, the VSW-FDK and LI-FDK results have similar resolution and the DD-FDK result has lower

resolution, as shown in Figure 3.10 (a) and (b). For the strips of smaller size and lower contrast, the VSW-FDK algorithm can improve the preservation of the details compared to the LI-FDK algorithm, as shown in Figure 3.10 (c) and (d).

In addition to the resolution comparison, a region of 30-by-30 pixels as indicated in the second row of Figure 3.9 was selected for calculating the background noise level of the reconstructed images. The standard deviation of the selected region is 6.5087×10^{-4} for the LI-FDK result, 5.7225×10^{-4} for the DD-FDK result and 4.6370×10^{-4} for the VSW-FDK result, respectively. This comparison shows the VSW-FDK result has lower noise level than the LI-FDK and DD-FDK.

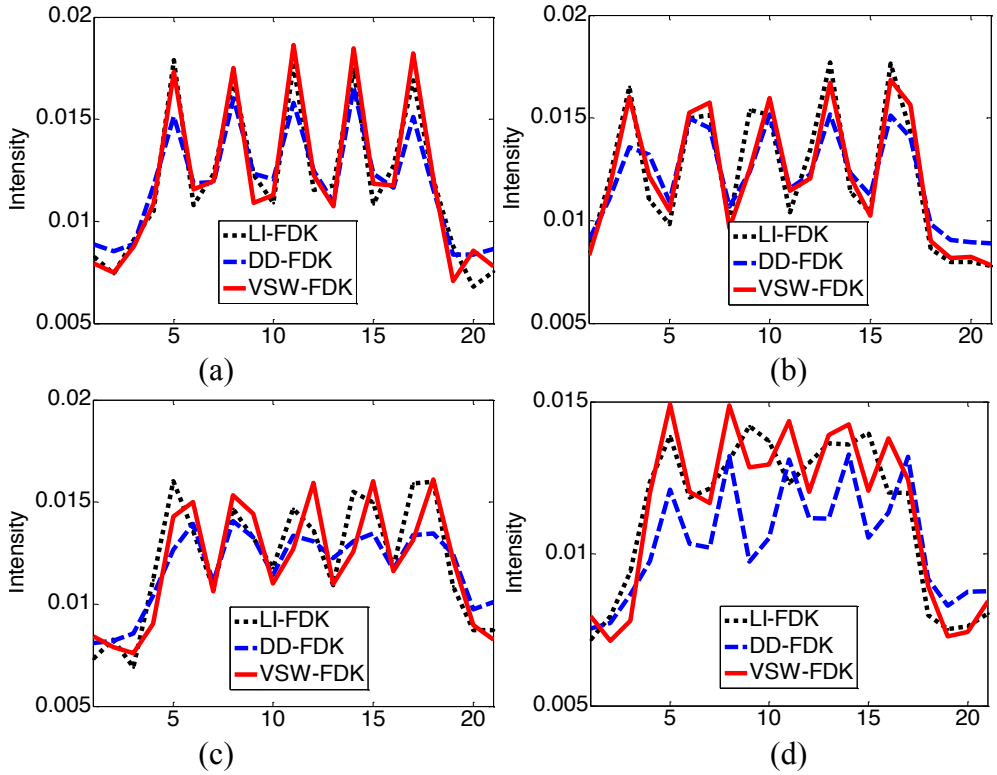

Figure 3.10. Profiles through the four types of strips as indicated in the second row of Fig. 3.9, respectively. (a) the profile for strips 1; (b) the profile for strips 2; (c) the profile for strips 3; and (d) the profile for strips 4.

In addition to the noise and resolution measurements, we further considered the CNR merit, which is one of the popular merits to quantify the image quality by considering the noise and contrast level of the desired image. A larger CNR value indicates that a higher contrast and lower noise level image is obtained; whereas a smaller CNR value means that a lower contrast and higher noise level image is obtained. The CNR is defined as:

$$CNR = \frac{|\mu_s - \mu_b|}{\sqrt{\sigma_s^2 + \sigma_b^2}} \tag{3.7}$$

where μ_s is the mean value of the signal, μ_b is the mean value of the background, σ_s^2 is the variance of the signal, and σ_b^2 is the variance of the background. In this study, the

117th slice of the transverse image, which contains different contrast disks, was used to compute the CNR values in 2D space. In order to ensure the results from all three algorithm have similar noise levels (i.e., $STD \approx 3.9\times10^{-4}$) in the select ROI as shown in Figure 3.11 (a) in the 117th slice image, Hanning windows were added in the filtering step during the reconstruction process. As shown in Figure 3.11, by assuming the small disks as signals (613 pixels) and the donut like (i.e., annulus) neighborhood pixels (578 pixels) were selected as background, the CNRs and the relative percent difference (i.e., $\Delta_{CNR(VSW/LI)}\%$ and $\Delta_{CNR(VSW/DD)}\%$ defined in (3.8)) were calculated and shown in Table 3.1. It can be observed that for the selected ROIs, the VSW-FDK algorithm shows up to 34.13% improvement in CNRs compared to the LI-FDK algorithm and up to 12.19% improvement compared to the DD-FDK algorithm.

$$\Delta_{CNR(VSW/LI)}\% = \frac{\left(CNR_{VW-FDK} - CNR_{LI-FDK}\right)}{CNR_{LI-FDK}} \times 100\%$$
$$\Delta_{CNR(VSW/DD)}\% = \frac{\left(CNR_{VW-FDK} - CNR_{DD-FDK}\right)}{CNR_{DD-FDK}} \times 100\% \quad (3.8)$$

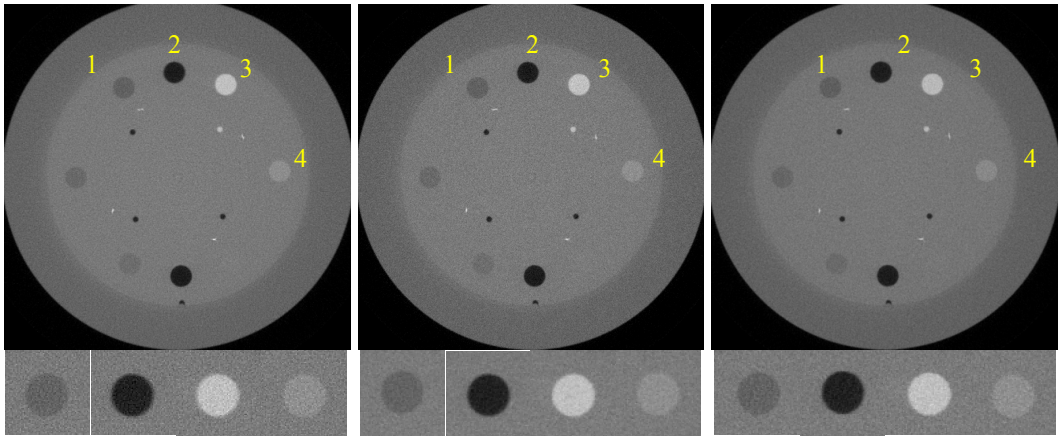

(a) (b) (c)

Figure 3.11. CatPhan® 600 results comparison at 117th slice: (a) The transverse image of the 117th slice from LI-FDK result. (b) The transverse image of the 117th slice from DD-FDK result. (c) The transverse image of the 117th slice from VSW-FDK result. The display window is [0, 0.034] mm^{-1}.

Table 3.1. The CNR values of the disks in Fig. 2.11.

ROI	CNR_{LI-FDK}	CNR_{DD-FDK}	$CNR_{VSW-FDK}$	$\Delta_{CNR(VSW/LI)}\%$	$\Delta_{CNR(VSW/DD)}\%$
1	2.6077	3.0704	**3.1773**	21.84	3.48
2	10.0386	12.0099	**13.3727**	33.21	11.35
3	6.9033	8.2529	**9.2591**	34.13	12.19
4	2.1363	2.5764	**2.7149**	27.08	5.38

In order to further compare the resolutions at a fixed noise level, we also quantitatively evaluate the resolution of the resulting images. The resolutions were

represented by the full-width-at-half-maximum (FWHM) values introduced in [51]. A larger FWHM value indicates that a low-contrast image is obtained and a smaller FWHM value means that a high-contrast image is obtained. Four edge spread functions (ESF) along four directions (i.e., up, down, left right) were calculated and averaged for FWHM value calculation. The FWHM values and the relative percent difference (as defined in Eq. (3.8)) were calculated and shown in Table 3.2. It can be observed that for the selected boundaries, the VSW-FDK algorithm showed up to 38.62% improvement in resolution compared to the LI-FDK algorithm and up to 18.24% improvement compared to the DD-FDK algorithm. Therefore, the proposed VSW-FDK algorithm achieves best resolution and highest CNR simultaneously among the three algorithms in the same noise level scenario.

Table 3.2. The FWHM values of the disks in the similar noise levels.($STD \approx 3.9\times10^{-4}$)

ROI	$FWHM_{LI-FDK}$	$FWHM_{DD-FDK}$	$FWHM_{VSW-FDK}$	$\Delta_{FWHM(VSW/LI)}\%$	$\Delta_{FWHM(VSW/DD)}\%$
1	2.2207	1.9877	**1.7061**	-23.17	-14.17
2	2.1644	1.6249	**1.3285**	-38.62	-18.24
3	1.8678	1.4609	**1.257**	-32.70	-13.96
4	2.1321	1.8085	**1.5945**	-25.21	-11.83

3.6 Clinical head CBCT data study

In this pilot clinical study, the raw projection data were acquired at 100kVp using the head protocol by the on-board imaging (OBI) device installed on a TrilogyTM (Varian Medical Systems, Palo Alto, CA) linear accelerator (LINAC). The X-ray tube current was set to be 80mA, the duration of the X-ray pulse at each projection view was 25ms. A total of 386 projection views were acquired for a 200-degree rotation on a circular orbit [90]. In this study, total 320 slices images with voxel size equals to $0.5\times0.5\times0.5$ mm^3 were reconstructed by the LI-FDK, DD-FDK and VSW-FDK algorithms, respectively.

Figure 3.12 shows the 230^{th} reconstructed transverse images by the three algorithms. The zooming images indicate that all algorithms could produce high resolution images. In order to evaluate the noise level of the resulting images, three 30-by-30 pixel ROIs, as indicated in Figure 3.12, were selected to calculate the standard deviation. The results are shown in Table 3.3. It can be seen from Table 3.3 that the VSW-FDK algorithm shows up to 35.30% noise reduction as compared to the LI-FDK algorithm and up to 32.50% noise reduction as compared to the DD-FDK algorithm. These results show that the VSW-FDK algorithm can effectively suppress the noise as compared to the LI-FDK and DD-FDK algorithms.

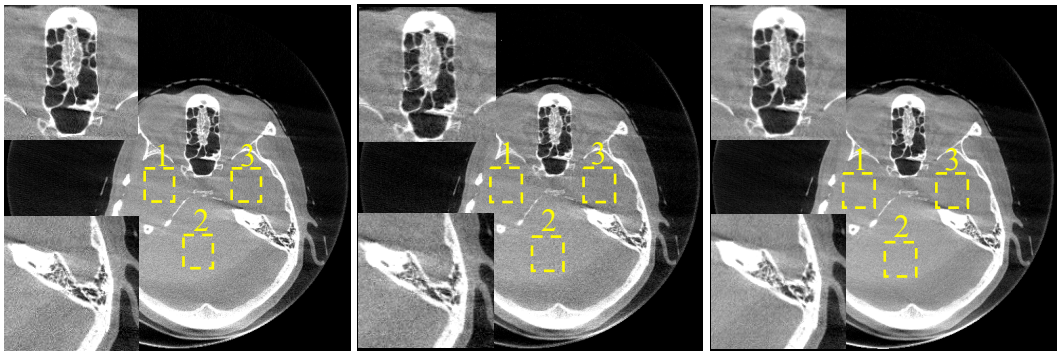

(a) (b) (c)

Figure 3.12. Clinical head CBCT results comparison: (a) The transverse image of the 230th slice from LI-FDK result. (b) The transverse image of the 230th slice from DD-FDK result. (c) The transverse image of the 230th slice from VSW-FDK result. The display window is [0, 0.036] mm^{-1}.

Table 3.3. The standard deviation (SD) of the ROIs in Fig. 3.12.

ROI	SD (LI-FDK)	SD (DD-FDK)	SD (VSW-FDK)	$\Delta_{SD(VSW/LI)}\%$	$\Delta_{SD(VSW/DD)}\%$
1	8.0741×10^{-4}	8.2352×10^{-4}	$\mathbf{5.7707\times10^{-4}}$	-33.70	-29.93
2	10.9000×10^{-4}	10.0013×10^{-4}	$\mathbf{7.0523\times10^{-4}}$	-35.30	-32.50
3	9.6540×10^{-4}	8.8472×10^{-4}	$\mathbf{6.7853\times10^{-4}}$	-29.72	-23.31

3.7 Discussion and conclusion

In this chapter, we investigated a new VSW-FDK algorithm to improve the noise properties of analytic CBCT image reconstruction. A new technique for fast calculating the intersecting volumes of the X-ray beam with image voxels in the back-projection step was developed to eliminate the effect of distance-dependent factors in the FDK formula. In the computer simulated stationary noise case study, both of the theoretically predicted variance images and the empirically estimated variance images concurred and demonstrated that the VSW-FDK algorithm can result in uniformly distributed noise across the FOV. In addition, the proposed algorithm showed good noise control as compared to the conventional LI-FDK and the current state-of-the-art DD-FDK algorithms. The results also showed the potentials to suppress the axial plane cone angle ring effects in the variance images by considering the distance along the rotation axis direction.

In the experimental physical phantom study, the performance enhancement by the VSW-FDK algorithm was evaluated by repeated scanning data, where the resulting variance images were consistent with the observations in the computer simulated digital phantom study.

To further evaluate the quality of the resulting images in a more quantitative manner, we conducted comprehensive studies by using a CatPhan® 600 physical phantom and a clinical dataset which contained more detector rows along the axial directions (i.e., 140 slices and 320 slices, respectively). The proposed VSW-FDK algorithm showed up to 34.13% CNR improvement and 38.62% resolution improvement as compared to the LI-

FDK algorithm and up to 12.19% CNR improvement and 18.24% resolution improvement as compared to the DD-FDK algorithm at a fixed noise level in CatPhan® 600 physical phantom study. It also showed up to 35.30% standard deviation reduction in the clinical data study as compared to the LI-FDK result and 32.50% reduction as compared to the DD-FDK result. Therefore, it can be concluded that the proposed VSW-FDK algorithm has more prominent noise control and fine structure preserving abilities for CBCT image reconstruction.

At last, there are some tasks that can be done in the future. The first one is adapting the proposed VSW technique to the forward-projection operation in iterative image reconstructions for low-dose CT reconstruction. The VSW-based forward-projection model and the benefit of utilizing the VSW model in iterative image reconstructions as compared to the distance-driven and separable footprints methods can be investigated. Another task is reducing the computational time. The computational time for the VSW-FDK algorithm is currently longer than that of the LI-FDK algorithm (about four times) due to the area calculations and has similar computational time as the DD-FDK algorithm. For iterative image reconstruction, the system matrix computational time is not so important, because the system matrix can be pre-computed and loaded at once into memory prior to reconstruction. However, for the on-the-fly-reconstruction methods, such as the FDK algorithm, reducing the computational time is always desired. Accelerating the computation can be achieved by using multi-core CPU and GPU hardware which can compute the results in a more efficient and parallel fashion.

Chapter 4 . Low-mAs X-ray CT image reconstruction by adaptive weighted TV-constrained penalized-reweighted least squares

According to the discussion in chapter 1, one strategy to decrease the total dosage delivered to the patient is lower the X-ray flux towards each detector bins such as lower the tube current or tube voltage. However, the quality of low-dose CT image is severely degraded due to excessive photon quantum noise and electronic noise. An accurate noise modeling is a fundamental and always impacts the low-dose CT image quality. In this chapter, a PWLS base image reconstruction strategy was introduced for low-mAs X-ray CT by incorporating the AwTV penalty term and a noise variance model of projection data. An AwTV penalty is introduced in the objective function by considering both piecewise constant property and local nearby intensity similarity of the desired image. Furthermore, the weight of data fidelity term in the objective function is determined by our recent study on modeling variance estimation of projection data in the presence of electronic background noise. The presented AwTV-PRWLS algorithm can achieve the highest full-width-at-half-maximum measurement and lowest standard deviation as compared to the conventional TV-PRWLS algorithm. In addition, I also compared the effectiveness of accurate noise modeling in this algorithm. The results indicated the accurate noise model indeed benefit the image quality on both visualization evaluations and quantitative evaluations.

4.1 Introduction

Reducing the X-ray exposure (i.e., lower milliampere-seconds (mAs) or lower kilovoltage-peak (kVp)) to the patients is one direct strategy for lower the radiation dose [92]. However, the image quality in this case would be significantly degraded due to excessive quantum noise if no noise controlling [34, 99]. Efforts have been devoted to restore the ideal line integrals or sinogram data (i.e., projection data after log-transformation) from the acquired low-mAs projection data for the purpose of improving the image quality via either statistics based sinogram restoration [46, 48, 92] or statistics based iterative image reconstruction [25, 26, 93]. For yielding a successful solution, the AwTV penalty [52, 55] is introduced in the objective function by considering both piecewise constant property and local nearby intensity similarity of the desired image, which is one of motivations for this present study. In order to achieve a reasonable balance between resolution and contrast-to-noise ratio in the reconstruction, the associated weights in the AwTV model are expressed as an exponential function, which can be adaptively adjusted with the local image-intensity gradient for the purpose of preserving the edge details. The differences between the AwTV penalty and conventional TV penalty will be discussed in this chapter. In addition, previous statistical model in the image reconstruction algorithms does not consider the electronic background noise. In this study, we consider two principle sources of causing the CT

noise, i.e., photon counting statistics and the electronic background noise. Thus, more accurate model with consideration of the electronic noise is more desired for low-dose statistical image reconstruction (SIR), which is the other motivation of this present study. It is worth to note that the penalty term and the explored statistical model in this study differentiate the ones from the previous reports on TV-PWLS [20, 69, 105].

4.2 Adaptive weighted total variation model

In theory, the conventional TV model is based on the assumption of piecewise constant distribution for the desired image, and the assumption often leads to the associated cost function optimization suffering from over-smoothing on the edges in the reconstructed images. Meanwhile, the edge details are vital information for diagnosis in clinic. In order to mitigate the over-smoothing of edges in the conventional TV minimization, a new AwTV model is proposed as follows:

$$\|\mu\|_{AwTV} = \sum_{s,t} \sqrt{w_{s,s-1,t,t}\left(\mu_{s,t} - \mu_{s-1,t}\right)^2 + w_{s,s,t,t-1}\left(\mu_{s,t} - \mu_{s,t-1}\right)^2}, \tag{4.1}$$

$$w_{s,s-1,t,t} = \exp\left[-\left(\frac{\mu_{s,t} - \mu_{s-1,t}}{\delta}\right)^2\right] \quad \text{and} \quad w_{s,s,t,t-1} = \exp\left[-\left(\frac{\mu_{s,t} - \mu_{s,t-1}}{\delta}\right)^2\right], \tag{4.2}$$

where δ in the weights ($w_{s,s-1,t,t}$ and $w_{s,s,t,t-1}$) is a scale factor which controls the strength of the diffusion during each iteration.

By the form of AwTV in Eq. (4.1), it is possible to fully consider the gradient of the desired image and also to include the change of local voxel intensities. Specifically, for a smaller change of voxel intensity, a stronger weight can be given; whereas for a larger change of voxel intensity, a weaker weight may be given. Through this diffusion-type weighting process, an adaptive smoothing is encouraged in reference to the difference between neighboring voxels' intensities. From the viewpoint of scale-space in the diffusion framework, the AwTV of the desired image will no longer be linearly and uniformly calculated for each diffusion direction from a voxel, rather the calculation will be adaptive to the local information of the image with an exponential form. Intuitively, the AwTV model of Eq. (4.1) approaches to the conventional TV model as the weight goes to 1, thus the TV model may be considered as a special case of the AwTV model when $\delta \to \infty$.

4.3 Implementation of the AwTV-PRWLS method

By incorporating the AwTV prior in the PRWLS cost function introduced in chapter 2 (i.e., Eq. (2.25)), the objective function of the AwTV-PRWLS method for CT image reconstruction can be written as:

$$\mu^* = \arg\min_{\mu \geq 0} (\hat{p} - A\mu)^T \Sigma^{-1} (\hat{p} - A\mu) + \beta \|\mu\|_{AwTV}, \tag{4.3}$$

Generally, to yield a unique convergence solution, the convex of the objective function in Eq. (4.3) should be considered. It can be easily observed that the data fidelity term in Eq. (4.3) is a convex quadratic form while the associated AwTV prior term is not convex due to the nonlinear distribution about the local intensity of the image. Hence, it is difficult to get a global optimal solution from Eq.(4.3) directly. Meanwhile, inspired by the optimization strategy as described in the previous works [61, 93], the weights can

be pre-calculated separately before each iteration step and given the pre-calculated weights the convex of AwTV prior term can be well achieved. As a result, through a traditional optimization algorithm performing on the objective function in Eq. (4.3), at least one local convergence solution can be generated. Practically, the estimated image after several iterations would convergence to a stable one with only minor changes of intensity, which means to the weights almost unchanged after several iterations. In other words, one converged solution always can be yielded by the optimization method as described in the previous works [61, 93]. In this study, based on the previous works in SIR [29, 69, 93], a modified Gaussian Seidel (GS) update strategy was performed on the optimization of the objective function in Eq. (4.3). It should be mentioned, due to the weights are pre-calculated before each iteration and are considered as constants in each iteration, the minimizing of AwTV penalized cost function should have similar property as the TV penalized cost function [69]. To summarize, the pseudo-code of the present algorithm about the AwTV-PRWLS can be listed as follows:

Initialization :

$\hat{\mu} = \mathrm{FDK}\{\hat{p}\};$

$\hat{r} = \hat{p} - A\hat{\mu};$

$\sigma_{p_i}^2 = \frac{1}{I_{i0}} \exp(\hat{p}_i)\left(1 + \frac{\sigma_{e,i}^2 - 1.25}{I_{i0}} \exp(\hat{p}_i)\right), \quad i = 1,2,....M;$

$s_j = a_j' \Sigma^{-1} a_j, \quad \forall j;$

$w_{jm} = \exp\left[-\left(\frac{\mu_j - \mu_m}{\delta}\right)^2\right], \; m \in N_j;$

For each iteration :

For each pixel $j = \{s,t,z\}$:

For each neighbor $m \in N_j$

if $m \in M = \{s-1,t,z\} \cup \{s,t-1,z\} \cup \{s,t,z-1\}$

$$w'_{jm} := \frac{w_{jm}}{\sqrt{\sum_{m \in M} w_{jm}\left(\mu_j - \mu_m\right)^2 + \varepsilon}};$$

if $m = \{s+1,t,z\}$,

$$w'_{jm} := \frac{w_{jm}}{\sqrt{w_{s,s+1,t,t,z,z}(\mu_{s+1,t,z} - \mu_j) + w_{s+1,s+1,t,t-1,z,z}(\mu_{s+1,t,z} - \mu_{s+1,t-1,z}) + w_{s+1,s+1,t,t,z,z-1}(\mu_{s+1,t,z} - \mu_{s+1,t,z-1}) + \varepsilon}};$$

else if $m = \{s,t+1,z\}$,

$$w'_{jm} := \frac{w_{jm}}{\sqrt{w_{s,s,t+1,t,z,z}(\mu_{s,t+1,z} - \mu_j) + w_{s,s-1,t+1,t+1,z,z}(\mu_{s,t+1,z} - \mu_{s-1,t+1,z}) + w_{s,s,t+1,t+1,z,z-1}(\mu_{s,t+1,z} - \mu_{s,t+1,z-1}) + \varepsilon}};$$

else if $m = \{s,t,z+1\}$,

$$w'_{jm} := \frac{w_{jm}}{\sqrt{w_{s,s,t,t,z+1,z}(\mu_{s,t,z+1} - \mu_j) + w_{s,s-1,t,t,z+1,z+1}(\mu_{s,t,z+1} - \mu_{s-1,t,z+1}) + w_{s,s,t,t-1,z+1,z+1}(\mu_{s,t,z+1} - \mu_{s,t-1,z+1}) + \varepsilon}};$$

end if

$\hat{\mu}_j^{old} := \hat{\mu}_j;$

$$\hat{\mu}_j^{new} := \frac{a_j' \Sigma^{-1} \hat{r} + s_j \hat{\mu}_j^{old} + \beta \sum_{\mathbf{m} \in N_j} w'_{jm} \hat{\mu}_m^{old}}{s_j + \beta \sum_{\mathbf{m} \in N_j} w'_{jm}};$$

$\hat{\mu}_j := \max\{0, \hat{\mu}_j^{new}\};$

$\hat{r} := \hat{r} + a_j\left(\hat{\mu}_j^{old} - \hat{\mu}_j\right);$

end for

end for

25: update $w'_{jm} = \exp\left[-\left(\frac{\mu_j - \mu_m}{\delta}\right)^2\right]$, $m \in N_j$;

26: update $\sigma^2_{p_i} = \frac{1}{I_{i0}}\exp(\tilde{p}_i)\left(1 + \frac{\sigma^2_{e,i} - 1.25}{I_{i0}}\exp(\tilde{p}_i)\right)$, $i = 1,2,....M$, where $\tilde{p} = A\hat{\mu}$;

27: end if stop criterion is satisfied.

where a_j denotes the column vector of the system matrix *A*, w'_{jm} are the weights for the neighboring voxels *m*, which are updated in each iteration, ε is a relax parameter introduced to avoid the denominator going to zero, *M* is the total projection ray numbers. In line 2, an initial estimate of the to-be-reconstructed image is set to be the result of FDK. The initial estimation of the variances of measuring projection data $\sigma^2_{p_i}$ for *i=1…M* are calculated from the acquired projection data. And according to the result of FDK, the anisotropic weights are initialized in line 6. From line 8 to line 24, each pixel is updated continuously by the GS strategy. By incorporating the weights or the neighboring voxels, an updating equation is performed at line 20. Then the anisotropic weights are updated based on new estimated intensities of voxels after one iteration at line 25. The variances of measuring projection data are also updated based on the re-projected measurements from the new intensities at line 26. It is worth to note that by setting the anisotropic weight to 1, the above pseudo-code for the present AwTV-PRWLS algorithm corresponds to the TV-PRWLS algorithm [69]. The final results will be obtained as the stop criterion condition is met as indicated at line 27. Specifically, in this study, the value of mean square error (MSE) between the results from the current iteration and the previous iteration is used as the stop criterion.

4.4 Data acquisition

To calculate the variance of the projection data, the mean number of incident photons along projection path *i* should be estimated according to Eq. (2.20). It is known that the incident photon number is mainly determined by the protocols of the tube current and the duration of X-ray pulse. Ideally, the incident photons should be uniformly distributed across the FOV. However, considering the concavity of the human body, a bow-tie attenuation filter is often installed between the human body and the X-ray source [91], which makes the incident photons across the FOV no longer uniform. To accurately estimate the incident intensity over the FOV at a specific mAs level, an air scan was first performed at the same mAs level. Figure 4.1 shows an example of the incident X-ray intensity in low-mAs case acquired by ExactArms (kV source/detector arms) of a Trilogy ™ treatment system (Varian Medical Systems, Palo Alto, CA) [91] by averaging the projections of one circle rotation. For the low-mAs case, the X-ray tube current was set at 10mA and the duration of the X-ray pulse at each projection view was set to be 10 ms. For the corresponding normal-mAs case, the tube current was set at 80mA and the duration of the X-ray pulse at each projection view was 12 ms. In this study, the tube voltage was all set to be 125 kVp for all the cases.

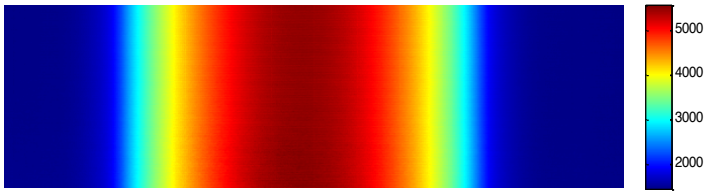

Figure 4.1. Incident X-ray intensity image across the field of view with 10 mA tube current and 10 ms pulse time in cone-beam geometry.

The cone-beam CT projection data acquired by the same CT system from CatPhan® 600 phantoms were used to evaluate the performance of the present AwTV-PRWLS algorithm in this study. A total of 634 projection views were acquired for a fully 360-degree rotation on a circular orbit. The dimension of each projection image is 1024×768 pixels. To reduce computational time, the projection data were down-sampled by a factor of 2. Only 8 out of 768 slices from the projection image were selected for image reconstruction. The source-to-isocenter distance is 100 cm and the source-to-detector distance is 150 cm. The array size of the reconstructed image is 350×350×8 and the associative voxel size is 0.776×0.776×0.776 mm^3. Sparse-view projection data are extracted evenly over 360 degrees from full projection views for further analysis.

In this study, three type of data: (1) full-view 10mA projection data; (2) sparse-view 80mA projection data; and (3) sparse-view 10mA projection data were studied. Table 4.1 shows the methods will be used in this section. To compare the impact of the *priori model* (i.e., penalty term), the AwTV-PRWLS were compared to TV-PRWLS for different parameters. To compare the influence of the variance estimation model of projection on the PRWLS method, the proposed AwTV/TV-PRWLS were compared to the AwTV/TV penalized uniform weighted least square strategy (AwTV/TV-PUWLS), which were use uniform weights in the statistical part (i.e., Σ was equal to identity matrix in Eq. (4.3)). In addition, to validate the statistical model, the proposed AwTV/TV-PRWLS were compared to the AwTV/TV-POCS methods.

Table 4.1. Description of three methods

Name	Formula
AwTV/TV-PRWLS	$\mu^* = \arg\min_{\mu\geq 0}(\hat{p}-A\mu)^T\Sigma^{-1}(\hat{p}-A\mu)+\beta\|\mu\|_{AwTV/TV}$;
AwTV/TV-PUWLS	$\mu^* = \arg\min_{\mu\geq 0}(\hat{p}-A\mu)^T(\hat{p}-A\mu)+\beta\|\mu\|_{AwTV/TV}$;
AwTV/TV-POCS	$\mu^* = \arg\min_{\mu\geq 0}\|\mu\|_{AwTV/TV}$ subject to $\|p-A\mu\|\leq\varepsilon$;

4.5 Image quality measures

One of the most important merits for medical image evaluation is the resolution. The high resolution image delivers clear messages to the physicians for diagnoses; the low resolution image loses some small features, which is more dangerous for clinical image. However, mitigating the artifacts from noise or missing data due to the reduction of X-ray exposure while maintaining good structure information is more challenging for the general CT image reconstruction methods. To quantitatively describe the resolution level

of the reconstructed image, the FWHM is always calculated for evaluation purpose. In order to obtain an FWHM value, a Gaussian-like function is used to fit the ESF or an impulse response in the reconstructed image. Through those fitted curves, it can be observed the high-resolution image will often have a higher peak value and low-resolution image often has a lower peak value. To quantize this observation, the FWHM values of the fitted Gaussian broadening kernel are calculated by $2.35\sigma_R$, where σ_R is the standard deviation of the Gaussian broadening kernel [52]. Then, high resolution image will have a smaller FWHM value and low contrast image will have a larger FWHM value.

Beside the merit of FWHM value, another merit – the noise level of the desired image is also very important for diagnosis. The physicians are hardly to locate the polyp from a noisy image. To quantitatively describe the noise level of the image, a uniform area (i.e., ROI) is always been selected to calculate the standard deviation. The smaller standard deviation indicates the image has a low-level noise, and a higher standard deviation indicates a noisy image is obtained. Then, if we combine the resolution (i.e., FWHM value) with the noise level merit, we can draw a curve to describe the trade-off between them, which will indicate the performance of image reconstruction algorithms. We call this curve as resolution-noise trade-off curve. The curve of an outstanding algorithms will very close to the original point, which indicates a high resolution and low noise level result image sill be generated.

Besides those two merits, the convergence analysis for an image reconstruction algorithm is necessary. A stable algorithm will always ensure the results converge to a global minimum. In the following section of results, we will focus our study on these three merits.

4.6 Physical phantom study

4.6.1 Influence of the priori model on the PRWLS method

To investigate the effects of the two prior models, i.e. TV and AwTV model, the full-view 10mA data was utilized for this study. The resolution of the resulting image was calculated from the ESF along the horizontal profile as indicated by the yellow dot lines on the top cold circle shown in Figure 4.2. In addition, a small region is selected as indicated by the yellow dot circle in Figure 4.2 to calculate the standard deviation σ_N. By varying the penalty parameter β from 20 to 8×10^4, we can obtain two resolution-noise tradeoff curves in the coordinates $\left(2.35\sigma_R, \sigma_N\right)$ for the TV-PRWLS and AwTV-PRWLS algorithms with $\delta = 0.006$ as shown in Figure 4.3.

From Figure 4.3, it can be observed that the result of AwTV-PRWLS algorithm has a higher resolution compared to the TV-PRWLS algorithm at the same noise level. In addition, a better balance between the noise and resolution can be observed as $\beta = 140$. In order to further validate the effects of parameter δ in the adaptive weights to the resulting image, a group of resolution-noise pairs were calculated towards the different δ values from 0.002 to 6 at $\beta = 140$ as shown in Figure 4.4.

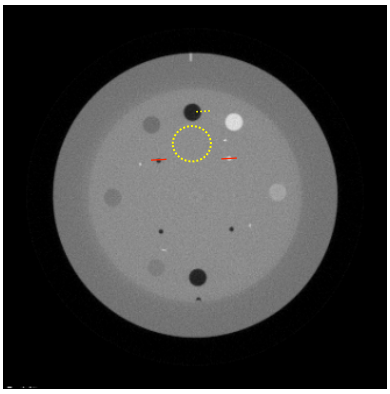

Figure 4.2. The reconstructed transverse image of the CatPhan® 600 phantom from full-view normal-mAs projection data.

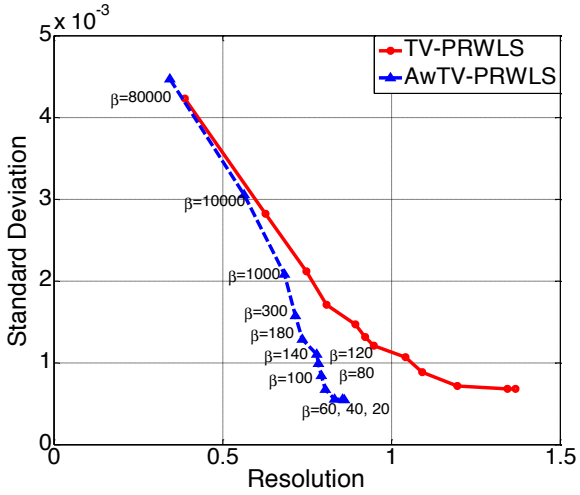

Figure 4.3. The resolution-noise tradeoff curves of the transverse reconstructed images of the CatPhan® 600 phantom by the TV-PRWLS and AwTV-PRWLS algorithms.

As shown in Figure 4.4, the resolution-noise tradeoff curve indicates that the reconstructed image by the AwTV-PRWLS algorithm has both good resolution and lowest noise level with $\delta = 0.006$ for the CatPhan® 600 phantom study. Moreover, it should be mentioned that as the value of δ decreases from 0.006 to 0.002, the noise level (i.e., standard deviation) increases noticeably from 5.0818×10^{-4} to 1.2×10^{-3}, and the associative resolution of the image decreases a little from 1.6293 to 1.6842. At the same time, as the value of δ increases from 0.006 to 6, the noise still maintains at a lower level while the resolution drops noticeably from 1.6293 to 2.2292 and finally locates at a fixed value when δ approaches a very large one. This result is consistent with our previous comparison study on the AwTV-POCS and TV-POCS [52] algorithms where the additional adaptive weights in the AwTV model show good property to preserve edges while mitigating noise of the resulting image.

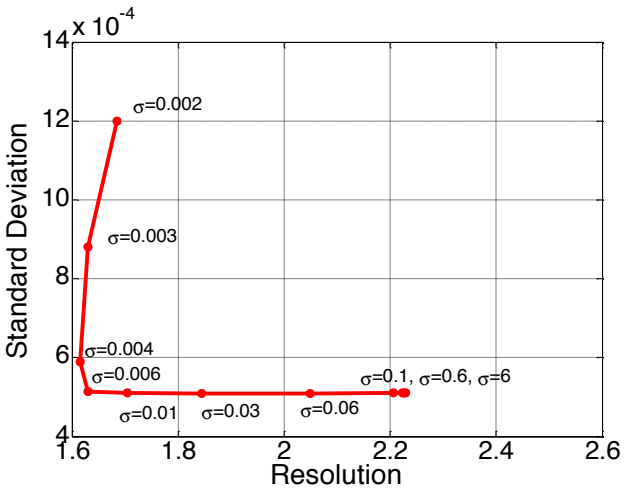

Figure 4.4. The resolution-noise tradeoff curve of the transverse reconstructed images of the CatPhan® 600 phantom by the AwTV-PRWLS algorithm with different δ values from 0.002 to 6.

4.6.2 Influence of the variance estimation model of projection on the PRWLS method

4.6.2.1 Visualization-based comparison

In this section, 79 projection views are extracted from the 80mA and 10mA projection data to generate type (2) and type (3) datum. Thus, the associative dosage can reduce to about 1/9, 1/8, and 1/72 of the dosage of full-view 80mA data, respectively. As for the comparison with the present AwTV-PRWLS, other three methods, i.e., the TV-PRWLS, AwTV- and TV-PUWLS were explored in this study. In the implementations, due to that a standard deviation can reflect the noise level of the to-be-reconstructed image, a ROI as indicated by the circle in was selected from the uniform background in the phantom to calculate standard deviation. To mitigate the effects caused by different parameter selection, different values of β were selected to keep the resulting images having the same noise level described by a standard deviation. Specifically, for the AwTV/TV-PRWLS methods, β=140 for all three types of data; for the AwTV/TV-PUWLS methods, β=5000.

A reconstructed slice of the CatPhan® 600 phantom is shown in Figure 4.5. The first row of Figure 4.5 is the results reconstructed from type 1 (i.e., full-view 10mA projection) data by the FDK and AwTV/TV-PRWLS and AwTV/TV-PUWLS methods. The second and third rows of Figure 4.5 are the results reconstructed from type 2 (i.e., 79-view 80mA projection) data and type 3 (i.e., 79-view 10mA projection) data. It can be seen that the FDK method cannot produce satisfied results in all the cases. In addition, the AwTV/TV-PRWLS methods achieve significant gains than the AwTV/TV-PUWLS methods in terms of noise suppression and resolution preservation. Small differences are also observed between the results from the AwTV-PRWLS and TV-PRWLS methods due to different penalty term settings. The related further discussion can be found in the following section.

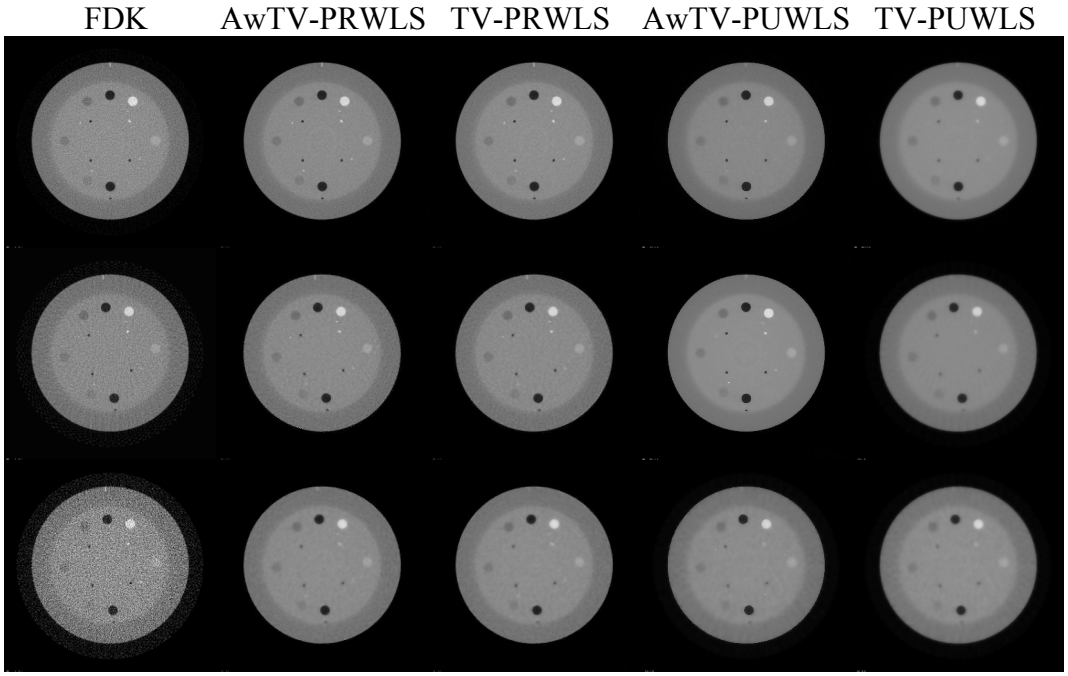

Figure 4.5. The reconstructed images of the CatPhan® 600 phantom by FDK, AwTV/TV-PRWLS, AwTV/TV-PUWLS. The first row shows the images reconstructed from the full-view 10mA projection data. The second row shows the images reconstructed from the 79-view 80mA projection data. The third row shows the images reconstructed from the 79-view 10mA projection data. The display window is [0, 0.03] mm^{-1}.

4.6.2.2 Profile-based comparison

Figure 4.6, Figure 4.7 and Figure 4.8 show the profiles passing through the two spots, as indicated by red line in Figure 4.2, in the images reconstructed from three types of data, respectively. A Gaussian like function is used to fit the profiles as indicated in the figures. From Figure 4.6, we can observe that in the case of full-view 10mA projection data, the peak values of the results from AwTV/TV-PRWLS are much higher than that from AwTV/TV-PUWLS in both cold and hot spots. We also observe the gains from our AwTV model compared to the conventional TV model. For the 79-view 80mA projection data case, the results are shown in Figure 4.7. In the 79-view 10mA projection data case, shown in Figure 4.8, although all the images are not acceptable (i.e., inferior results), we still observe some gains by using the AwTV-PRWLS frame work.

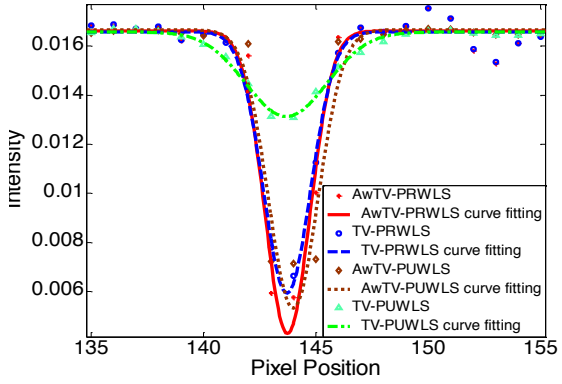

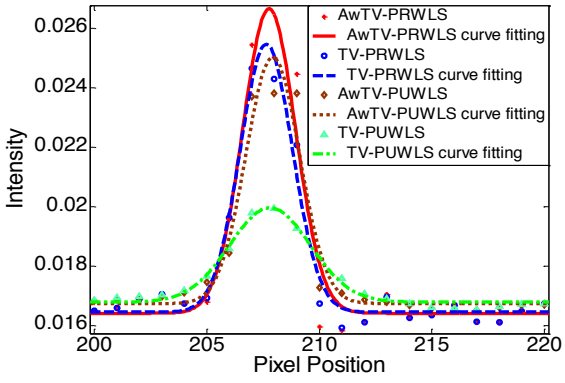

(a) (b)

Figure 4.6. Horizontal profiles of the CatPhan® 600 phantom images reconstructed by different algorithms from full-view 10mA projection data. Picture (a) shows the profiles across the cold spot (146th row, 135th to 155th column). Picture (b) shows the profiles across the hot spot (139th row, 200th to 220th column).

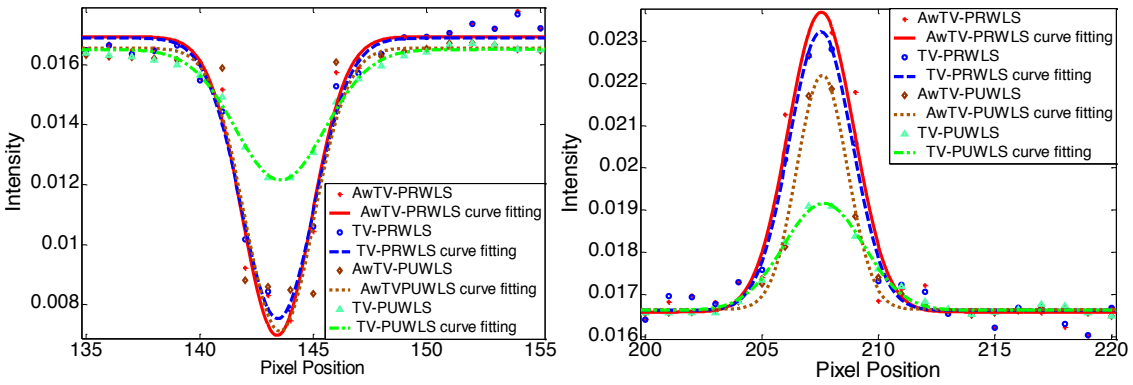

(a) (b)

Figure 4.7. Horizontal profiles of the CatPhan® 600 phantom images reconstructed by different algorithms from 79-view 80mA projection data. Picture (a) shows the profiles across the cold spot (146th row, 135th to 155th column). Picture (b) shows the profiles across the hot spot (139th row, 200th to 220th column).

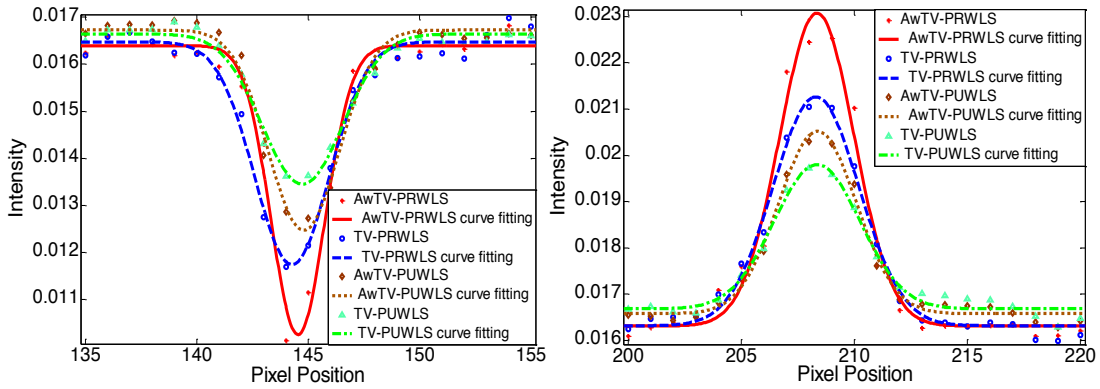

(a) (b)

Figure 4.8. Horizontal profiles of the CatPhan® 600 phantom images reconstructed by different algorithms from 79-view 10mA projection data. Picture (a) shows the profiles across the cold spot (146th row, 135th to 155th column). Picture (b) shows the profiles across the hot spot (139th row, 200th to 220th column).

4.6.2.3 FWHM measures

To further quantitatively analyze the gains from the present PRWLS method than the PUWLS method, the FWHM of the two spots (a cold spot and a hot spot) are calculated and shown in Table 4.2. Table 4.2 reveals the AwTV/TV-PRWLS methods can produce smaller values than the AwTV/TV-PUWLS methods on both hot and cold spots, which is consistent with our observation about the profile comparison. It should be mentioned that the FWHM values of the cold spots in the results from 79-view 80mA projection data by

AwTV-PUWLS has the smallest value than the other results. This apparent contradiction, however, is likely due to the curve fitting options which make the area under curve of the Gaussian-like bell shape are much smaller than others and can be illuminated by observing the curve fitting results as shown in Figure 4.7 (b).

Table 4.2. The FWHM value of the cold and hot spots in Figure 4.3

Data type of projection	Position	AwTV-PRWLS	TV-PRWLS	AwTV-PUWLS	TV-PUWLS
Full-views 10mA	cold spot	4.7470	4.7565	4.8222	5.7763
	hot spot	4.6836	4.9891	4.9749	6.0207
79-views 80mA	cold spot	5.0455	5.0689	5.2241	6.3967
	hot spot	4.4650	4.4979	3.5885	5.7085
79-views 10mA	cold spot	3.9222	5.3275	5.3181	6.0419
	hot spot	5.4802	6.1406	5.7246	6.3215

4.6.2.4 Convergence analysis of the AwTV-PWLS algorithm

The convergence property of the AwTV-PRWLS algorithm was documented by calculating the value of cost function Φ for the full-view 80mA projection CatPhan® 600 phantom data. Figure 4.9 shows the value of $\log(\Phi)$ versus the iteration steps for the AwTV-PRWLS algorithm. We can observe that the value of Φ decreases monotonously as the number of iteration steps increases. Finally, we found the objective value arrived at a stable value at the 20^{th} iteration and we believe the algorithm has converged sufficiently and the to-be-estimated image would only have tiny changes (hardly be observed by human eye) for further iteration.

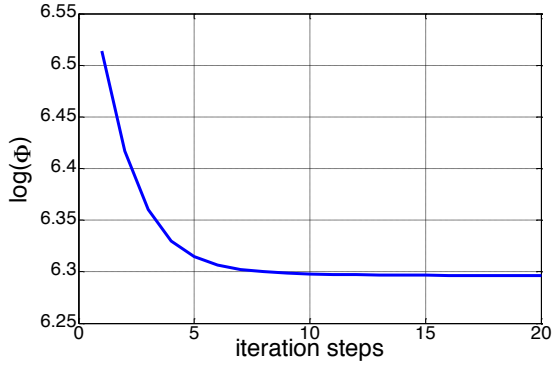

Figure 4.9. Convergence analysis of AwTV-PRWLS algorithm: $\log(\Phi)$ v.s. iteration steps.

4.7 Discussion and conclusion

In this chapter, we presented a statistical iterative reconstruction method based on the PRWLS strategy for CT image reconstruction. There are two motivations triggered this study. Firstly, we adopted a novel AwTV [52, 54] as a regularization term (i.e., the *a priori* term) to penalize the RWLS problem, which can mitigate the over-smoothing or recover more edge details compared to the conventional TV penalty. Secondly, the variances of the projection data are estimated with inclusion of the electronic background noise , which is considered to accurately describe the statistical property of the low-mAs

projection data. Although the effect of the electronic background noise is minor for normal-mAs CT projection data due to the large quantity of photons in the measurement, the detected number of photons in the case of low-mAs scan is dramatically decreased. Thus, the effects of the electronic background noise could not be ignored [63]. In this study, by using a new variance estimation of projection data as weights in the present AwTV-PRWLS strategy, the re-weighted least-squares term (i.e., the primary term) is more accurate than the uniform weighted least-squares without utilizing the statistical property. It should be mentioned that in a penalized likelihood image reconstruction, a widely-used smoothing penalty term can suppress the reconstruction variance dramatically and, therefore, make the task to see the gain by a more accurate variance description even challenging. Nevertheless, despite the challenging, it is not reasonable to reject the use of a more accurate variance description in the penalized likelihood image reconstruction framework.

Through extensive experiments with quantitative and qualitative measures, we found that the AwTV/TV-PRWLS strategies can yield more details than the AwTV/TV-PUWLS strategies in all three types of datasets. For example, as we can see from the resolution-noise tradeoff curves and the FWHM studies, the advantage of the AwTV term compared to the conventional TV term is significant noticeable. Furthermore, the AwTV-based strategies show more efficiency to accurately preserve edge details than the conventional TV term.

In summary, the present AwTV-PRWLS strategy is a more efficient way to accurately reconstruct the image from low-mAs (i.e., 10mA) full projection data and the AwTV-POCS strategy is a more efficient way to reconstruct the image from sparse-view normal-mAs (i.e., 80mA) projection data. As we mentioned at the beginning of this paper, the efficiencies of the AwTV model compared to other priors are still unknown and shall be investigated. Therefore, the comparison between the AwTV prior and other prior terms such as the generalized Gaussian Markov random field (GGMRF) prior [4], reweight TV prior [11] and TV-stokes prior [49, 51] or prior information from previous scan [13, 62, 64] will be one task to continue this research. In addition, how to solve the TV/AwTV problem efficiently and accurately will be another task in our future studies [39, 42]. Another interesting topic is how to utilize TV-based image reconstruction methods toward different clinical applications such as high resolution micro-CT [78] or multiple objects reconstruction [59], which could be another task to continue this research.

Chapter 5 . Adaptive-weighted total variation minimization for sparse data toward low-dose X-ray CT image reconstruction

Another strategy to decrease the total dosage besides decreasing photon flux at each projection view is to reduce the number of projection views per rotation around the body and maintain the photon flux at each projection. Previous studies have shown that by minimizing the TV of the to-be-estimated image with some data and other constraints, a piecewise-smooth X-ray CT can be reconstructed from sparse-view projection data without introducing noticeable artifacts. However, due to the piecewise constant assumption for the image, a conventional TV minimization algorithm often suffers from over-smoothness on the edges of the resulting image. To mitigate this drawback, we present an AwTV minimization algorithm in this chapter. Inspired by the previously-reported TV-POCS implementation, a similar AwTV-POCS implementation was developed to minimize the AwTV subject to data and other constraints for the purpose of sparse-view low-dose CT image reconstruction. To evaluate the presented AwTV-POCS algorithm, both qualitative and quantitative studies were performed by computer simulations and phantom experiments. The results show that the presented AwTV-POCS algorithm can yield images with several noticeable gains, in terms of noise-resolution tradeoff plots and full width at half maximum values, as compared to the corresponding conventional TV-POCS algorithm. The comparisons between the AwTV/TV-POCS and AwTV/TV-PRWLS algorithms introduced in previous chapter are also studied in this chapter in different types of low-dose projection data.

5.1 Introduction

In 1992, Rudin *et al.* reported that the total variation norm of the to-be-estimated solution is essentially the l_1-norm of derivatives, and they further showed that this norm can be utilized to address the ill-posed image restoration problem [75]. Then the TV model was adapted to nuclear images in [72]. In 2006, Sidky *et al*. adapted the concept of TV minimization to consider the piecewise constant or sparse source distribution and formulated an innovative algorithm, called TV-POCS, to perform CT image reconstruction from sparse-sampled or sparse-view projection data [79]. Later in 2008, Sidky *et al*. presented an updating algorithm, i.e., the ASD-POCS [71], for TV minimization with improved robustness against the cone-beam artifacts from sparse or limited projection-views with comparison to other classical methods, e.g., the well-known EM algorithm. This ASD-POCS algorithm, simply called TV-POCS hereafter, can be considered as a new attempt to reconstruct images of sparse signals from under-sampled projection data for CT applications. Although the images reconstructed by the TV-POCS algorithm from sparse-sampled data are close to the true source distributions, over-smoothing in the reconstructed image is frequently seen due to the assumption of isotropic edge property in calculating the TV term. Recently, a TV-based edge preserving (EPTV) model [88] was proposed to address the issue of the original TV, and

was claimed to preserve edges by bringing in different weights in the TV term from edges and constant areas of the to-be-estimated image.

In the proposed AwTV model, different with the EPTV model, we consider the anisotropic (rather than isotropic) edge property of an image and propose a novel AwTV-POCS method for low-dose CT image reconstruction from sparse-sampled projection data. Inspired by the TV-POCS implementation [79, 80], a similar implementation, called AwTV-POCS, is developed to minimize the AwTV with subjection to data and other constraints for the purpose of dose reduction via CT image reconstruction from sparse data.

5.2 CT Imaging Model with the Presented AwTV Minimization

According previous discussion in section 4.2, in order to mitigate the over-smoothing of edges in the conventional TV minimization, a new imaging model with AwTV minimization is proposed as follows:

$$\min_{\mu\geq 0}\|\mu\|_{AwTV} \quad \text{subject to} \quad |p-A\mu|\leq\varepsilon, \tag{5.1}$$

where the AwTV of the to-be-reconstructed image, i.e., $\|\mu\|_{AwTV}$, is defined in previous section as:

$$\|\mu\|_{AwTV}=\sum_{s,t}\sqrt{w_{s,s-1,t,t}\left(\mu_{s,t}-\mu_{s-1,t}\right)^2+w_{s,s,t,t-1}\left(\mu_{s,t}-\mu_{s,t-1}\right)^2}, \tag{5.2}$$

$$w_{s,s-1,t,t}=\exp\left[-\left(\frac{\mu_{s,t}-\mu_{s-1,t}}{\delta}\right)^2\right] \quad \text{and} \quad w_{s,s,t,t-1}=\exp\left[-\left(\frac{\mu_{s,t}-\mu_{s,t-1}}{\delta}\right)^2\right], \tag{5.3}$$

where δ in the weights ($w_{s,s-1,t,t}$ and $w_{s,s,t,t-1}$) is a scale factor which controls the strength of the diffusion during each iteration. The AwTV model approaches to the conventional TV model when $\delta\to\infty$.

5.3 Presentation of the AwTV-POCS algorithm

Due to the nonlinear form of the AwTV with respect to the image intensity, it is numerically difficult to utilize directly the second-order derivative for the purpose of effectively minimizing the objective function Eq. (5.2). Inspired by the optimization strategy as described in [61], the weights can be pre-computed at current iteration for the AwTV minimization at the next iteration. By this strategy, the gradient descent technique is adapted to minimize the AwTV of the SART-estimated intermediate image where only the first-order derivative of the AwTV term respect to each voxel value is needed, which can be approximately expressed as:

$$\begin{aligned}\frac{\partial\|\mu\|_{AwTV}}{\partial\mu_{s,t}}\approx&\frac{2w_{s,s-1,t,t}\left(\mu_{s,t}-\mu_{s-1,t}\right)+2w_{s,s,t,t-1}\left(\mu_{s,t}-\mu_{s,t-1}\right)}{\sqrt{\xi+w_{s,s-1,t,t}\left(\mu_{s,t}-\mu_{s-1,t}\right)^2+w_{s,s,t,t-1}\left(\mu_{s,t}-\mu_{s,t-1}\right)^2}}\\&+\frac{-2w_{s+1,s,t,t}\left(\mu_{s+1,t}-\mu_{s,t}\right)}{\sqrt{\xi+w_{s+1,s,t,t}\left(\mu_{s+1,t}-\mu_{s,t}\right)^2+w_{s+1,s+1,t,t-1}\left(\mu_{s+1,t}-\mu_{s+1,t-1}\right)^2}}\end{aligned} \tag{5.4}$$

$$+\frac{-2w_{s,s,t+1,t}\left(\mu_{s,t+1}-\mu_{s,t}\right)}{\sqrt{\xi+w_{s,s,t+1,t}\left(\mu_{s,t+1}-\mu_{s,t}\right)^2+w_{s,s-1,t+1,t+1}\left(\mu_{s,t+1}-\mu_{s-1,t+1}\right)^2}},$$

where ξ is a relax parameter introduced to avoid the denominator going to zero.

Similar to the ASD-POCS approach [80], the optimization of the objective function Eq. (5.2) is implemented by the following iterative scheme, named as AwTV-POCS algorithm. For an image with the array size of $s \times t$, each of the general iterations of I cycles includes J iteration cycles of POCS operation and K iteration cycles of AwTV minimization by gradient descent. The relax parameter ω in the POCS operation decreases as the iteration increases and the step-size τ of the gradient descend also decreases as the iteration increases. Summarily, the pseudo-code for the presented AwTV-POCS algorithm is listed as follows:

initial: $\mu_{s,t}^{(0)} := 1;\ s = 1,2,...,S, t = 1,2,...,T;$
initial: $\delta,\ \varepsilon,\ \tau; \omega = 1;$
while (stop criterion is not met)
  for j = 1,2,...,J; (POCS)
    if j == 1;
      $\mu_{s,t}^{(j)} := SART(\mu_{s,t}^{(0)}, \omega);$
    else $\mu_{s,t}^{(j)} := SART(\mu_{s,t}^{(j-1)}, \omega);$ $s = 1,2,...,S, t = 1,2,...,T;$
    end if
  end for
if $\mu_{s,t}^{(J)} > 0$, then $\mu_{s,t}^{(J)} = \mu_{s,t}^{(J)};$ $s = 1,2,...,S, t = 1,2,...,T;$
  else $\mu_{s,t}^{(J)} := 0;$ $s = 1,2,...,S, t = 1,2,...,T;$
end if
$dp := \left\| A\mu_{s,t}^{(J)} - A\mu_{s,t}^{(0)} \right\|_2;$ $s = 1,2,...,S, t = 1,2,...,T;$
$d\mu_{SART} := \left\| \mu_{s,t}^{(J)} - \mu_{s,t}^{(0)} \right\|_2;$ $s = 1,2,...,S, t = 1,2,...,T;$
$w_{s,s-1,t,t} = \exp\left[-\left(\frac{\mu_{s,t}^{(J)} - \mu_{s-1,t}^{(J)}}{\delta} \right)^2 \right]$ and $w_{s,s,t,t-1} = \exp\left[-\left(\frac{\mu_{s,t}^{(J)} - \mu_{s,t-1}^{(J)}}{\delta} \right)^2 \right];$
for $k = 1,2,...,K;$ (AwTV gradient descent)
  $\mu_{s,t}^{(J+k)} := \mu_{s,t}^{(J+k-1)} - d\mu_{SART} \cdot \tau \cdot \frac{\nabla \left\| \mu_{s,t}^{(J+k-1)} \right\|_{AwTV}}{\left| \nabla \left\| \mu_{s,t}^{(J+k-1)} \right\|_{AwTV} \right|};$
  end for
if $dp < \varepsilon;$
  $\omega := 0.995 \times \omega;$
end if
$\mu_{s,t}^{(0)} := \mu_{s,t}^{(J+K)};$
calculate the criterion;
$\tau = \tau * 0.995;$
end if stop criterion is satisfy

In line 1, an initial estimate of the to-be-reconstructed image is set to be uniform with voxel value of 1. In line 2, four parameters, δ, ε , ω and τ, are initialized before the iteration starts. Specifically, the error tolerance ε is initialized based on the noise level of the data. The initial value of δ in the weights of AwTV term will be discussed later in the Result Section, and so are the parameters ω and τ. Each outer loop (lines 3-23) is performed by two separated iteration steps, i.e., the POCS (or the SART) (lines 4-12) and the gradient descent for the AwTV minimization (lines 16-18). The weights are pre-computed using latest image estimation $\mu_{s,t}^{(J)}$ in line 15. By setting the weight to 1, the above pseudo-code for the presented AwTV-POCS algorithm is applicable to the TV-POCS algorithm [79, 80]. A brief discussion on the stop criterion for both TV-POCS and AwTV-POCS implementations is given below.

5.4 Stop criterion for the AwTV-POCS and TV-POCS algorithms

In order to ensure the solution of the objective function Eq. (5.2) obtained by the above presented AwTV-POCS implementation is an optimal estimate, the associative Karush-Kuhn-Tucker (KKT) condition should be satisfied, similar to that in the TV-POCS implementation, as reported in [80]. For the TV-POCS algorithm implementation, the KKT condition can be satisfied with an indicator factor $c_\alpha = -1.0$ where c_α is defined as:

$$c_\alpha = \frac{\vec{d}_{TV} \cdot \vec{d}_{data}}{\left|\vec{d}_{TV}\right| \cdot \left|\vec{d}_{data}\right|}, \tag{5.5}$$

where $\vec{d}_{TV}$ is a vector of derivative of the TV term, and $\vec{d}_{data}$ is a vector of derivative of the data constraints using the Lagrangian multiplier. For the presented AwTV-POCS algorithm implementation, a similar indicator factor can also be used to describe the KKT condition for an optimal estimate. As stated in [80], $c_\alpha = -1.0$ is a necessary condition for an optimal solution for the TV minimization with sufficient data constraints. The necessary condition of $c_\alpha = -1.0$ may not be reached unless a great number of iteration cycles are executed, which may not be practical. In the AwTV-POCS algorithm, we discovered that very small or imperceptible changes was noticeable in the reconstructed images when c_α went below -0.6. Thus, in our algorithm implementation, we used $c_\alpha < -0.6$ as stop criterion in line 23 of the above pseudo-code.

To evaluate the differences between the resulting images from the AwTV-POCS and TV-POCS approaches, several computer simulation and phantom experiment studies were performed and reported in the following section.

5.5 Digital phantom studies

For simplicity, without loss of generality, a parallel-beam CT imaging geometry was used for the purpose of measuring the gain of the AwTV minimization with comparison to the conventional TV minimization. This geometry was modeled with 1024 bins on a 1D detector for 2D image reconstruction. The distance between the centers of two neighboring detector elements or bins is 0.25mm. Given the digital phantom, the noise-

free transmission data was computed by the use of the Lambert-Beer's law, $I_i = I_i^o \exp(-\bar{p}_i)$, where $\bar{p}_i$ is the line integral of the phantom intensity distribution along the ray *i*, I_i^o is the mean number of incident photons. Given the noise-free data, the noisy transmission data were simulated based on the assumption for the statistical model of the measurements.

5.5.1. Design of a modified Shepp-Logan phantom and computation of line integrals

According to the mass attenuation coefficients as listed in Table 5.1 for different tissues at 80 KeV in [43], a modified Shepp-Logan phantom was carefully designed as shown in Figure 5.1 for simulation studies. The dimensions of the phantom are $256\times256mm^2$, consisting of 512×512 pixels.

Table 5.1. Mass attenuation coefficients and the relate densities for different tissues.

Body tissue	Mass attenuation coefficients μ/ρ (m^2/kg)	The density of tissue (kg/m^3) in 20°C
Air, dry	1.661×10^{-2}	1.205
Water	1.835×10^{-2}	1000
Muscle	1.822×10^{-2}	1040
Fat	1.805×10^{-2}	920
Bone	2.083×10^{-2}	1850

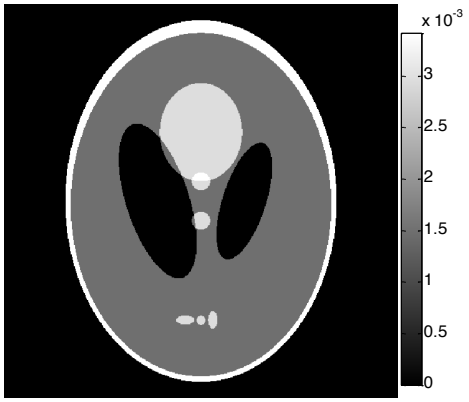

Figure 5.1. A modified Shepp-Logan phantom with display window [0, 0.0034] mm^{-1}.

With the parallel-beam imaging geometry, the noise-free sinogram can be computed by the line integration of the attenuation coefficients along the corresponding projection paths. A set of noise-free sinograms was computed with 1024 detector bins per view and several different numbers of projection views, i.e., 20, 40 and 60, at equal angular increment on 360 degrees around the phantom.

5.5.2. Parameter selection

To reconstruct the image of the Shepp-Logan phantom μ_j of Figure 5.1 from the above simulated noisy sinogram data p_i, we followed the description in [79, 80] to

implement their TV-POCS algorithm. In a similar way to implement our AwTV-POCS algorithm, the parameter of δ in the weight of (5.3) shall be determined. By some experimental trials, the value of this scale factor was set to 0.6×10^{-2} to simulate the strength of the diffusion model [73, 91]. For the EPTV-POCS method, the scale factor was also set to 0.6×10^{-2} for comparison purpose. In addition to this parameter, another factor of $\xi=1.0\times10^{-5}$ in Eq. (5.4) was set to ensure that the denominators will not go to zero. For the TV-POCS, EPTV-POCS and AwTV-POCS algorithms, each of the general iteration consisted of 10 POCS iterations and 10 gradient descent iterations. The strop criterion was discussed in previous section. The error tolerance ε for the data constraint will be discussed later. The initial value of ω and τ were set as 1 and 0.7×10^{-5}, respectively, similar to that in [79, 80, 90].

5.5.3. Visualization-based evaluation

In this evaluation study, two numerical experiments were performed: (1) image reconstruction from noise-free data; and (2) image reconstruction from noisy data. In each numerical experiment, images were reconstructed from the data simulated with 20, 40, 60 projection views, respectively, by the use of the AwTV-POCS algorithm with comparison to the TV-POCS and EPTV-POCS algorithms.

5.5.3.1. Noise free cases

Figure 5.2 shows the results from the noise-free experiment. It can be observed that the images reconstructed by the TV-POCS, EPTV-POCS and AwTV-POCS are visually much better than the results of FBP in all the cases of 20, 40, 60 projection views. The difference between the images from the TV-POCS, EPTV-POCS and AwTV-POCS can be observed by using a narrow grayscale display window as shown in Figure 5.3. Regions of interest (ROIs) in Figure 5.3 were selected to examine some details of the reconstructed images. The corresponding ROIs results are shown in Figure 5.4. It can be seen that, in the case of 20 projection views, the results of AwTV-POCS and EPTV-POCS algorithms demonstrate some gains in terms of edge preserving. Meanwhile, the gains gradually disappeared as more projection views were used. It is worth to note that a little over-enhancement at the edges in the EPTV-POCS reconstruction can be observed as shown in the second row of Figure 5.4, which is consistent with the results published in [88]. From 60 projection views, all the TV-POCS, EPTV-POCS and AwTV-POCS algorithms generated good quality images with high similarity.

To further visualize the difference between the three approaches in the cases of 20, 40 and 60 projection views, horizontal profiles of the resulting images were drawn across the 410^{th} row for each case and are shown in Figure 5.5, Figure 5.6 and Figure 5.7, where the corresponding profile from the true phantom image is given for reference. In each case, three ROIs were selected to inspect the difference of the results. Figure 5.5 (b)-(d) show that the AwTV-POCS and EPTV-POCS algorithms can achieve better profiles matching with the ideal ones than the TV-POCS algorithm. And the gain from the AwTV-POCS is observable as compared to results of the EPTV algorithm. As the number of projection views increased, the results of TV-POCS, EPTV-POCS and AwTV-POCS algorithms approached to that of the true phantom image. However, the improved edge preservation by the AwTV-POCS is still visible in the results from 60 projection views, see Figure 5.7.

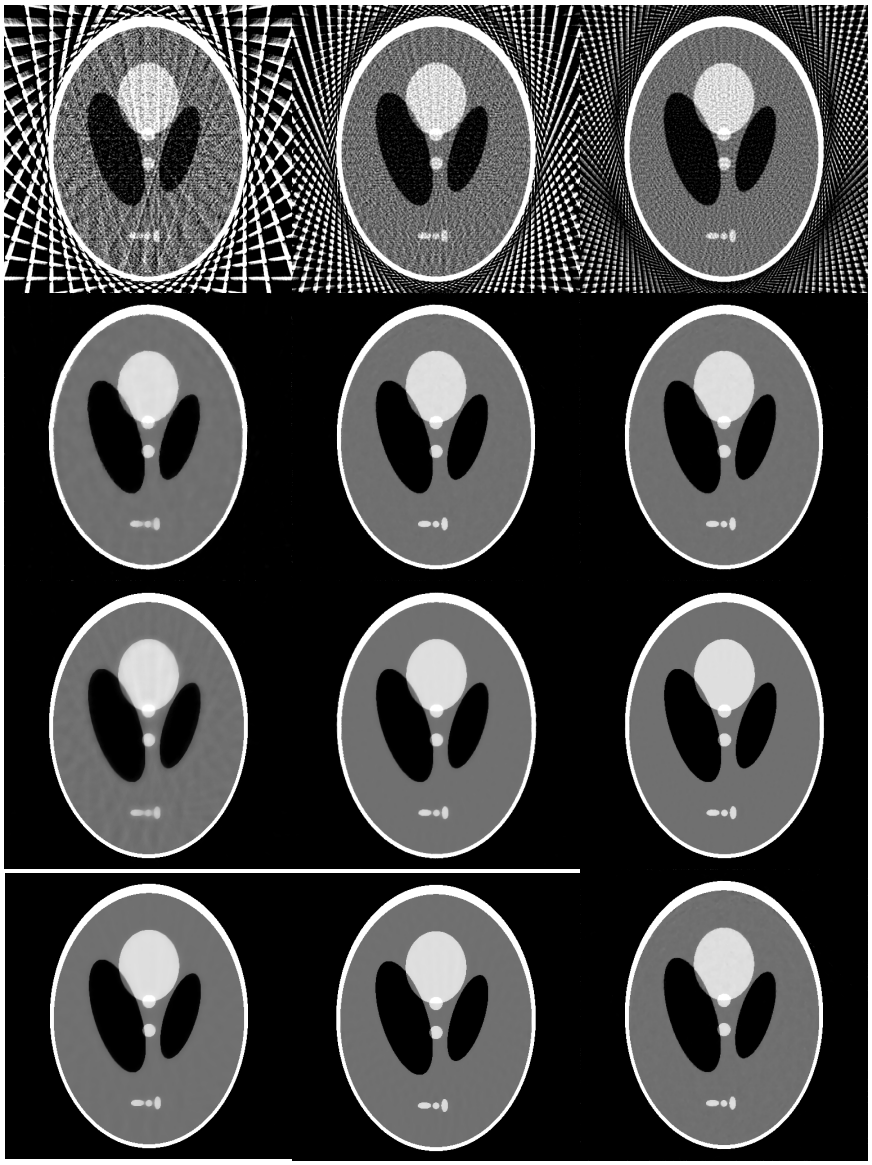

Figure 5.2.The images reconstructed by the FBP (1st row), TV-POCS (2nd row), EPTV-POCS (3rd row) and AwTV-POCS (4th row) algorithms from 20 (left column), 40 (middle column), and 60 (right column) projection views, respectively. The display window is [0, 0.0034] mm^{-1}.

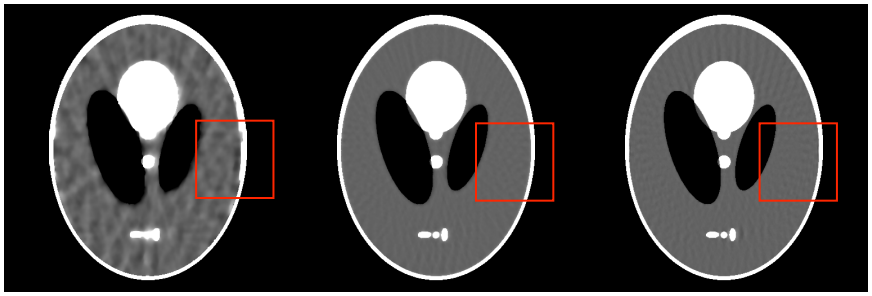

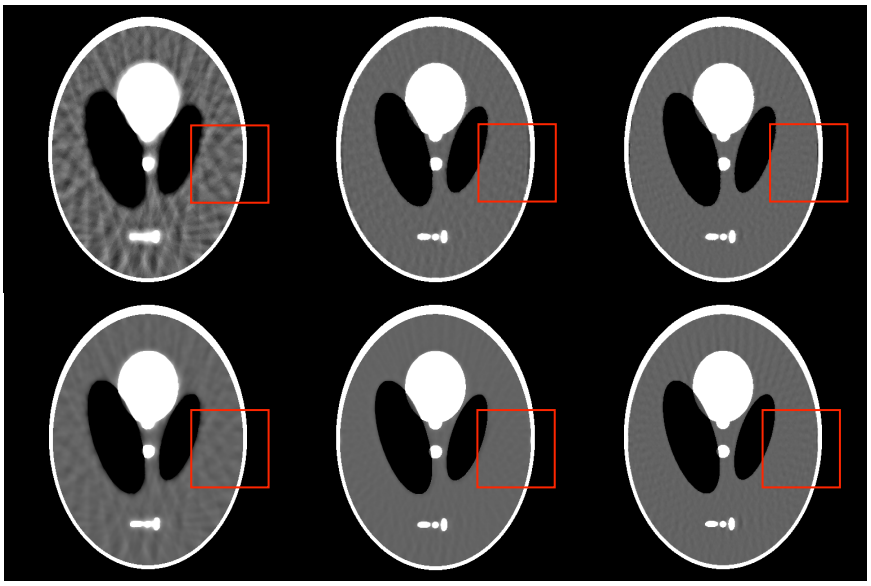

Figure 5.3. The images reconstructed by the TV-POCS (top row), EPTV-POCS (middle row) and AwTV-POCS (bottom row) algorithms from 20 (left column), 40 (middle column), and 60 (right column) projection views, respectively. The display window is [0.0013, 0.0018] mm^{-1}.

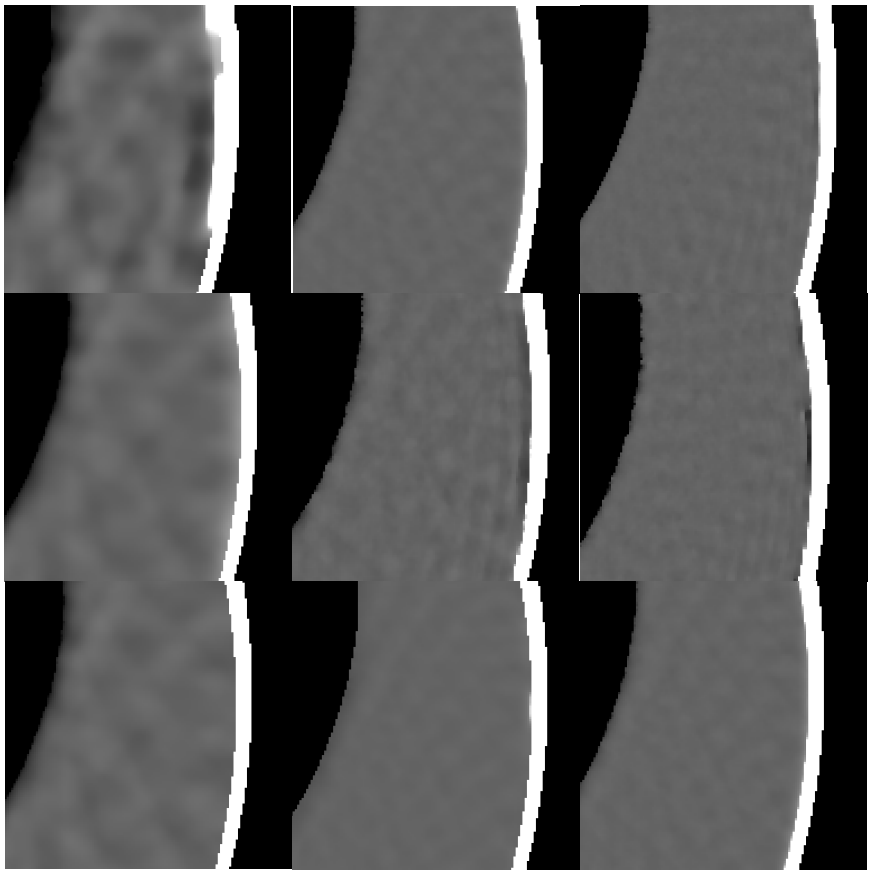

Figure 5.4. The ROIs of the images reconstructed by the TV-POCS (top row), EPTV-POCS (middle row) and AwTV-POCS (bottom row) algorithms from 20 (left column),

40 (middle column), and 60 (right column) projection views, respectively. The display window is [0.0013, 0.0018] mm-1.

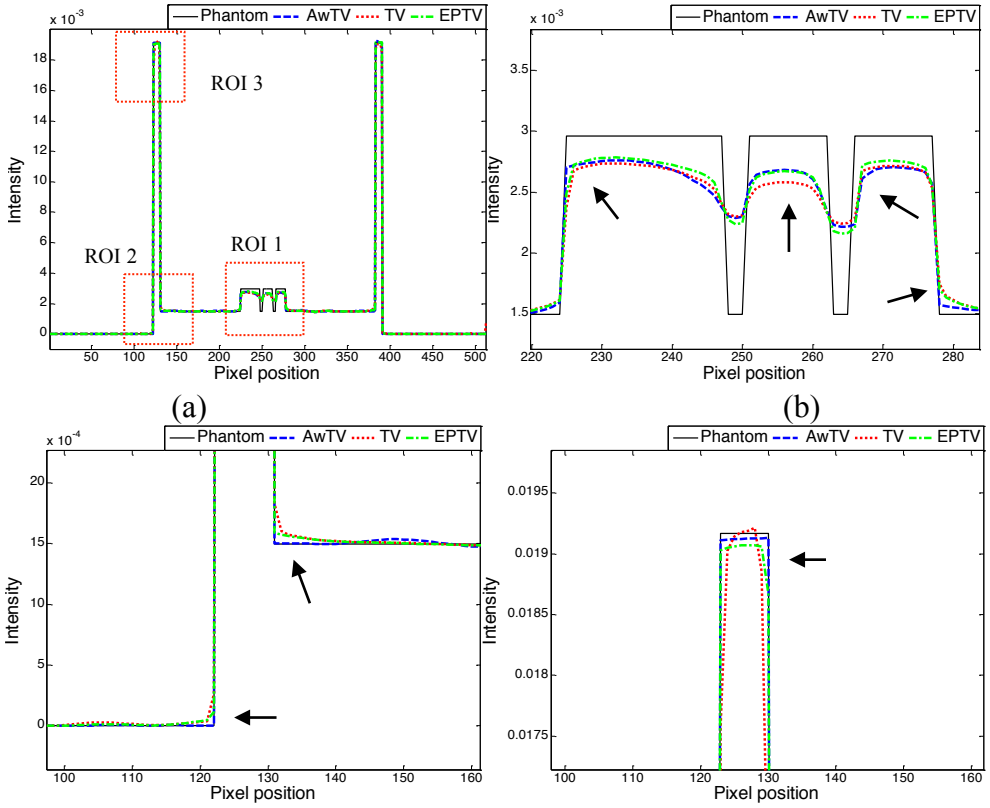

Figure 5.5.Horizontal profiles (410th row) of the images reconstructed by different algorithms from 20 projection views of noise-free data. Picture (a) shows the overall profiles. Pictures (b), (c) and (d) show the partial profiles of the three ROIs indicated in (a).

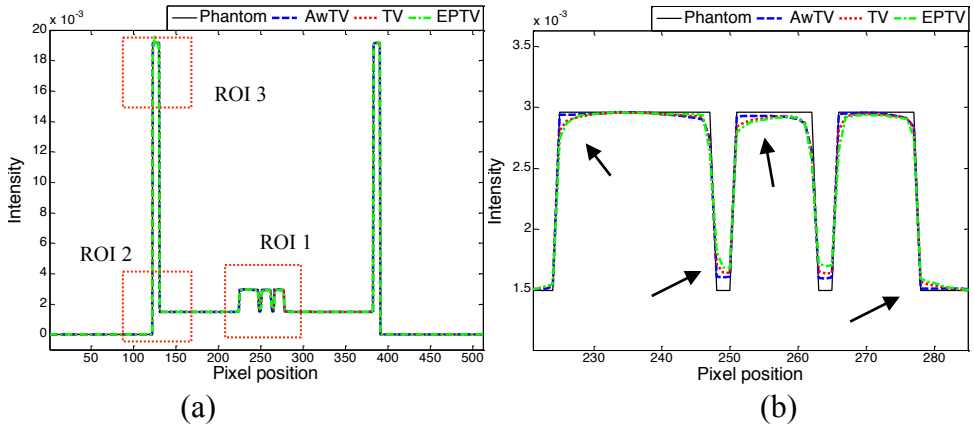

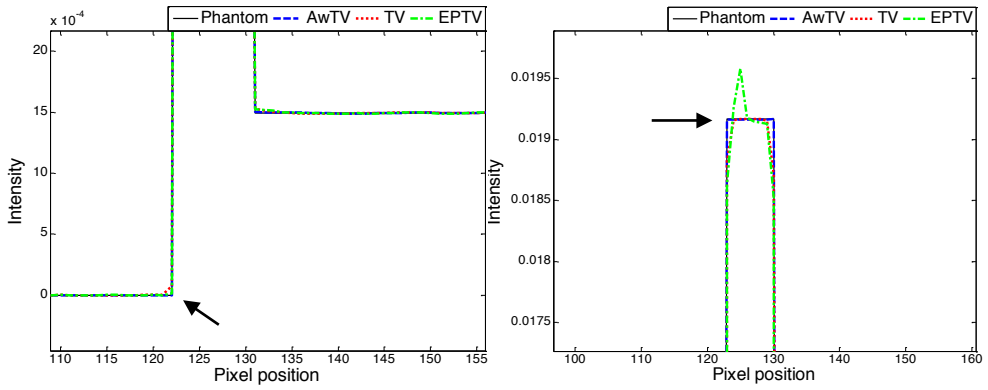

(c) (d)

Figure 5.6. Horizontal profiles (410th row) of the images reconstructed by different algorithms from 40 projection views of noise-free data. Picture (a) shows the overall profiles. Pictures (b), (c) and (d) show the partial profiles of the three ROIs indicated in (a).

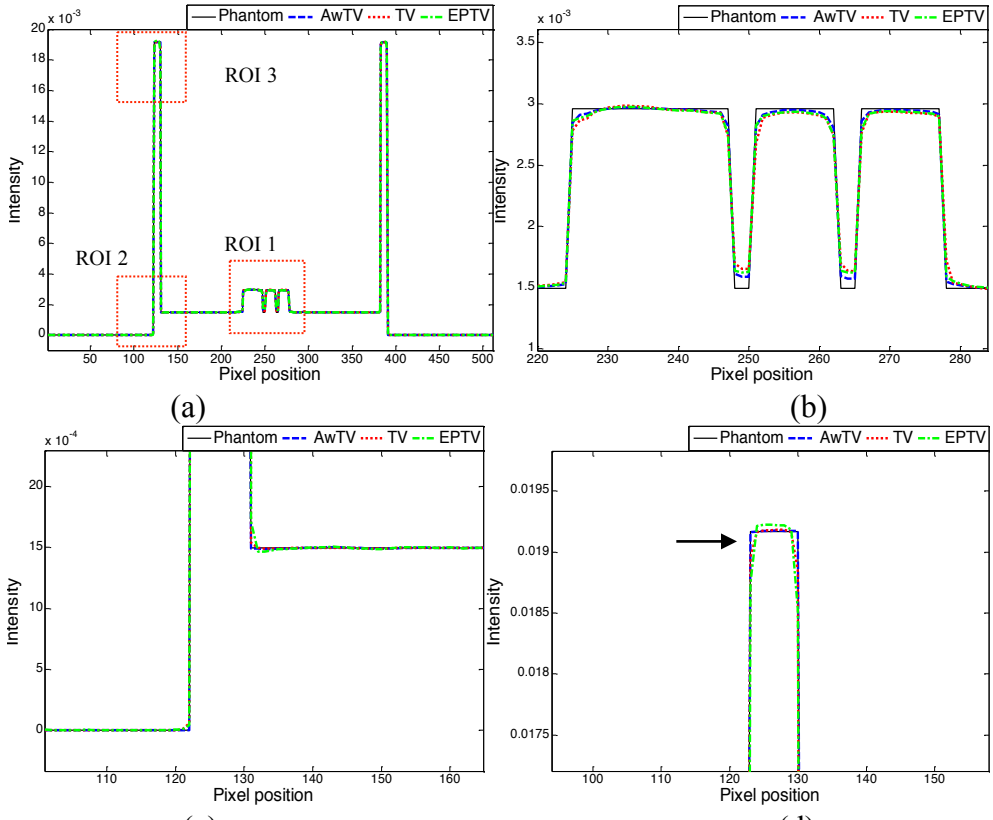

(a) (b)

(c) (d)

Figure 5.7. Horizontal profiles (410th row) of the images reconstructed by different algorithms from 60 projection views of noise-free data. Picture (a) shows the overall profiles. Pictures (b), (c) and (d) show the partial profiles of the three ROIs indicated in (a).

The above noise-free simulation studies concurred with our previous discussion about the advantage of using adaptive weights for edge preservation in the AwTV model as

compared to the conventional TV and EPTV models. To further support our previous discussion, studies on noisy projection data were performed and reported in the next section below.

5.5.3.2. Noisy cases

In this section, image reconstruction from noisy data was performed to analyze the robustness to noise of the AwTV-POCS algorithm. For all the AwTV-POCS, EPTV-POCS and TV-POCS algorithms, the value of the tolerance parameter ε were chosen to be 0.085, 0.082 and 0.078 for the 20, 40, and 60 projection views, respectively. A smaller ε value was chosen for a larger number of projection views by the reason that the constraints would be more restrictive for more data samples. Figure 5.8 shows that the FBP images have noticeable artifacts as compared to the images reconstructed by the TV-POCS, EPTV-POCS and AwTV-POCS algorithms from 20, 40, and 60 projection views of the noisy sinogram data.

A narrow grayscale display window was presented to examine the differences among the results of the three latter approaches as shown in Figure 5.9 and Figure 5.10. Compared to the TV-POCS and EPTV-POCS algorithms, the AwTV-POCS algorithm preserved more edge details for 20 and 40 projection views and generated similar results for 60 projection views.

The horizontal profiles of the images reconstructed in the case of 20, 40 and 60 projection views of noisy data along the 410^{th} row are shown in Figure 5.11, Figure 5.12 and Figure 5.13, respectively, with the corresponding profile of the true phantom image as a reference. These profiles also show that the AwTV-POCS preserved the edge details better that the TV-POCS in the noisy case for 20, 40 and 60 projection views, except for the display of Figure 5.13 (b) which shows similar performance. The profiles also show that the results of AwTV-POCS and EPTV-POCS strategy is very close but some gains from the present AwTV-POCS can be observed as shown in Figure 5.11(b)-(c)-(d) and Figure 5.12 (b)-(d). These noisy simulation studies were consistent with our previous observations in the noise-free cases, and further concurred with our previous discussion about the advantage of using the adaptive weights for edge preservation in the AwTV model as compared to the conventional TV model. With the same tendency as in the noise-free cases, the profiles in the noisy cases show that the reconstruction quality increased as the number of projection views increased. In the case of 60 projection views, the resulting images were closed to the true phantom image by all the TV-POCS, EPTV-POCS and AwTV-POCS approaches.

For the purpose of focusing on the edge analysis of the AwTV model, quantitative evaluation using observer detection power and computer simulation data is given in the Appendix of this chapter.

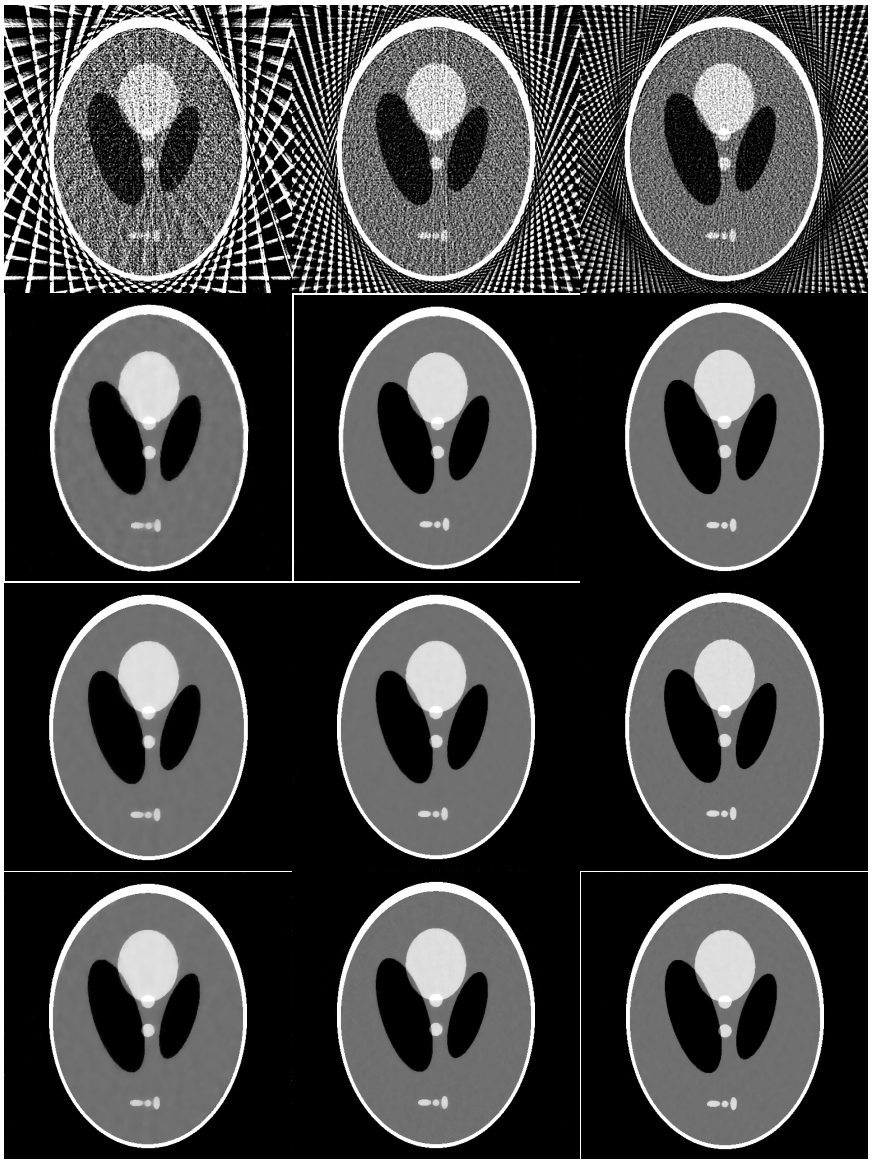

Figure 5.8. The images reconstructed by the FBP (1st row), TV-POCS (2nd row), EPTV-POCS (3rd row) and AwTV-POCS (4th row) algorithms from 20 (left column), 40 (middle column), and 60 (right column) projection views of noisy sinogram data, respectively. The display window is [0, 0.0034] mm^{-1}.

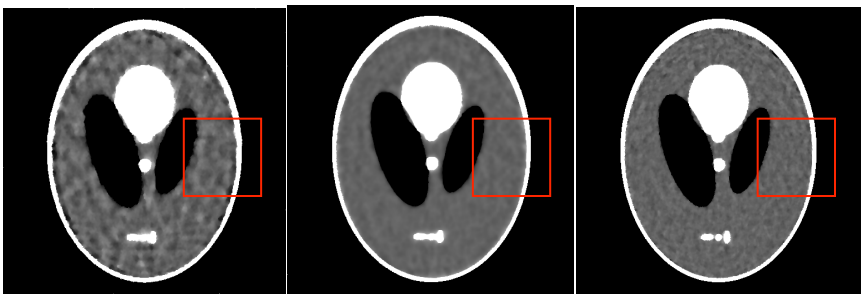

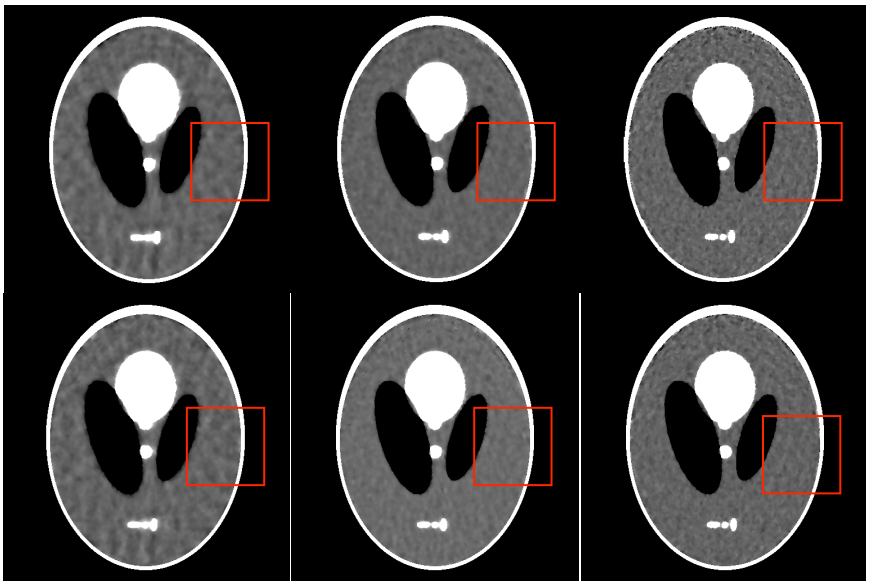

Figure 5.9.The images reconstructed by the TV-POCS (top row), EPTV-POCS (middle row) and AwTV-POCS (bottom row) algorithms from 20 (left column), 40 (middle column), and 60 (right column) projection views of noisy sinogram data, respectively. The display window is [0.0013, 0.0018] mm^{-1}.

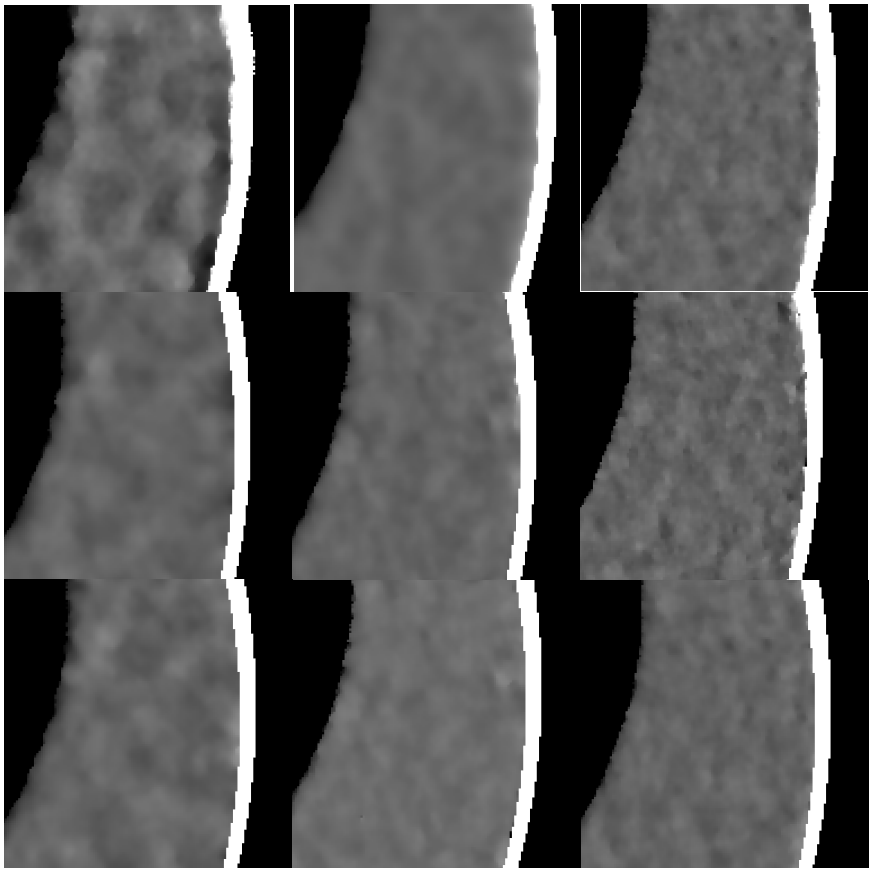

Figure 5.10.The ROIs of the images reconstructed by the TV-POCS (top row), EPTV-POCS (middle row) and AwTV-POCS (bottom row) algorithms from 20 (left column),

40 (middle column), and 60 (right column) projection views of noisy sinogram data, respectively. The display window is [0.0013, 0.0018] mm-1.

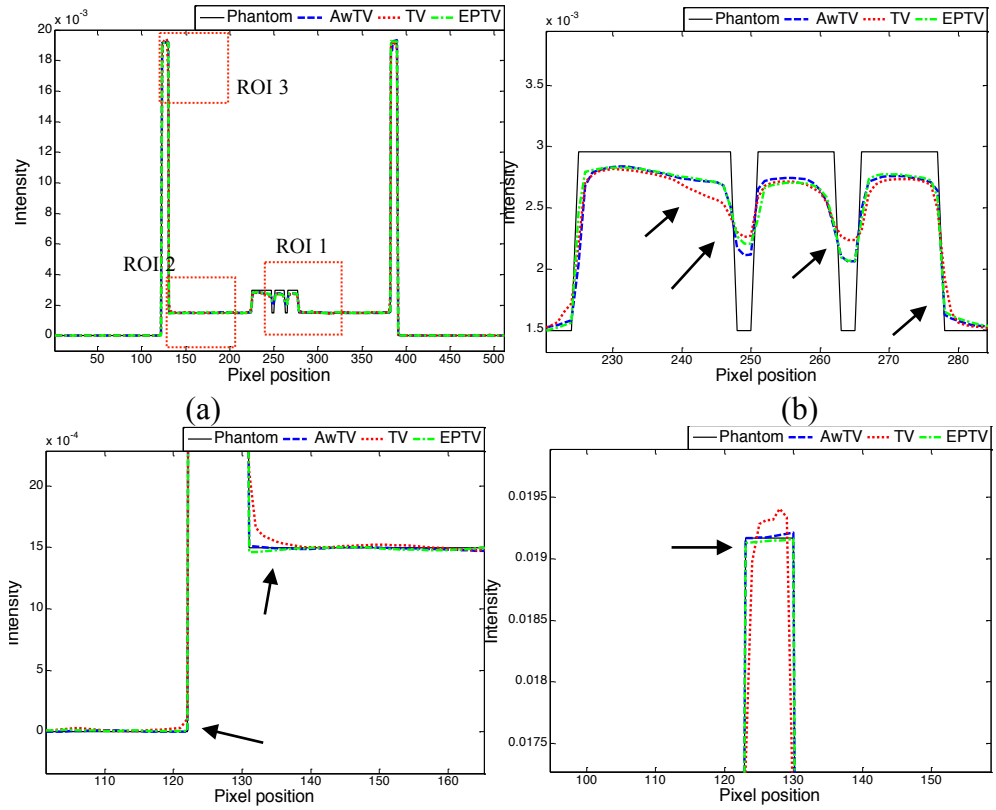

Figure 5.11.Horizontal profiles (410th row) of the images reconstructed by different algorithms from 20 projection views of noisy data. Picture (a) shows the overall profiles. Pictures (b), (c) and (d) show the partial profiles of the three ROIs indicated in (a).

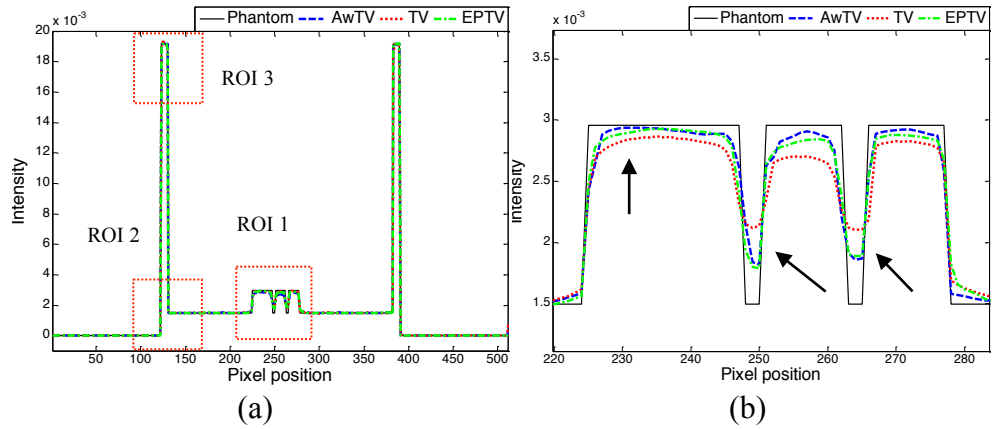

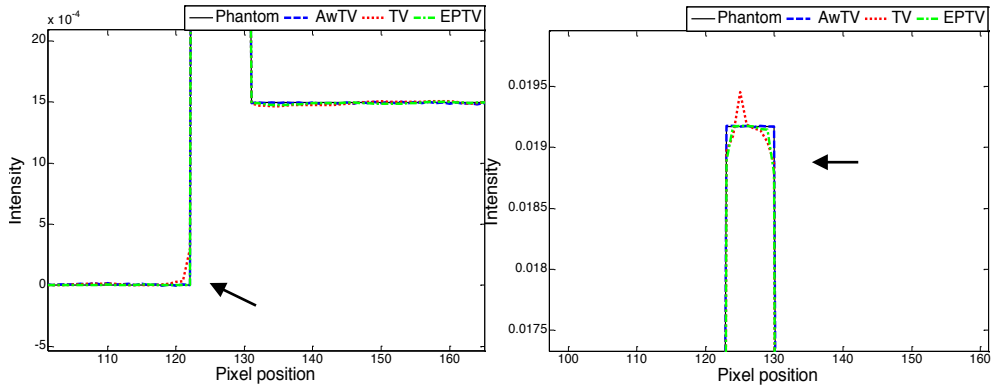

(c) (d)

Figure 5.12.Horizontal profiles (410th row) of the images reconstructed by different algorithms from 40 projection views of noisy data. Picture (a) shows the overall profiles. Pictures (b), (c) and (d) show the partial profiles of the three ROIs indicated in (a).

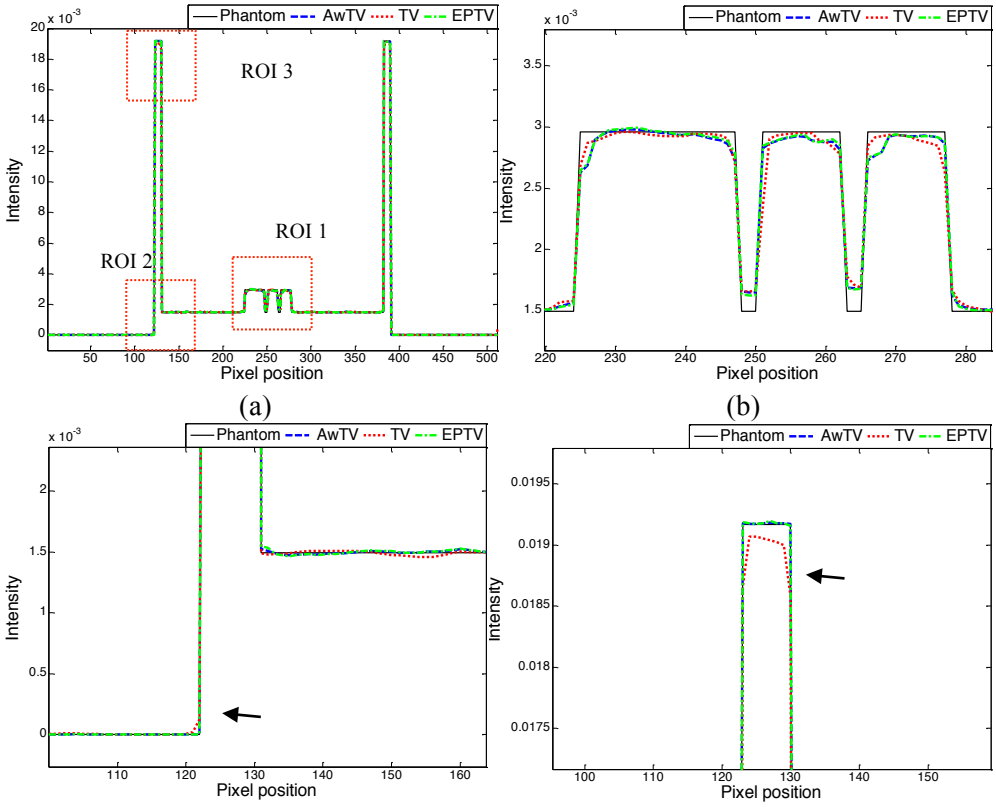

(a) (b)

(c) (d)

Figure 5.13.Horizontal profiles (410th row) of the images reconstructed by different algorithms from 60 projection views of noisy data. Picture (a) shows the overall profiles. Pictures (b), (c) and (d) show the partial profiles of the three ROIs indicated in (a).

5.5.4. Convergence analysis

The signal-to-noise ratio (SNR) and mean-square-errors (MSE) metrics have been widely used to measure the noise level and image quality for a known signal, respectively.

In this study, the convergence performance of the AwTV-POCS and TV-POCS algorithms was documented by calculating the SNR and the MSE versus the iteration steps. The definitions of SNR and MSE are listed as follows:

$$SNR = \frac{\sum_{s,t}^{M} \mu_{s,t}^2}{\sum_{s,t}^{M} \left(\mu_{s,t} - \hat{\mu}_{s,t}\right)^2}, \tag{5.6}$$

$$MSE = \frac{1}{M} \sum_{s,t}^{M} (\mu_{s,t} - \hat{\mu}_{s,t})^2, \tag{5.7}$$

where $\mu_{s,t}$ is the true value of the attenuation coefficient at voxel location index (*s, t*) and $\hat{\mu}_{s,t}$ is the reconstructed attenuation coefficient at voxel (*s, t*), M was defined before as the total number of image voxels. Each algorithm was executed up to 1,000 iteration steps to ensure its convergence to a stable solution.

Figure 5.14 shows the SNR and MSE versus the iteration steps for the AwTV-POCS and TV-POCS algorithms, respectively. Graphs Figure 5.14(a) and Figure 5.14(b) indicate that both the two algorithms converged robustly and reached their stable solutions after around 450 iterations. In addition to the SNR and MRE measures, the stop criterion c_α of Eq. (5.5) was also considered. It dropped below –0.6 after 492 general iteration steps. As shown in Figure 5.14(a), the SNR of the AwTV-POCS reconstructions approached to 38dB at 1,000 iterations, as compared to the 27.5dB by the TV-POCS algorithm at the same number of iteration steps. This indicates that the AwTV-POCS algorithm can improve the SNR in reconstructions over the TV-POCS algorithm. From the curve of the MSE versus iteration steps, as shown in Figure 5.14(b), it can be observed that the reconstructions of the AwTV-POCS algorithm have a lower MSE level than that of the TV-POCS algorithm, indicating that the reconstructed images by the AwTV-POCS can be more accurate than the results of the TV-POCS algorithm.

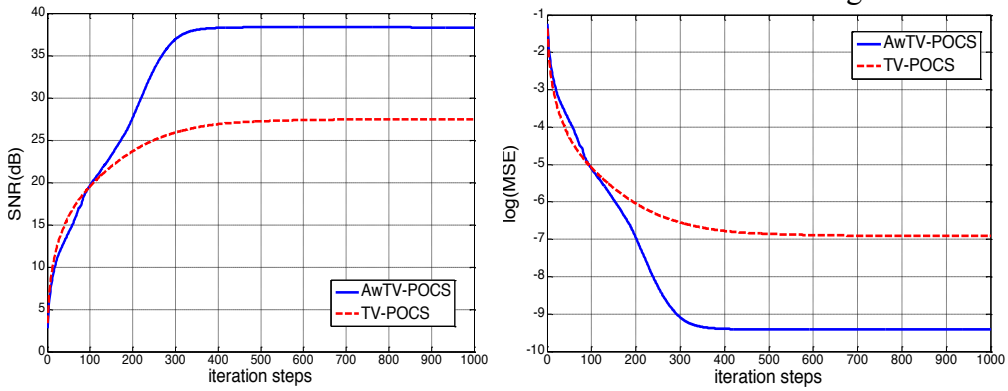

(a) (b)

Figure 5.14. Comparison between AwTV-POCS and TV-POCS algorithms (a) -- SNR v.s. iteration steps. (b) -- log(MSE) v.s. iteration steps.

5.5.5. Receiver operating characteristic study

One of the important tasks for medical image analysis is helping the physicians to detect lesions or abnormalities. The receiver operating characteristic (ROC) curve, which

plots the tradeoff between the true-positive (TP) and true-negative scores, is extensively used as a valuable merit to evaluate the diagnostic accuracy for a medical imaging system and/or image reconstruction algorithm. In practice, the ROC curve can be generated by the pairs of the TP fraction and false positive fraction [81, 92] with different confidence thresholds. The most common measure for comparison of the ROC curves is the area under the curve (AUC). An image reconstruction algorithm, which generates a larger AUC, usually has a higher capability for detection of abnormalities.

Human observer is one of the most desired observers, but the procedure needs an experienced physician to manually evaluate each case, which is time consuming for processing a large number of cases. The channelized hoteling observer (CHO) is one of the most efficient numerical observers that can help us to evaluate the algorithms without performing the human observer procedure. In our studies, we utilized the four octave-wide rotationally symmetric frequency channels proposed by Myers and Barrett [66], which have been shown to give good predictions of a human observer procedure in abnormal detection. In our implementation of the CHO procedure, each reconstructed image generated a four-element feature vector according to the four channels, and the CHO was trained for the AwTV-POCS and TV-POCS algorithms, respectively. A group of scalar rating values were produced from different independent ensemble of the feature vectors of the reconstructed images in two class of categories (i.e., with or without lesion) by using the CHO_MAT code [1]. The scores were subsequently analyzed using the ROCKIT [2] and the AUC values were calculated to document the detection efficiency.

Since a large sample size is needed to perform the ROC study, computer simulation is usually the choice. For the detection task, a low contrast small lesion of radius 3 mm was simulated as a growth from the big ellipse in the Shepp-Logan phantom as shown in Figure 5.15, where the arrow indicates the lesion. Four intensity contrast levels of the added lesion were considered as 1.5%, 3.0%, 4.5% and 6.5%, respectively, higher than that of the background to evaluate the performance of detection efficiency for the two reconstruction algorithms, i.e., TV-POCS and AwTV-POCS.

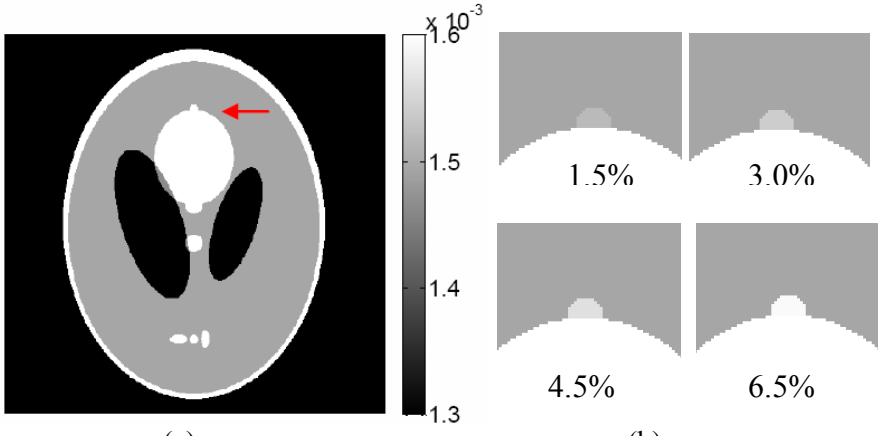

(a) (b)

Figure 5.15. (a) shows the modified Shepp-Logan phantom used for the ROC studies, where the display window is [0.0013, 0.0016]. (b) shows the lesion at 1.5%, 3.0%, 4.5%, and 6.5% contrast levels, respectively, the display window is [0.0013, 0.0016] mm^{-1}.

Noise-free projections from the Shepp-Logan phantom of Figure 5.15(a) without and with the lesion at each lesion contrast level of Figure 5.15(b) were first computed as described in Section 6.5.1 above. A total of five sets of noise-free data were computed. One set has no lesion and the other four sets have the lesion with the four different contrast levels in Figure 5.15(b). From each noise-free dataset, a total of 500 noisy realizations were generated using the same noise model of Section 2.2 above. These noisy sinogram data were then reconstructed by the two algorithms of TV-POCS and AwTV-POCS, respectively. A ROI of 19×19 pixel array size on each reconstructed image was selected around the lesion structure as the input of the CHO_MAT code. The series of ratings from the CHO output were subsequently analyzed using the ROCKIT package with bi-normal model. For each contrast level of the lesion, the ROC curves obtained from the two algorithms are shown in Figure 5.16, and the AUC values are listed in Table 5.2.

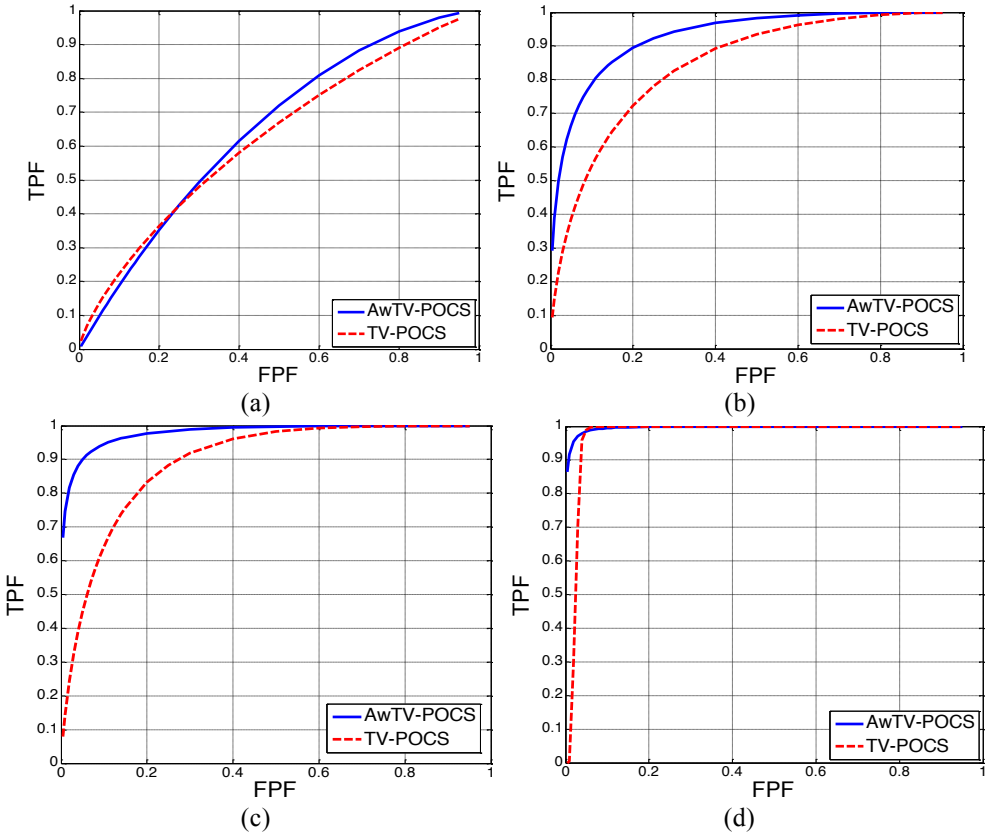

Figure 5.16. The ROC curves of the two algorithms: AwTV-POCS and TV-POCS. Graph (a) shows the ROCs for the lesion with 1.5% contrast level. Graph (b) shows the ROCs for the lesion with 3% contrast level. Graph (c) shows the ROCs for the lesion with 4.5% contrast level. Graph (d) shows the ROCs for the lesion with 4.5% contrast level.

From Figure 5.16 and Table 5.2, it can be seen that at 1.5% level, the AUC value from the AwTV-POCS was 0.6496 and from the TV-POCS was 0.6264. The one-tailed p-value was 0.3473 (greater than 0.05), which indicates that the difference between the two algorithms are not statistically significant at the 1.5% contrast level. In other words, both algorithms could not be able to detect the low-contrast lesion effectively. At the higher

contrast levels of 3.0% and 4.5%, the AUC value from the AwTV-POCS was 0.9301 and 0.9796, respectively, whereas 0.846 and 0.894 from the TV-POCS. The one tailed p-value of the two algorithms was 0.0089 and 0.0039, respectively, which are less than 0.05, indicating the difference between these two algorithms is statistically significant at the 3% and 4.5% contrast levels. In other words, the AwTV-POCS can outperform the TV-POCS for the lesion contrast levels at 3.0% and 4.5%. To get further insight into these two algorithm, we considered the next higher contrast level of 6.5%. At this level, the AUC value of the AwTV-POCS algorithm reached 0.9964, indicating a perfect detection performance; and the value of the TV-POCS algorithm is slightly smaller, i.e., 0.9711. At such high contrast level, both algorithms can detect the lesion successfully, and it is expected that they shall perform similarly.

Table 5.2. The AUC measures and the one-tailed P-values for different lesion contrast levels from the AwTV-POCS and TV-POCS reconstructions. Note N/A in the right lower corner indicates that the value could not be obtained by the ROCKIT package.

Lesion's Intensity	AwTV-POCS (AUC)	TV-POCS(AUC)	One-tiled P-value
1.5%	0.6496	0.6264	0.3473
3.0%	0.9301	0.8460	0.0089
4.5%	0.9796	0.8940	0.0033
6.5%	0.9964	0.9711	N/A

From the above ROC studies for different lesion contrast levels, it can be observed that the AwTV-POCS can outperform the TV-POCS in detecting small low contrast lesions because of the modeling of edge properties in the AwTV model. It is expected that both algorithms will perform similarly if the lesion contrast level is too low where both will surely fail, and too high where both will surely succeed. Although the results indicated that the AwTV-POCS has advantages compared to the TV-POCS strategy, more experiments using clinical data are needed in further studies.

5.5.6. Bias v.s. variance tradeoff

Another common merit for imaging system evaluation is the bias v.s. variance tradeoff plot, which is also one of the general figures of merit for evaluating the quality of reconstructed images. The plot describes the strength of the signal in relationship to the quantity of noise.

In this study, we focused on the robustness to different noise levels of the two algorithms (i.e., TV-POCS and AwTV-POCS) in their reconstructions from the 20 projection views, where these two algorithms showed noticeable difference in the computer simulation studies. A ROI of 19×19 array size on the uniform image intensity was selected inside the top middle ellipse, as indicated in Figure 5.17(a). Six different values of I_i^o from 5.0×10^3 to 2.5×10^6 were selected to simulate noisy data at the corresponding noise levels. At each noise level, 100 noisy data samples were simulated and their reconstructions were performed by the use of the two algorithms, respectively. These reconstructions were then used to calculate the bias and variance. According to the description in [15, 97], the bias and variance are expressed as follows:

$$bias(\mu) = \frac{\sum_{s,t\in W} \left| \bar{\hat{\mu}}_{s,t} - \mu_{s,t} \right|}{\sum_{s,t\in W} \left| \mu_{s,t} \right|}, \tag{5.8}$$

$$Variance = \frac{1}{M_W} \overline{\sum_{s,t\in W} \left(\hat{\mu}_{s,t} - \bar{\hat{\mu}}_{s,t} \right)^2} \tag{5.9}$$

where $\mu_{s,t}$ is the true value of the attenuation coefficient at voxel location index (*s, t*), $\hat{\mu}_{s,t}$ is the reconstructed attenuation coefficient at voxel (*s, t*), and $\bar{\hat{\mu}}_{s,t}$ is the sample mean from the 100 samples of the resulting images at voxel (*s*, *t*). The over bar in (B1) and (B2) denotes the mean over the 100 noise realization samples. *W* is the pixel's indices within the ROI and M_W is the number of voxels in the ROI.

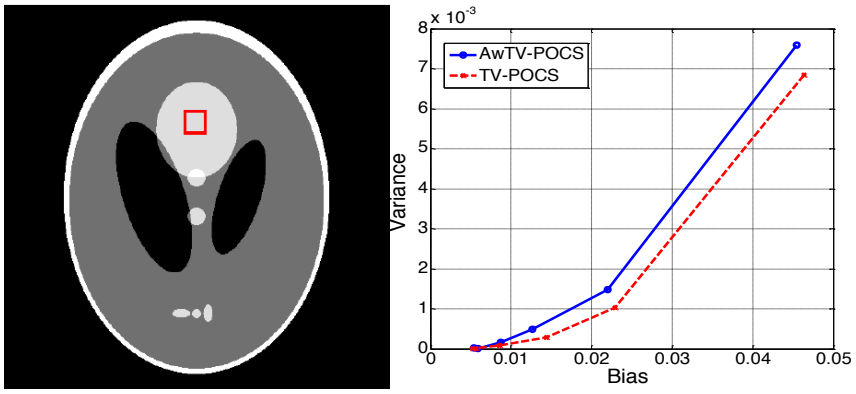

(a) (b)

Figure 5.17. The bias-variance plots for AwTV-POCS and TV-POCS algorithms. Picture (a) shows the modified Shepp-Logan phantom with display window [0, 0.0034] mm-1, where a rectangle ROI in the top middle ellipse is selected. Graph (b) shows the bias-variance curves for different noise levels.

Figure 5.17(b) shows the bias-variance plots of the AwTV-POCS and TV-POCS algorithms. Both algorithms can yield very small bias and variance values at low noise level (approaching to the origin of the plot), indicating that they can reconstruct high quality images at low noise level for the sparse-signal Shepp-Logan phantom with 20 projection views. When the noise level went up as the incident photon number went down below $I_i^o = 1\times10^5$, some difference between these two algorithms were observed. At the same variance or the same noise level, the images reconstructed by the AwTV-POCS have less bias as compared to the results of the TV-POCS. In other words, the AwTV-POCS can outperform the TV-POCS in terms of the bias-variance plots.

5.5.7. Resolution-noise tradeoff study of digital phantom study

The parameter δ of the weight $w_{s,s',t,t'}$ in the AwTV model (i.e. Eq.(5.3)) plays an important role for the AwTV-POCS algorithm. Its effect on the image resolution and noise tradeoff was investigated in this study. The image resolution was calculated from the ESF (a measurement of the broadening of a step edge) along the horizontal profile on the small vertical ellipse which is indicated at the right bottom of Figure 5.18(a). The calculation procedure is based on the descriptions in [46, 92], where the edge broadening

kernel is assumed as a Gaussian function with standard deviation σ_R, and an error function parameterized by σ_R is used to describe the ESF. By fitting a horizontal profile through the center of the small vertical ellipse to an error function, the parameter σ_R can be obtained. With the similar concept as introduced in previous section, the FWHM of the fitted Gaussian broadening kernel is calculated by $2.35\sigma_R$, which indicates the resolution of the reconstructed image. In this study, the image noise was calculated from the pixels in a small square ROI, which was selected nearby the small vertical ellipse at the bottom right of Figure 5.18(a). The standard deviation, σ_N, of the local uniform region in the ROI was used as the noise indicator. By varying the weight parameter δ from 0.3×10^{-2} to 6.0, we can obtain a curve in the coordinates (σ_R,σ_N). Figure 5.18(b) shows three curves corresponding to the AwTV-POCS reconstructions from 20, 40, and 60 projection views, respectively. The resolution and noise tradeoff improved as the number of projection views increased. This observation concurs with the expectation in general sense, indicating the validity of the plots. For all the three cases of 20, 40, and 60 projection views, the standard deviation σ_N or noise measure of the reconstructed images decreased as δ increased, indicating that the images became "smoother". In the meanwhile, the resolution measure σ_R of the reconstructed images also increased as δ increased, indicating that the edges became more "blurry". This observation also concurs with the expectation in general sense, further indicating the validity of the plots.

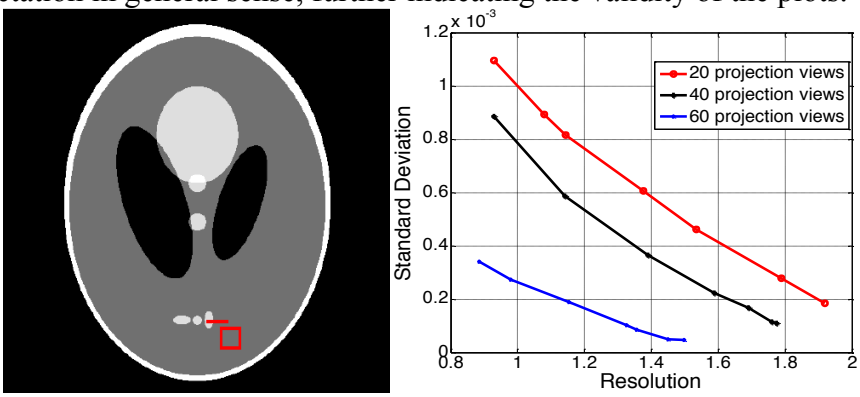

(a) (b)

Figure 5.18.The resolution noise tradeoff curves from the Shepp-Logan phantom study. Picture (a) shows the modified Shepp-Logan phantom with display window [0, 0.0034] mm-1, where the square at the right bottom location is the selected ROI, the line on the right bottom small ellipse indicates the location of the profiles. Graph (b) shows the resolution-noise tradeoff curves from the reconstructed images using different values of δ for the 20, 40, and 60 projection views, respectively.

5.6 Physical phantom Studies

To further realize the potential gain of the AwTV-POCS with comparison to the TV-POCS in more realistic cases, cone-beam data were acquired from two physical phantoms using a commercial CT scanner.

5.6.1 Experiment with the CatPhan® 600 Phantom

An image slice of the CatPhan® 600 phantom is shown in Figure 5.19. Cone-beam CT projection data were acquired by an Acuity simulator (Varian Medical System, Palo Alto, CA) [91] with the same protocol as described in chapter 4 section 4.6. A total of 634 projection views were acquired for a fully 360-degree rotation on a circular orbit. Sparse projection datasets can be extracted from the total 634 projection views. For example, 63, 79, and 158 views, respectively, were extracted which are evenly distributed over 360 degrees. To ensure convergence to a stable solution, the parameter c_α was set as -0.6 for AwTV-POCS algorithm and -0.5 for TV-POCS algorithm. Two POCS iterations and twelve gradient descent iterations were performed in each general loop. The execution time for each general iteration step was around 45 seconds on a HP PC with Intel Xeon X5450 CPU and 24 gigabyte memory. The 3D AwTV term was defined similarly as the 2D AwTV term and can be expressed as:

$$\|\mu\|_{AwTV-3D} = \sum_{s,t,z} \sqrt{w_{s,s-1,t,t,z,z}(\mu_{s,t,z} - \mu_{s-1,t,z})^2 + w_{s,s,t,t,z,z-1}(\mu_{s,t,z} - \mu_{s,t,z-1})^2 + w_{s,s,t,t-1,z,z}(\mu_{s,t,z} - \mu_{s,t-1,z})^2} \quad \textbf{(5.10)}$$

where z is the voxels' index along the z-axis direction. By setting the weight as 1, the conventional TV term is obtained.

5.6.1.1 Visualization-based comparison

The reconstructed images are shown in Figure 5.19 and Figure 5.20. The reconstruction by the well-known Feldkamp–Davis–Kress (FDK) method with Hanning window at Nyquist frequency cutoff is shown as reference image.

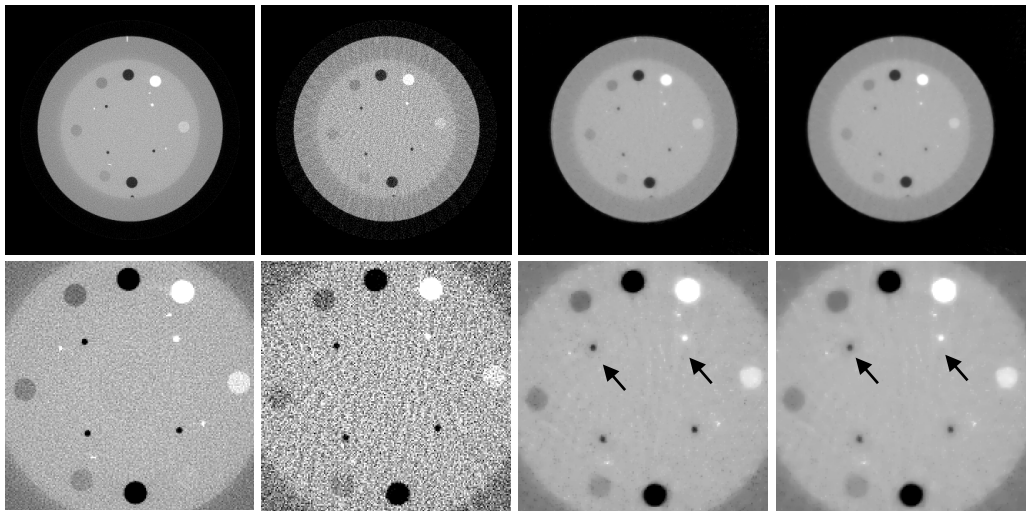

(a) (b) (c) (d)

Figure 5.19. CatPhan® 600 phantom image reconstructions by different algorithms from 63 projection views. Column (a) shows the reconstruction by the FDK method from the total 634 projection views as a reference. Column (b) shows the reconstruction by the FDK algorithm from 63 projection views. Column (c) shows the reconstruction by the AwTV-POCS algorithm from 63 projection views. Column (d) shows the reconstruction by the TV-POCS algorithm from 63 projection views. The bottom row shows the zoomed pictures. The display window of top row is [0, 0.024]. The display window of bottom row is [0.008, 0.02] mm^{-1}.

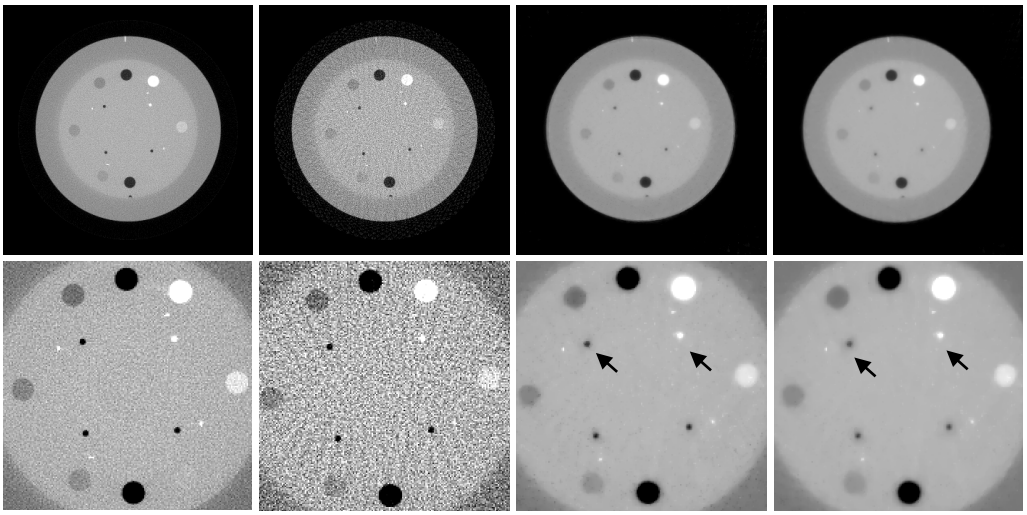

(a) (b) (c) (d)

Figure 5.20. CatPhan® 600 phantom image reconstructions by different algorithms from 79 projection views. Column (a) shows the reconstruction by the FDK algorithm from the total 634 projection views as a reference. Column (b) shows the reconstruction by the FDK algorithm from 79 projection views. Column (c) shows the reconstruction by the AwTV-POCS algorithm from 79 projection views. Column (d) shows the reconstruction by the TV-POCS algorithm from 79 projection views. The bottom row shows the zoomed pictures. The display window of top row is [0, 0.024]. The display window of bottom row is [0.008, 0.02] mm^{-1}.

From Figure 5.19, it is seen that both the AwTV-POCS and TV-POCS algorithms reconstructed much better images as compared to the result of the FDK method from 63 projection views. In addition, the result of the AwTV-POCS shows more details on the edges than the result of the TV-POCS as indicated by the arrows in Figure 5.19(c) and Figure 5.19(d). As the number of projection views increased, the visually difference on the results of the AwTV-POCS and TV-POCS algorithms became not significant except for some small difference between the spots as indicated by the arrows in Figure 5.20(c) and Figure 5.20(d). This observation is consistent with our previous conclusion in the Shepp-Logan numerical phantom simulation study.

5.6.1.2 Resolution-noise tradeoff study for physical phantom

A similar resolution-noise tradeoff evaluation was also performed using the reconstruction results from 63 and 79 projection views, respectively, of the CatPhan® 600 phantom. The corresponding resolution-noise tradeoff curve is shown in Figure 5.21. Thus, according to the tendency of the resolution-noise tradeoff curves, it is possible to obtain an optimal resolution-noise tradeoff in the reconstruction by determining a proper value for δ. In all the simulation and experiment studies, a small value was used as the initial guess for the δ value. Staring from this small value, we increased the value empirically until a proper value δ was obtained, which rendered visual-appearing results. For example, $\delta = 0.6\times10^{-2}$ was found in the Shepp-Logan phantom cases, $\delta = 0.9\times10^{-2}$

in the CatPhan® 600 phantom cases, and $\delta = 0.01$ in the anthropomorphic head phantom cases. Comparing to the TV-POCS reconstructions, the results from the AwTV-POCS algorithm did not show noticeable difference when $\delta > 1$.

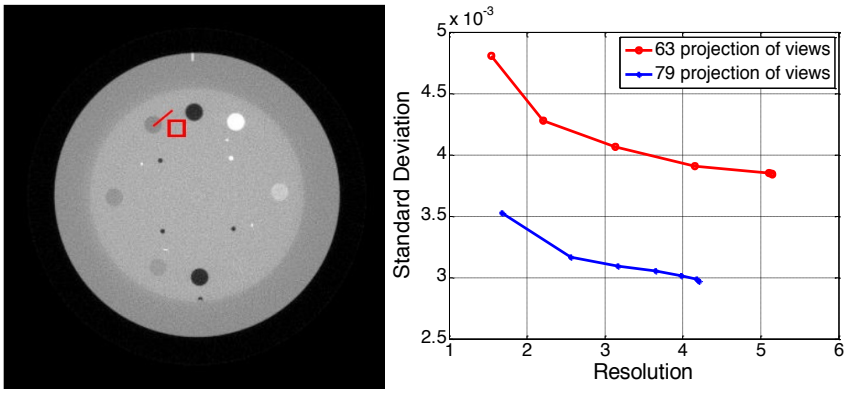

(a) (b)

Figure 5.21.The resolution noise tradeoff curves from the CatPhan® 600 phantom study. Picture (a) shows the CatPhan® 600 phantom with display window [0, 0.024] mm-1, where the square at the left top location is the selected ROI, the line on the left top small circle indicates the location of the profiles. Graph (b) shows the resolution-noise tradeoff curves from the reconstructed images using different values of δ for the 63 projection views.

5.6.2 Experiment with the anthropomorphic Head Phantom

An image slice of the Anthropomorphic Head phantom is shown in Figure 5.22. Cone-beam projection data were acquired from the anthropomorphic head phantom by the same protocol as used for the CatPhan® 600 phantom study. In order to observe the difference between the results from the AwTV-POCS and TV-POCS algorithms, we extracted 79 and 158 projection views from the full views for sparse image reconstruction. A ROI was selected to inspect the fine structures of the reconstructed results as indicated in Figure 5.22 (a). The resulting image and the ROI observations are shown in Figure 5.22 and Figure 5.22.

By inspecting the images reconstructed from 79 projection views as shown in Figure 5.22, it can be seen that some fine structures of the soft tissue, such as the structures of ear, are lost for both AwTV and TV models due to the sparse projection views. Despite this, some gains from the AwTV model are noticeable at both the ear location and the cold spots as indicated in the Figure 5.22 (c) and (d). By comparison to the CatPhan® 600 phantom result of Figure 5.20, the loss of the fine structures in the results of head phantom as shown in Figure 5.23 indicate that the measurements required for sparse image reconstruction should be associated with the structure of the signals. Intuitively, more projection views are needed to recover the fine structures in the head phantom. Based on this intuition, we performed another experiment by the use of 158 projections. Figure 5.23 shows the reconstructed results from the 158 projections. Significant improvement in recovering the small structures is seen by the use of more projections for both TV and AwTV models. The gain by the AwTV model is also noticeable as indicated by right lower circle in Figure 5.23 (c) and (d). These results are consistent

with those from the Shepp-Logan phantom simulation study. This then suggests that the presented AwTV model can preserve the edge details better than the TV model for image reconstruction from sparse-viewed projections.

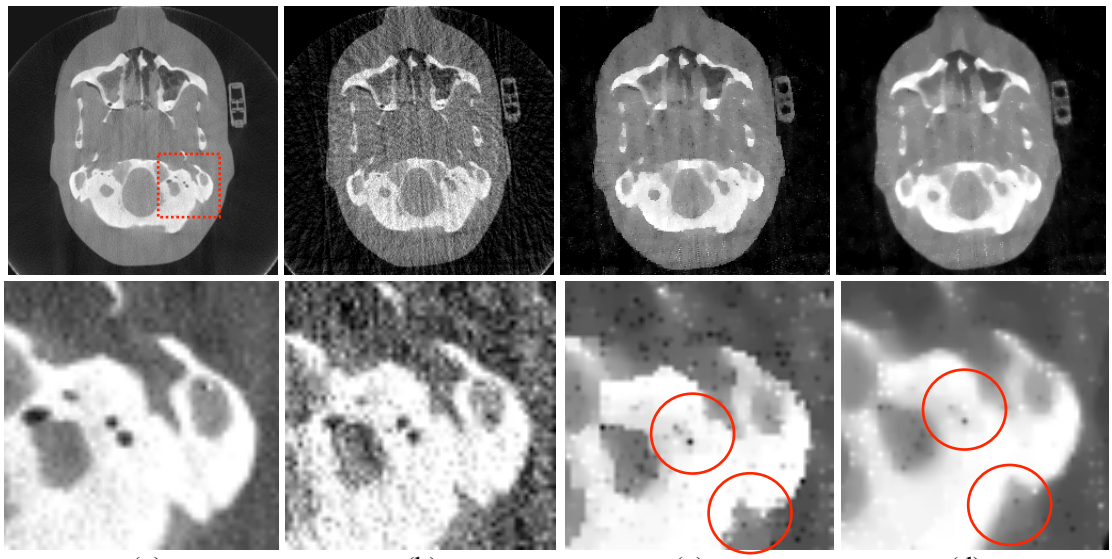

(a) (b) (c) (d)

Figure 5.22. Head phantom image reconstructions by different algorithms from 79 projection views. Column (a) shows the reconstruction by the FDK algorithm from the total 634 projection views as a reference. Column (b) shows the reconstruction by the FDK algorithm from 79 projection views. Column (c) shows the reconstruction by the AwTV-POCS algorithm from 79 projection views. Column (d) shows the reconstruction by the TV-POCS algorithm from 79 projection views. The bottom row shows the zoomed pictures. The display window is [0, 0.03]mm-1 for the first row and [0.01,0.03] mm-1 for the second row.

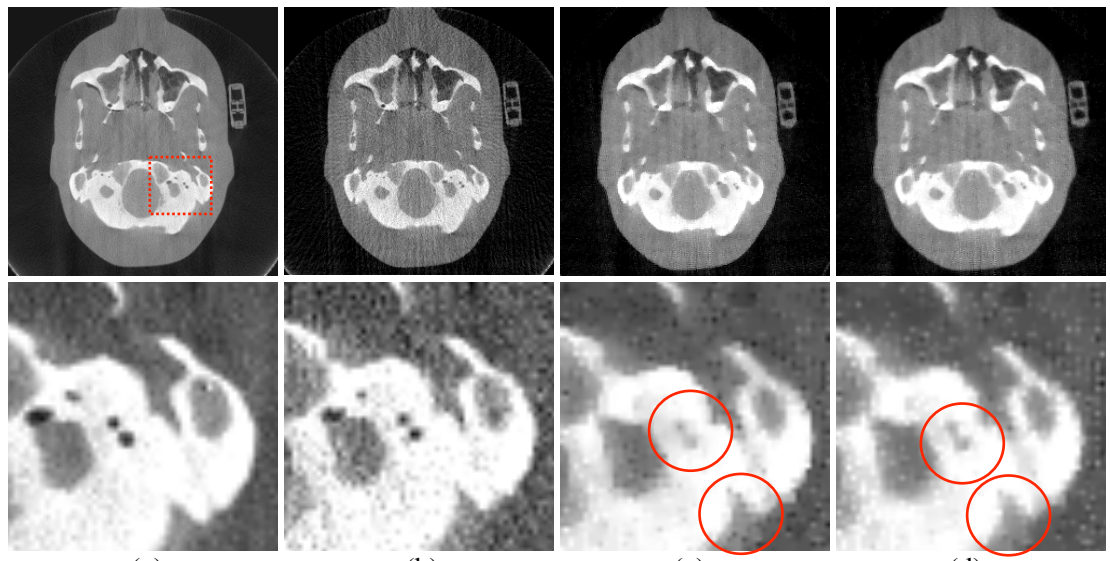

(a) (b) (c) (d)

Figure 5.23. Head phantom image reconstructions by different algorithms from 158 projection views. Column (a) shows the reconstruction by the FDK algorithm from the

total 634 projection views as a reference. Column (b) shows the reconstruction by the FDK algorithm from 158 projection views. Column (c) shows the reconstruction by the AwTV-POCS algorithm from 158 projection views. Column (d) show the reconstruction by the TV-POCS algorithm from 158 projection views. The bottom row shows the zoomed pictures. The display window is [0, 0.03] mm^{-1} for the first row and [0.01,0.03] mm^{-1} for the second row.

5.7 Comparison of the AwTV/TV-PRWLS and AwTV/TV-POCS methods

In this section, I compare the AwTV/TV-PRWLS methods introduced in previous chapter with the AwTV/TV-POCS methods by using different types of data.

5.7.1 CatPhan® 600 phantom study

5.7.1.1 Visualization-based comparison

According to our previous study [52], the AwTV/TV-POCS algorithms show satisfactory results for image reconstruction from sparse-view 80mA projection data. To further validate the two types of strategy (i.e., the POCS and PRWLS) for different types of projection data measurements, the AwTV/TV-PRWLS and AwTV/TV-POCS algorithms are implemented to reconstruct three types of data (i.e., full-view 10mA projection, 79-view 80mA projection and 79-view 10mA projection). In the AwTV/TV-PRWLS strategies, the penalty parameter β was selected to be 140 to ensure the backgrounds have similar noise levels as the full-view 80mA FDK image. For the AwTV/TV-POCS approaches, five POCS steps and two TV gradient descent steps [52, 79, 80] were executed in each general loop to achieve the results with similar noise level. The results are shown in Figure 5.24.

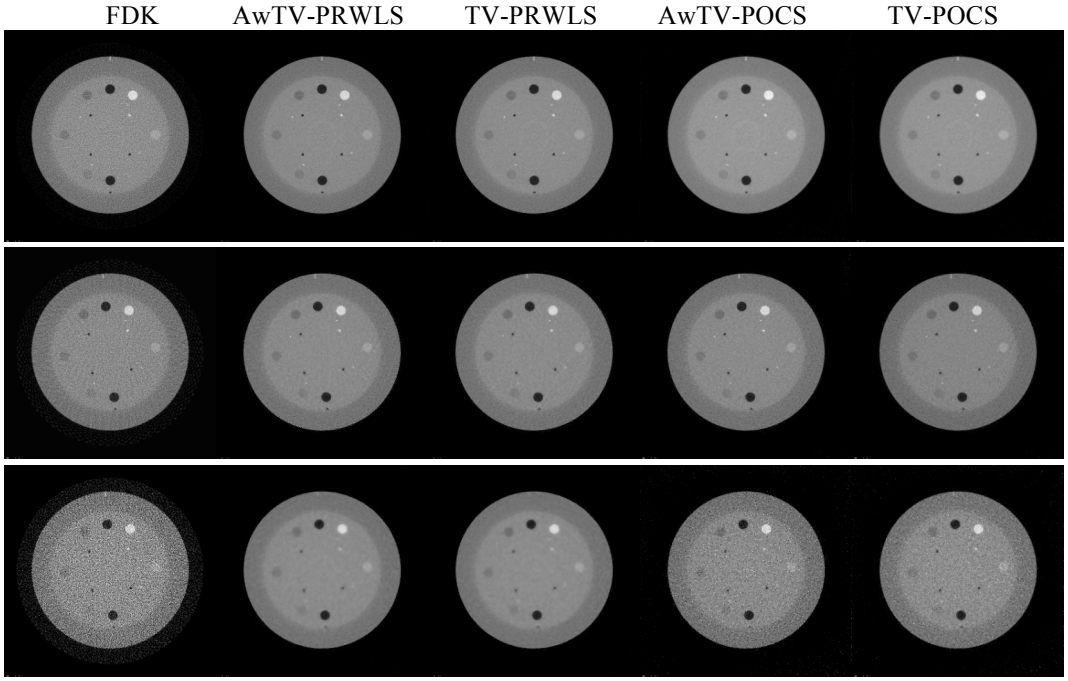

Figure 5.24. The reconstructed images of the CatPhan® 600 phantom. The first row shows the images reconstructed from the full-view 10mA projection data. The second

row shows the images reconstructed from the 79-view 80mA projection data. The third row shows the images reconstructed from the 79-view 10mA projection data. The display window is [0, 0.03] mm^{-1}.

5.7.1.2 Profile-based comparison

To further compare the reconstructed images, the profiles were calculated as shown in Figure 5.25, Figure 5.26 and Figure 5.27. Figure 5.25 indicates that the results from AwTV/TV-PRWLS have higher peak values on both spots indicating better performance on edge preserving for full–view 10mA projection data. Figure 5.26 indicates that the results from AwTV/TV-POCS have higher peak values on both spots for 79-view 80mA projection data. Obviously, in the 79-view 10mA projection data case (i.e., shown in Figure 5.27), it is difficult to make any confidential conclusion for the inferior results. Although we observe the AwTV/TV-POCS shows some improvement to the AwTV/TV-PRWLS, the background noise is much higher than the results from AwTV/TV-PRWLS.

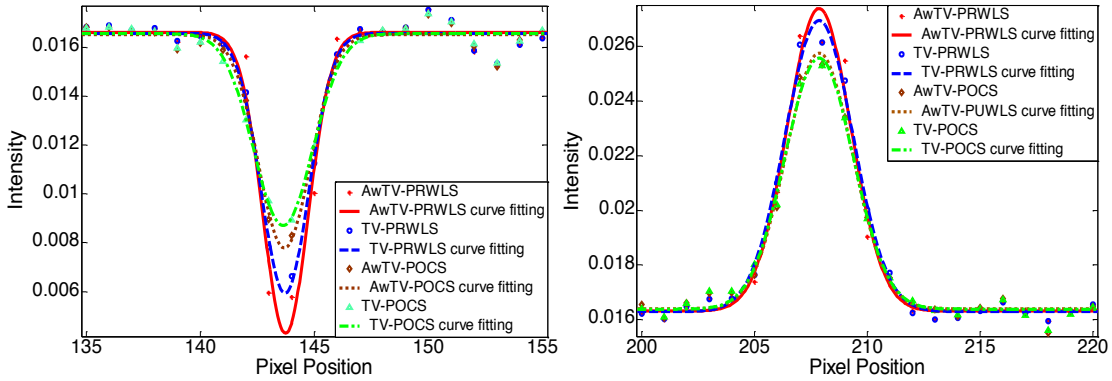

(a) (b)

Figure 5.25.Horizontal profiles of the CatPhan® 600 phantom images reconstructed by different algorithms from full-view 10mA projection data. Picture (a) shows the profiles across the cold spot (146th row, 135th to 155th column). Picture (b) shows the profiles across the hot spot (and 139th row, 200th to 220th column).

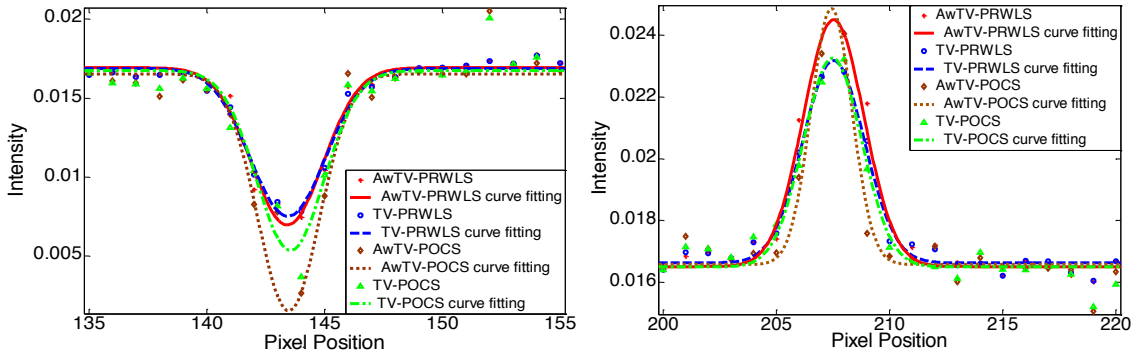

(a) (b)

Figure 5.26.Horizontal profiles of the CatPhan® 600 phantom images reconstructed by different algorithms from 79-view 80mA projection data. Picture (a) shows the profiles across the cold spot (146th row, 135th to 155th column). Picture (b) shows the profiles across the hot spot (and 139th row, 200th to 220th column).

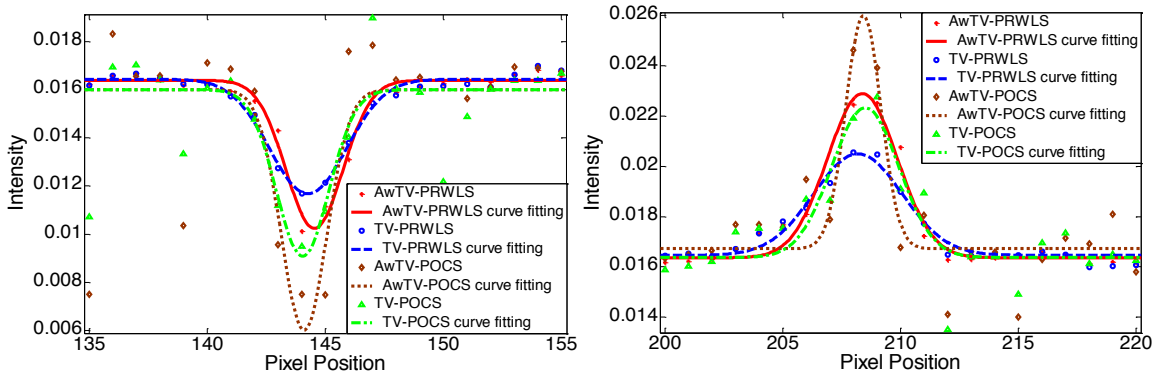

(a) (b)

Figure 5.27.Horizontal profiles of the CatPhan® 600 phantom images reconstructed by different algorithms from 79-view 10mA projection data. Picture (a) shows the profiles across the cold spot (146th row, 135th to 155th column). Picture (b) shows the profiles across the hot spot (and 139th row, 200th to 220th column).

5.7.1.3 FWHM measures

The FWHM values of those fitted profiles are shown in Table 5.3, which are consistent with our conclusion for profile comparison. From Table 5.3, we can observe that for full-views 10mA case, the AwTV-PRWLS method has the smallest value compared to other three methods on both cold and hot spots. In the case of 79-views 80mA projection data, the AwTV-POCS has the smallest value which corresponds to the highest resolution. In the case of 79-views 10mA projection data, all the four methods failed to reconstruct good results.

Table 5.3. The FWHM values of the cold and hot spots

Data type of projection	Position	AwTV-PRWLS	TV-PRWLS	AwTV-POCS	TV-POCS
Full-views 10mA	cold spot	4.7470	4.7565	4.9797	4.9816
	hot spot	4.6836	4.9891	4.8880	5.0220
79-views 80mA	cold spot	5.0455	5.0689	4.8504	4.9162
	hot spot	4.4650	4.4979	2.9963	4.2629
79-views 10mA	cold spot	3.9222	5.3275	3.1866	3.6049
	hot spot	5.4802	6.1406	2.4487	4.4086

5.7.2 Anthropomorphic head phantom study

Figure 5.28 shows the transverse images of the anthropomorphic head phantom reconstructed by different methods from the cone-beam projection data acquired with 125 kVp, 80mA and 10mA protocols. For the cases of sparse-view projection measurements from the 80mA and 10mA, 113 views from the full views were extracted as sparse-view data for image reconstruction.

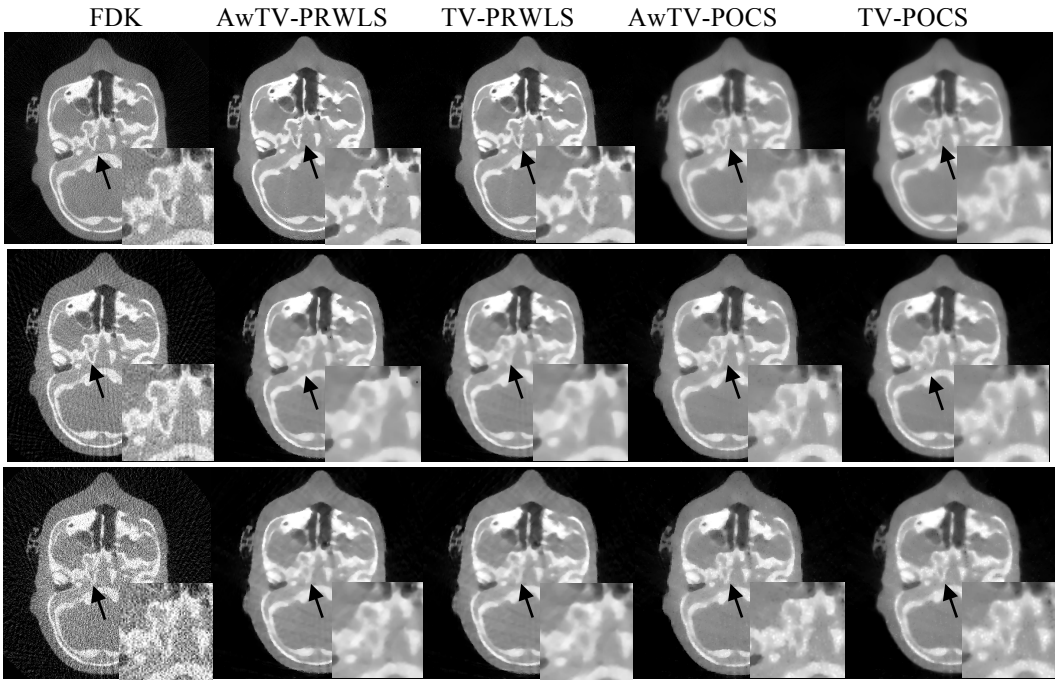

Figure 5.28. Transverse reconstructed images of the anthropomorphic head phantom from three types of data. The first row shows the images reconstructed from the full-view 10mA projection data. The second row shows the images reconstructed from the 113-view 80mA projection data. The third row shows the images reconstructed from the 113-view 10mA projection data. The display window is [0, 0.03] mm^{-1}.

The first column of Figure 5.28 shows the images reconstructed by the FDK method from the three types of projection data. It can be observed that the FDK method did not produce satisfactory results from these three types of data due to the noise and artifacts caused by the missing data or both. The first row of Figure 5.28 shows the images reconstructed by the FDK, AwTV/TV-PRWLS and AwTV/TV-POCS methods from the full-view 10mA projection data. It can be observed that, in this case, both the AwTV/TV-PRWLS algorithms can efficiently suppress noise without losing the bone structures. On the contrary, to keep the same noise level with the results from AwTV/TV-PRWLS method, the images reconstructed by the AwTV/TV-POCS methods are softer and over-smoothed to suppress noise. The second row of Figure 5.28 shows the images reconstructed from the 113-view 80mA projection data. It can be seen that both the AwTV/TV-POCS methods show some advantages compared to the results of the AwTV/TV-PRWLS methods. The third row of Figure 5.28 shows the images reconstructed from the 113-view 10mA projection data. It can be seen that all the four strategies mentioned above cannot produce satisfactory results. Furthermore, the associative horizontal profiles across the 102^{th} to 180^{th} columns at the 180^{th} row are plotted in Figure 5.29. It can be seen that the profile of the results from AwTV-PRWLS is much closer to the full-view 80mA FDK image in the case of full-views 10mA projection data. In the both the cases of sparse-views with 80mA and 10mA, the AwTV-POCS shows better performance than other methods.

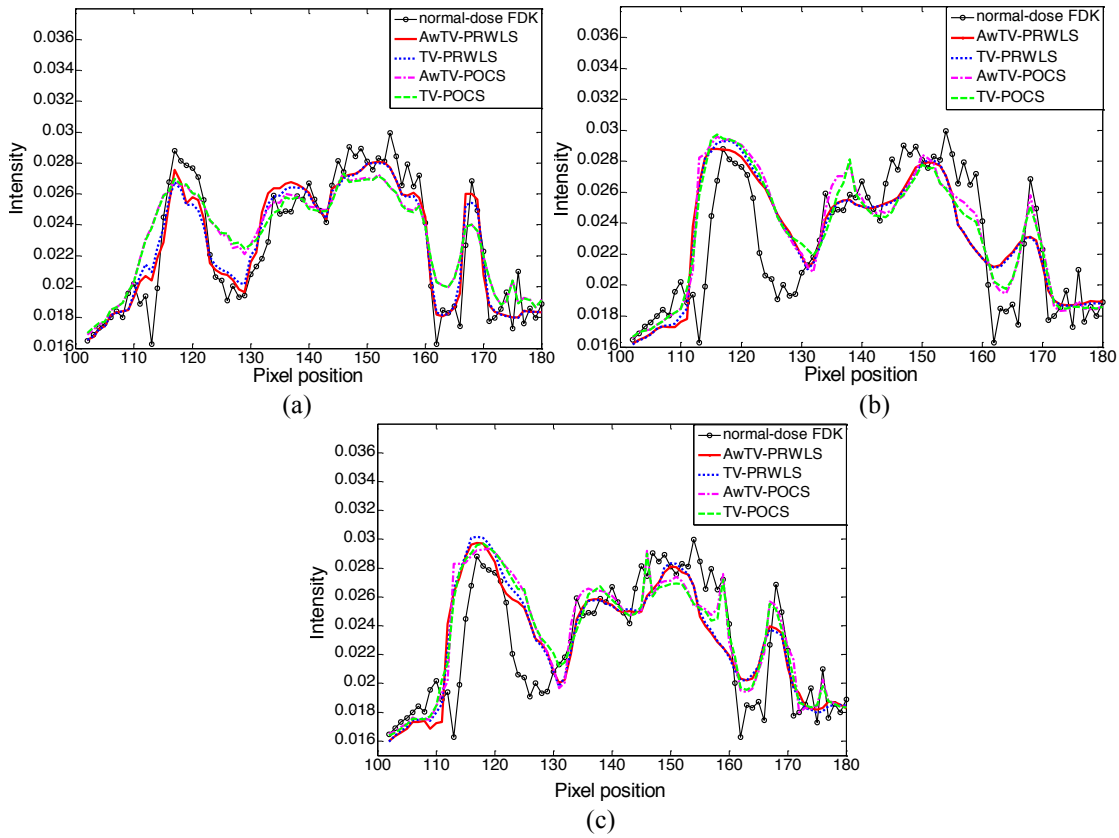

Figure 5.29.The horizontal profiles (102th to 180th columns at 180th row) of the reconstructed images from: (a) the full-view 10mA projection data; (b) the 113-view 80mA projection data; and (c) the 113e-view 10mA projection data.

5.8 Discussion and Conclusion

In this chapter, we introduced a novel adaptive-weighted total variation minimization model for low-dose CT image reconstruction from sparse-view projection measurements. By introducing an anisotropic diffusion-based adaptive weight to preserve the edge information in the conventional TV minimization paradigm, the gain in mitigating the over-smoothing on the edges in the conventional TV minimization was observed by comparing the performance of the presented AwTV-POCS implementation with the established TV-POCS algorithm [79, 80].

In the computer simulation studies, the visual comparison via displaying the results of AwTV-POCS, EPTV-POCS and TV-POCS algorithms showed that the AwTV model enabled to reconstruct image satisfactorily without introducing artifacts from 20 projection views in both noise-free and noisy data cases compared to the conventional TV model and the EPTV model. Moreover, it should be noted that as the number of projection views increased to 40 and 60, all the algorithms improved the reconstruction quality compared to the results from 20 projection views. Similar tendency has also been observed in experiment studies (i.e., the CatPhan® 600 and anthropomorphic head phantoms). The reason is that a denser sampling of the data, by increasing the number of projection views, has stronger constraints to the sparse-view reconstruction optimization problem and, therefore, restricts the result much closer to the true image. This

observation is consistent with the previous work of Bian *et.al.* [3]. In addition, more importantly, the present AwTV model can yield noticeable gain in preserving the fine structures and edges than the conventional TV model. In addition to the visual inspection, several more quantitative merits were utilized to analyze the differences between the presented AwTV and the conventional TV models. The following conclusions can be drawn from these quantitative measures.

Firstly, using the similar parameters for both TV and AwTV models (except parameter δ, which is only for the AwTV), the FWHM measure indicates that the results from the AwTV-POCS algorithm has higher peak and smaller values in both cold and hot spots as compared to the conventional TV-POCS algorithm. Thus, it could be concluded that the AwTV-POCS algorithm has a higher capability to preserve edge details compared to the conventional TV-POCS algorithm for sparse-view CT image reconstruction.

Secondly, the resolution-noise tradeoff study showed that the resolution in AwTV-POCS reconstructed images decreases with increasing the value of scale parameter δ. In the meanwhile, the standard deviation of image noise decreases. This observation indicates that a smoother image is obtained with a larger δ value. On the contrary, while decreasing the δ, the resolution and noise level increased, indicating a sharper image being obtained. Based on this observation, it could be concluded that the weight in AwTV model for edge information can give an optimal image quality by a proper value of δ, and the determination of this proper value is currently empirical.

Third, the ROC study using the Shepp-Logan phantom indicated that both TV-POCS and AwTV-POCA algorithms have similar detection performances when the small lesion's contrast is too low or too high. In the former case both algorithms would certainly fail, while in the latter case both algorithms would certainly succeed. However, when the small lesion contrast is in the between, the values of the AUC (area under the curve) of the ROC of the AwTV-POCS are statistically significantly higher than that of the TV-POCS. In addition, the bias-variance tradeoff study indicated that both algorithms have smaller bias and variance values at lower noise levels and their values are very close when the noise level is very low. However, at the same variance level, the AwTV-POCS has less bias than the TV-POCS. Although both the results from the ROC study and bias-variance analysis indicated that the AwTV-POCS algorithm can have higher quantitative capability in its reconstructions than the TV-POCS algorithm.

Fourth, the convergence study showed that both TV-POCS and AwTV-POCS algorithms converged to their stable solutions, respectively, and had similar convergence rates, see Figure 5.14. The converged solution of the AwTV-POCS had higher SNR and less MSE than that of the TV-POCS. Thus, it could be concluded that the AwTV-POCS can reconstruct more accurate images than the TV-POCS.

Based on both the qualitative inspection and quantitative measure of the reconstructions from the AwTV-POCS and TV-POCS algorithms, the gain by incorporating the edge characteristics into the AwTV model is noticeable. The gain shall be attributed to the AwTV model because both algorithms were implemented similarly in data constraints and numerical calculations, except for the TV and AwTV terms. Thus, it could be conjectured that the AwTV model can gain in different implementations in the case of both the parallel-beam projection geometry and nonparallel-beam projection geometries.

Except the above measurements, we also compared the AwTV/TV-POCS strategies and AwTV/TV-PRWLS strategies with three types of datasets. Both the FWHM value and visual comparison via displaying the results of the AwTV/TV-PRWLS and AwTV/TV-POCS strategies have demonstrated that the AwTV/TV-PRWLS methods can reconstruct satisfactory image from full-view 10mA projection data. Compared to the AwTV/TV-PRWLS strategies, the AwTV/TV-POCS strategies require that the estimated projections data should obey high fidelities to the observed projection data. Meanwhile, in practice, this condition is really hard to be met in low-mAs CT measurements. On the other side, the PRWLS model can be mathematically proven to follow the concept of MAP estimation, which fully utilizes the statistical property of the noise model of the signal. As a result, the AwTV/TV-PRWLS strategies could converge to a close solution when the number of projections is enough. As shown in section 5.7, we can conjecture the AwTV/TV-PRWLS strategies would show some advantages than the AwTV/TV-POCS strategies in full-projection view case. We may conclude that PRWLS method can obtain a more accurate solution the other present method in this study.

In the studies using the sparse-view 80mA projection data, both the AwTV/TV-POCS strategies show more advantages than the AwTV/TV-PRWLS strategies in terms of achieving smaller FWHM values. Due to the piecewise constant hypothesis and the knowledge of the high SNR of the observed data, the AwTV/TV-POCS strategies always aim to find an unique optimal solution having a minimum AwTV/TV value from the feasible region [8]. However, the AwTV/TV-PRWLS strategies always look for the solution from an unconstraint minimization problem, which indicated there would be multiple candidate solutions meet the minimization condition [80]. In addition, there is no such mechanism to tell us which is the best. Thus, it could be more possible to reconstruct a satisfactory result from a sparse-view 80mA case by using the AwTV/TV-POCS strategies.

It is worth to note that all AwTV/TV-POCS and AwTV/TV-PRWLS algorithms fail to produce satisfactory results in the case of the sparse-view 10mA projection data. One possible reason is that there are always some unsatisfied conditions for using these two types of strategies (i.e., the low-fidelity of the detected projection data in the POCS strategy and the low number of observations in the PRWLS strategy).

In summary, the present AwTV-POCS strategy is a more efficient way to reconstruct the image from sparse-view normal-mAs (i.e., 80mA) projection data and the AwTV-PRWLS strategy is a more efficient way to accurately reconstruct the image from low-mAs (i.e., 10mA) full projection data.

Chapter 6. Total variation-stokes strategy for sparse-view X-ray CT image reconstruction

Previous chapters have shown that by minimizing the AwTV/TV of the to-be-estimated image with some data and/or other constraints, a piecewise-smooth X-ray computed tomography image can be reconstructed from sparse-view projection data. However, due to the piecewise constant assumption for the TV model, the reconstructed images are frequently reported to suffer from the blocky or patchy artifacts. To eliminate this drawback, we present a TVS-POCS reconstruction method in this chapter. The TVS model is derived by introducing isophote directions for the purpose of recovering possible missing information in the sparse-view data situation. Thus the desired consistencies along both the normal and the tangent directions are preserved in the resulting images. Compared to the previous TV-based image reconstruction algorithms, the preserved consistencies by the TVS-POCS method are expected to generate noticeable gains in terms of eliminating the patchy artifacts and preserving subtle structures. To evaluate the presented TVS-POCS method, both qualitative and quantitative studies were performed using digital phantom, physical phantom and clinical data experiments. The results reveal that the presented method can yield images with several noticeable gains, measured by the universal quality index and the full-width-at-half-maximum merit, as compared to its corresponding TV-based algorithms. In addition, the results further indicate that the TVS-POCS method approaches to the gold standard result of the filtered back-projection reconstruction in the full-view data case as theoretically expected, while most previous iterative methods may fail in the full-view case because of their artificial textures in the results.

6.1 Introduction

Although good results have been reported from the above AwTV/TV-based methods, some artificial phenomena have been observed because of the presence of undesired data noise and the use of unsuitable or imperfect prior penalty term. For example, the TV-based image reconstruction results showed some patchy artifacts [3, 33, 52, 85] and Tang *et al.* claimed that the TV model usually suffers from the staircase and patchy artifacts due to the piecewise constant assumption [85]. This assumption always neglects the smoothly changing voxel values in the desired image which makes the isophote lines in some part of the images were artificially distorted. Those patchy artifacts are misleading and fatal for clinical diagnosis. For example, in lung nodule studies, the patchy artifacts may obfuscate the real lung node with vessels in 2D transverse images.

In order to eliminate the undesired patchy artifacts of the above mentioned TV-based methods, a high order derivative model: total variation stokes (TVS) model [74, 82], which was aimed to eliminate the patchy artifacts by introducing tangent direction of isophote lines, was adapted in this study for low-dose CT image reconstruction from sparse-view data. To enforce the sparse-view data constraints, we incorporate the POCS strategy [79, 80] in our proposed TVS-based reconstruction method, which is called

TVS-POCS method hereafter. The TVS-POCS method involves two procedures in its implementation: (1) estimation of tangent field from initial or intermediate images; and (2) image reconstruction with data constraints in the normal field, which is derived from the estimated tangent field. The introduction of the tangent field is corresponding to the utility of an incompressible velocity field to preserve the image consistency along the isophote directions, or more specifically to retain continuous and smooth isophote lines. By imposing the condition that the tangent field is divergence free, the experimental outcome of this study revealed the possibility to recover the missing data in the tangent field, indicating the utility of the CS concept [2]. By the same divergence free condition, this study further revealed another gain in recovery of the isophote lines in the tangent field, indicating the more consistency on the isophote lines for continuity and smoothness. Thus, visually pleasant images with smooth regions and continuous boundaries were obtained, where the staircase and patchy artifacts caused by the over-smoothing along the normal directions in the above TV-based approaches were efficiently mitigated.

6.2 TVS model

For simplicity, the model presentation is given in a 2D space. For a given 2D image $f(\mu)$, where μ is the desired attenuation coefficient in CT image, two orthogonal vectors in the image domain, i.e., the normal vector $\mathbf{n}$ and the tangent vector $\boldsymbol{\tau}$ of the image, are mathematically defined as:

$$\mathbf{n} = \nabla f(\mu) = \left(\frac{\partial f(\mu)}{\partial \mu_x}, \frac{\partial f(\mu)}{\partial \mu_y} \right)^T \text{ and } \boldsymbol{\tau} = \nabla^{\perp} f(\mu) = \left(\frac{\partial f(\mu)}{\partial \mu_y}, -\frac{\partial f(\mu)}{\partial \mu_x} \right)^T, \tag{6.1}$$

where ∇ denotes the differential operator, T represents the transpose operator, and $\nabla^{\perp}$ is the orthogonal differential operator, subscripts x and y are the indices of the directions of the attenuation coefficients. According to the connection between the isophote direction of the image and the fluid velocity in Navier-Stokes equation [2], the two vectors should satisfy the irrotationality and incompressibility conditions respectively, which can be mathematically expressed as:

$$\nabla \times \mathbf{n} = 0 \text{ and } \nabla \cdot \boldsymbol{\tau} = 0. \tag{6.2}$$

where the left equation, i.e., the cross product of the differential operator and the normal vector $\mathbf{n}$ equals zero, shows the curl of the normal vector is zero, which indicates that the normal vector is a conservative vector field and correspondingly the image vectors have continuous gradient (i.e., normal vectors) changes. The right equation, i.e., the dot product of the differential operator and the tangent vector $\boldsymbol{\tau}$ equals zero, shows the divergence of the tangent vector is zero, which guarantees that there always exists an image such that its isophote directions are restored vectors for the image consistency. The above two equations indicate the potentials for smoothly changing pixels across an image with preservation of edge details via restoring the missing data along the isophote directions [83]. Therefore, the image could be reconstructed by solving the steady equation with constraints from Eq. (6.2).

Inspired by previous studies [74, 82], the steady equation could be achieved by minimizing the TVS of the desired image. Therefore, instead of directly minimizing the TV norm of the desired image as we did in TV-based method, we minimize the TV norm of the tangential vector with the incompressibility constraints. This tangent field estimation (hereafter called the "TFE") can be mathematically calculated by:

$$\min_{\boldsymbol{\tau}} \sum_{i=1}^{N} \left|\nabla \tau_i\right| \qquad \text{subject to} \qquad \nabla \cdot \boldsymbol{\tau} = 0 \tag{6.3}$$

where i denotes the indices of the pixel of the desired image with N pixels.

Based on the definition of TV, the Eq. (6.3) is convex [79]. One simple way to solve such partial differential equations is described in [84] by using the augmented Lagrangian (AL) method, where it is claimed that the recently proposed dual method [10] and the split Bregman iteration method [30] can be either deduced from or equivalent to the AL method. Thus, the cost function for (6.3) can be further written as:

$$L(\tau, \lambda) = \sum_{i=1}^{N} \left|\nabla \tau_i\right| + \lambda \sum_{i=1}^{N} \left(\nabla \cdot \tau_i\right) + \frac{\beta}{2} \sum_{i=1}^{N} \left(\nabla \cdot \tau_i\right)^2, \tag{6.4}$$

where λ denotes the Lagrange multiplier to deal with the constraints and β represents a penalty parameter. In this study, inspired by previous work in [82], we let $\beta = 1$. By solving the Eq. (6.4), the saddle point of this optimization problem should meet the following conditions,

$$-\nabla \cdot \left(\frac{\nabla \tau_i}{\left|\nabla \tau_i\right|} \right) - \nabla \lambda - \nabla \left(\nabla \cdot \tau_i\right) = 0, \text{ for } i=1, 2, ..., N; \tag{6.5}$$

$$\nabla \cdot \tau_i = 0, \textit{for } i=1, 2, ..., N; \tag{6.6}$$

The gradient-descent method is utilized to calculate the solution of (6.5) and (6.6) by introducing an artificial step variable t_1:

$$\frac{\partial \tau_i}{\partial t_1} - \nabla \cdot \left(\frac{\nabla \tau_i}{\left|\nabla \tau_i\right|} \right) - \nabla \lambda - \nabla \left(\nabla \cdot \tau_i\right) = 0 \text{ for } i=1, 2, ..., N; \tag{6.7}$$

$$\frac{\partial \lambda}{\partial t_1} - \nabla \cdot \tau_i = 0 \text{ for } i=1, 2, ..., N; \tag{6.8}$$

For description purpose, we defined the following operators and vectors:

1. Define the forward/backward difference operators along x and y directions as $D_x^{\pm}$ and $D_y^{\pm}$;

2. Define the centered difference operators along x and y directions as C_x^h and C_y^h, where h corresponds to the order of neighbors of the central pixels. In this study, we set h=1;

3. Define the average operators (i.e., average of the nearby pixels, e.g., the four neighbors in 2D case) along x and y directions as M_x and M_y;

4. Define a vector *(u, v)* as:

$$\boldsymbol{\tau} = \nabla^{\perp} f(\mu) = \left(\frac{\partial f(\mu)}{\partial \mu_y}, -\frac{\partial f(\mu)}{\partial \mu_x} \right)^T = (u, v)^T \text{ and } \mathbf{n} = \nabla f(\mu) = \left(\frac{\partial f(\mu)}{\partial \mu_x}, \frac{\partial f(\mu)}{\partial \mu_y} \right)^T = (u, -v), \tag{6.9}$$

Then, the values of the variable *u, v* and λ at step n+1 can be calculated from:

$$v^{n+1} = v^n + \Delta t_1 \left(D_x^- \left(\frac{D_x^+ v^n}{T_1^n} \right) + D_y^- \left(\frac{D_y^+ v^n}{T_2^n} \right) + D_x^- \left(\lambda^n + Div\left(\tau^n\right) \right) \right), \tag{6.10}$$

$$u^{n+1} = u^n + \Delta t_1 \left(D_x^- \left(\frac{D_x^+ u^n}{T_2^n} \right) + D_y^- \left(\frac{D_y^+ u^n}{T_1^n} \right) + D_y^- \left(\lambda^n + Div\left(\tau^n\right) \right) \right), \tag{6.11}$$

$$\lambda^{n+1} = \lambda^n + \Delta t_1 \left(D_x^+ v^n + D_y^+ u^n \right), \tag{6.12}$$

where

$$Div\left(\tau^n\right) = D_x^+ v^n + D_y^+ u^n, \tag{6.13}$$

$$T_1 = \sqrt{\left(M_x\left(C_y^h v^n\right)\right)^2 + \left(D_x^+ v^n\right)^2 + \left(D_y^+ u^n\right)^2 + \left(M_y\left(C_x^h u^n\right)\right)^2 + \varepsilon_1}, \tag{6.14}$$

$$T_2 = \sqrt{\left(M_y\left(C_x^h v^n\right)\right)^2 + \left(D_y^+ v^n\right)^2 + \left(D_x^+ u^n\right)^2 + \left(M_x\left(C_y^h u^n\right)\right)^2 + \varepsilon_1}, \tag{6.15}$$

ε_1 is a relax parameter introduced to avoid the denominator going to zero, and Δt_1 was defined before as an artificial step variable to control the updating step length.

Once we have the estimated isophote lines from the TFE step, we can use them as a prior knowledge for recovering the desired images. However, it is impossible to directly utilize this efficient method to CT image reconstruction because there is no such prior image available for isophote lines estimation. To overcome this shortage, a novel TVS-POCS method which combines the CT image modeling and TVS model to solve the CT image reconstruction from sparse-view data problem is detailed in the following section.

6.3 CT image reconstruction from sparse-view data

6.3.1 The presented TVS-POCS method

Inspired by the computational advantages of the two-step iterative framework for minimization of dual condition problems as introduced in [74, 82] for image denoising and inpainting, we adapted the framework in this work to address the CT image reconstruction problems from sparse-view data. The desired image is reconstructed by fitting the normal vector of the desired image to the computed normal image with constraints from data fidelity. This step is called as image reconstruction (hereafter called "IR") step. Mathematically, this is achieved by solving the following minimization problem:

$$\min_{\mu} \sum_{i=1}^{N} \left(\left|\nabla f\left(\mu_i\right)\right| - \nabla f\left(\mu_i\right) \cdot \frac{\mathbf{n}}{|\mathbf{n}|} \right) \text{subject to} \left|P - A\mu\right| \le \sigma^2, \tag{6.16}$$

In this equation an error tolerance parameter σ^2 is introduced to denote the inconsistency in acquired projection data due to noise. After obtaining the restored tangent vector $\boldsymbol{\tau}^*$ from TFE step (i.e., Eq.(6.3)), the corresponding optimized normal vector $\mathbf{n}^*$ are calculated for low-dose CT image reconstruction. Then the desired image's normal vectors shall fit the computed normal vector $\mathbf{n}^*$ with constraints from the data fidelity. According to the description in ASD-POCS method [80], we consider the objective function (i.e., the left formula of (6.16)) and the constraints (i.e., the right formula of (6.16)) separately for image reconstruction after the normal vectors $\mathbf{n}^*$ are calculated.

The objective function can be written as:

$$L(f(\mu)) = \sum_{i=1}^{N} \left(|\nabla f(\mu_i)| - \nabla f(\mu_i) \cdot \frac{n}{|n|} \right), \tag{6.17}$$

Note that the minimization of Eq.(6.17) is non-convex and difficult to solve numerically. Inspired by the similar idea in [12], a numerical approximation was introduced in the iterative formula to ensure the convexity of the minimization problem. The minimization of Eq.(6.17) can be performed by the Euler-Lagrange (EL) method. The corresponding set of EL equations for the saddle point is:

$$\nabla \cdot \left(\frac{\nabla f(\mu)}{|\nabla f(\mu)|} - \frac{\mathbf{n}}{|\mathbf{n}|} \right) = 0, \tag{6.18}$$

According to [74], the updating scheme of (6.18) can be mathematically expressed as:

$$\mu^{n+1} = \mu^n + \Delta t_2 \left(D_x^- \left(\frac{D_x^+ f^n(\mu)}{T_3^n} - n_1 \right) + D_y^- \left(\frac{D_y^+ f^n(\mu)}{T_4^n} - n_2 \right) \right), \tag{6.19}$$

where

$$T_3 = \sqrt{\left(D_x^+ f(\mu)\right)^2 + \left(M_x \left(C_y^h f^n(\mu)\right)\right)^2 + \varepsilon_2}, \tag{6.20}$$

$$T_4 = \sqrt{\left(D_y^+ f(\mu)\right)^2 + \left(M_y \left(C_x^h f^n(\mu)\right)\right)^2 + \varepsilon_2}, \tag{6.21}$$

$$n_1 = \frac{u}{\sqrt{u^2 + \left(M_x \left(M_y v\right)\right)^2 + \varepsilon_3}} \text{ and } n_2 = \frac{v}{\sqrt{v^2 + \left(M_y \left(M_x u\right)\right)^2 + \varepsilon_3}}, \tag{6.22}$$

where ε_2 and ε_3 were two relax parameters introduced to avoid the denominator going to zero, Δt_2 is an artificial step variable.

The constraints in Eq. (6.16) reflect the data modeling and were solved by using the POCS strategy. However, directly utilizing the two-procedure framework (i.e. Eqs.(6.3) and(6.16)) may not be feasible due to the lack of prior image. Therefore, in this study, the desired image was obtained by performing the above two procedures (i.e., TFP step and IR step) in an alternating fashion until a stopping criterion is satisfied. The flowchart for TVS-POCS method is described in Figure 6.1 and the corresponding details of the two-step implementation are given below.

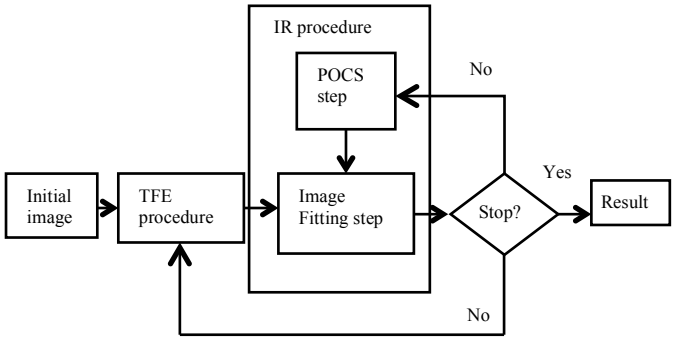

Figure 6.1. The flowchart of the TVS-POCS method.

6.3.2 Pseudo-code of the TVS-POCS reconstruction algorithm

The pseudo-code for the presented TVS-POCS image reconstruction algorithm is listed as follows:

1: initial: $\mu^{(0)}$;
2: initial: $\Delta t_1, \Delta t_2, \varepsilon_1, \varepsilon_2$ and ε_3;
3: caculate the initial vectors u and v from $\mu^{(0)}$;
4: while stop criterion is not met;
5: for n =1,2,..., N; (TFE)
6: calculate τ^n, T_1^n, T_2^n;

$$v^{n+1} = v^n + \Delta t_1 \left(D_x^- \left(\frac{D_x^+ v^n}{T_1^n} \right) + D_y^- \left(\frac{D_y^+ v^n}{T_2^n} \right) + D_x^- \left(\lambda^n + Div\left(\tau^n\right) \right) \right),$$

$$u^{n+1} = u^n + \Delta t_1 \left(D_x^- \left(\frac{D_x^+ u^n}{T_2^n} \right) + D_y^- \left(\frac{D_y^+ u^n}{T_1^n} \right) + D_y^- \left(\lambda^n + Div\left(\tau^n\right) \right) \right),$$

$$\lambda^{n+1} = \lambda^n + \Delta t_1 \left(D_x^+ v^n + D_y^+ u^n \right),$$

7: end for;
8: for j = 1,2,..., J; (POCS)
9: if j == 1;
10: $\mu^{(j)} := SART(\mu^{(0)}, \omega)$;
11: else $\mu^{(j)} := SART(\mu^{(j-1)}, \omega)$;
12: end if;
13: end for;
14: if $\mu_{x,y}^{(J)} > 0$, then $\mu_{x,y}^{(J)} = \mu_{x,y}^{(J)}$; $x = 1,2,...,X, y = 1,2,...,Y$;
15: else $\mu_{x,y}^{(J)} := 0$; $x = 1,2,...,X, y = 1,2,...,Y$;
16: end if;
17: for i = 1,2,..., I; (IR)
18: calculate n_1, n_2, T_3^i, T_4^i ;

19: $$\mu^{i+1} = \mu^i + \Delta t_2 \left(D_x^- \left(\frac{D_x^+ \mu^i}{T_3^i} - n_1 \right) + D_y^- \left(\frac{D_y^+ \mu^i}{T_4^i} - n_2 \right) \right), \quad x = 1,2,...,X, y = 1,2,...,Y;$$

20: end for;
21: end if stop criterion is satisfy.

In line 1, an initial estimate of the to-be-reconstructed image is set to be uniform ones. In line 2, five parameters, Δt_1 , Δt_2, ε_1, ε_2 and ε_3, are initialized before iteration starts. The selection of parameters will be discussed in next section. In line 3, the initials of two vectors (i.e., u and v) are calculated from the initial image values. Each outer loop (lines 4-21) is performed by two separated parts, i.e., N TFE steps for tangential vector estimation (line 5-7) and IR step which contains J POCS steps (lines 8-16) and I image fitting steps (lines 17-20). In line 21, an adequate stop criterion is selected to stop the iterations.

6.4 Parameter selection

6.4.1 Selection of the iteration number for sub-iterations

The selection of iteration number for each sub-iteration step is important for obtaining satisfies results in an efficient time. Although, a large number of iterations can ensure that a converged solution is obtained, it may take a long time. Due to the characteristic of two step iterative framework, adequate number of the TFE iteration in each general loop is usually enough to give us an intermediate solution for performing the following IR step.

In the IR step, inspired by the similar idea as proofed in [80], several steps in image fitting steps were performed to nudge the image toward the TVS solution. In order to yield the image within the feasible region, the parameters and step number selection in POCS step were following the instruction described in [80].

6.4.2 Selection of the artificial step variables Δt_1 and Δt_2

Similar to other optimization problems, the artificial step variables Δt_1 and Δt_2 control the step lengths of the updating procedure. Clearly, a too large step length would unavoidably increase the variation of the solution, resulting the cost function may not converge steadily. On the other hand, a too small step length will require a large number of iterative cycles to reach a steady value, which will unavoidably increase the computational time. Thus, how to choose adequate optimal parameters is an important issue.

In our experimental studies, we found the results were less sensitive to the value of Δt_1. For all reconstruction cases, the value range $1\times10^{-7} \le \Delta t_1 \le 1\times10^{-6}$ has always led to convergence of the estimated tangent vectors. The Δt_2 value affected the smoothness of the computed normal vectors, and its selection was related to the noise level and sampling rate of the projection data. A less smooth normal vector requires a smaller value of Δt_2, vice versa. The selection of Δt_2 values will be reported for difference cases in the following section.

6.4.3 Selection of the relax parameters

In order to ensure that the denominators would not go to zero, ε_1, ε_2 and ε_3 were introduced as relax parameters. It should be mentioned that the ε_1, ε_2 and ε_3 may have different values due to the different scales of the different denominators (i.e., Eqs. (6.14), (6.15), (6.20) and (6.21)). In this study, we manually choose them equal to the same value 10^{-9}, which is small enough for all the denominators.

6.4.4 Selection of the stop criterion

The selection of the stop criterion often depends on the convergence of the desired algorithm. In this study, the MSE metric, which calculates the similarity between the resulting image and true image, was used to measure the quality of the desired image. The MSE is defined as follows:

$$MSE = \frac{1}{N}\sum_{i=1}^{N}\left(f(\mu_i) - \hat{f}(\mu_i)\right)^2, \tag{6.23}$$

where $\hat{f}(\mu_i)$ represents the true attenuation coefficient at pixel i and $f(\mu_i)$ denotes the reconstructed attenuation coefficient at pixel i, N is the total number of pixels of the desired image. A small MSE value indicates a small difference value between the two images and vice versa. In this study, we stop the reconstruction process when the change of the reconstructed image becomes very small. Therefore, when MSE is small enough, the reconstruction is stopped.

6.5 Digital phantom study

6.5.1 Data simulation

In the digital phantom study, the Shepp-Logan phantom was modified based on the mass attenuation coefficients of different tissues in the objects as indicated in [52]. For simplicity, without loss of generality, a parallel-beam CT imaging geometry was used for sinogram data simulation. This geometry was modeled with 1024 bins on a 1D detector for 2D image reconstruction, and several sets of projection data with different numbers of views, i.e., 20, 40 and 60, were simulated at equal angular increment on 360 degrees around the phantom. The distance between the centers of two neighboring detector elements or bins is 0.25mm and pixel size is 0.5mm×0.5mm. For the purpose of focusing on the sparse issue for low-dose CT imaging, no noise was considered in the noise-free cases (i.e., ideal cases). In order to further analyze the robustness of the proposed method for controllable noise, a Poisson distributed quantum noise plus Gaussian distributed electronic noise were introduced to simulate noisy transmission data as indicated in [52, 63]. The noisy transmission data at each view were simulated at low dose level, i.e., 120 kVp and 40 mAs [52, 63]. Then the transmission data were converted to sinogram data by the use of the Lambert-Beer' law.

6.5.2 Parameter selection

For the TVS-POCS method, sufficient iterative cycles were executed to ensure its convergence to a stable solution, where each of the iterative cycle consisted of 40 TFE iterations, 10 POCS iterations and 50 image fitting iterations. In both noise-free and noisy cases, Δt_1 was selected as 1×10^{-7}. Since the noise levels are different in the ideal and low-mAs data acquisitions, Δt_2 was set to 6×10^{-5} for noise-free cases and 8×10^{-5} for noisy cases. For the ASD-POCS and AwTV-POCS algorithms, each of their iterative cycles included 10 POCS iterations and 10 gradient descent iterations. The initial value of ω and τ were set as 1 and 0.7×10^{-5}, respectively. The scale factor used in the AwTV model [52] was set to 0.6×10^{-2}. The stop criteria of ASD-POCS and AwTV-POCS algorithms were the same as discussed in [52]. For the FBP method, the Hanning window at 0.5 Nyquist frequency cutoff was implemented to suppress the high frequency noise.

6.5.3 Convergence analysis

Due to the alternating minimization framework, it is challenging to prove the convergence of the present TVS method. Although, each procedure monotonically decrease the objective functions, respectively [74, 82], it does not mean the convergence

of the reconstruction process. Inspired by the similar idea as the adaptive dictionary based statistical iterative reconstruction (ADSIR) method in [101], with appropriate parameters selection, our proposed algorithm indeed yielded a steady state. Figure 6.2 shows the $\lg(MSE)$ versus the iteration steps for the proposed TVS method from 20, 40 and 60 projection views in noise-free cases, respectively. We can observe that the proposed algorithm can converge to a steady status (i.e., $\lg(MSE) = -6.3$) after enough iteration steps in term of MSE measure. In addition, the convergence speed was accelerated as the number of projection views increased with the fixed parameter settings. For example, the $\lg(MSE)$ value converged to a small level at about 500^{th} step for the case of 20-views, meanwhile for the case of 60-views, only about 200 steps were needed. The results demonstrated that with appropriate parameters selection the present algorithm can successfully minimize the objective functions with a satisfactory solution in different cases.

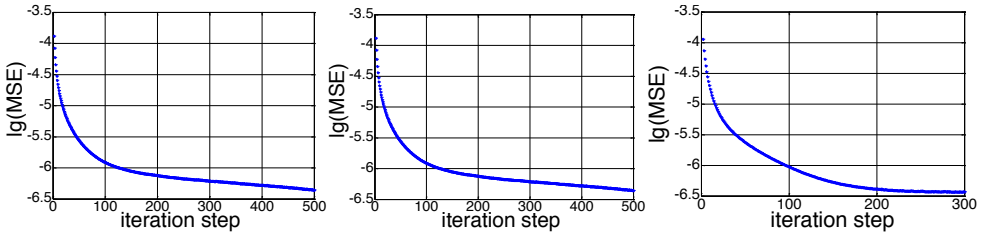

(a) (b) (c)

Figure 6.2. $\lg(MSE)$ v.s. iteration steps for TVS-POCS algorithm: (a) 20 projection views; (b) 40 projection views; (c) 60 projection views.

6.5.4 Visualization-based evaluation

The results from the 20-, 40- and 60-view projection data in the noise-free cases are shown in Figure 6.3. It can be seen that the images reconstructed by the ASD/AwTV-POCS and TVS-PCOS methods were better than the results of FBP in term of visual inspection. Noticeable difference among the results can be observed at the selected ROI with a narrow grayscale display window. As a result, the conventional TV-based ASD-POCS algorithm is visualized to suffer severe unevenness and patchy artifacts, especially in the uniform area. Although the AwTV-POCS algorithm yields some improvements due to the diffusion type weights in penalty term, there still exists slight unevenness in the uniform area. Meanwhile, the gains from the TVS method are remarkable over other methods in term of unevenness suppression and edge details preservation. Furthermore, Figure 6.4 shows the results from the noisy data. We can see that the TVS method also outperformed the other three in the noisy cases.

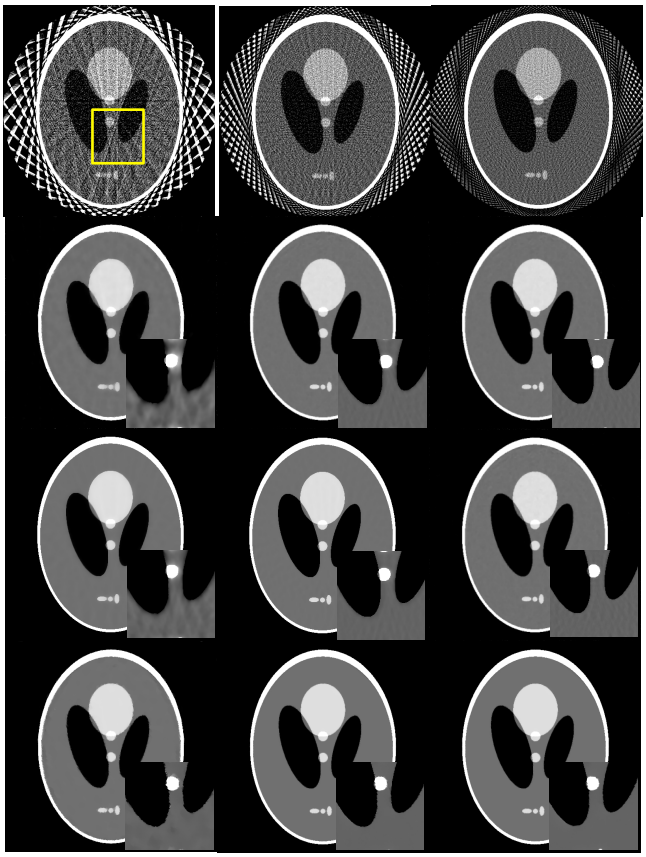

Figure 6.3.The images reconstructed by FBP (1st row), ASD-POCS (2nd row), AwTV-POCS (3rd row) and TVS-POCS (4th row) algorithms from 20 (left column), 40 (middle column), and 60 (right column) projection views in noise-free cases, respectively. The display window is [0, 0.0034] mm^{-1} for the full field of view (FOV) images and is [0.0013, 0.0018] mm^{-1} for the ROI images.

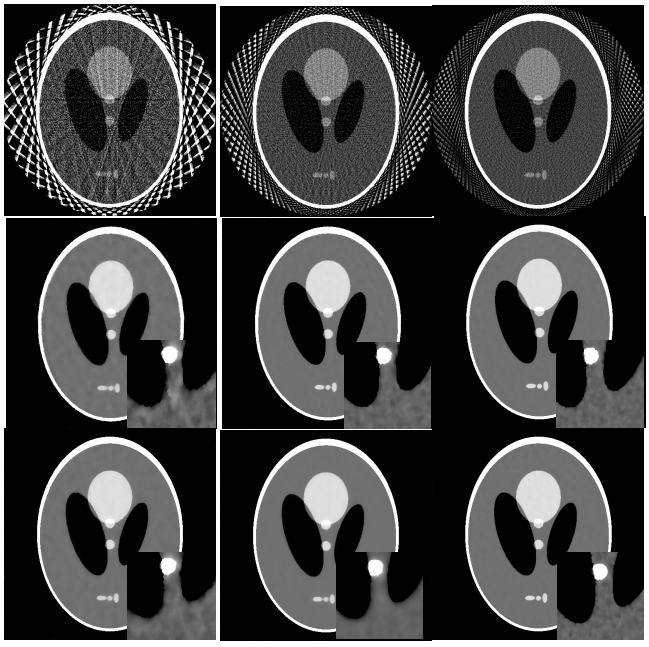

Figure 6.4.The images reconstructed by FBP (1st row), ASD-POCS (2nd row), AwTV-POCS (3rd row) and TVS-POCS (4th row) algorithms from 20 (left column), 40 (middle column), and 60 (right column) projection views in noisy cases, respectively. The display window is [0, 0.0034] mm^{-1} for the full FOV images and is [0.0013, 0.0018] mm^{-1} for the ROI images.

6.5.5 Profile-based comparison

To further visualize the difference among three TV- and TVS- based approaches, horizontal profiles of the resulting images in both noise-free and noisy cases were drawn across the 410th row, from the 267th column to the 417th column for each case and are shown in Figure 6.5 and Figure 6.6, wherein the corresponding profile of the true phantom was given as references. As a result, the TVS-POCS method achieved the best matching results (to the reference) in the 20-view case in both noise-free and noisy cases. Although the results of ASD/AwTV-POCS and TVS-POCS algorithms approached to the true phantom values as the number of projection views increased (i.e., 40, 60 projection views), the gains from the TVS-POCS method are still remarkable over other methods in term of the improvements at the uniform area and edges.

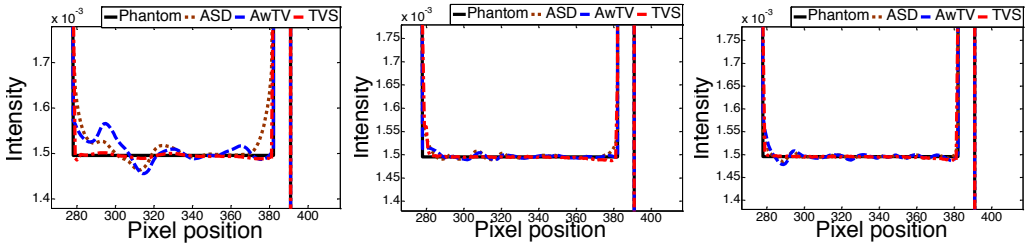

(a) (b) (c)

Figure 6.5. Horizontal profiles (410th row) of the images reconstructed from different numbers of projection views for noise-free cases: (a) 20 projection views; (b) 40 projection views; and (c) 60 projection views.

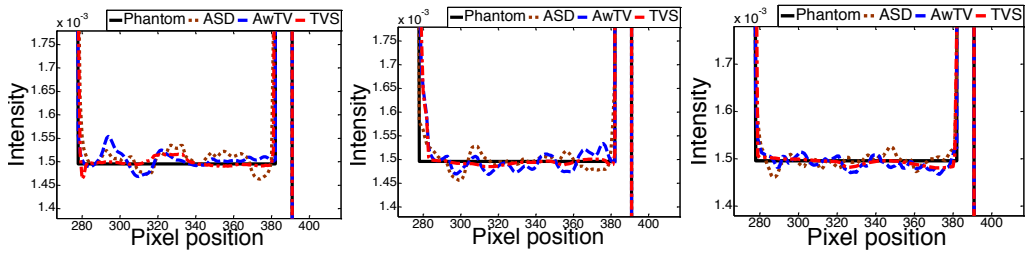

(a) (b) (c)

Figure 6.6. Horizontal profiles (410th row) of the images reconstructed from different numbers of projection views for noisy cases: (a) 20 projection views; (b) 40 projection views; and (c) 60 projection views.

6.5.6 Universal quality index study

To perform the quantitative analysis of the TVS-POCS method in the digital phantom study, the universal quality index (UQI), which measures the similarity between the desired image and its baseline image were studied in this section for both noise-free and noisy cases [85]. Three factors, i.e., loss of correlation, luminance distortion and contrast distortion are considered in the UQI indices [109]. Let $f_0(\mu)$ denote the true image used as the baseline image, and $f_1(\mu)$ denote the resulting or testing images, and then the mean, variance and co-variance in a ROI with N' pixels are defined as [3]:

$$\bar{f}_j(\mu) = \frac{1}{N'}\sum_{n=1}^{N'} f_j(\mu_n) \qquad j=0 \text{ or } 1, \tag{6.24}$$

$$\sigma_j^2 = \frac{1}{N'-1}\sum_{n=1}^{N'}\left(f_j(\mu_n) - \bar{f}_j(\mu)\right)^2 \qquad j=0 \text{ or } 1, \tag{6.25}$$

$$Cov\{f_1(\mu), f_0(\mu)\} = \frac{1}{N'-1}\sum_{n=1}^{N'}\left(f_1(\mu_n) - \bar{f}_1(\mu)\right)\left(f_0(\mu_n) - \bar{f}_0(\mu)\right), \tag{6.26}$$

Then, the UQI is defined as:

$$UQI = \frac{2Cov\{f_1(\mu), f_0(\mu)\}}{\sigma_1^2 + \sigma_0^2}\frac{2\bar{f}_1(\mu)\bar{f}_0(\mu)}{\bar{f}_1^2(\mu) + \bar{f}_0^2(\mu)}, \tag{6.27}$$

By definition, the range of UQI values is between zero and one. A higher UQI value indicates a higher similarity between the testing image and the baseline image, and vice versa. The ROI which contained multiple edges as indicated by a rectangular window in Figure 6.3 was selected to calculate the UQI values. The curves of UQI values versus the number of projection views for the noise-free case are shown in Figure 6.7.

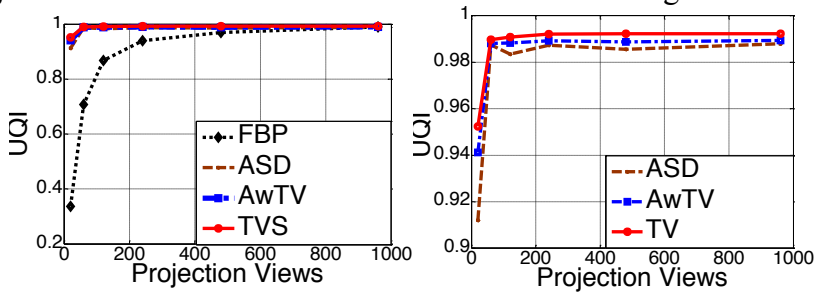

(a) (b)

Figure 6.7. UQI study in the noise-free case: (a) The UQIs versus the number of projection views; and (b) zoom-in views of (a) for ASD/AwTV-POCS and TVS-POCS comparison.

In the full-view case (i.e., >= 960 views), the UQI values of all the three methods (two TV-based ones plus the TVS-POCS) approached to that of the FBP result, which has the highest UQI value as expected by theory and therefore was set as the gold standard as the number of projection views were sufficient large. As the number of

projection views decreased, , the results from three methods are much closer to the true image as compared to the FBP results in the sparse-view cases, which are consistent with the CS theory. In order to visualize the difference among the ASD/AwTV-POCS and TVS results, a zoom-in view of Figure 6.7(a) is shown in Figure 6.7 (b). From this figure we can observe that TVS curve is the closest one to the gold standard among the three methods. Thus, we can conclude that the TVS method can be more likely to produce matching results compared to the TV-based ASD/AwTV-POCS methods in the sparse-view noise-free cases. Besides the overall comparison of the three methods' curves, we also observed small ripples from the ASD-POCS results at 480 and 120 views, which indicated that the ASD-POCS method introduced some undesired textures (i.e., patchy artifacts) in these sparse-view cases. However, the UQI curve from the TVS method monotonously decreased as the number of projection views decreased, which indicated a better performance in the sparse-view cases.

In the noisy cases, the curves of the UQI values versus the number of projection views are shown in Figure 6.8. From this figure, we can observe that the curves have very similar trends as the curves in the noise-free cases shown in Figure 6.8. The results demonstrate that the TVS method yields noticeable gains in this UQI study for both noise-free and noisy cases compared to the FBP and ASD/AwTV-POCS methods.

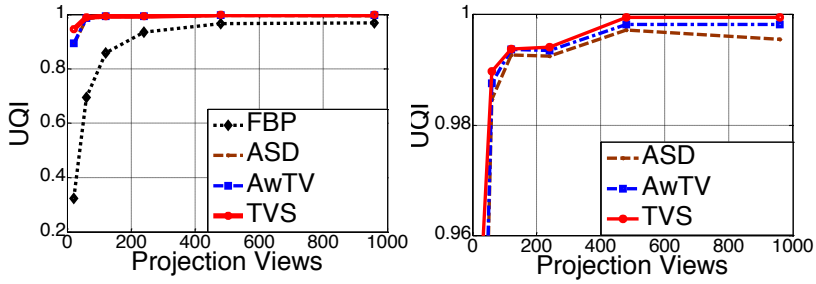

Figure 6.8. UQI study in the noisy case: (a) The UQIs versus projection views curves; (b) zoom-in views of (a) for ASD/AwTV-POCS and TVS-POCS comparison.

6.6 Physical phantom study

To further evaluate the performance of the proposed TVS-POCS method with comparison to the TV-based ASD/AwTV-POCS algorithms in a more realistic environment, we conducted a CatPhan® 600 physical phantom study. Compared to the simulated noisy projection data in the digital phantom study, the physical phantom projection data contain more complex and unpredictable noise coming from the X-ray source, detectors and system electronics, etc., and are more close to the projection data acquired at clinics.

6.6.1 Parameter selection

For the TVS-POCS method, each of the general iteration consisted of 40 TFE iterations, 10 POCS iterations and 50 image fitting iterations. The stop criteria (i.e., $\lg(MSE)$ between the images from current step and previous step) was set to be -8.5, which made the iterative process stop at the 97th iteration. The parameters were set as: $\Delta t_1 = 1\times10^{-7}$, $\Delta t_2 = 1\times10^{-6}$. For the ASD-POCS and AwTV-POCS algorithms, each of

the general iteration contained two POCS iterations and 12 gradient descent iterations as indicated in [52]. The indicator factor c_α defined in [52] was set to be -0.6 for the AwTV-POCS algorithm and -0.5 for the ASD-POCS algorithm, and both values were used as stop criteria to ensure a steady solution. The initial step length was 0.5 for the POCS iteration and 1.2×10^{-4} for the gradient descent step. The scale factor was set to 0.6×10^{-2} for the AwTV model. The reconstruction by the FBP method with Hanning window at 0.8 Nyquist frequency cutoff, which treated the noise at each projection view satisfactorily, was generated as the reference image.

6.6.2 Visualization-based evaluation

Figure 6.9 illustrates the physical phantom results from different methods. It can be seen that all the three methods (ASD/AwTV-POCS and TVS-POCS) produced much better images as compared to the FBP method in the sparse 63-views case. Compared to the gold standard image of the full-view FBP reconstruction, the FBP result in the sparse 63-view case suffered from severe artifacts due to the low sampling rate and noisy data measurement. The ASD/AwTV-POCS algorithms suffered from the artifacts in a less degree. In the zooming ROI images at the bottom of this figure, the TVS-POCS result shows a very pleasant image quality. Compared to the ASD/AwTV-POCS results, the TVS-POCS result is smooth in the uniform area and has better contrast on both hot and cold spot as indicated by the arrows in Figure 6.9 (c), (d) and (e). It should be mentioned that due to the ultra-low angle sampling, it is hard to recover the boundary of the low-contrast circle without distortion.

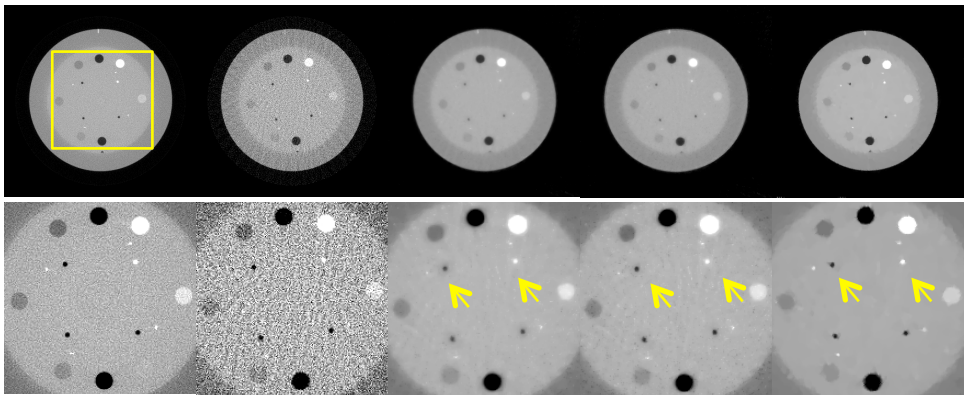

(a) (b) (c) (d) (e)

Figure 6.9.CatPhan® 600 phantom image reconstructions by different algorithms from the 63 projection views. Column (a) shows the reconstruction by the FBP method from the full or total 634 projection views as a reference. Column (b) shows the reconstruction by the FBP method from the sparse or 63-projection views. Column (c) shows the reconstruction by the AwTV-POCS method from the 63 projection views. Column (d) shows the reconstruction by the ASD-POCS method from the 63 projection views. Column (e) shows the reconstruction by the TVS method from the 63 projection views. The bottom row shows the zoomed pictures. The display window of top row is [0, 0.0271]mm-1. The display window of bottom row is [0.0039, 0.0258]mm^{-1}.

6.6.3 Profile-based comparison

In order to further compare the performance of the TVS-POCS method to the ASD/AwTV-POCS algorithms in this CatPhan® 600 physical phantom study, profiles passing through the two spots, as indicated by the arrows in Figure 6.9, were fitted by a Gaussian like function and shown in Figure 6.10. From this figure, it can be observed that the peak values of the TVS-POCS result are much higher than that of the TV-based ASD/AwTV-POCS results, which indicate that the TVS method yielded a higher resolution than other methods. To further quantitatively analyze the gains of the TVS method, the full-width-at-half-maximum (FWHM) values of the two spots (a cold spot and a hot spot) are discussed in next section.

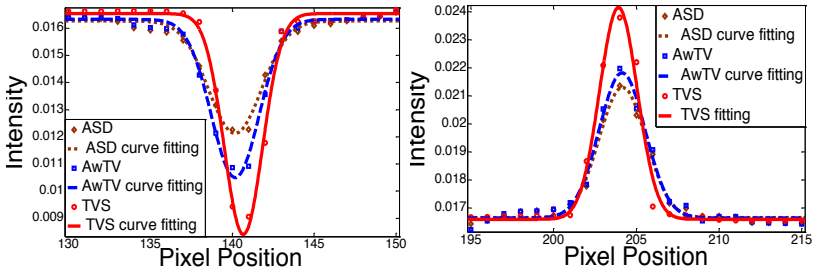

(a) (b)

Figure 6.10.Horizontal profiles of the CatPhan® 600 phantom images reconstructed by different algorithms from the 63-view 80mA projection data. Picture (a) shows the profiles across the cold spot (along the 146th row, from the 135th to the 155th column). Picture (b) shows the profiles across the hot spot (along the 139th row, from the 200th to the 220th column).

6.6.4 FWHM measures

The FWHM of the Gaussian curves in Figure 6.10 were calculated and shown in Table 6.1, revealing that the TVS method produced smaller FWHM values than the ASD-POCS and AwTV-POCS methods on both the hot and cold spots and indicating that higher contrast spots were obtained by the TVS-POCS method. These FWHM measures are consistent with our observations in the profile comparison study.

Table 6.1. The FWHM values of the cold and hot spots in Figure 6.7.

Position	ASD-POCS	AwTV-POCS	TVS-POCS
cold spot	5.1582	4.8763	**3.8799**
hot spot	4.6789	4.5966	**3.7647**

6.6.5 UQI study

In this UQI evaluation, the gold standard image was the FBP reconstruction in the full-view case was utilized as the baseline image. The UQI curves of the selected ROIs as indicated by rectangular window in Figure 6.9 are shown in Figure 6.11. From this figure, we can observe: (1) the ASD/AwTV-POCS and TVS-POCS results have much higher UQI values than the FBP result in the sparse-view cases and they approached to the gold standard in the full-view case; and (2) the TVS-POCS results have higher UQI

values than that of the ASD/AwTV-POCS results. Thus, the TVS-POCS method can produce more close matching results compared to the TV-based algorithms in the sparse-view cases.

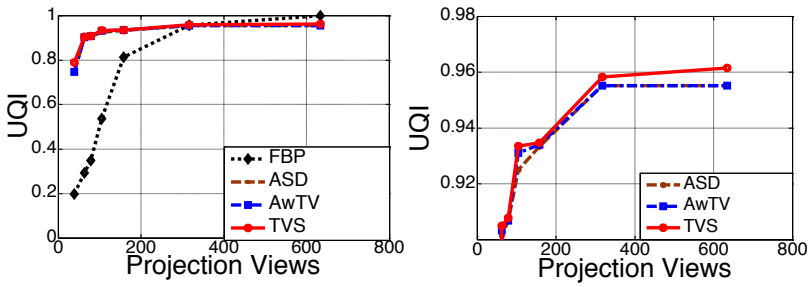

(a) (b)

Figure 6.11. (a) the curves of UQI values versus the numbers of projection views; and (b) the zoom-in views of (a).

6.7 Clinical data analysis

6.7.1 Data acquisition

In this pilot clinical study, the raw projection data were acquired from two patients (patient #1 and patient #2) who were scheduled for CT-guided lung needle biopsy for lung nodule analysis under the approval of the Institutional Review Board (IRB) of the Stony Brook University. The patients were scanned by a Siemens SOMATOM Sensation 16-slice spiral CT scanner in non-FFS model (i.e., 1,160 projection views per 360°, 0.3103448° for the tube angle increment). The number of channels in each detector row was 672, the fan angle increment for each channel was 0.0775862° and the bin size along the z axis was 0.75mm. The radius of the focal spot circle was 570mm, and distance between the source and the detector plane was 1,040mm. The FOV was $51.2\times51.2\text{cm}^2$ with the corresponding pixel size of $1\times1\text{mm}^2$. The tube voltage was set to 120kVp and the tube current were set to 100mAs (i.e., the normal-mAs level for preparation) and 40mAs (i.e., the low-mAs level for roughly looking for the nodules), and 20mAs (i.e., the ultral-low-mAs level for needle puncture).

The spiral cone-beam raw data from the 16-slice CT system are usually rebinned into multi-slice fan-beam projection data by considering the effects of pitch (i.e., the movement of the patient along the z axis) [67]. In this study, we were interested in the image slice containing the lung nodule and therefore extracted the corresponding sinogram from the multi-slice fan beam sinogram data. For each patient, three sinograms were extracted corresponding to the normal, low and ultra-low mAs levels, respectively. The FBP reconstruction from the full-view 100mAs data was assumed as our gold standard image.

6.7.2 Evaluations at a fixed mAs level with varying projection view sampling

In reality, one of our mostly concerned questions about low-dose CT image reconstruction would be stated as "how many projection views are necessary to reconstruct satisfactory images at a fixed mAs level?" Accordingly, most researchers agreed that the sparsity of the desired image and the noise in the projection data would be two important factors [8, 13, 23, 33, 52, 79, 80, 101]. In this study, we evenly extract

116, 232, 290, 386, 580 and 1,160 projection views from the sinogram data acquired at 100mAs (i.e., normal-mAs level) to ensure the same noise level for each projection view of the sparse-view data. Therefore, the overall dosage of each sparse case depends only on the number of projection views.

6.7.2.1 Visualization-based evaluation

The reconstructed images from the patient #1's sinogram data are shown in Figure 6.12,Figure 6.13 and Figure 6.14. Clearly, the FBP algorithm had the worst results in the sparse cases, and the ASD/AwTV-POCS methods had more patchy artifacts than the TVS-POCS method in 580, 386 and 290-view cases. If the number of projection views decreased below 290, all the three methods (two TV-based plus the presented TVS-based) generated more straight artifacts and severe noise due to the severe insufficient measurement. The zoom-in-view in Figure 6.13 and Figure 6.14 illustrated that the TVS reconstruction from the 290-projection views has superior image quality for the clinical biopsy purpose. However, to produce a similar image reconstruction with the TVS-POCS method, the ASD/AwTV-POCS methods need at least 386 projection views. The results further demonstrate that the gains from the TVS-POCS method over the gold standard image in dose reduction would be (386-290)/290% or 33%.

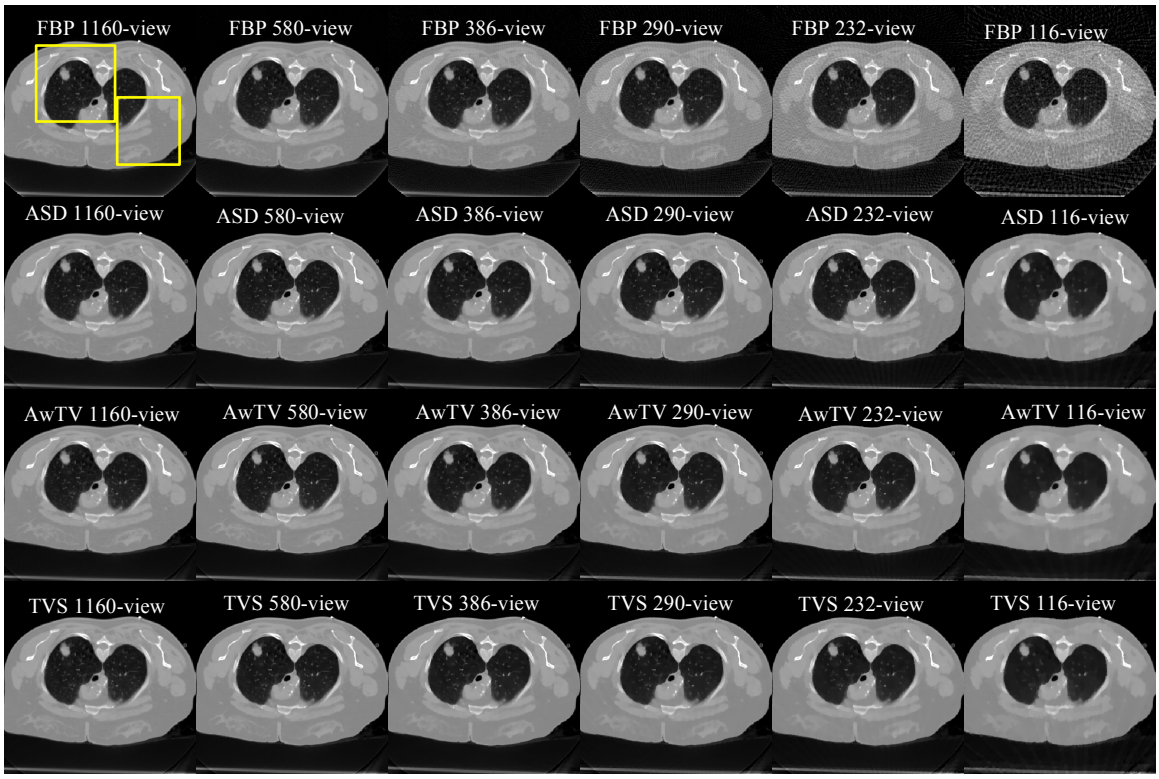

Figure 6.12.The images reconstructed by FBP (1st row), ASD-POCS (2nd row), AwTV-POCS (3rd row) and TVS-POCS (4th row) methods from 1,160-, 580-, 386-, 290-, 232- and 116-projection views. The display window is [0, 0.0587]mm^{-1}.

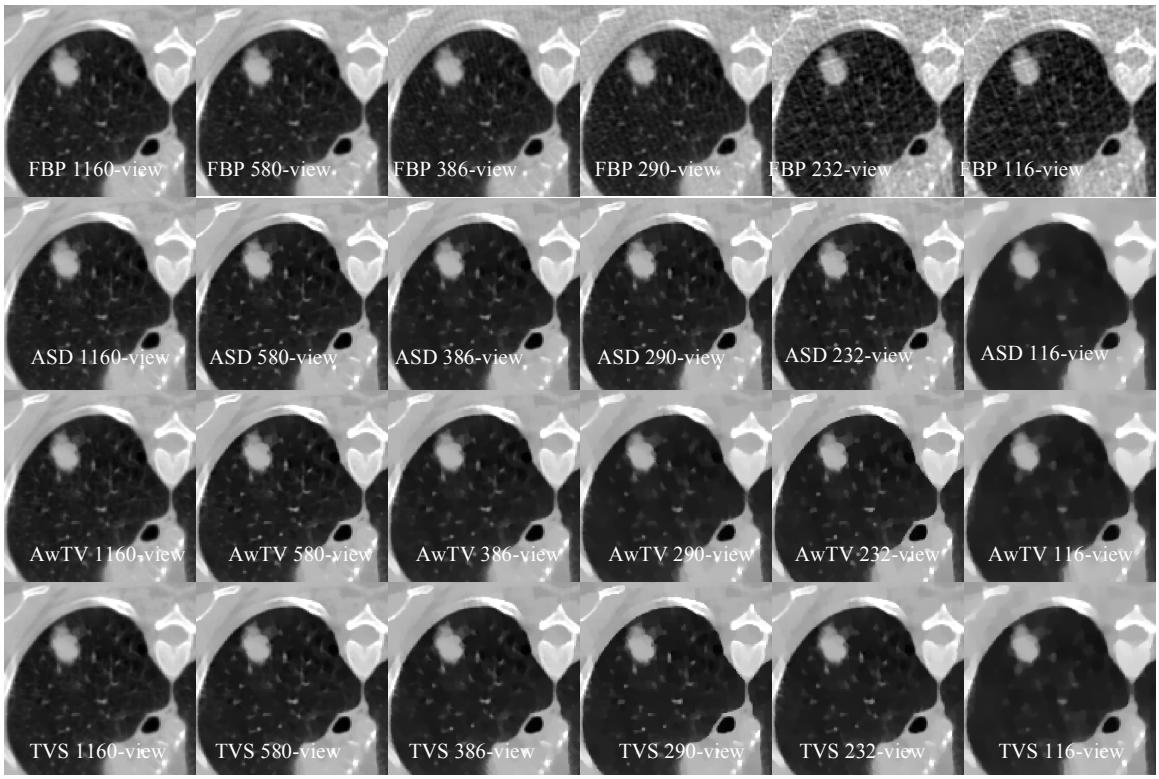

Figure 6.13.The zoom-in views of images reconstructed by FBP (1st row), ASD-POCS (2nd row), AwTV-POCS (3rd row) and TVS (4th row) methods from 1,160-, 580-, 386-, 290-, 232- and 116-projection views. The display window is [0,0.0373]mm^{-1}.

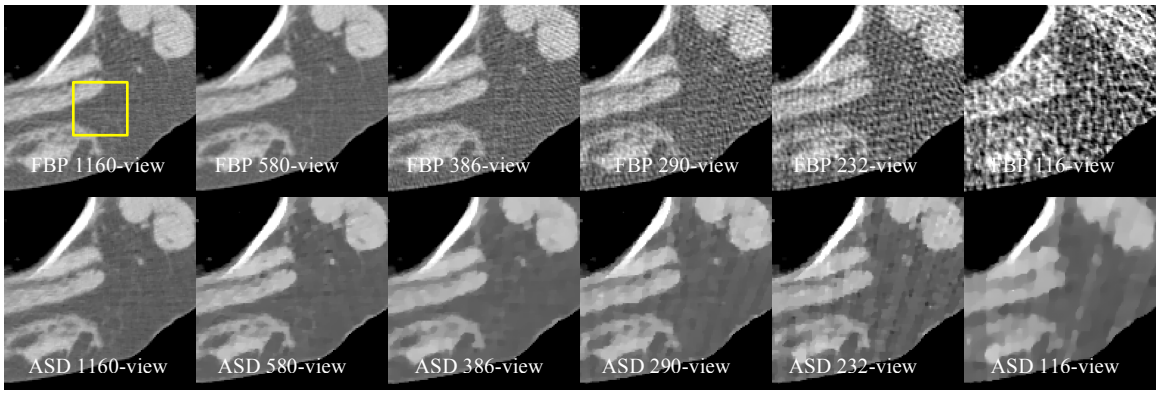

Figure 6.14.The zoom-in views of images reconstructed by FBP (1st row), ASD-POCS (2nd row), AwTV-POCS (3rd row) and TVS (4th row) methods from 1,160-, 580-, 386-, 290-, 232- and 116-projection views. The display window is [0.0373, 0.0587]mm^{-1}.

6.7.2.2 Normal vector flow study

In order to further verify the improvement of the TVS-POCS method over the TV-based ones, small ROIs from the 290-view results as indicated by rectangular window in Figure 6.14 were selected to plot the normal vector flow (NVF) images and the plots are shown in Figure 6.15. In this figure, the NVF image of the FBP reconstruction from the full-view (or 1,160-view) data was drawn as gold standard. According to our knowledge,

the gradual changes of the intensities in the desired image are often shown as ordered arrows in the NVF images, while the noise in the image are often shown as disordered arrows, as shown in Figure 6.15(a) and (b). From Figure 6.15(c) and (d), it can be seen that although the disordered arrows were illuminated by the use of AwTV/TV-POCS methods, some ordered arrows were falsely replaced by small dots as indicated by the circles. The replacements were caused by patchy artifacts, which tried to uniform all the intensities within a local patch. Meanwhile, the NVF images of the TVS-POCS methods illustrate that the more ordered arrows were recovered, which indicated small textures of the resulting image were well preserved, as indicated by circle in Figure 6.15(e).

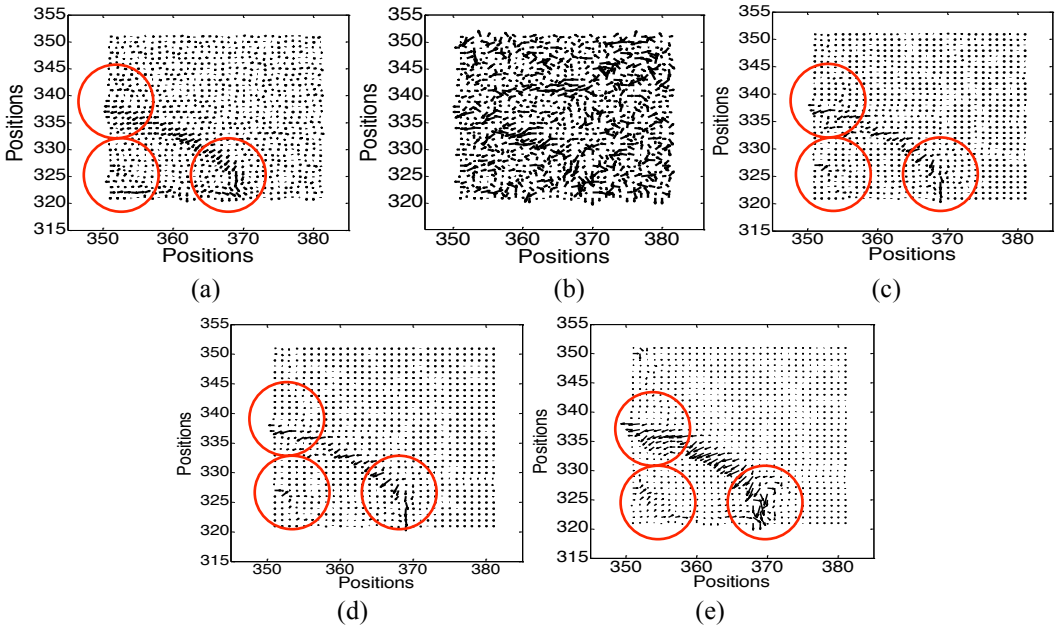

Figure 6.15.The NVF images of the reconstructed images from: (a) the 1,160 views by FBP (the gold standard); (b) the 290 views by FBP; (c) the 290 views by ASD-POCS; (d) the 290 views by AwTV-POCS; and (e) the 290 views by TVS-POCS.

6.7.2.3 UQI study

The above reconstructed images were also quantitatively evaluated by the UQI measure, as shown in Figure 6.16. The results indicate that all three methods (two TV-based plus the TVS-based) approached to the full-view FBP reconstruction (or the gold standard reference) with significant gains over the FBP method at sparse-view cases with less than 580 projection views. The zoom-in-display of the curves is in Figure 6.16 (b), which shows that the TVS-POCS method outperformed the ASD/AwTV-POCS algorithms. These results are consistent with our previous observations in both digital and physical phantom studies.

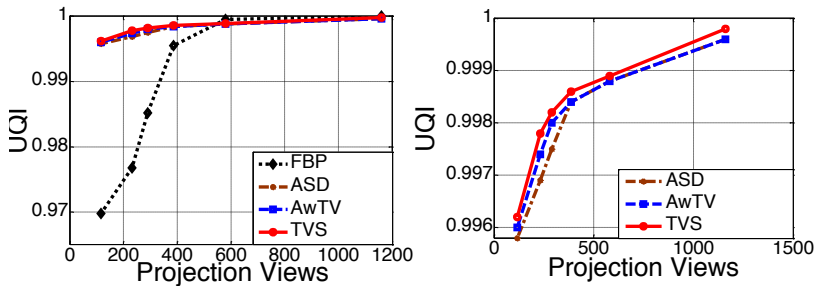

Figure 6.16.(a) The curves of the UQI values versus the numbers of projection views; and (b) the zoom-in views of (a).

For low-dose CT image reconstruction, another concerning question would be stated as "what is the better way to minimize the dosage (i.e., decreasing the number of projection views or decreasing the photon flux). In addition, we also interest about the robustness of the proposed TVS-POCS method in low-mAs or ultra-low-mAs cases. In order to assess the performance of TVS-POCS algorithm for low-dose image reconstruction from the same total dosage level, we implement the following experiments .

6.7.3 Evaluations at a fixed total dose with varying projection view sampling

For low-dose CT image reconstruction, another most concerned question would be stated as "what is the better way to minimize the dosage (i.e., decreasing the number of projection views or decreasing the photon flux). As we mentioned in the introduction section, decreasing the number of projections will cause aliasing artifacts due to the low sampling rate, which also has been observed in the previous sections. On the other hand, instead of reducing the numbers of projection views, decreasing the photon flux per view will unavoidable increase the noise level at each view. In order to exam the performance of the proposed TVS method at a fixed total dose level, three types of data were manipulated from the original raw data as follows:

Data type (a) -- 232-view normal-mAs scan: 232 projection views were evenly extracted from the 100mAs scan;

Data type (b) -- 580-view low-mAs scan: 580 projection views were evenly extracted from the 40mAs scan;

Data type (c) -- Full-view ultra-low-mAs scan: 1,160 projection views from the 20mAs scan.

It is necessary to point out that the term of "fixed total dose" may not be defined rigorously. Some reports had pointed out that the actual dose effects of reducing mAs level may different from that of decreasing the number of projection views. The clinical dosage analysis is beyond the scope of this study and we assume the three types of data have the identical dosage effect.

Table 6.2.The parameters for FBP, ASD/AwTV-POCS and TVS methods.

Method	Parameters
ASD/AwTV-POCS	10 POCS iterations and 10 gradient descent iterations in each outer loop;
	Step length of 0.8 for POCS step in all three types of data;
	Step lengths of 4×10^{-5} , $4\times10^{-5}, 3\times10^{-5}$ for gradient descent in the data type a, b and c, respectively;
	The stop criteria as discussed in [15, 19].
TVS	50 TFE iterations and 100 IR iterations (include 10 POCS iterations before IR iterations) in each outer loop for data type (a); 40 TFE iterations and 50 IR iterations (include 10 POCS iterations before IR iterations) in each outer loop for data type (b) and (c);
	Step length of 0.8 for POCS step in IR iterative process for all three types of data;
	$\Delta t_1 = 6\times10^{-7}$ for all three data type;
	$\Delta t_2 = 1\times10^{-6},\ 6\times10^{-7},\ 1\times10^{-7}$ for all three data types (a), (b) and (c), respectively;
	Stop criteria of -8 (i.e., $\lg(MSE)$ between the images from current step and previous step) as discussed above.

Figure 6.17 shows the reference images reconstructed from patient #1's full-view data acquired with normal, low and ultra-low-mAs protocols by FBP. The results show more noise when decreasing the incoming photon numbers, as expected. By using the parameters in Table 6.2, the reconstructed results are shown in Figure 6.18, which shows the ASD/AwTV-POCS and TVS methods outperformed the FBP for all the three types of data.

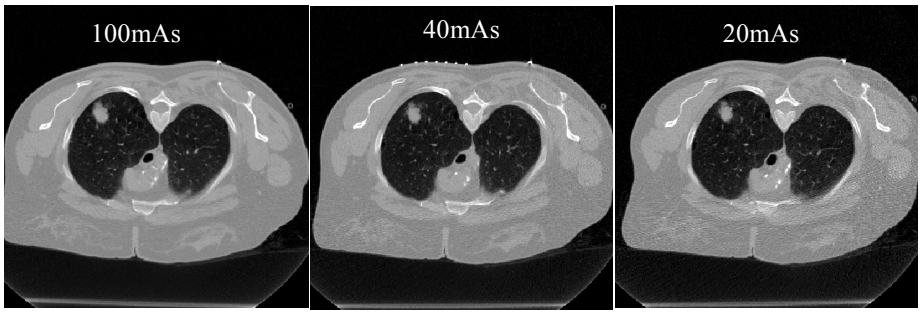

Figure 6.17. The images reconstructed by FBP from 100mAs (left), 40mAs (middle) and 20mAs (right), respectively. The display window is [0, 0.032] mm^{-1}.

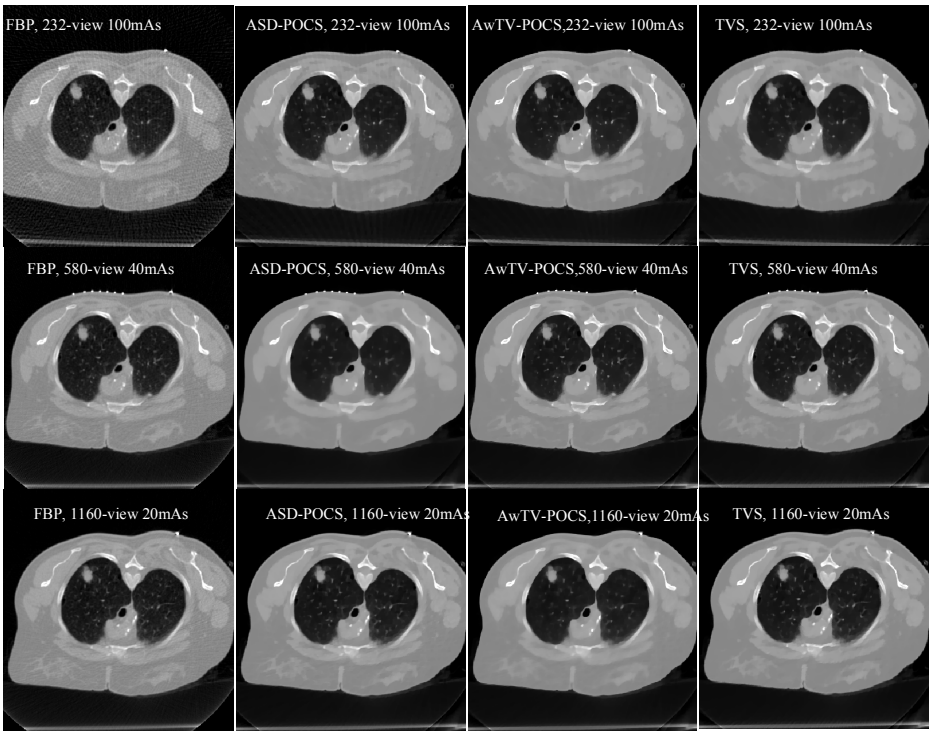

Figure 6.18. The images reconstructed by FBP (1st column), ASD-POCS (2nd column), AwTV-POCS (3rd column) and TVS (4th column) methods from data type (a) (1st row), data type (b) (2nd row), and data type (c) (3rd row), respectively. The display window is [0, 0.032] mm^{-1}.

The magnified region near the nodule is shown in Figure 6.19. The FBP result from data type (a) contains straight artifacts due to the low sampling rate. By comparison of ASD/AwTV-POCS and TVS results, we observe more severe straight artifacts in the ASD-POCS result than the AwTV-POCS and TVS results.

For the case of data type (b), it is seen that the FBP result suffered both streak artifacts and photon noise, the ASD/AwTV-POCS and TVS results were substantially better. However, the gradual changes at the boundary of the nodule in the ASD-POCS result was over smoothed and blurred, as indicated by the arrows in Figure 6.19. The AwTV-POCS and TVS results indicate some improvements. Some small patchy artifacts were still observable from the AwTV-POCS result compared to the TVS result.

For the case of data type (c), the FBP result indicates higher photon noise due to the lower mAs level. Although both the ASD-POCS and AwTV-POCS results show abilities to suppress photon noise, they suffer the patchy artifacts due to the piecewise constant assumption. The TVS method outperformed those two algorithms by more effectively suppressing noise and patchy artifacts while keeping the subtle structures, as indicated by the arrows in Figure 6.19. In addition, the low-contrast parts as indicated by arrows were well preserved during the image reconstruction process.

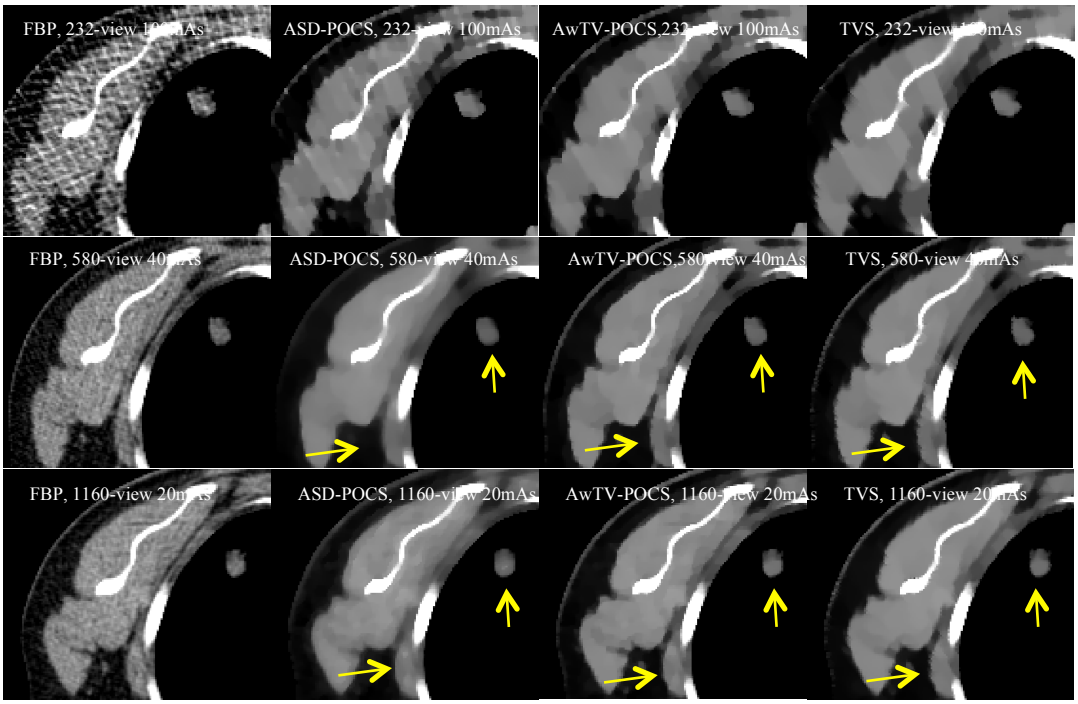

Figure 6.19The zoom-in view results by FBP (1st column), ASD-POCS (2nd column), AwTV-POCS (3rd column) and TVS (4th column) from data type (a) (1st row), data type (b) (2nd row), and data type (c) (3rd row), respectively. The display window is [0, 0.032] mm^{-1}.

In order to further visualize the improvement of the proposed TVS method, the same three types of data from patient #2 were extracted and then reconstructed. The reconstructed images and their magnified regions near the nodule are shown in Figure 6.20 and Figure 6.21. In Figure 6.21, the TVS results demonstrated the improvement both in the uniform area and near the boundary for all three types of data.

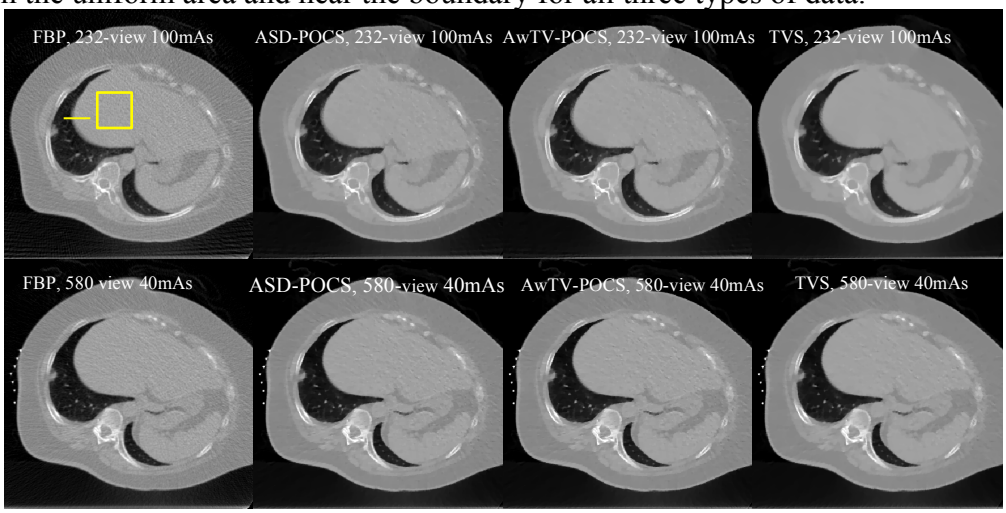

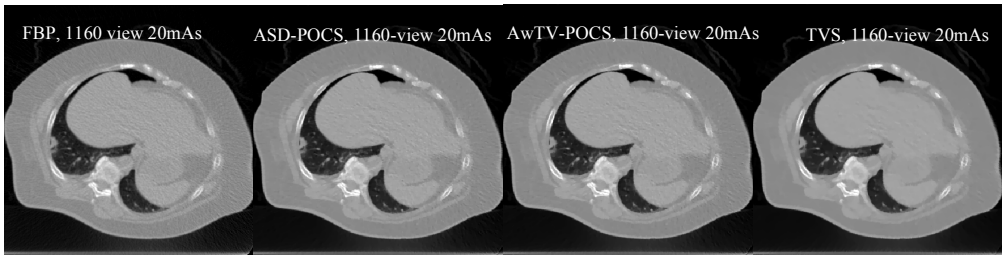

Figure 6.20. The images reconstructed by FBP (1st column), ASD-POCS (2nd column), AwTV-POCS (3rd column) and TVS (4th column) from data type (a) (1st row), data type (b) (2nd row), and data type (c) (3rd row), respectively. The display window is [0, 0.032] mm^{-1}.

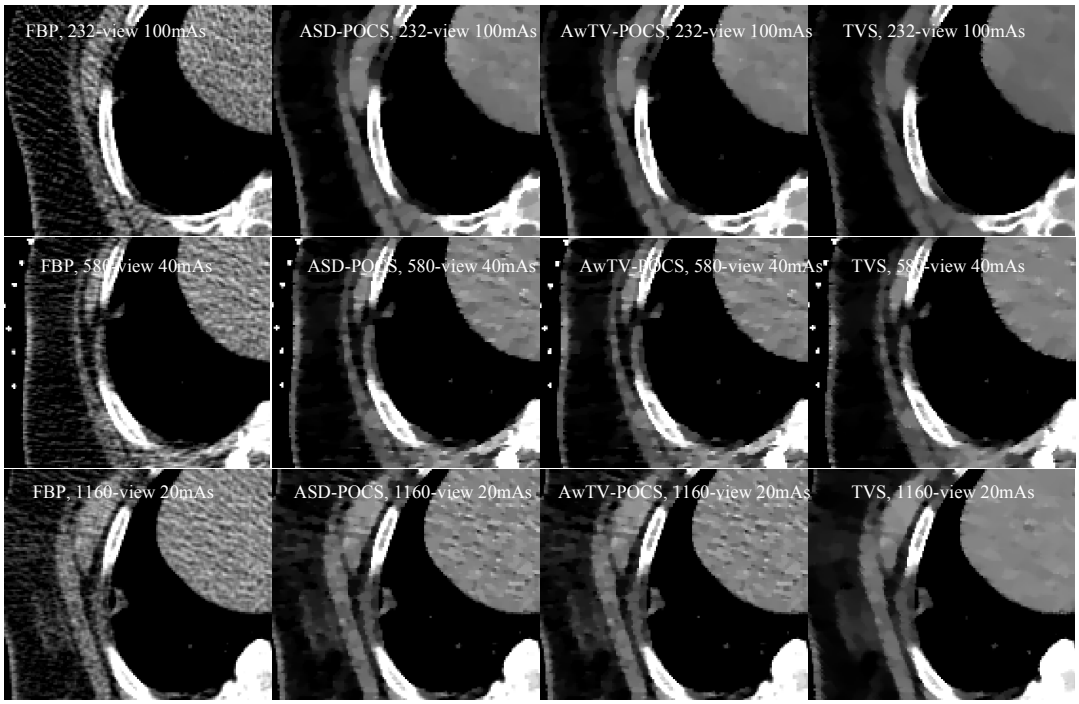

Figure 6.21. The zoom-in view results by FBP (1st column), ASD-POCS (2nd column), AwTV-POCS (3rd column) and TVS (4th column) from data type (a) (1st row), data type (b) (2nd row), and data type (c) (3rd row), respectively. The display window is [0, 0.032] mm^{-1}.

The standard deviations of the selected region as indicated in Figure 6.20 were measured from the reconstructed results to quantify the noise level of the results. The values are presented in Figure 6.22(a). From this figure, we can conclude that a small standard deviation or noise level can be achieved by the TVS method for image reconstruction from type (a) data.

The resolution of the reconstructed images of Figure 6.20 was also quantitatively evaluated by the FWHM studies. The results are shown in Figure 6.22 (b), which indicates that a higher resolution image can be reconstructed by the proposed TVS method from data type (c) as compared to the TV-based algorithms.

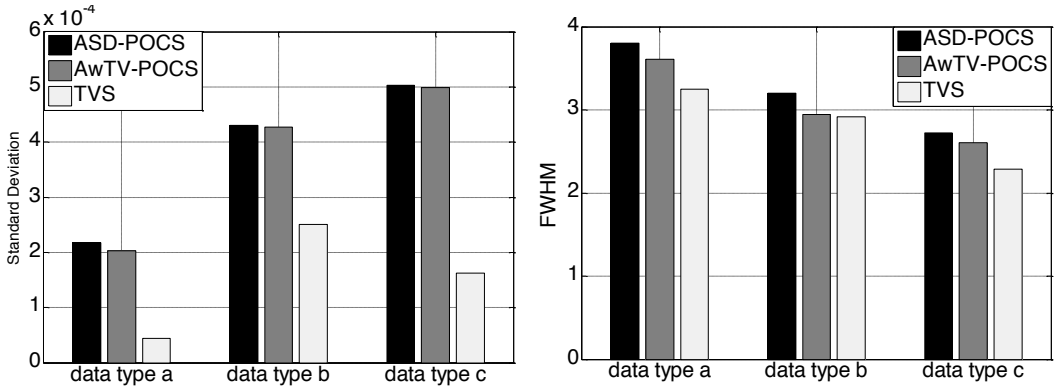

(a) (b)

Figure 6.22. (a) Noise standard deviation for the three methods at different data types; (b) FWHM for the three methods at different data types.

6.8 Discussion and conclusion

In this chapter, we presented a TVS-POCS method for CT image reconstruction from sparse-view data and investigated this method by computer simulations, physical phantom experiments, and clinical pilot studies.

Different from the previous TV and AwTV regularization strategies, the isophote directions were introduced in the TVS model. The key motivation for the TVS model was to retain the continuous property of the image along both the tangent and the normal directions. Use of the TVS-POCS method for image reconstruction from sparse-view data has been shown to improve the quality of the image reconstruction by mitigating the patchy artifacts of the previous TV and AwTV regularization strategies. Moreover, this new method has been shown to improve the preservation of both gradually varying boundaries and sharply changing edges.

In our digital phantom study, the convergence was shown to be monotonically decreasing toward a steady solution. The TVS-POCS method outperformed the ASD/AwTV-POCS algorithms for image reconstruction from sparse-view data in both noise-free and noisy cases. The TVS-POCS method eliminated the patchy artifacts and produced pleasant results at the uniform regions and also around the edges. In addition to visual inspection of the results, we also performed several quantitative evaluations by using different merits. The profile analysis and UQI study indicated the improvement by the TVS-POCS method.

While the projection data in the physical phantom study suffered the photon count noise and electrical background noise, the outcomes rendered a similar conclusion as that of the digital phantom data. This reflects the robustness of the TVS-POCS method to a more realistic scanning environment.

In the clinical pilot data study, beside the photon count noise and electrical background noise due to the scanning system, the projection data were affected by more variables from the subjects. Many reconstruction methods failed to demonstrate their gains in clinical data case, although their performances in phantom studies were impressive. In our clinical data case, we tested the proposed method in two different scenarios. In the first scenario, we reduced the number of projection views at a fixed mAs level. The TVS-POCS method outperformed the other two TV-based algorithms on

both visual inspection and UQI study. In the second scenario (shown in Appendix), we investigated three possible ways to reduce the radiation dose: (i) reducing the number of projection views, (ii) lowering the mAs level, and (iii) reducing both the number of views and the mAs level. For a given dose level, the TVS-POCS result from the data type (a) showed the least noise level while the TVS-POCS result from the data type (c) showed the best resolution. However, due to the statistical properties of the projection data acquired from low-mAs or ultra-low-mAs protocols were not considered in our image modeling, it was difficult to make a conclusive conclusion about which was the best way to decrease radiation dose, although the TVS-POCS method seems to perform consistently better than other TV-based algorithms in all the three types of data configuration. Thus, an open question would be if the TVS model is still advanced than the TV-based model when we use the statistical-based iterative image reconstruction methods, such as the PRWLS method. Addressing this question is one of our research tasks in the future.

At last, there are still some other open questions that need be answered in the future. The first one is about how to accurately determine an adequate value for each of the parameters. This interesting question perplexes almost all the iterative image reconstruction algorithms. In our TVS model, there are parameters whose values need to be determined: Δt_1, Δt_2, $\varepsilon_1, \varepsilon_2$ and ε_3. In implementation, the value of Δt_1 depends only on the intensities of the desired image and can be determined before running the algorithm. The value of $\varepsilon_1, \varepsilon_2$ and ε_3 are always chosen to be small values to achieve a smooth convergence. Parameter Δt_2 is related to the smoothness of the normal vector, a large Δt_2 will often lead to an over-smoothed image. Thus, we can give a large initial value to Δt_2, and then gradually decrease the value to recover subtle information of the resulting images. Another question is about the computational cost. The computational time for the TVS-POCS method is longer than that of the TV-based ASD/AwTV-POCS algorithms because it needs extra time for the tangent vector estimation. So the gain in image reconstruction quality comes with the cost of longer computing time. Accelerating the computation can be achieved by using multi-core CPU and GPU hardware which can compute the result in a more efficient and parallel fashion. The acceleration hardware cost may be a less concerning issue as new computer technologies are available. An alternative acceleration may be the development of an alternative efficient computing algorithm for the TVS-POCS method. Addressing the above open questions could be one task in the future research.

Chapter 7 .Low-dose CT chest imaging reconstruction with TV-stokes algorithm

Previous chapters have demonstrated that the TVS-POCS method which incorporate tangent vector and normal vector in objection function, has ability to reduce noise and eliminate patchy artifacts appeared in conventional TV minimization results. The results in chapter 6 show that the image qualities of TVS-POCS results are advanced than the AwTV/TV-POCS results in both phantom and clinical data cases. In order to evaluate the feasibility of utilizing TVS-POCS method for clinical diagnosis, comprehensive clinical evaluations are desired. This chapter aims to assess the potential of the TVS-POCS reconstruction algorithm from sparse projection data for low-dose computed tomography (CT) imaging of the chest, particularly for screening of lung nodules, a precursor of the lung cancer. One hundred patients, who were scheduled for lung biopsy at Stony Brook University Hospital, were recruited to this study under informed consent after approval of Institutional Review Board. A normal-dose CT scan (i.e., 1,160 projection views per rotation, 120kVp, 100mAs) of the chest was acquired from each patient to setup the biopsy procedure. From the normal-dose CT scan, three subsets of 580, 386 and 290 projection views per rotation were evenly extracted respectively to mimic three low-dose CT imaging scenarios (i.e., sparse-view scans) with corresponding dose reduction to 50%, 33% and 25% of the total dose of the full-view or normal-dose scan. A standard filtered back-projection (FBP) algorithm was applied to the full-view 1,160 projections to produce a full-dose standard image as the ground truth for comparison purpose. In each low-dose scenario, both the FBP and our presented TVS algorithms were applied to reconstruct the corresponding low-dose images. The reconstructed low-dose images were evaluated by computer-based quantitative merits as well as an experienced thoracic radiologist against the ground truth. In the computer-based quantitative evaluation, the merits of standard deviation (SD), contrast noise ratio (CNR) and universal quality index (UQI) were computed from the low-dose images against the ground truth. In the expert radiologist's evaluation, all the low-dose and ground truth images of the 100 patients were randomly displayed on a 2.5 megapixel monitor in soft tissue and lung windows. These images were graded by using a five-point scale from 0 to 4 (0: non-diagnostic; 1: severe artifact with low confidence; 2: moderate artifact or moderate diagnostic confidences; 3: mild artifact or high confidence; and 4: well depicted without artifacts). For the clinical task of screening lung nodules, the expert radiologist marked the detection of each lung nodule on each of the randomly displayed volume images. This preliminary clinical study indicates the presented TVS algorithm can produce significantly higher image quality for sparse-view low-dose CT chest imaging compared to the standard FBP method. At 50% dose level of the full-dose result, the TVS algorithm showed similar image quality and comparable performance on nodule detection as the full-dose scan. Therefore, a dose reduction of 50% may be claimed.

7.1 Material and method

7.1.1 Study population

This study was performed using clinical data sets acquired prospectively from one hundred sequential patients who were scheduled for lung nodule biopsy at Stony Brook University Hospital and recruited under informed consent after approval of our Institutional Review Board. The patient group comprised 58 women (age range, 28-92 years; average age, 70.5 years) and 42 men (age range, 23-92 years; average age, 69 years). Each patient has at least one lung nodule of 5mm and larger, which was found by a national lung screening program and was then referred to undergoing the biopsy procedure at Stony Brook University Hospital. By the previous studies in the literature, each patient would have approximately 20% of chance to have smaller nodules which were not reported in the lung screening program document. These unreported small nodules will serve the targets for the detection evaluation of this study.

7.1.2 Data acquisition and experiment setup

In this study, all the raw projection data were acquired using a Siemens SOMATOM Sensation 16-slice spiral CT scanner in non-FFS model (i.e., 1,160 projection views per 360° rotation, 0.3103448° for the tube angle increment) for clinical biopsy purposes. The number of channels in each detector row was 672, the fan angle increment for each channel was 0.0775862°. The radius of the focal spot circle was 570mm, and the distance between the source and the detector plane was 1,040mm. The FOV was 51.2×51.2 cm^2 with the corresponding pixel size of 1×1 mm^2. The tube voltage was set to 120kVp and the tube current was set to 100mAs for the setup of the biopsy scans. The spiral cone-beam raw data from this CT system were rebinned into multi-slice fan-beam by considering the effects of pitch [67]. Subsequent images were obtained based on biopsy protocol.

In order to mimic the sparse-view CT system, views were evenly extracted from the full-projection view data sets to create 290, 386, 580 and 1,160 (full) projection view data sets. Since the noise levels for each projection view of the sparse-view data were assumed to be the same, the overall dosage of each case depends only on the number of projection views. The corresponding total dosage levels for four cases were reduced to 25%, 33.3%, 50% and 100% of full, respectively.

7.1.3 CT image reconstruction techniques

In this study, comparison of total variation stokes- projection onto convex sets (TVS-POCS) [51] method and conventional FBP method was performed. For simplicity, the TVS-POCS method is called as TVS hereafter. To achieve fast convergence, the FBP reconstructions from low-dose cases were used as initial images in this application. Notice that a small artificial step length preserves more textures but requires more steps to converge; however a larger artificial step length may suppress fine structures in the images. The parameters selection and stop criteria of the TVS method in this study can be determined empirically based on the discussion in [51].

In practice, the FBP reconstructions from full-view 100mAs data are often used for clinical diagnosis due to the high image quality. Therefore, we use the FBP reconstructions from the 1160-view data sets as our reference standard images. Figure

7.1 shows one example of the reconstructions from four cases by both FBP method and TVS method.

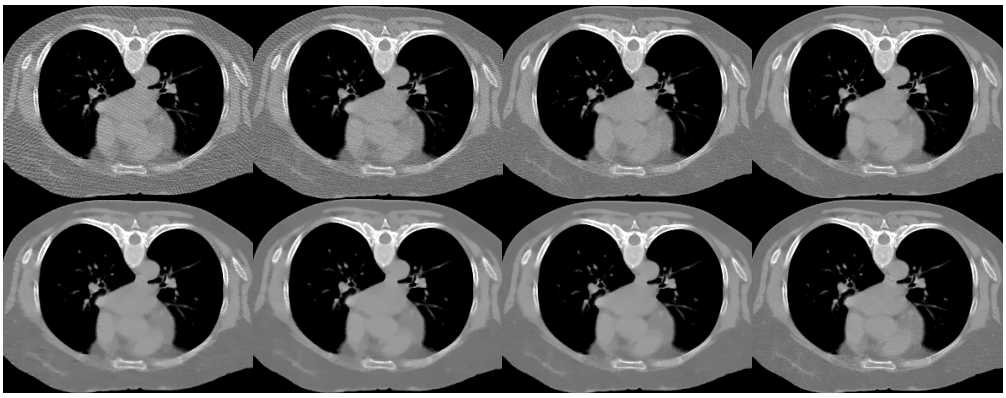

Figure 7.1: CT images reconstructed with FBP (top row) and TVS (bottom row) from (a) 290-view (25% dose level), (b) 386-view (33.3% dose level), (3) 580-view (50% dose level) and (4) 1160-view (full-dose level).

7.1.4 Image quality evaluations

The image quality evaluations in the following part mainly consist of two parts: (1) computer based quantitative metric evaluations and (2) human based qualitative evaluations. The computer based quantitative metric evaluations can characterize the inherent image qualities, such as noise level, image contrast level and similarity between the estimated results and the reference standard. In contrast to the computer based quantitative metric evaluations, the human based evaluation assesses the potential of utilizing the images for specific clinical purposes. In this study, a radiologist, who has over ten years experience in lung nodule diagnosis, assessed the feasibility of utilizing the low-dose reconstructions for diagnosis.

7.1.4.1 Computer based quantitative metrics

Standard deviation

The noise level of the reconstructions was characterized by standard deviation metric. A smaller standard deviation value indicates a lower noise level and better noise control; whereas a larger standard deviation value means a higher noise level and worse noise control. For both FBP results and TVS results, the standard deviation values were calculated at six 25mm^2 ROIs including two lung ROIs (right lung and left lung), two fat ROIs (one from the left part of chest, the other from the right part of chest), and two aorta ROIs, as indicated by red square in Figure 7.2. The standard deviation value mean and the noise reduction mean and median were calculated based on the reconstructions from TVS and FBP methods.

Contrast noise ratio

The contrast-to-noise ratio (CNR) quantifies the image quality by considering both noise and contrast level of the reconstructed image. A larger CNR value indicates that a higher contrast and lower noise level image is obtained; whereas a smaller CNR value means that a lower contrast and higher noise level image is obtained. According the

CNR definition introduced in [50], the aorta ROI and its nearby lung region were used to compute the CNR.

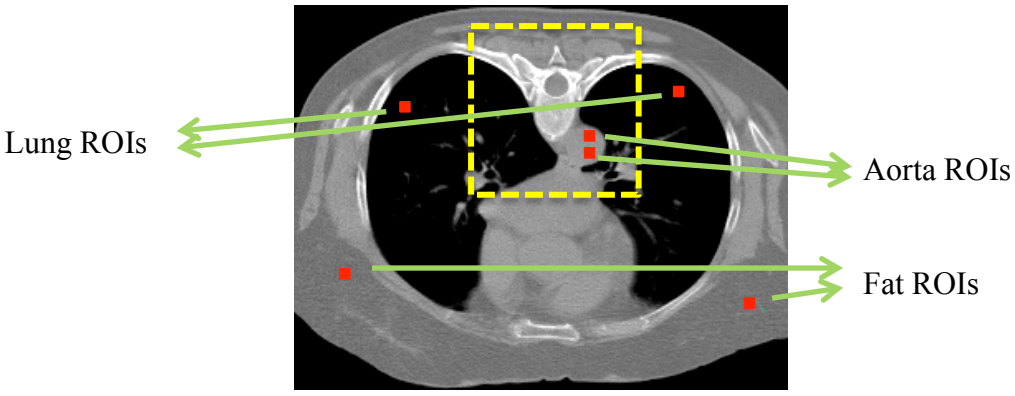

Figure 7.2.: Six ROIs (i.e., two lung regions, two fat regions and two aorta regions) for standard deviation evaluations.

Universal quality index

The UQI is a quantitative metric measuring the similarity between the reconstructed image and its baseline image. Three factors, i.e., loss of correlation, luminance distortion and contrast distortion are considered in the UQI indices [49] [109]. By definition, the range of UQI values is between zero and one. A higher UQI value indicates a higher similarity between the testing image and the baseline image, and vice versa. The 100 cm^2 ROI which contained multiple tissue types as indicated by a yellow rectangular window in Figure 7.2 was selected to calculate the UQI values and the corresponding images reconstructed from full-view data by FBP were used as baseline images.

7.1.4.2 Human based qualitative evaluations

To assess the feasibility of utilizing the TVS algorithm for clinical applications, the reconstructions (a series of 30 axial images) were reviewed by a radiologist with ten years of thoracic imaging experience. Each series of images were displayed on a 2 Mega Pixel monitor (type and company). The radiologist was able to scroll through the images and change window and levels. However, each series of images was assessed at standard lung and soft tissue window (1600, -500; 300, 80). The series of images were randomly presented to the radiologist who was blinded to all patient data, as well as the number of projections and the types of reconstruct. Inspired by the previous study in [60], the images were graded by using a five-point scale from 0 to 4 (0, non-diagnostic; 1, severe artifact with low confidence; 2, moderate artifact or moderate diagnostic confidences; 3, mild artifact or high confidence; 4, well depicted without artifacts). The mean scores and histogram of scores were calculated for both FBP and TVS methods in different dose-level cases; and a two-sample t-test was performed to compare the image qualities of TVS with FBP method. Statistical analyses were performed using the Matlab software package.

7.2 Results

7.2.1 Standard deviation

The standard deviations of four cases (i.e., 290, 386, 580 and 1160-projection view) for the six measured ROIs are shown in Tables 7.1, 7.2, 7.3 and 7.4. From

Table 7.1, it can be observed that the mean and median noise levels of the TVS reconstructions are much lower than the FBP results. In 290-view case, the mean noise reductions of the TVS reconstruction compared to the FBP reconstructions (standard deviation of TVS reconstruction was divided by standard deviation of FBP reconstruction) were between 6.5232 (right lung region) and 20.6393 (right fat region). As we increase the number of projection views, in 386-view case, the mean noise reductions were between 7.3974 (right lung region) and 22.2440 (right fat region). In 580-view case, the minimum mean noise reduction was reduced to 4.5336 (left lung region) and the maximum mean noise reduction was reduced to 11.3148 (right fat region). In the full-view case (i.e., 1160-view), the mean noise reductions of six ROIs were between 1.5052 (right lung region) and 1.6154 (right fat region). The noise suppression is also observable in Figure 7.1. In sparse view cases, the FBP reconstructions in different view cases show very similar noise patterns caused by the low-sampling frequency (lower than the Nyquist frequency) artifacts. However, in the TVS reconstructions, this type of noise was found to be effectively suppressed by solving optimization problems; therefore, the corresponding standard deviation/noise was reduced.

Table 7.1.The standard deviation of 290-projection view

	Lung (left)	Lung (right)	Fat (left)	Fat (right)	Aorta (left)	Aorta (right)
mean FBP	87.1291	77.9305	96.3335	92.7961	84.9795	85.7834
mean FBP	**20.5535**	**18.6733**	**19.3541**	**19.2342**	**20.0625**	**20.8308**
noise reduction (mean)	6.5232	7.5138	8.2158	20.6393	10.4380	14.1738
noise reduction (median)	5.1673	5.1797	5.7010	6.5174	5.5819	7.4658

Table 7.2. The standard deviation of 386-projection view

	Lung (left)	Lung (right)	Fat (left)	Fat (right)	Aorta (left)	Aorta (right)
mean FBP	68.8568	62.6756	79.1202	76.3875	69.1062	69.0569
mean FBP	**16.5386**	**13.8556**	**13.8145**	**13.0735**	**14.9473**	**14.6869**
noise reduction (mean)	7.5052	7.3974	12.4217	22.2440	11.3580	13.1736
noise reduction (median)	5.2351	5.4255	7.9132	8.7276	6.7352	7.7991

Table 7.3. The standard deviation of 580-projection view

	Lung (left)	Lung (right)	Fat (left)	Fat (right)	Aorta (left)	Aorta (right)
mean FBP	53.3901	48.6273	57.2561	55.6576	53.5815	54.5977
mean FBP	**16.8950**	**15.8446**	**14.6587**	**13.8180**	**17.1981**	**17.7778**
noise reduction (mean)	4.5336	4.7049	6.4701	11.3148	7.2098	8.1552
noise reduction (median)	3.7281	3.5996	4.3872	5.2397	4.6063	4.8129

Table 7.4. The standard deviation of 1160-projection view

	Lung (left)	Lung (right)	Fat (left)	Fat (right)	Aorta (left)	Aorta (right)
mean FBP	38.2264	36.7691	37.4466	37.6661	37.4699	39.3193
mean FBP	**28.1595**	**27.2540**	**26.2156**	**26.5132**	**26.7926**	**28.5811**
noise reduction (mean)	1.5397	1.5052	1.5677	1.6154	1.5689	1.5818
noise reduction (median)	1.3905	1.3818	1.4762	1.4834	1.5481	1.5391

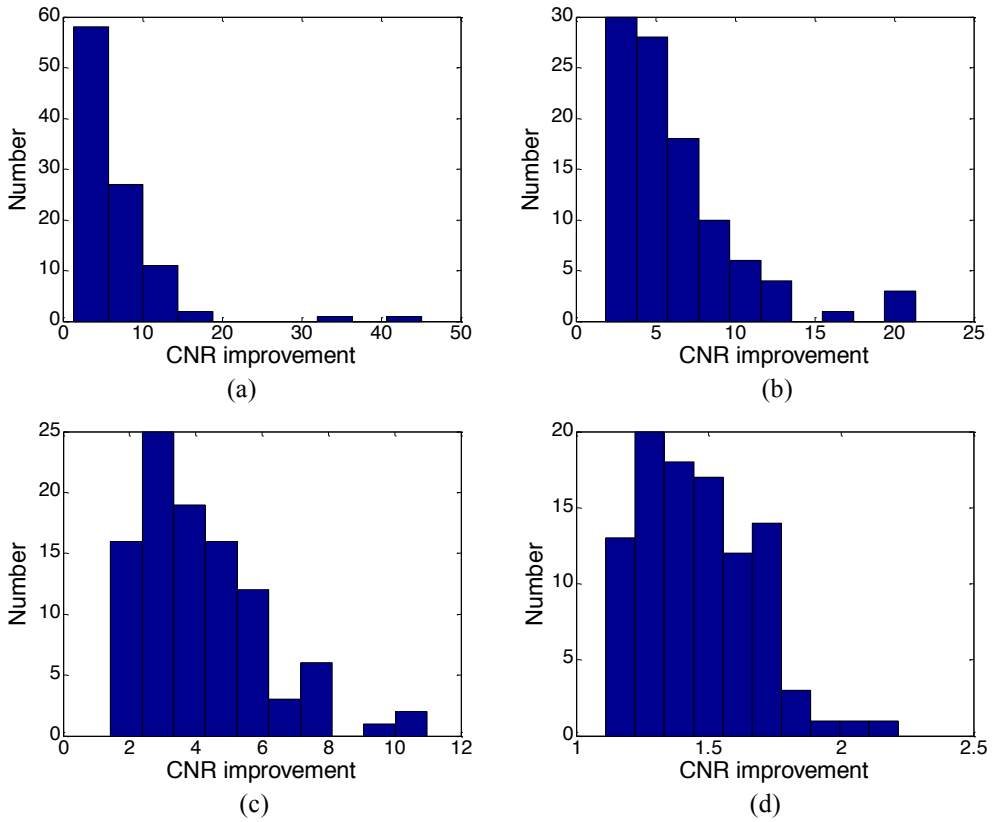

Figure 7.3. (a) The CNR improvement histogram of 290-projection view case. (b) The CNR improvement histogram of 386-projection view case. (c) The CNR improvement histogram of 580-projection view case. (d) The CNR improvement histogram of 1160-(full)-projection view case.

7.2.2 Contrast noise ratio

In order to quantify the CNR improvement, we let the CNR improvement equal to the ratio of TVS CNR results and FBP CNR results. Figure 7.3 (a) shows the histogram of CNR improvements in 290-projection case. In this figure, the TVS method can achieve up to 40 CNR improvement compared to the FBP method. The mean of CNR improvements for 100 patients was 6.1776 and median of CNR improvements was 4.9153. In 386-projection view case, as shown in Figure 7.3 (b), the TVS method achieves up to 20 CNR improvements; the mean of CNR improvement is 6.1776 and the median of CNR improvement was 4.9153. As the number of projection increase, the

mean of CNR improvement reached 4.1757 in 580-projection view case and 1.4586 in 1160-projection view case. The median CNR improvement reached 3.7622 in 580-projection view case and 1.4342 in 1160-projection view case, as shown in Figure 7.3 (c) and Figure 7.3 (d). The results demonstrate a dramatic image quality gains from the TVS method over the FBP method.

7.2.3 Universal quality index

Based on our previous discussion, the similarity between the reconstructions and known baseline images can also be evaluated by UQI. In this study, we choose the FBP reconstructions from full-view (1160 view) data as our baseline images. In 290 projection-view case, as shown in Figure 7.4, the results indicate that 31% of the FBP UQIs were between 0.99 and 1 and 33% between 0.98 and 0.99. In contrast to the FBP results, 52% of TVS UQIs were between 0.99 and 1, 27% between 0.98 and 0.99. The mean of TVS UQI was 0.9758 and median of TVS UQI was 0.9905; the mean of FBP UQI was 0.9670 and median was 0.9857, which indicates more TVS reconstructions were closer to the baseline image compared to the FBP methods in 290-projection view case.

In 386 projection-view case, as shown in Figure 7.5, the FBP UQIs between 0.99 and 1 increased to 37%; the TVS UQIs between 0.99 and 1 increased to 74%. The mean and median UQI values of TVS results (mean: 0.9891, median 0.9972) were still larger than the corresponding FBP results (mean: 0.9914, median 0.9974), which is consistent with our observations in 290-projection view case.

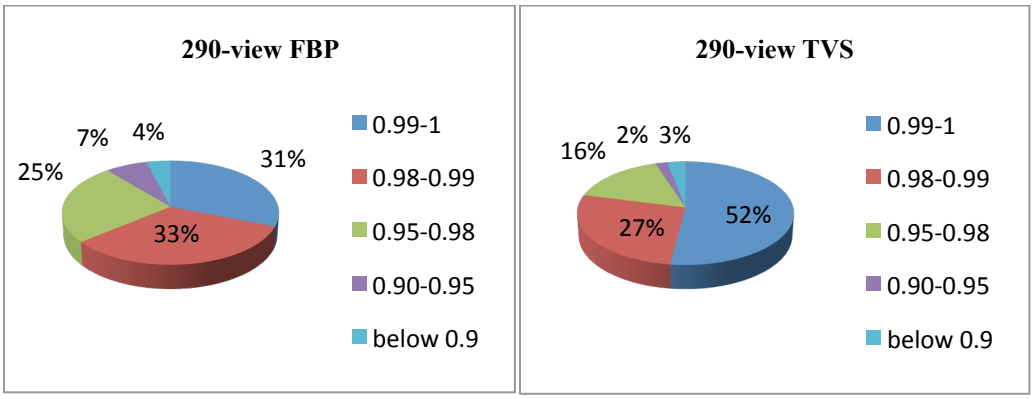

(a) (b)

Figure 7.4. The UQI of reconstructions in 290-projection view case: (a). FBP reconstruction UQIs; (b) TVS reconstruction UQIs.

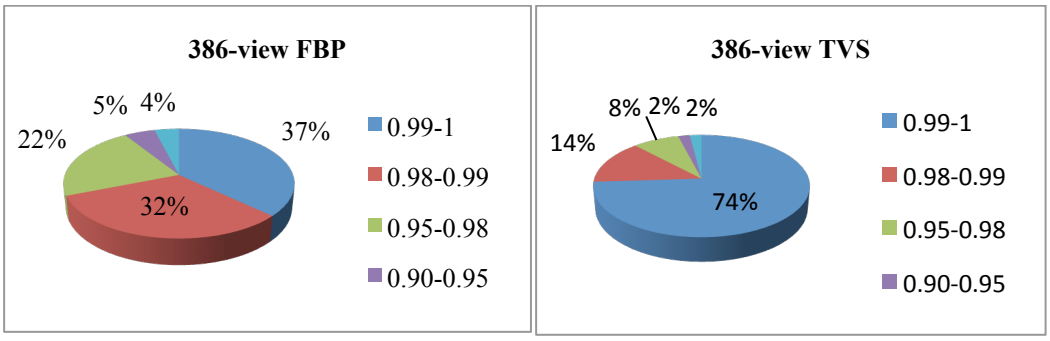

(a) (b)

Figure 7.5. The UQI of reconstructions in 386-projection view case: (a). FBP reconstruction UQIs; (b) TVS reconstruction UQIs.

However, as the number of projection view increases to 580, the UQI of the FBP reconstructions surpasses that of the TVS reconstructions, as shown in Figure 7.6. The mean and median of TVS UQIs were 0.9891 and 0.9972 and corresponding mean and median of FBP UQIs were 0.9914 and 0.9974, which indicates more FBP results are closer to the baseline images (i.e., FBP results from full-view data) in 580-view case. Similarly, in full (1160)-projection view case, the UQIs of all FBP results are equal to one. The mean and median of TVS reconstruction in the full-view cases were 0.9953 and 0.9995, respectively. The results in 1160-projection case are shown in Figure 7.7.

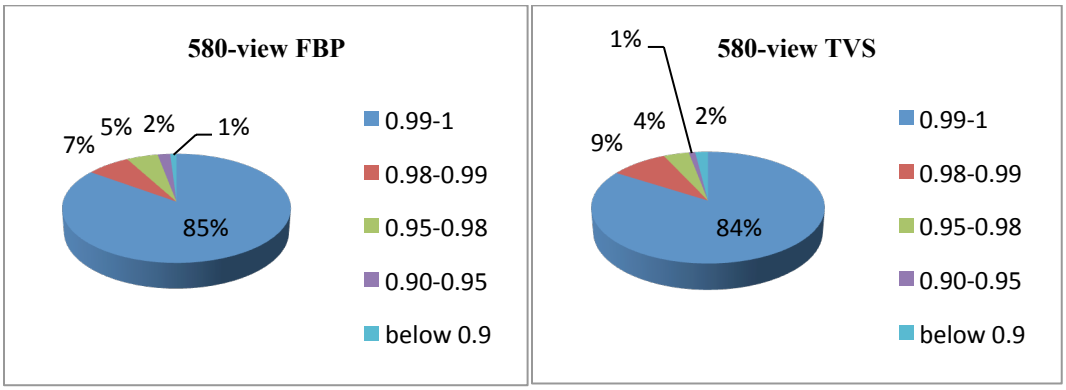

(a) (b)

Figure 7.6. The UQI of reconstructions in 580-projection view case: (a). FBP reconstruction UQIs; (b) TVS reconstruction UQIs.

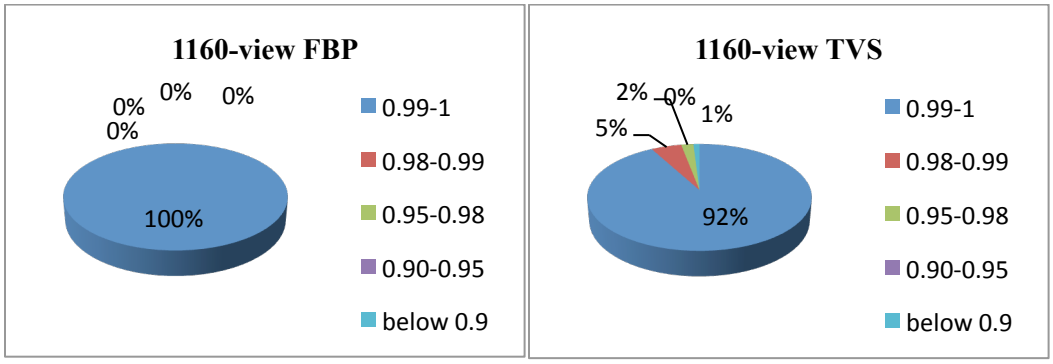

(a) (b)

Figure 7.7. The UQI of reconstructions in 1160-projection view case: (a). FBP reconstruction UQIs; (b) TVS reconstruction UQIs.

7.2.4 Image quality scores

From Table 7.5, the mean image quality for TVS reconstructions was improved over the corresponding FBP results in all cases. In 290- projection view case, the mean image quality score for FBP results in soft tissue display window was 1.79 and 1.96 in lung

display window; the mean image quality scores for TVS results was 2.66 for soft tissue display window and 2.35 for lung display window. The TVS results show better image quality and were statically significantly different with FBP results (p value<0.01 for both display windows). In 386- projection view case, the mean image quality scores for FBP results was 2.12 for soft tissue display window and 2.34 for lung display window; the mean image quality scores for TVS results increased to 2.9 for soft tissue display window and 2.63 for lung display window. The difference in image qualities was statically significantly different with p value less than 0.01. In the 580-projection view case, the scores for FBP results were 2.43 and 2.69; the corresponding TVS results were 3.14 and 2.99 (p value<0.01 for both display windows). Based on the definition of image quality scores, the radiologist described high diagnostic confidence about the TVS results but only had moderate diagnostic confidences about the FBP results. In 1160 projection view case, although the radiologist had high confidence for both FBP and TVS results, the mean scores for TVS results (soft tissue window: 3.25, lung window: 3.28) are still higher than the FBP results (soft tissue window: 2.92, lung window: 3.17), which indicate better image quality of TVS reconstructions. For the image displayed in lung window, the p value was 0.2897, which indicated the difference between the two group results was not significant in the full view case. The trend of image scores versus total projection numbers are shown in Figure 7.8.

Table 7.5.Mean image quality scores in soft tissue display window and lung display window

	290-view		386-view		580-view		1160-view	
	Soft tissue	Lung	Soft tissue	Lung	Soft tissue	Lung	Soft tissue	Lung
FBP	1.79	1.96	2.12	2.34	2.43	2.69	2.92	3.17
TVS	2.66	2.35	2.9	2.63	3.14	2.99	3.25	3.28
p value	<0.01	<0.01	<0.01	<0.01	<0.01	<0.01	<0.01	0.2897

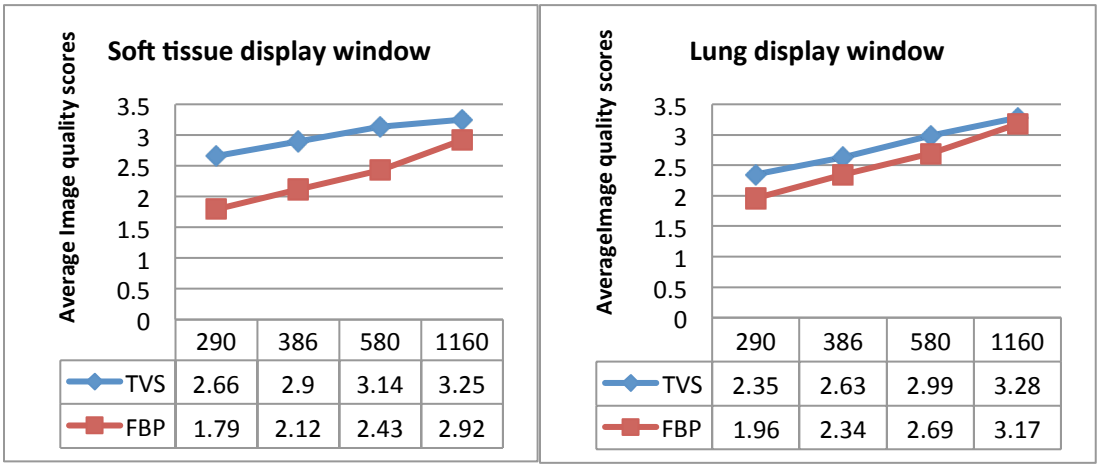

(a) (b)

Figure 7.8. The mean image quality scores for four different dosage levels: (a) soft tissue display window; (b) lung display window.

7.2.5 Lung nodule detection

In reality, the most concerning question is "how can the new numerical algorithm assist the diagnosis?" In order to answer this question, the total number of lung nodules detected, by an experience thoracic radiologist, in the 3D reconstructed series of axial images was recorded for each of the different dosage levels (i.e. 290, 386, 580 and 1160 projection-view) were identified. The results of this experiment are shown in Figure 7.9. In 290-projection view cases, the radiologist detected 9 more nodules using the TVS reconstructions (142 nodules in total) as compared to the FBP reconstructions (133 nodules in total). Some low contrast small nodules were recovered by suppressing noise and streaks. In 386-projection view case, the total number of detected lung nodules from TVS reconstructions increased to 143 and the number of detected nodules using FBP reconstructions was 139. As we increased the projection numbers to 580, which has half dosage of the normal CT scan, the radiologist detected 145 nodules from TVS reconstructions as compared to 139 nodules from FBP reconstructions. It should be noted that at this TVS dosage level, the number of detected nodules was larger than the detected nodule number (i.e., 144) from the ground truth sets (i.e., the FBP reconstructions from 1160-projection views). This observation indicates that the TVS reconstructions from half dosage (i.e., 580-projection view) meet the diagnostic requirements and can reach the similar diagnostic level as the baseline images (i.e., ground truth). In 1160-projection view case, 151 lung nodules were detected from TVS reconstructions as compared to 144 nodules in FBP reconstructions, which indicates the TVS method may further improve images quality and enhance the efficiency of lung nodule detection even in full-view case.

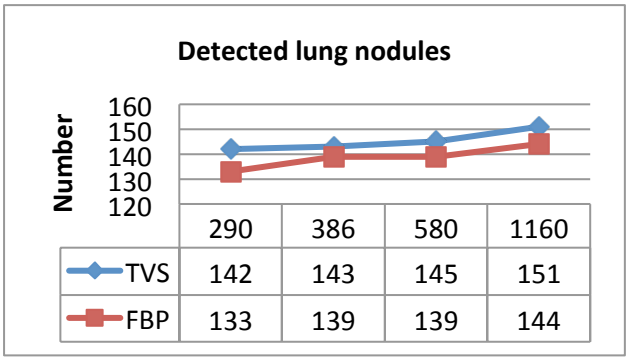

Figure 7.9.The total number of detected lung nodules versus projection view numbers

7.3 Discussion and conclusion

In this chapter, we investigated the feasibility of utilizing TVS algorithm for thoracic imaging. In order to analyze the efficiency and universality of the TVS algorithm, the projection data was acquired from a large population (i.e., 100 patients). Both FBP and TVS algorithms were applied to reconstruct images from the similar data sets. As compared to the conventional FBP algorithm, the TVS algorithm can substantially improve image quality by reducing noise and artifacts in the low-dose case. The results potentially support the concept of low-dose technique and demonstrate the TVS method can improve diagnostic image quality in low-dose case.

In computer based quantitative evaluations, the TVS reconstructions have low standard deviations, which indicate better noise control compared to the FBP reconstructions. However, similar to other iterative image reconstruction algorithms, the resulting images always show nonlinear noise properties. For example, as we increase the total projection number, the standard deviation value of the conventional analytical (i.e., FBP) reconstructions monotonically decreased. However, the standard deviations of the TVS method in 1160-projection view case are higher than the corresponding standard deviation in 580-projection view case. This is reasonable since the noise levels and noise patterns of the iterative image reconstruction results depend on many factors such as models, parameter selections, stop criteria, initial guess, boundary conditions and so on. In the CNR study, the results demonstrated the TVS method indeed improves the contrast of the image and this contrast improvement was also proved in the nodule detection study. It should be noted that although substantial prior models have been investigated to preserve/enhance the edges of the iterative reconstructions [4, 52, 93], the TVS model preserves the edge information by retaining the isophote information， which is usually natural and authentic. In the UQI study, the results show that 74% reconstructions are almost identical to the baseline images (UQI value>0.99) in the 33.3% dosage reduction case as compared to 37% for FBP reconstructions. The results also indicate the TVS algorithm can reduce the artifacts and preserve image quality in low-dose scenario.

In the human based qualitative evaluations, the radiologist had high diagnostic confidence in the TVS reconstructions at 50% dosage reduction in both soft tissue and lung window, which indicates the dosage can be reduced to 50% without compromising diagnostic image quality. In the scenario of 386 projections, i.e. dose reduction to 33%, although the radiologist claimed moderate diagnostic confidences for the reconstructions from both methods, the TVS reconstructions have much higher image quality scores in both soft tissue and lung window compared to the FBP reconstructions. In the scenario of 290 projections, i.e. dose reduction to 25%, the radiologist claimed moderate confidence for TVS reconstructions and low confidence for the FBP reconstructions. Therefore, it could be concluded that about half radiation dosage is enough to obtain high quality image by TVS method. In the our lung nodule detection study, since the TVS method can preserve edges and suppress noise and artifacts, the radiologist was able to observe more lung nodules, which were submerged in noise or artifacts. In 50% dosage reduction case, the radiologist detected even more lung nodules than the ground truth, since the iterative reconstruction can eliminate the streak artifacts by multiple forward and backward projections. In contrast, it is hard to remove the streaks by using the conventional analytical method.

Finally, it should be mentioned that similar to other iterative image reconstruction algorithms, there are some disadvantages of the TVS method. For example, as we mentioned before, the iterative reconstructions often show nonlinear noise properties and therefore, how to accurately evaluate the noise level and noise patterns is still an open question to be answered. Another problem for iterative image reconstruction method is the implementations often require high computational cost. The optimization often consumes large computing time. In practice, although the iterative image reconstructions show better image quality than the conventional analytical method, most CT scanners still insist on conventional analytical methods due to fast computing time. The slow computing time of the TVS method could be compromised by utilizing parallel

computing, however, the subsequential higher hardware cost for the parallel computing would be another limitation of the iterative reconstruction.

In summary, although the iterative reconstruction still has some limitations such as long computing time and higher hardware cost, the results from the iterative reconstructions are still very promising. The TVS results shown in this study suggest that the TVS method can efficiently suppress the noise and improve image quality in the low-dose case. In addition, the TVS reconstructions from 50% dosage can be used for lung nodule detection with high diagnostic confidence. Therefore, the TVS method could be used as an alternative modality for low-dose image reconstruction in the future.

Chapter 8. Current and future directions in CT image reconstruction

8.1 Low-dose CT image reconstruction

Due to the rapid growth of new clinical applications and the large demands of CT imaging, radiation dose reduction during CT scans was an important issue in the past decades. As the development of hardware and software, more and more hardware based new techniques and software based numerical algorithms have been investigated to solve the CT reconstruction problems. Although great efforts have been devoted by both manufacturers and researchers over the years, the minimum radiation dosage for CT reconstruction without scarifying image quality is still an open question. There is no doubt that the low-dose CT topic will be continuously concerned in the future.

In this dissertation, a volume-shadow weighting based FDK algorithm was proposed to improve cone-beam CT image reconstruction. Both computer simulations and real data show that the proposed VSW-FDK method indeed solves the non-uniform noise propagation problem in cone-beam CT without introducing extra artifacts. This new technique can be also applied in iterative image reconstruction method for low-dose CT. For example, a new transfer/system matrix can be calculated based on the same volume-shadow weighting concept [50].

In addition to improve the projection geometry, the numerical algorithm for low-dose CT image reconstruction is another important factor to improve image quality. Based on the nature of the algorithms, the numerical algorithms are classified to two categories: SIR and algebraic reconstruction. In the SIR, the noise model and prior model are two important factors for noise reduction and artifacts removal. In this dissertation, based on the Poisson plus Gaussian noise model [63], a penalized re-weighted least-squares method with AwTV prior model was investigated for 3D CT image reconstruction. The simulation studies and experimental studies were carried out to evaluate the performance of the proposed method as compared to the conventional TV modeling method. The results show the proposed AwTV-PRWLS method can reduce artifacts and improve the resolution of the resulting images. A similar AwTV model was also adapted to solve the sparse-view CT reconstruction problem. Compared to the low-mAs full view data, the sparse-view reconstructions from conventional FBP method were degraded due to the steak artifacts and noise caused by the low-sampling rates. An AwTV-POCS algorithm was also investigated in this paper to suppress noise and artifacts. The results indicate that the proposed method can indeed improve the image quality as compared to the TV-POCS method [79, 80]. In chapter 6, a TVS method was introduced to solve the patchy artifacts appeared in conventional TV/AwTV-POCS method. Since the piecewise constant assumption of TV model, the conventional TV minimization results always show “blocky” artifacts. In clinical diagnosis, this kind of “blocky” artifact is dangerous; it can mimic some textures that don’t exist in the true image. The TVS model is proposed to solve this kind of artifacts by introducing tangential vectors. The results show that the TVS model can indeed solve this problem. The clinical impacts of TVS-

POCS method are assessed in this dissertation. By using the proposed TVS-POCS method for chest nodule diagnosis, the total dosage delivered to the patients can be reduced at least 50%. Therefore, 50% dosage level is believed to be the optimized dosage level that can be achieved by TVS-POCS method for lung nodule diagnosis. It should be mentioned although there are many prior models have been investigated over the years to improve the conventional IR results beside our models, the optimum prior model for IR is still unknown. Therefore, the prior model would still be an interesting research direction in the future for low-dose CT image reconstruction.

Another research direction for low-dose CT research would be reducing IR computing. Although many advanced algorithms have been developed in the past decades by using advanced computing technique, such as parallel computing by GPU, the IR is still time-consuming as compared to the analytical method. Since the high demand of CT imaging, the fast computing time is always desired to reduce the reconstruction cost which can benefit both patients and doctors.

8.2 Spectral CT reconstruction

In addition to the current low-dose reconstruction direction, another direction for CT reconstruction development would be the spectral CT or dual energy CT (DECT) reconstructions. Compared to the conventional CT, the DECT has the potential to reduce beam hardening artifacts and provide material composition information, which will benefit many clinical applications, such as kidney stone diagnosis, lesion diagnosis, virtual material removal, etc. The DECT projection data are often acquired from two different energy levels. Since the harm of radiation exposure, directly utilizing the conventional CT geometry to scan patient twice is unacceptable. In order to minimize the radiation delivered to patients during DECT procedure and increase the efficiency of data acquisition, many techniques have been invented to acquire two different energies projection data from one scan, such as tube-switching, dual-layer detector and photon counting detector technique. As we mentioned at the early of this chapter, reducing the radiation dosage is always desired for CT scan. Therefore, the proposed numerical algorithm in this dissertation can be adapted to the DECT image reconstruction for dose reduction. For example, the proposed statistical iterative image reconstruction numerical algorithms can be used for DECT image reconstruction with known noise modeling, which is discussed in Appendix. The feasibility and benefit of utilizing conventional CT numerical algorithms in spectral CT is unknown and need to be analyzed in the future.

Appendix A. Noise modeling and image reconstruction algorithms for Dual Energy CT

Dual-energy computed tomography (DECT) is a recent advancement in CT technology, which can reduce beam hardening artifacts and provide material composition information compared to conventional CT. Recently, by using the same concept in low-dose CT reconstruction, the SIR methods were introduced to DECT image reconstruction for radiation dose reduction [108]. The statistical noise modeling of measurements plays an important role in conventional CT SIR and impacts on the image quality. In DECT, the measurements are often decomposed to basis material sinograms. Unlike the conventional CT sinogram data, the decomposed basis material sinograms have strong correlations. Although an accurate DECT noise modeling contains correlations is expected to benefit the image quality in SIR, the amount of improvement is unknown and difficult to study. Directly utilizing the accurate noise model in some numerical methods is challenging due to the non-diagonal properties. This appendix shows a preliminary study in DECT noise modeling. The performances of the two noise models (i.e., accurate noise model and simplified model by ignoring correlations) in numerical methods are evaluated and then the corresponding image quality is assessed by analyzing the bias and variance tradeoff. The results indicate that using the non-diagonal covariance matrix in SIR is challenging; some numerical methods may spend extreme long time to converge. The bias-variance curve shows that in the same bias level, the accurate noise modeling has up to 20% noise reduction compared to the simplified model. Due to this significant improvement, the correlations between two decomposed sinograms should not be neglected. An efficient numerical algorithm with the consideration of accurate noise model is necessary for DECT image reconstruction.

A.1. PWLS for spectral CT

Chapter 4 has shown the SIR has the potential to improve image quality for low-dose CT image reconstruction. In this section, we adapt the SIR framework to DECT image reconstruction for radiation dose reduction. In conventional CT, the SIR methods rely on an accurate statistical modeling of the CT measurements and can greatly improving image quality by increasing resolution as well as reducing noise in low-dose CT image reconstruction [106]. Inspired by the similar idea, we use the quadratic approximation to the log likelihood function in [26, 76] to write the cost function of DECT image reconstruction as:

$$\Phi(c) = \left(\tilde{L} - Ac\right)^T W \left(\tilde{L} - Ac\right) + \beta c^T R c \qquad \text{(A.1)}$$

where $\tilde{L}$ is the measured basis material sinograms, A is the transfer/system matrix, c is the unknown basis materials coefficients vector, β is the regularization parameter, R is a regularization matrix, W is the weighting matrix which relates to the noise modeling.

An accurate variance modeling of sinograms can improve the image quality for conventional SIR. Unlike conventional CT sinogram data, the basis material sinograms in DECT have strong correlation between the two basis material measurements from the same projection path. Although an accurate DECT noise modeling with correlations is expected to benefit the image quality in SIR, the amount of improvement is unknown and difficult to study. In addition, directly utilizing the accurate noise model in some numerical methods is challenging due to the non-diagonal weighting matrix. Therefore, two main tasks are discussed in this section: (1) evaluating the numerical algorithms with accurate noise model; (2) quantifying the impact of accurate noise model in DECT by simulation study.

A.2. Covariance modeling of basis material decomposed sinograms

According to the Lambert-Beer's Law, the sinogram data (i.e., projection data) on the ray path l are obtained by [110]:

$$g_{H/L}(l) = -\ln \int_E w_{H/L}(E) \exp\left[-\mu_1(E) L_1(l) - \mu_2(E) L_2(l)\right] dE, \qquad \text{(A.2)}$$

where $\mu(E)$ indicates the energy dependent attenuation coefficients, $w_H(E)$ and $w_L(E)$ are the system weighting coefficients in high and low energy [111], $L_{1,2}(l)$ are the basis material sinograms of materials 1 and 2 along the path l.

Inspired by the previous study [26], we apply the first order Taylor expansion of Eq. (A.2) at the expected value of the basis material sinograms $\left(\mathrm{E}\left(L_1(l)\right), \mathrm{E}\left(L_2(l)\right)\right)$. In reality, this term could be replaced by the measured value of the basis material sinograms $(\tilde{L}_1(l), \tilde{L}_2(l))$:

$$\begin{bmatrix} g_H(l) \\ g_L(l) \end{bmatrix} \approx \begin{bmatrix} g_H(l) \\ g_L(l) \end{bmatrix}_{(\tilde{L}_1(l),\tilde{L}_2(l))} + \begin{bmatrix} \frac{\partial g_H(l)}{\partial L_1(l)} & \frac{\partial g_H(l)}{\partial L_2(l)} \\ \frac{\partial g_L(l)}{\partial L_1(l)} & \frac{\partial g_L(l)}{\partial L_2(l)} \end{bmatrix}_{(\tilde{L}_1(l),\tilde{L}_2(l))} \times \begin{bmatrix} L_1(l) - \tilde{L}_1(l) \\ L_2(l) - \tilde{L}_2(l) \end{bmatrix}, \qquad \text{(A.3)}$$

Then, we can write the basis material sinograms as:

$$\begin{bmatrix} L_1(l) \\ L_2(l) \end{bmatrix} \approx \begin{bmatrix} \tilde{L}_1(l) \\ \tilde{L}_2(l) \end{bmatrix} + \left(\begin{bmatrix} \frac{\partial g_H(l)}{\partial L_1(l)} & \frac{\partial g_H(l)}{\partial L_2(l)} \\ \frac{\partial g_L(l)}{\partial L_1(l)} & \frac{\partial g_L(l)}{\partial L_2(l)} \end{bmatrix}_{(\tilde{L}_1(l),\tilde{L}_2(l))} \right)^{-1} \begin{bmatrix} g_H(l)\big|_{((\hat{L}_1(l),\hat{L}_2(l))} - g_H(l)\big|_{((\tilde{L}_1(l),\tilde{L}_2(l))} \\ g_L(l)\big|_{((\hat{L}_1(l),\hat{L}_2(l))} - g_L(l)\big|_{((\tilde{L}_1(l),\tilde{L}_2(l))} \end{bmatrix}, \qquad \text{(A.4)}$$

The covariance matrix of $L_1(l)$ and $L_2(l)$ is:

$$\Sigma_L = T \Sigma_g T^T, \text{ and } \quad T = \left(\begin{bmatrix} \frac{\partial g_H(l)}{\partial L_1(l)} & \frac{\partial g_H(l)}{\partial L_2(l)} \\ \frac{\partial g_L(l)}{\partial L_1(l)} & \frac{\partial g_L(l)}{\partial L_2(l)} \end{bmatrix}_{(\tilde{L}_1(l),\tilde{L}_2(l))} \right)^{-1}, \qquad \text{(A.5)}$$

Σ_L and Σ_g are the covariance matrix of the basis material sinograms and conventional sinogram data, respectively. To simplify the numerical algorithm, one could modify Σ_L to a simplified diagonal matrix $\hat{\Sigma}_L$ by ignoring the correlations.

The procedure of basis material decomposition sinogram covariance calculation can be described by:

1: Calculate the conventional variance matrix of sinogram data by using Eq. (2.20);

2: Calculate the partial derivative of g_H and g_L for each projection ray;

3: Calculate the covariance matrix of basis material decomposition sinogram based on Eq.(A.5).

A.3. Dual-energy CT image reconstruction

In order to compare the covariance models, we define two weighting matrixes for Eq.(A.1) as:

$$W_1 = \left(\Sigma_L\right)^{-1} \text{and } W_2 = \left(\hat{\Sigma}_L\right)^{-1} \tag{A.6}$$

Inserting (A.6) to (A.1), the expectation of basis material coefficients can be yielded by solving $c^* = \arg\min \Phi(c)$. For a low dimensional problem, the closed form solution is mathematically expressed as:

$$c = \left(A^T W A + \beta R\right)^{-1} A^T W \tilde{L}, \tag{A.7}$$

And the theoretical covariance matrix of the basis materials coefficients is:

$$\text{cov}(c) = \left(A^T W A + \beta R\right)^{-1} A^T W \Sigma_{\tilde{L}} \left(\left(A^T W A + \beta R\right)^{-1} A^T W\right)^T, \tag{A.8}$$

The bias and variances are two important quantitative metrics for an estimator. In order to justify the impact of different noise models, Eq.(A.7) and Eq. (A.8) are used for computing results' bias and variance in our following evaluation studies.

A.4. Simulation setup

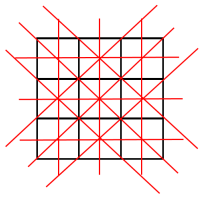

(a)

10	00	00
10	10	00
10	10	10

(b)

Figure A.1. (a) simulation problem projection geometry, (b) non-uniform phantom; the first elements in each pair indicates the coefficients of cortical bone and second elements indicates the coefficients of water

In reality, it is almost impossible to directly calculate the solution from the closed form expression due to the enormous dimension of transfer matrix. In order to assess the performance of different covariance model (i.e., W_1 and W_2) in SIR, a low dimensional simulation problem was carefully designed and its solution are calculated from closed from. Figure A.1 shows the projection geometry and a three-by-three pixel phantom with known ground truth. A total of four projection views, which contain three parallel rays at

each projection view, were designed to simulate the DECT sinogram at 80kVp and 135kVp with known normalized x-ray source emits spectrums and detector responsivity of 1.4mm thick GdOS detector. We assume both 80kVp and 135kVp rays go through the identical locations for the same projection rays.

In this study, we define the regularization term as:

$$\beta c^T Rc = \sum_j \left(\beta_1 (c_{L_1,j} - c_{L_1,j-1})^2 + \beta_2 (c_{L_2,j} - c_{L_2,j-1})^2 \right) \qquad (A.9)$$

where β_1 and β_2 are the regularization parameter for the regularization of cortical bone and water, respectively.

A.5. Numerical solution

In this section, two different numerical algorithms (i.e., iterative coordinate descent (ICD) and separable paraboloidal surrogates (SPS) methods) are utilized to examine the performance of two weighting matrixes in SIR. In this study we let $\beta_1 = 0.00276$, $\beta_2 = 0.00092$ in W_1 weighting case and $\beta_1 = 0.0057$, $\beta_2 = 0.0019$ in W_2 weighting case to achieve the same solution bias. Figure 4 shows the objective values versus the iteration steps for the two noise models, respectively. In Figure A.2 (a), ICD method reaches a smaller objective value in the W_1 weighting case, which indicates the ICD method results a more accurate solution than the SPS method. We also observe in this accurate noise model case, the ICD method converge slower than the simplified noise model in Figure A.2 (b). In Figure A.2 (b), it can be seen from the figure that both ICD and SPS methods can reach the same stable status at around 10 iterations. It can be concluded that solving the accurate noise model is challenge (i.e., lower converge rate) for conventional numerical algorithms.

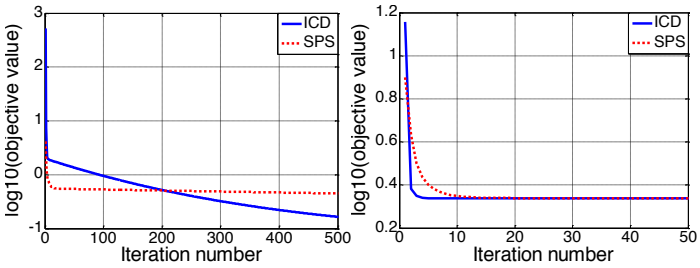

Figure A.2. Convergence of numerical methods with (a) W_1 weighting and (b) W_2 weighting.

A.6. Bias-variance tradeoff

Based on the conclusion from previous section, using accurate model in DECT image reconstruction is challenge due to the correlation terms. In order to quantify the improvement of using the accurate noise model in image reconstruction, we study the bias-variance tradeoff in this section. The mono-energy image variance at a selected region of interest (ROI) is used as the noise metric in this study. The biases of the results are presented by mono-energy image bias at the selected ROI. In this study, we choose

the second pixel (i.e., first row, second column, free of boundary condition) as our ROI and the photon energy is 50 keV.

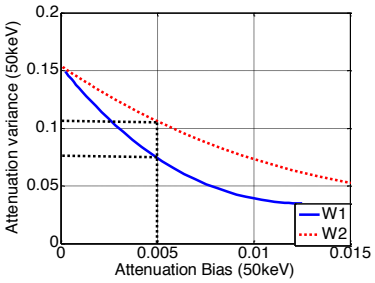

Figure A.3. Noise metric versus RMSE curve.

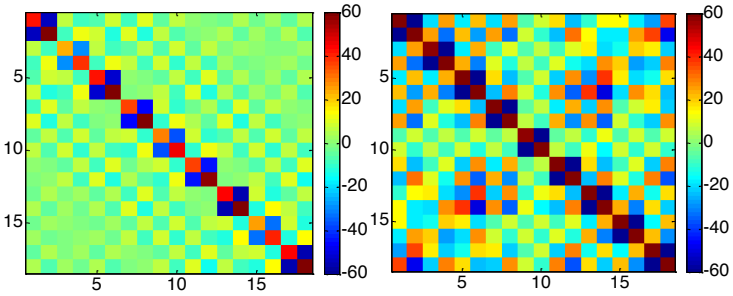

Figure A.4. Covariance matrixes of the closed form solutions (non-uniform water phantom). (a) W_1 solution; (b) W_2 solution.

Figure A.3 shows a bias-variance. From the figure, we observe that for a fixed bias level, W_1 weighting can produce the lower noise result; for a fixed variance, W_1 weighting results have lower bias. When the bias is 0.0053, the corresponding noise of W_1 weighting is about $(\sqrt{(0.1027/0.0713)}-1)\% = 20.02\%$ lower than that of W_2 weighting. The corresponding covariance images of material decomposition images are shown in Figure A.4. Similar result was also observed at other pixels. Therefore, we can conclude that the W_1 weighting indeed performs better than the W_2 weighting in this DECT image reconstruction simulation study. Therefore, the accurate noise model with correlation term can improve the reconstructed image quality and should not be simplified.

A.7. Conclusion

In numerical methods study, the accurate noise model based ICD method and SPS method show extremely slow convergence rate compared to the simplified model. The accurate model makes the variables mixed and difficult to be separated in SPS method. On the contrary, the simplified diagonal covariance model, which makes the variables separable, performs well in both ICD and SPS methods. In order to quantify the impact of accurate noise model to image quality, a bias-variance tradeoff curve was studied. The result indicates the accurate model could achieve up to 20% noise reduction compared to the simplified model.

In summary, using accurate noise model in SIR will significantly benefit the DECT image quality. The correlations between the coupled decomposed sinograms should not be neglected although they challenge some numerical algorithms.

Bibliography

[1] "CHO_MAT: Matlab image quality toolbox," Department of Radiology, University of Arizona.

[2] M. Bertalmio, A. L. Bertozzi, and G. Sapiro, "Navier-Stokes, fluid dynamics, and image and video inpainting," *2001 Ieee Computer Society Conference on Computer Vision and Pattern Recognition, Vol 1, Proceedings,* vol. 1, pp. 355-362, 2001.

[3] J. Bian, J. H. Siewerdsen, X. Han, E. Y. Sidky, J. L. Prince, C. A. Pelizzari, and X. Pan, "Evaluation of sparse-view reconstruction from flat-panel-detector cone-beam CT," *Physics in Medicine and Biology,* vol. 55, no. 22, pp. 6575-99, Nov 21, 2010.

[4] C. Bouman, and K. Sauer, "A generalized Gaussian image model for edge-preserving MAP estimation," *IEEE Transactions on Image Process,* vol. 2, no. 3, pp. 296-310, 1993.

[5] R. N. Bracewell, "Strip integration in radio astronomy," *Australian Journal of Physics,* vol. 9, no. 2, pp. 198, 1956.

[6] D. J. Brenner, and E. J. Hall, "Computed tomography--an increasing source of radiation exposure," *The New England Journal of Medicine,* vol. 357, no. 22, pp. 2277-84, Nov 29, 2007.

[7] T. M. Buzug, *Computed tomography: from photon statistics to modern cone-beam CT*: Springer, 2008.

[8] E. J. Candès, J. Romberg, and T. Tao, "Robust uncertainty principles: Exact signal reconstruction from highly incomplete frequency information," *IEEE Transactions on Information Theory,* vol. 52, no. 2, pp. 489-509, 2006.

[9] E. J. Candes, and M. B. Wakin, "An introduction to compressive sampling," *IEEE Signal Processing Magazine,* vol. 25, no. 2, pp. 21-30, 2008.

[10] T. F. Chan, G. H. Golub, and P. Mulet, "A nonlinear primal-dual method for total variation-based image restoration," *SIAM Journal on Scientific Computing,* vol. 20, no. 6, pp. 1964-1977, 1999.

[11] M. Chang, L. Li, Z. Chen, Y. Xiao, L. Zhang, and G. Wang, "A few-view reweighted sparsity hunting (FRESH) method for CT image reconstruction," *Journal of X-Ray Science and Technology,* vol. 21, no. 2, pp. 161-76, 2013.

[12] D.-Q. Chen, L.-Z. Cheng, and F. Su, "A new TV-Stokes model with augmented Lagrangian method for image denoising and deconvolution," *Journal of Scientific Computing,* vol. 51, no. 3, pp. 505-526, 2011.

[13] G. H. Chen, J. Tang, and S. Leng, "Prior image constrained compressed sensing (PICCS)," *Proc Soc Photo Opt Instrum Eng,* vol. 6856, pp. 685618, Mar 3, 2008.

[14] G. H. Chen, P. Theriault-Lauzier, J. Tang, B. Nett, S. Leng, J. Zambelli, Z. Qi, N. Bevins, A. Raval, S. Reeder, and H. Rowley, "Time-resolved interventional cardiac C-arm cone-beam CT: an application of the PICCS algorithm," *IEEE Transactions on Medical Imaging,* vol. 31, no. 4, pp. 907-23, Apr, 2012.

[15] Y. Chen, J. Ma, Q. Feng, L. Luo, P. Shi, and W. Chen, "Nonlocal prior bayesian tomographic reconstruction," *Journal of Mathematical Imaging and Vision,* vol. 30, no. 2, pp. 133-146, 2007.

[16] A. M. Cormack, "Representation of a function by its line integrals, with some radiological applications," *Journal of Applied Physics,* vol. 34, no. 9, pp. 2722, 1963.
[17] I. Daubechies, M. Defrise, and C. De Mol, "An iterative thresholding algorithm for linear inverse problems with a sparsity constraint," *Communications on pure and applied mathematics,* vol. 57, no. 11, pp. 1413-1457, 2004.
[18] B. De Man, and S. Basu, "Distance-driven projection and backprojection in three dimensions," *Physics in Medicine and Biology,* vol. 49, no. 11, pp. 2463-2475, 2004.
[19] B. De Man, and S. Basu, "A study of noise and spatial resolution for 2D and 3D filtered backprojection reconstruction," *Nuclear Science Symposium and Medical Imaging Conference, 2004 IEEE,* vol. 6, pp. 3937-3939, 2004.
[20] M. Defrise, C. Vanhove, and X. Liu, "An algorithm for total variation regularization in high-dimensional linear problems," *Inverse Problems,* vol. 27, no. 6, pp. 065002, 2011.
[21] O. Demirkaya, "Reduction of noise and image artifacts in computed tomography by nonlinear filtration of projection images," *Proceeding of SPIE Medical Imaging 2001,* vol. 4322, pp. 917-923, July, 2001.
[22] F. Dennerlein, F. Noo, J. Hornegger, and G. Lauritsch, "Fan-beam filtered-backprojection reconstruction without backprojection weight," *Physics in Medicine and Biology,* vol. 52, no. 11, pp. 3227-40, Jun 7, 2007.
[23] D. L. Donoho, "Compressed sensing," *IEEE Transactions on Information Theory,* vol. 52, no. 4, pp. 1289-1306, 2006.
[24] A. J. Einstein, M. J. Henzlova, and S. Rajagopalan, "Estimating risk of cancer associated," *The Journal of the American Medical Association,* vol. 298, no. 3, pp. 317-23, Jul 18, 2007.
[25] I. A. Elbakri, and J. A. Fessler, "Efficient and accurate likelihood for iterative image reconstruction in X-ray computed tomography," *Proceeding of SPIE Medical Imaging 2003,* vol. 5032, pp. 1839-1850, February, 2003.
[26] I. A. Elbakri, and J. A. Fessler, "Statistical image reconstruction for polyenergetic X-ray computed tomography," *IEEE Transactions on Medical Imaging,* vol. 21, no. 2, pp. 89-99, Feb, 2002.
[27] Y. Fan, H. Lu, H. Zhu, J. Wang, Q. Lin, and Z. Liang, "A novel noise suppression solution in cone-beam CT images," *Proceeding of SPIE Medical Imaging 2011,* vol. 7961, pp. 79613K-79613K-7, 2011.
[28] L. A. Feldkamp, L. C. Davis, and J. W. Kress, "Practical cone-beam algorithm," *Journal of the Optical Society of America A,* vol. 1, no. 6, pp. 612, 1984.
[29] J. A. Fessler, "Penalized weighted least-squares image reconstruction for positron emission tomography," *IEEE Transactions on Medical Imaging,* vol. 13, no. 2, pp. 290-300, 1994.
[30] T. Goldstein, and S. Osher, "The split Bregman method for l1-regularized problems," *SIAM Journal on Imaging Sciences,* vol. 2, no. 2, pp. 323-343, 2009.
[31] R. Gordon, R. Bender, and G. T. Herman, "Algebraic reconstruction techniques (ART) for three-dimensional electron microscopy and X-ray photography," *Journal of Theoretical Biology,* vol. 29, no. 3, pp. 471-481, 1970.

[32] N. H, and M. O, "CT system for spirally scanning subject on a movable bed synchronized to x-ray tube revolution," *U.S. Patent No. 4,789,929*, 1988.
[33] X. Han, J. Bian, D. R. Eaker, T. L. Kline, E. Y. Sidky, E. L. Ritman, and X. Pan, "Algorithm-enabled low-dose micro-CT imaging," *IEEE Transactions on Medical Imaging,* vol. 30, no. 3, pp. 606-20, Mar, 2011.
[34] J. Hsieh, "Adaptive streak artifact reduction in computed tomography resulting from excessive x-ray photon noise," *Medical Physics,* vol. 25, no. 11, pp. 2139, 1998.
[35] J. Hsieh, *Computed tomography: principles, design, artifacts, and recent advances*: SPIE Bellingham, WA, 2009.
[36] J. Hsieh, "Nonstationary noise characteristics of the helical scan and its impact on image quality and artifacts," *Medical Physics,* vol. 24, no. 9, pp. 1375, 1997.
[37] J. Huang, Y. Zhang, J. Ma, D. Zeng, Z. Bian, S. Niu, Q. Feng, Z. Liang, and W. Chen, "Iterative image reconstruction for sparse-view CT using normal-dose image induced total variation prior," *PLoS One,* vol. 8, no. 11, pp. e79709, 2013.
[38] D. A. Jaffray, J. H. Siewerdsen, J. W. Wong, and A. A. Martinez, "Flat-panel cone-beam computed tomography for image-guided radiation therapy," *International Journal of Radiation Oncology*Biology*Physics,* vol. 53, no. 5, pp. 1337-1349, 2002.
[39] X. Jia, Y. Lou, J. Lewis, R. Li, X. Gu, C. Men, W. Y. Song, and S. B. Jiang, "GPU-based fast low-dose cone beam CT reconstruction via total variation," *Journal of X-Ray Science and Technology,* vol. 19, no. 2, pp. 139-54, 2011.
[40] P. M. Joseph, "An improved algorithm for reprojecting rays through pixel images," *IEEE Transactions on Medical Imaging,* vol. 1, no. 3, pp. 192-6, 1982.
[41] A. C. Kak, and M. Slaney, *Principles of computerized tomographic imaging*: Society for Industrial and Applied Mathematics, 2001.
[42] A. S. Khaled, and T. J. Beck, "Successive binary algebraic reconstruction technique: an algorithm for reconstruction from limited angle and limited number of projections decomposed into individual components," *Journal of X-Ray Science and Technology,* vol. 21, no. 1, pp. 9-24, 2013.
[43] F. Khan, *The physics of radiation therapy*: Williams & Wilkins Publisher, 1984.
[44] W. A. Klender, W. Seissler, E. Klotz, and P. Vock, "Spiral volumetric CT with single-breath-hold technique, continuous transport, and continuous scanner rotation," *Radiology,* vol. 176, no. 1, pp. 181-3, 1990.
[45] P. J. La Rivière, "Penalized-likelihood sinogram smoothing for low-dose CT," *Medical Physics,* vol. 32, no. 6, pp. 1676, 2005.
[46] P. J. La Rivière, J. Bian, and P. A. Vargas, "Penalized-likelihood sinogram restoration for computed tomography," *IEEE Transactions on Medical Imaging,* vol. 25, no. 8, pp. 1022-1036, 2006.
[47] P. J. La Riviere, and D. M. Billmire, "Reduction of noise-induced streak artifacts in X-ray computed tomography through spline-based penalized-likelihood sinogram smoothing," *IEEE Transactions on Medical Imaging,* vol. 24, no. 1, pp. 105-111, 2005.
[48] T. Li, X. Li, J. Wang, J. Wen, H. Lu, J. Hsieh, and Z. Liang, "Nonlinear sinogram smoothing for low-dose X-ray CT," *IEEE Transactions on Nuclear Science,* vol. 51, no. 5, pp. 2505-2513, 2004.

[49] Y. Liu, L. Chen, H. Zhang, K. Wang, J. Ma, and Z. Liang, "TV-stokes strategy for sparse-view CT image reconstruction," *Proceedings of SPIE Medical Imaging 2013,* vol. 8668, pp. 86683D, March 6, 2013.

[50] Y. Liu, Y. Fan, H. Lu, and Z. Liang, "Improved area-simulating-volume method for X-ray CT re-projection and back-projection operations," *Conference Record of Nuclear Science Symposium and Medical Imaging Conference 2013*, November, 2013.

[51] Y. Liu, Z. Liang, J. Ma, H. Lu, K. Wang, H. Zhang, and W. Moore, "Total variation-stokes strategy for sparse-view X-ray CT image reconstruction," *IEEE Transactions on Medical Imaging,* vol. 33, no. 3, pp. 749-63, Mar, 2014.

[52] Y. Liu, J. Ma, Y. Fan, and Z. Liang, "Adaptive-weighted total variation minimization for sparse data toward low-dose x-ray computed tomography image reconstruction," *Physics in Medicine and Biology,* vol. 57, no. 23, pp. 7923-56, Dec 7, 2012.

[53] Y. Liu, J. Ma, Y. Fan, and Z. Liang, "An investigation on computed tomography image reconstruction with compressed sensing by l1 norm prior image constraints," *Nuclear Science Symposium and Medical Imaging Conference (NSS/MIC), 2011 IEEE*, pp. 2682-2687, 2011.

[54] Y. Liu, J. Ma, H. Zhang, J. Wang, and Z. Liang, "Low-dose CT image reconstruction by adaptive-weighted TV-constrained penalized weighted least-squares approach," *Proceedings of The Second International Conference on Image Formation in X-Ray Computed Tomography*, pp. 41-45, June, 2012.

[55] Y. Liu, J. Ma, H. Zhang, J. Wang, and Z. Liang, "Low-mAs X-ray CT image reconstruction by adaptive-weighted TV-constrained penalized re-weighted least-squares," *Journal of X-Ray Science and Technology,* vol. 22, no. 4, pp. 437-57, July,29, 2014.

[56] Y. Long, J. A. Fessler, and J. M. Balter, "3D forward and back-projection for X-ray CT using separable footprints," *IEEE Transactions on Medical Imaging,* vol. 29, no. 11, pp. 1839-50, Nov, 2010.

[57] H. Lu, I.-T. Hsiao, X. Li, and Z. Liang, "Noise properties of low-dose CT projections and noise treatment by scale transformations," *Nuclear Science Symposium and Medical Imaging Conference Record, 2002 IEEE,* vol. 3, pp. 1662-1666, November, 2002.

[58] H. Lu, X. Li, T. Hsiao, and Z. Liang, "Analytical noise treatment for low-dose CT projection data by penalized weighted least-square smoothing in the KL domain," *Proceeding of SPIE Medical Imaging 2002,* vol. 3, pp. 146-152, November, 2002.

[59] Y. Lu, Z. Yang, J. Zhao, and G. Wang, "TV-based image reconstruction of multiple objects in a fixed source-detector geometry," *Journal of X-Ray Science and Technology,* vol. 20, no. 3, pp. 277-89, 2012.

[60] M. G. Lubner, P. J. Pickhardt, J. Tang, and G. H. Chen, "Reduced image noise at low-dose multidetector CT of the abdomen with prior image constrained compressed sensing algorithm," *Radiology,* vol. 260, no. 1, pp. 248-56, Jul, 2011.

[61] J. Ma, Q. Feng, Y. Feng, J. Huang, and W. Chen, "Generalized Gibbs priors based positron emission tomography reconstruction," *Computers in Biology and Medicine* vol. 40, no. 6, pp. 565-71, Jun, 2010.

[62] J. Ma, J. Huang, Q. Feng, H. Zhang, H. Lu, Z. Liang, and W. Chen, "Low-dose computed tomography image restoration using previous normal-dose scan," *Medical Physics,* vol. 38, no. 10, pp. 5713-31, Oct, 2011.

[63] J. Ma, Z. Liang, Y. Fan, Y. Liu, J. Huang, W. Chen, and H. Lu, "Variance analysis of x-ray CT sinograms in the presence of electronic noise background," *Medical Physics,* vol. 39, no. 7, pp. 4051-65, Jul, 2012.

[64] J. Ma, H. Zhang, Y. Gao, J. Huang, Z. Liang, Q. Feng, and W. Chen, "Iterative image reconstruction for cerebral perfusion CT using a pre-contrast scan induced edge-preserving prior," *Physics in Medicine and Biology,* vol. 57, no. 22, pp. 7519-42, Nov 21, 2012.

[65] S. Matej, J. A. Fessler, and I. G. Kazantsev, "Iterative tomographic image reconstruction using Fourier-based forward and back-projectors," *IEEE Transactions on Medical Imaging,* vol. 23, no. 4, pp. 401-12, Apr, 2004.

[66] K. J. Myers, and H. H. Barrett, "Addition of a channel mechanism to the ideal-observer model," *Journal of the Optical Society of America A,* vol. 4, no. 12, pp. 2447, 1987.

[67] F. Noo, M. Defrise, and R. Clackdoyle, "Single-slice rebinning method for helical cone-beam CT," *Physics in Medicine and Biology,* vol. 44, no. 2, pp. 561-570, 1999.

[68] F. Noo, M. Defrise, R. Clackdoyle, and H. Kudo, "Image reconstruction from fan-beam projections on less than a short scan," *Physics in Medicine and Biology,* vol. 47, no. 14, pp. 2525-2546, 2002.

[69] L. Ouyang, T. Solberg, and J. Wang, "Effects of the penalty on the penalized weighted least-squares image reconstruction for low-dose CBCT," *Physics in Medicine and Biology,* vol. 56, no. 17, pp. 5535-52, Sep 7, 2011.

[70] X. Pan, "Optimal noise control in and fast reconstruction of fan-beam computed tomography image," *Medical Physics,* vol. 26, no. 5, pp. 689, 1999.

[71] X. Pan, and L. Yu, "Image reconstruction with shift-variant filtration and its implication for noise and resolution properties in fan-beam computed tomography," *Medical Physics,* vol. 30, no. 4, pp. 590, 2003.

[72] V. Y. Panin, G. L. Zeng, and G. T. Gullberg, "Total variation regulated EM algorithm [SPECT reconstruction]," *IEEE Transactions on Nuclear Science,* vol. 46, no. 6, pp. 2202-2210, 1999.

[73] P. Perona, and J. Malik, "Scale-space and edge detection using anisotropic diffusion," *IEEE Transactions on Pattern Analysis and Machine Intelligence,* vol. 12, no. 7, pp. 629-639, 1990.

[74] T. Rahman, X. C. Tai, and S. Osher, "A TV-Stokes denoising algorithm," *Scale Space and Variational Methods in Computer Vision, Proceedings,* vol. 4485, pp. 473-483, 2007.

[75] L. I. Rudin, S. Osher, and E. Fatemi, "Nonlinear total variation based noise removal algorithms," *Physica D: Nonlinear Phenomena,* vol. 60, no. 1-4, pp. 259-268, 1992.

[76] K. Sauer, and C. Bouman, "A local update strategy for iterative reconstruction from projections," *IEEE Transactions on Signal Processing,* vol. 41, no. 2, pp. 534-548, 1993.

[77] K. Sauer, and B. Liu, "Nonstationary filtering of transmission tomograms in high photon counting noise," *IEEE Transactions on Medical Imaging,* vol. 10, no. 3, pp. 445-52, 1991.

[78] K. Sen Sharma, X. Jin, C. Holzner, S. Narayanan, B. Liu, D. Wang, M. Agah, L. Wang, H. Yu, and G. Wang, "Experimental studies on few-view reconstruction for high-resolution micro-CT," *Journal of X-Ray Science and Technology,* vol. 21, no. 1, pp. 25-42, 2013.

[79] E. Y. Sidky, C.-M. Kao, and X. Pan, "Accurate image reconstruction from few view and limited angle data in divergent beam CT," *Journal of X-ray Science and Technology,* vol. 14, no. 2, pp. 119-139, 2006.

[80] E. Y. Sidky, and X. Pan, "Image reconstruction in circular cone-beam computed tomography by constrained, total-variation minimization," *Physics in Medicine and Biology,* vol. 53, no. 17, pp. 4777-807, Sep 7, 2008.

[81] M. R. software, "ROCKIT," Department of Radiology, University of Chicago.

[82] X.-C. Tai, S. Osher, and R. Holm, "Image inpainting using a TV-stokes equation," *Image Processing Based on Partial Differential Equations Mathematics and Visualization 2007*, pp. 3-22, 2007.

[83] X. C. Tai, S. Borok, and J. Hahn, "Image Denoising Using TV-Stokes Equation with an Orientation-Matching Minimization," *Scale Space and Variational Methods in Computer Vision, Proceedings,* vol. 5567, pp. 490-501, 2009.

[84] X. C. Tai, and C. L. Wu, "Augmented Lagrangian Method, Dual Methods and Split Bregman Iteration for ROF Model," *Scale Space and Variational Methods in Computer Vision, Proceedings,* vol. 5567, pp. 502-513, 2009.

[85] J. Tang, B. E. Nett, and G. H. Chen, "Performance comparison between total variation (TV)-based compressed sensing and statistical iterative reconstruction algorithms," *Physics in Medicine and Biology,* vol. 54, no. 19, pp. 5781-804, Oct 7, 2009.

[86] X. Tang, J. Hsieh, A. Hagiwara, R. A. Nilsen, J. B. Thibault, and E. Drapkin, "A three-dimensional weighted cone beam filtered backprojection (CB-FBP) algorithm for image reconstruction in volumetric CT under a circular source trajectory," *Physics in Medicine and Biology,* vol. 50, no. 16, pp. 3889-905, Aug 21, 2005.

[87] J.-B. Thibault, K. D. Sauer, C. A. Bouman, and J. Hsieh, "A three-dimensional statistical approach to improved image quality for multislice helical CT," *Medical Physics,* vol. 34, no. 11, pp. 4526, 2007.

[88] Z. Tian, X. Jia, K. Yuan, T. Pan, and S. B. Jiang, "Low-dose CT reconstruction via edge-preserving total variation regularization," *Physics in Medicine and Biology,* vol. 56, no. 18, pp. 5949-67, Sep 21, 2011.

[89] J. Wang, "Noise reduction for low-dose X-ray computed tomography," *Unpublished PhD dissertation, Stony Brook University, Stony Brook*, 2006.

[90] J. Wang, H. Guan, and T. Solberg, "Inverse determination of the penalty parameter in penalized weighted least-squares algorithm for noise reduction of low-dose CBCT," *Medical Physics,* vol. 38, no. 7, pp. 4066, 2011.

[91] J. Wang, T. Li, Z. Liang, and L. Xing, "Dose reduction for kilovotage cone-beam computed tomography in radiation therapy," *Physics in Medicine and Biology,* vol. 53, no. 11, pp. 2897-909, Jun 7, 2008.

[92] J. Wang, T. Li, H. Lu, and Z. Liang, "Penalized weighted least-squares approach to sinogram noise reduction and image reconstruction for low-dose X-ray computed tomography," *IEEE Transactions on Medical Imaging,* vol. 25, no. 10, pp. 1272-1283, 2006.

[93] J. Wang, T. Li, and L. Xing, "Iterative image reconstruction for CBCT using edge-preserving prior," *Medical Physics,* vol. 36, no. 1, pp. 252, 2009.

[94] J. Wang, H. Lu, T. Li, and Z. Liang, "An alternative solution to the nonuniform noise propagation problem in fan-beam FBP image reconstruction," *Medical Physics,* vol. 32, no. 11, pp. 3389, 2005.

[95] J. Wang, H. Lu, Z. Liang, D. Eremina, G. Zhang, S. Wang, J. Chen, and J. Manzione, "An experimental study on the noise properties of X-ray CT sinogram data in Radon space," *Physics in Medicine and Biology,* vol. 53, no. 12, pp. 3327-41, Jun 21, 2008.

[96] J. Wang, K. Sauer, J.-B. Thibault, Z. Yu, and C. Bouman, "Prediction coefficient estimation in Markov random fields for iterative X-ray CT reconstruction," *Proceeding of SPIE Medical Imaging 2012,* vol. 8314, pp. 831444, February, 2012.

[97] M. N. Wernick, E. J. Infusino, and M. Milosevic, "Fast spatio-temporal image reconstruction for dynamic PET," *IEEE Transactions on Medical Imaging,* vol. 18, no. 3, pp. 185-95, Mar, 1999.

[98] B. R. Whiting, "Signal statistics in x-ray computed tomography," *Proceedings of SPIE Medical Imaging 2002,* vol. 4682, pp. 53-60, 2002.

[99] J. Xu, and B. M. Tsui, "Electronic noise modeling in statistical iterative reconstruction," *IEEE Trans Image Process,* vol. 18, no. 6, pp. 1228-38, Jun, 2009.

[100] Q. Xu, X. Mou, G. Wang, J. Sieren, E. A. Hoffman, and H. Yu, "Statistical interior tomography," *IEEE Transactions on Medical Imaging,* vol. 30, no. 5, pp. 1116-28, May, 2011.

[101] Q. Xu, H. Yu, X. Mou, L. Zhang, J. Hsieh, and G. Wang, "Low-dose X-ray CT reconstruction via dictionary learning," *IEEE Transactions on Medical Imaging,* vol. 31, no. 9, pp. 1682-97, Sep, 2012.

[102] M. Yavuz, and J. A. Fessler, "Statistical image reconstruction methods for randoms-precorrected PET scans," *Medical Image Analysis,* vol. 2, no. 4, pp. 369-378, 1998.

[103] J. You, and G. L. Zeng, "Hilbert transform based FBP algorithm for fan-beam CT full and partial scans," *IEEE Transactions on Medical Imaging,* vol. 26, no. 2, pp. 190-9, Feb, 2007.

[104] H. Yu, and G. Wang, "Compressed sensing based interior tomography," *Physics in Medicine and Biology,* vol. 54, no. 9, pp. 2791-805, May 7, 2009.

[105] H. Yu, and G. Wang, "A soft-threshold filtering approach for reconstruction from a limited number of projections," *Physics in Medicine and Biology,* vol. 55, no. 13, pp. 3905-16, Jul 7, 2010.

[106] Z. Yu, J. B. Thibault, C. A. Bouman, K. D. Sauer, and J. Hsieh, "Fast model-based X-ray CT reconstruction using spatially nonhomogeneous ICD optimization," *IEEE Trans Image Process,* vol. 20, no. 1, pp. 161-75, Jan, 2011.

[107] G. L. Zeng, Y. Li, and A. Zamyatin, "Iterative total-variation reconstruction versus weighted filtered-backprojection reconstruction with edge-preserving filtering," *Physics in Medicine and Biology,* vol. 58, no. 10, pp. 3413-31, May 21, 2013.
[108] R. Zhang, J. B. Thibault, C. Bouman, K. Sauer, and J. Hsieh, "Model-based iterative reconstruction for dual-energy X-ray CT using a joint quadratic likelihood model," *IEEE Transactions on Medical Imaging*, Sep 17, 2013.
[109] W. Zhou, and A. C. Bovik, "A universal image quality index," *IEEE Signal Processing Letters,* vol. 9, no. 3, pp. 81-84, 2002.
[110] Y. Zou, and M. D. Silver, "Analysis of fast kV-switching in dual energy CT using a pre-reconstruction decomposition technique," *SPIE Proceeding,* vol. 6913, pp. 691313-691313-12, 2008.
[111] Y. Zou, and M. D. Silver, "Analysis of fast kV-switching in dual energy CT using a pre-reconstruction decomposition technique," *Proceeding of SPIE Medical Imaging 2008,* vol. 6913, pp. 691313-691313-12, 2008.